Microstructures of TiAl additively manufactured by EBM and LMD

By

Johnson Jacob

Submitted in total fulfilment of the requirements of the degree of Doctor of Philosophy

April 2020

Department of Mechanical Engineering

The University of Melbourne

Thesis Abstract

Titanium aluminide (mainly TiAl) based intermetallic alloys have superior mechanical properties up to ~800 °C and are much lighter than the currently used nickel superalloys. They have been developed for turbine engine applications in the aerospace, automobile and energy industries. Because of the inherent brittleness of TiAl, conventional manufacturing requires specially designed post processing, which is not cost and time effective. Additive manufacturing (AM) is considered as an alternative production technique, that can replace the conventional process. AM facilitate printing of complex TiAl components directly from alloy powders. Solid-state transformations (SST) associated with the unique layer-by-layer manufacturing and in situ cyclic heating in AM offer the potential to tailor the microstructure of components, creating opportunity for improving mechanical properties. The aim of this study is to systematically investigate the microstructural evolution at different processing conditions and the effect of in situ heat treatment on different solid-state transformations of γ-TiAl alloy during additive manufacturing by Electron Beam Melting (EBM) and Laser Engineered Net Shaping (LENS).

Nearly fully dense Ti-48Al-2Cr-2Nb samples with minimum defects were printed by EBM and LENS, at high, medium and low energy input conditions. Detailed microstructural characterisation along the build direction of samples printed by EBM at a high energy density (ED) of 6 J/mm^2 was conducted. X-Ray Diffraction (XRD) studies and analytical electron microscopic analysis at different locations along the build direction of the sample revealed microstructural instabilities such as discontinuous coarsening (DC) and α_2 decomposition, caused by the in situ cyclic heating with the peak temperature of each cycle approaching close to the melting point of TiAl and gradually reducing in intensity. Discontinuous coarsening with associated grain boundary migration was identified to be the dominant solid-state transformation taking place in α_2+γ primary lamellar structure (PLS), resulting in high coherence lamellar interphases in the TiAl alloy produced by both EBM and LENS. It was shown that DC replaces fine PLS by coarsened lamellae with reduced colony size, along with significant change in chemical composition and volume fraction of phases.

Reduction in interphase energy achieved by the coarsening of lamellae, with an average coarsening ratio around 18.6, was identified as a driving force for DC. High chemical free energy in PLS mainly caused by supersaturated α_2 phase with a non-equilibrium phase fraction

of 26%, can be considered as another factor inducing DC. Ascertaining this assumption, α_2 phase fraction approaches its equilibrium composition after 11 cycles of in-situ heating. Colony size also considerably reduced as a consequence of DC reaction. β phase formation, which is identified as another side outcome of these driving forces, shows a variation in phase fraction with build temperature, from 3.5% at 950 °C to 8% at 1050 °C. DC, along with β phase formation greatly influences microstructural morphology and mechanical properties of TiAl. Similar trend was observed in LENS fabricated samples. The major variation was the absence of β formation in LENS, which is attributed to the lack of pre-heating during LENS. Alloy modifications such as addition of 0.5 Si (at.%) as experimented in this study, result in precipitate pinning at interphase, potentially reducing excessive coarsening.

This study summarises the process of DC and beta phase formation in TiAl alloys during EBM and LENS processes and discusses the strategies to regulate DC and beta formation through AM of TiAl and utilize the intrinsic solid-state transformations in AM for controlling the microstructure to achieve application specific material properties.

DECLARATION

This is to certify that

(i) The thesis comprises only my original work towards the PhD except where indicated in the Preface,

(ii) Due acknowledgement has been made in the text to all other material used,

(iii) The thesis is less than 100,000 words in length, exclusive of tables, maps, bibliographies and appendices.

_____

Johnson Jacob

April 2020

ACKNOWLEDGEMENTS

I would like to thank everyone who has helped me for the completion of this Thesis. Above all I would like to offer special thanks to the following people; I thank my principle Supervisor Prof. Kenong Xia for his continuous encouragement, support and valuable guidance during my research work. I also thank my co supervisor Dr. Edward Lui for his discussions and support.

I would also like to express my sincere gratitude to my external supervisor Mr. Stefan Gulizia, for giving me the opportunity to work on this interesting project at the Commonwealth Scientific and Industrial Research Organisation (CSIRO). I also thank my second external supervisor Dr. Darren Fraser from CSIRO, for his patience, helpful input, and supportive advice and contribution during this research work. His expertise and invaluable comments helped greatly in the completion of this thesis.

I also thank my external supervisor Prof. Ranjit Bauri, from IIT Madras, India for his discussions and visit to University of Melbourne.

I acknowledge the receipt of University of Melbourne postgraduate scholarships and financial and experimental supports from the Commonwealth Scientific and Industrial Research Organisation (CSIRO). I also acknowledge the facilities and technical assistance of the Bio21 Advanced Microscopy Unit at the University of Melbourne.

I thank all my colleagues at the University of Melbourne; all the Academic Staff and Students, and especially Dr. Prathap, Dr. Ahmad Dr. Yu Bai and Dan for all the support and the fun we had working together. I also thank the Academic staff and students at CSIRO manufacturing, where I spent most of my time for this work as a post graduate student, and especially Dr. Sri Lathabai, Peter, Tery, David, Robert, Yesim, Julian, Andrew Minh, Aaron, Mark, Geoff, Malija, Guan and Amal. I thank my family, for supporting me throughout and being patient to this very difficult period for me. My friends that have been so patient and supporting all this period. Especially, Richards, Manu and Jobin who were always there for me during the very difficult times.

Chinnu, I am not sure if I can ever be able to thank you enough. Without you I wouldn't be able to complete this. I specially appreciate you my baby Serah, for being patient at this very difficult period for me and making me happy with your angelic presence. Last but foremost I thank Almighty God for everything.

Table of Contents

List of figures

List of tables

Chapter 1: Motivation

In TiAl alloys the dual phase microstructure of α_2 (Ti_3Al) and γ (TiAl) has shown better combinations of mechanical properties compared to other microstructures. Different microstructural arrangements of these dual phases have been formed based on processing condition, alloy composition and post processing. Despite many suitable properties, TiAl alloys have not been widely used because of difficulties in conventional cast manufacturing due to lower ductility and thermal cracking in the material. Fully lamellar microstructures in TiAl can be made of alternating α_2 (Ti_3Al) and γ (TiAl) plates. These microstructures have exhibited relatively high creep resistance and fracture toughness, but low ductility and strength. Low ductility and strength have been the main disadvantages when compared with duplex microstructures. Properties have been shown to improve when refinement has been done to the fully lamellar microstructure.

Conventional processing such as casting has been associated with a coarse lamellar microstructure, and the process modifications available have been quite expensive to refine the grain size. Recently additive manufacturing (AM), mainly EBM, has proven to be a promising alternative to the casting of titanium aluminide alloys and has been done in a time and cost-effective manner. Previous research in this area has concentrated mainly on the effect of changes in process parameters on the mechanical properties, especially ductility and fatigue. The effect of microstructural changes has been clearly anticipated to be related to processing and subsequently to the mechanical properties, however, it is still an area of research that needs to be addressed in detail. In the case of AM, its' unique characteristics, like in situ thermal cycling and high rate of cooling, is predicted to affect microstructural evolution, and a non-equilibrium chemical composition is anticipated due to high cooling rate. This needs to be investigated by systematic analysis of AM processed TiAl. In this work there are several topics that have been chosen that require further investigation, including microstructure changes occurring with changes in alloy composition, processing routes, and post processing the as built material.

TiAl-based alloys have been especially designed for high-temperature applications and understanding the thermal stability of these alloys is of great importance. Several thermal instabilities like discontinuous coarsening (DC) of the primary lamellar structure, β phase

precipitation by the decomposition of α_2, and spheroidization and growth of γ phase, are noted in TiAl and relevant to AM. Different solid-state transformations in AM, directly influencing the as fabricated microstructure and mechanical properties, needs to be studied in detail. DC has a considerable role in microstructural evolution, mainly the colony size, inter lamellar thickness, and phase fractions of phases. Up until now, as per the author's knowledge, the discontinuous coarsening of TiAl alloys in EBM, is not reported in the literature.

The motivation of this study is to better understand the microstructural evolution in gamma TiAl during the EBM and LENS AM processes by doing systematic microstructural characterisation of the as fabricated and heat-treated samples. Conventional alloys for casting may not be best for AM and alloy development specifically to AM is also explored. It is expected that the research will lead to improved performance of TiAl, processed by AM.

Chapter 2: Literature Review

2.1. Titanium (Ti) Alloys

Titanium is a transition metal (group IV). Elemental Ti exists in various crystallographic structures. Commercially pure (CP) titanium has a hexagonal closed-packed (hcp) crystal structure, known as alpha (α) phase at room temperature. Temperature induced allotropic transformation occurs at β transus temperature (882 ±2 °C) at atmospheric pressure where the crystal structure of Ti changes from hcp to bcc crystal structure (β phase). Elemental addition to CP titanium alters the β transus temperature. Generally, addition of other elements is intended to improve the mechanical properties of an alloy rather than altering the phase transition temperature.

2.1.1 Classification of Ti alloys

Based on the element added and the dominant phase in their structures, Ti alloys are categorised into three- α, β and α+β alloys. Alpha (α) alloys contain α stabilizers at a larger concentration with small amount of β stabilizers. Generally, pure titanium and its alloys with elements like Al, O, Sn (non-transitional metals) are categorized as α alloys. These alloys exhibit high creep resistance and toughness. Their density is high, but ductility is usually low [1]. Beta (β) alloys contain β stabilizers at a larger concentration with small amount of α stabilizers. Titanium alloys with elements such as Nb, V, Cr and Mo (transitional metals) are categorized as β alloys. These alloys have high strength compared to α alloys, but corrosion resistance and ductility are low [1]. β alloys are useful at moderate temperatures. Alpha-Beta (α+β) alloys contain both α and β stabilizers. They have higher strength and responds well to heat treatments. Among these alloys, Ti–6Al–4V is mostly used, which has applications ranging from biomedical devices to marine and aerospace industries [1, 2].

2.1.2 Limitations of Conventional Ti alloys

Ti alloys are renowned for their better strength-to-weight ratio and corrosion properties in wide range of applications and has a recognisable role in engineering sector. Since maximum service temperature is 400 °C, despite attractive properties, their application is limited. This makes Ti alloys not suitable for critical light weight applications in aerospace and automobile industries. This prompted researchers to explore Ti based material at high aluminium concentration, with focus on two types of phases, both of which are classified as titanium aluminide phases [2].

2.2. Titanium Aluminides: An Overview

Titanium aluminides are intermetallic compounds. Intermetallics are compounds with ordered structure, formed between two metals (NiAl, TiAl, Ti_3Al etc.). In an alloy system, the solute atom in excess of solid solubility forms compound with solvent. This compound with fixed stoichiometric composition is known as intermetallic. These are somewhere between disordered metallic alloys and ceramics. Bonding in intermetallics is a combination of metallic, ionic and covalent bonds. The long-range ordering in intermetallic phases restricts deformation modes and as a result, provides a high melting point, increased high temperature strength but room temperature ductility is low.

TiAl-based alloys have been investigated for about half a century as an alternative to brittle ceramics and heavy Ni-based superalloys, for high temperature applications. Reduction in weight would be of huge benefit to rotating parts that work at higher temperatures. By using TiAl, this can be achieved to a great extent. The properties of TiAl are comparable to other superalloys and its high temperature properties are superior to titanium alloys. A brief comparison of mechanical properties of Ti, TiAl alloys and Ni-based superalloys is depicted in Table 2.1.

Table 2.1: Properties of TiAl, Ti and Ni superalloys [3].

Properties	TiAl	Ti_3Al	Ti	Ni-Super alloys
Crystal structure	$L1_0$	$D0_{19}$	hcp/bcc	fcc/$L1_2$
Density (gm/cm^3)	3.8	4.2	4.5	8-9
Elastic modulus (GPa)	160-180	100-150	95-115	190-220
Yield Strength (MPa)	400-650	700-1000	300-1300	250-1300
Ductility at RT (%)	1-4	1-4	10-40	5-50
Fracture toughness ($MPa\ m^{1/2}$)	10-30	10-30	20-80	25-50
Creep limit (˚C)	800-900	750	600	1100
Oxidation limit (˚C)	800-900	650	600	1100

Figure 2.1 shows superior specific strength and elastic modulus properties of TiAl alloys at higher temperatures. Figure 2.1(a) shows specific strength of various groups of alloys with temperatures. Figure 2.1 (b) shows specific elastic modulus comparison for alloy groups.

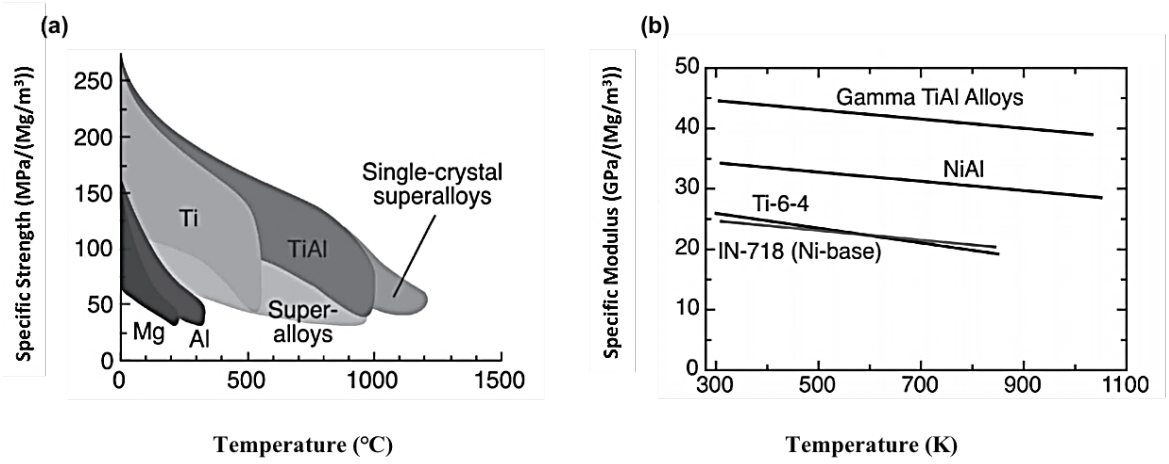

Figure 2.1: (a) Specific strength of various groups of alloys with temperatures, (b) Specific elastic modulus comparison for alloy groups [3].

TiAl intermetallic alloys have important commercial applications in automotive and aerospace industries, like low-pressure turbine (LPT) blades in gas turbine engines [4].

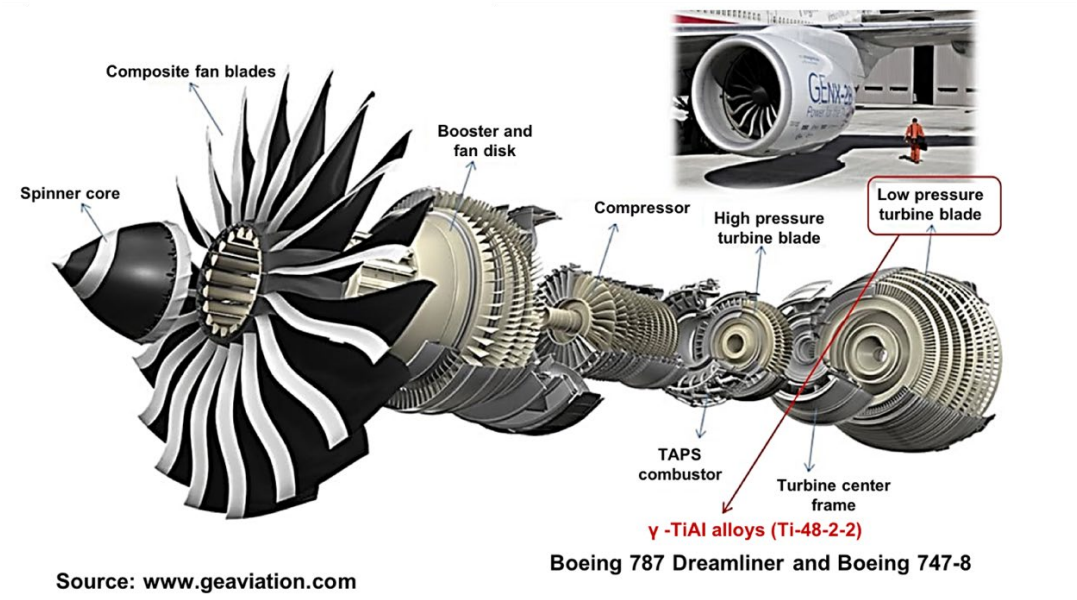

Figure 2.2: Open view of GENX engine, in which low pressure turbine blade is composed of γ-TiAl alloy [4].

Titanium aluminides replaced nickel super alloys in low-pressure turbine (LPT) blades. This development is expected to reduce the overall weight of the low-pressure gas turbine. According to GE, blades made from TiAl can reduce the weight of the entire low-pressure turbine by 20-30% [5]. The possibility of using TiAl in many more applications is progressing well with advanced manufacturing and development.

2.2.1 Ti-Al Binary Phase Diagram

Ti-Al binary phase diagram contains several intermetallic phases, but the alloy compositions of major technological interests have 43-50 at.% Al. These alloys are typically based on two ordered phases, γ and α_2, which are stable up to 1120 ºC. Among these compounds, the attention is directed towards titanium aluminide in the dual phase region made up of α_2 and γ phase, which shows wide range of microstructure and better combination of mechanical properties. Four solid phases of interest are: β-Ti, α-Ti, α_2 and γ. Figure 2.3 shows the Ti-Al binary phase diagram showing intermetallic phases.

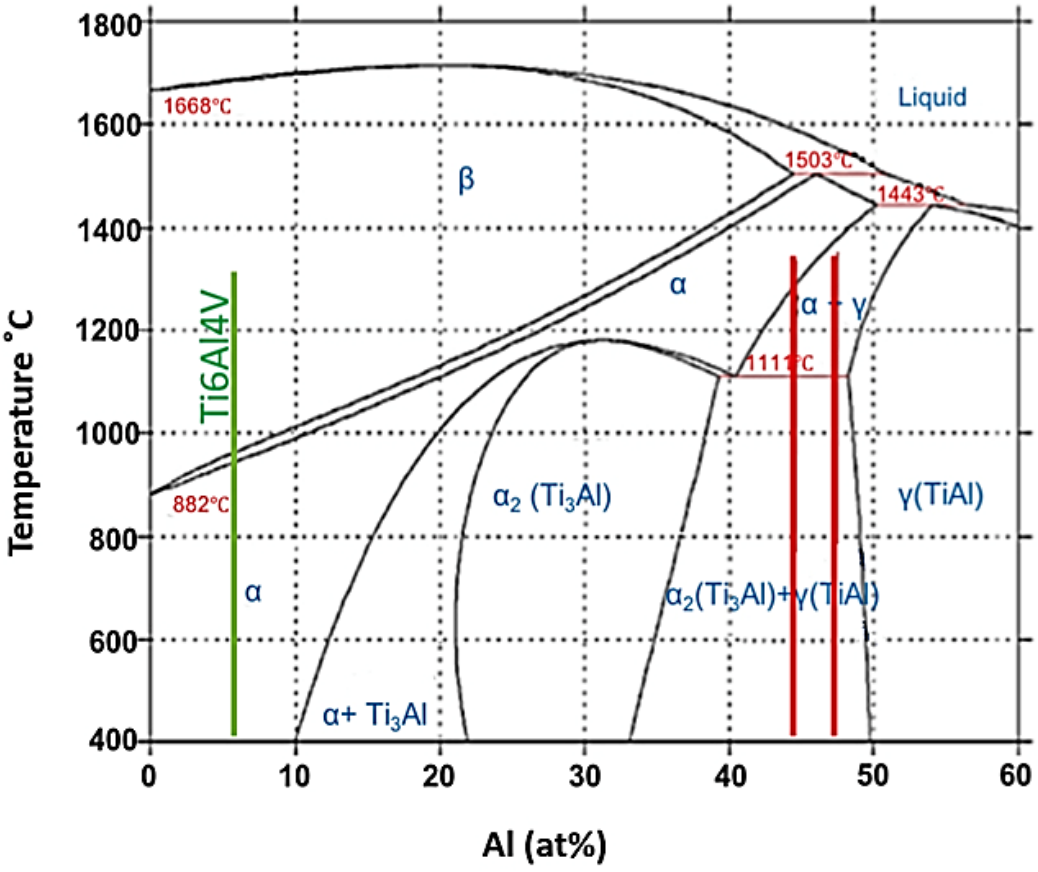

Figure 2.3: Ti-Al binary phase diagram [3].

2.2.2 α_2-Ti_3Al

Ti_3Al (α_2) phase has an Al content between 22 ~ 39 at.% and $D0_{19}$ ordered structure with a hexagonal symmetry and stacking sequence |ABAB|. Figure 2.4(a) shows the structure of ordered α_2 phase in TiAl system. Lattice parameters are a=0.577 nm, c=0.420 nm; and the (c/a) ratio is 0.73**.** [3, 6]. Titanium with hcp and bcc crystal structures are known as α and β titanium, respectively. α_2 phase is ordered form of α hcp, formed during cooling by $\beta \rightarrow \alpha \rightarrow \alpha_2$. On heating, it transforms back to disordered hcp structure at around 1125 ~ 1150 °C. α_2 phase exhibits better high temperature strength but ductility is found to be very low.

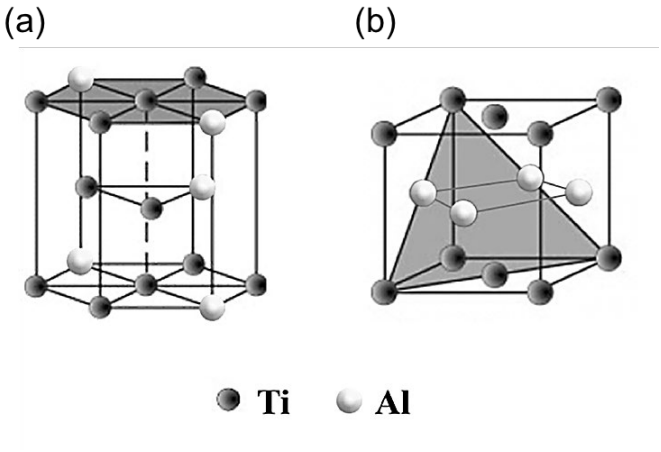

Figure 2.4: Structure of ordered phase in TiAl system (a) α_2-Ti_3Al, A3B:$D0_{19}$ (b) γ -TiAl, AB: $L1_0$.

2.2.3 γ-TiAl

TiAl (γ) phase exists within a wide composition range, containing 48.5 to 66 at.% Al. This is $L1_0$ type face-centred tetragonal structure with stacking sequence |ABCABC|. Figure 2.4 (b) shows the structure of γ phase in TiAl system. Figure 2.5 (a) and (b) shows arrangement of atoms on the close packed planes in γ and α_2 respectively. Close packed planes, {111}γ and (0001)α_2 and close packed directions, <110>γ and <1120>α_2, are parallel to one another when it comes to the orientation relationship between two phases [3, 6].

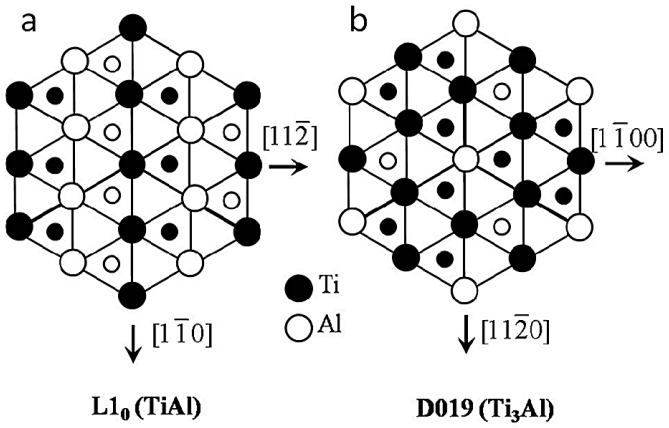

Figure 2.5: The close-packed planes in γ and α_2.

For a stoichiometric composition, room temperature lattice parameters of γ are c=4.08Å and a=3.995Å, c/a ratio around 1.02, small tetragonality. Lattice parameters are directly proportional to Al content. With increasing Al content tetragonal distortion increases. Whereas with a decreasing Al content, c/a ratio decreases, approaches unity and structure changes to ordered fcc. The six orientation variants of the γ phase are shown in Figure 2.6. Each hatched pattern corresponds to a specific variant [7].

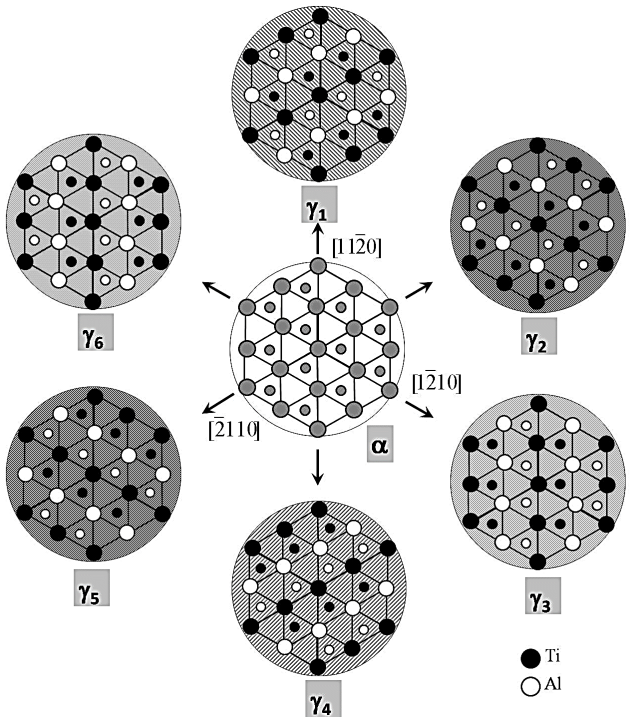

Figure 2.6: Six orientation variants of the γ phase.

2.2.4 β /B2 Phase

The bcc phase of TiAl is named as β phase and ordered counterpart of bcc phase is B2 [3, 8]. B2 phase, labelled as L_{20} is present in many systems, which are of superior importance in engineering field, like FeAl, NiAl based alloys. Beta phase is softer than α_2 and γ. β stabilized TiAl alloy has good high temperature formability at around 950 °C, due to the presence of beta. Finer β phase significantly controls mechanical properties. So, it is required to study the role of β phase in microstructural evolution and its effect on mechanical properties in detail.

2.2.5 α_2+γ dual phase

For engineering applications, the preferred TiAl form is the dual phase gamma TiAl, containing a fraction of 10- 30 % α_2, with γ phase (Al content is around 44-49 at.%). These alloys also contain other elements like Cr, B, Mo, Si, V, Nb, Mn, W and Ta [3, 9]. The purpose of these elemental additions is to improve the mechanical properties, especially strength, ductility, oxidation resistance and creep resistance. Details on elemental addition is discussed in a later section. Phase diagrams for multicomponent alloys are generally not available. However, the binary TiAl equilibrium phase diagram provides the necessary basic information. The dual phase TiAl generates a variety of microstructures depending upon the heat treatment schemes, thermo mechanical treatments and alloy additions.

2.3 Gamma Titanium Aluminide (α_2+γ dual phase) Microstructure

Considering γ- TiAl, the majority of commercial applications are reserved for materials with Al amount between 44-49 at.%. Based on their chemical composition and processing parameters, observed microstructure is broadly categorised into four classes: Near-gamma (NG), duplex (DP), near lamellar (NL) and fully lamellar (FL). A general schematic representation of TiAl microstructure is shown in Figure 2.7. DP/NG alloys are characterised by higher room temperature (RT) tensile strength, ductility and longer fatigue life than FL/NL alloys. Whereas FL/NL alloys have better creep resistance, higher fracture toughness and crack propagation resistance than DP/NG structures. A coarse-grained lamellar structure results in low RT tensile strength and ductility. Yield strength and ductility of Ti based alloys can be significantly increased by decreasing grain size [9, 10].

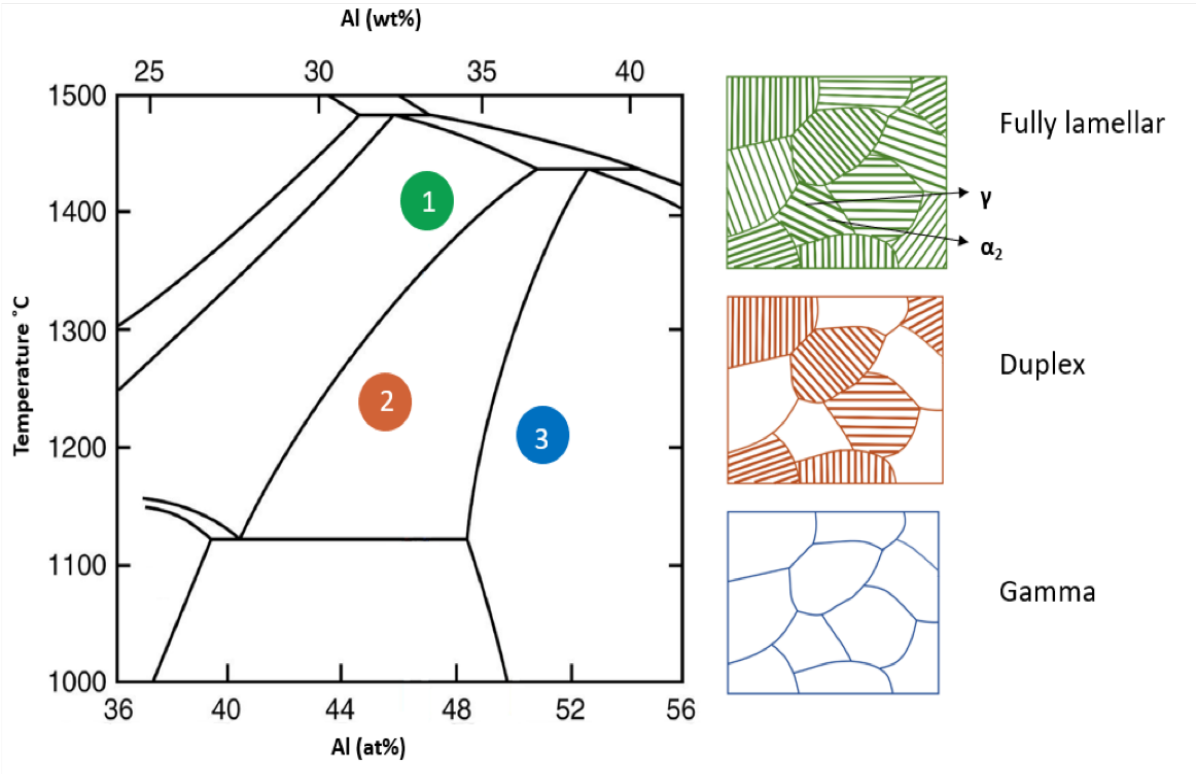

Figure 2.7: Schematic of common microstructures in TiAl alloys.

2.3.1 Near-gamma microstructure

Types of microstructures in γ–TiAl based alloys -near gamma, fully lamellar and duplex microstructure are shown in Figure 2.8. As shown in Figure 2.8, when TiAl alloy is aged for a long duration at temperatures T_1 in the (α + γ) two-phase field, "near- γ' microstructure is obtained. This consists mostly of equiaxed γ grains with small α_2 grains at the grain boundaries. Although this microstructure has good elastic modulus, its creep resistance, high temperature properties and fracture toughness are poor. This is more brittle and is not suitable for structural applications [10].

2.3.2 Fully lamellar microstructure

Figure 2.8 shows microstructural variation at different heat treatment conditions. The temperatures T1, T2, T3 and T4, are indicated relative to the respective phase transition temperatures [3]. When TiAl alloy is heat treated at temperatures above α-transus, in the single-phase field (e.g. at T_4 as in Figure 2.8) and furnace cooled, fully lamellar microstructure with coarse grains is obtained. Grain size of this microstructure is typically >300 μm in

conventional processing. This type of microstructure has received much attention because with respective to other standard microstructures, it has improved creep resistance, although poor ductility at room temperature is a drawback. Lamellae of this microstructure are made up of alternating layers of α_2 and γ laths. [11]

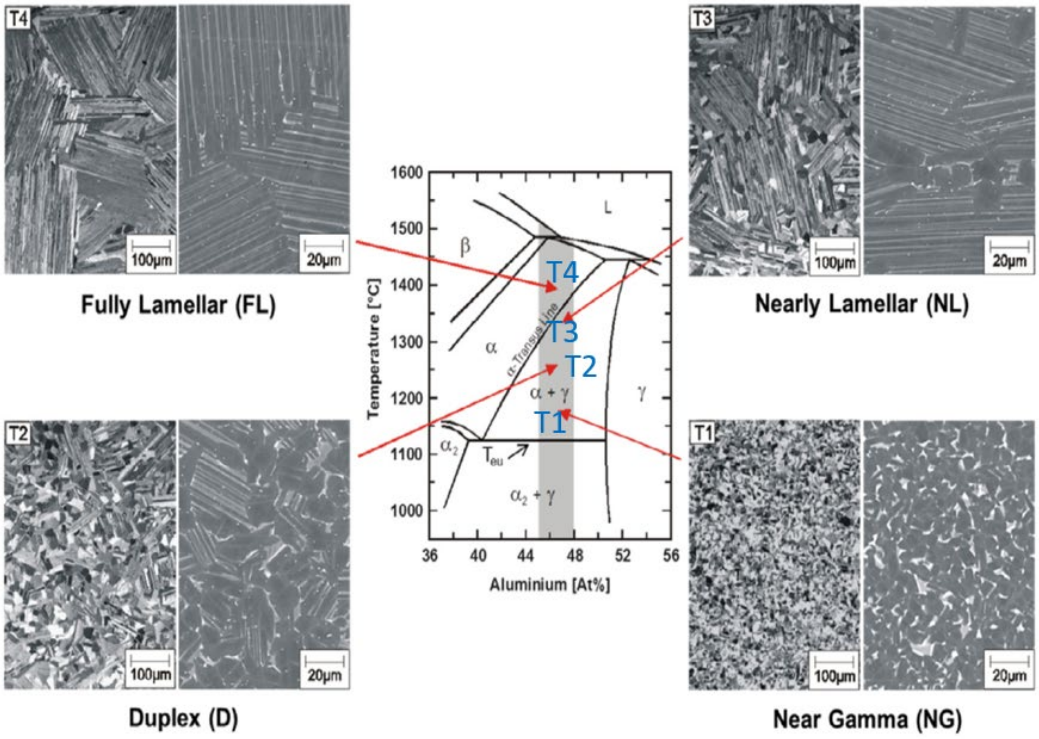

Figure 2.8: Types of microstructures in TiAl based alloys. The temperatures T1, T2, T3 and T4 of the heat treatments are indicated relative to the phase transition temperatures [3].

2.3.3 Duplex microstructure

Heat treatment at T_2 is expected to produce a uniform microstructure with approximately equal phase fractions of lamellar and equiaxed γ grains. At this temperature the initial quantities of α and γ phases are approximately equal, resulting in competitive growth of α and γ grains. Upon cooling, α_2 and γ lamellae are formed in the prior α grains via following the sequence, $\alpha \rightarrow$ lamellar (α/ γ) $\rightarrow$ lamellar (α_2/ γ). Heat treatment at T3 results in a lower phase fraction of equiaxed γ grains and a larger lamellar grain size because α phase predominates at this temperature. In contrast, heat treatment at T1 produces a higher phase fraction of equiaxed γ grains and fewer lamellar grains. It has been suggested that a lamellar grain volume fraction of

approximately 30% yields ideal balance in tensile properties [12]. Duplex microstructure has better tensile strength and ductility (up to 4% elongation) at room temperature; but it has inferior creep resistance and fracture toughness.

2.3.4 Microstructures and their effects on mechanical properties

TiAl alloys exhibit unique microstructures (duplex, nearly-lamellar, fully lamellar) with marked difference in properties including lamellar spacing, lamellar thickness, grain size and volume fraction of phases. This difference in microstructure significantly affects mechanical properties, especially tensile and creep properties. An ideal microstructure with all desired mechanical properties is not obtainable and the phase of interest for particular applications is not molded directly from the as-cast material. Among the microstructures, the duplex microstructure exhibits fairly balanced performance with respect to ductility and tensile strength. But the use is limited in high temperature, up to 760 °C due to its inferior creep properties [13,14]. Fully lamellar microstructure possesses optimum creep strength and fracture toughness among the three microstructures but shows limited ductility at room temperature. If lamellar grain size and spacing are refined, fully lamellar structure can exhibit better combination of properties than duplex, as smaller colony size of refined microstructure improves ductility and narrow lamellar spacing provides better creep and high temperature properties [3].

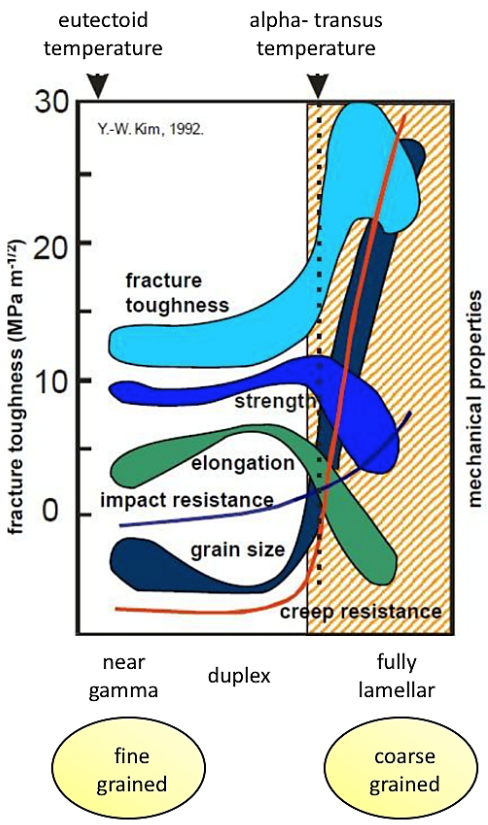

Figure 2.9: Mechanical properties versus microstructure of TiAl [14].

2.4 Solidification and phase transformations in TiAl

Solidification of γ- TiAl alloys happens mainly via the β phase or peritectically. Solidification path varies according to the composition of alloy and processing conditions and results in formation of vast variety of microstructures. Since alloying elements are also added to alter the morphology and mechanical properties, multicomponent alloys follow even more complex routes for phase transformation [15].

Gamma TiAl alloys typically have Al concentrations of 44 to 48 at.% and solidify according to the phase diagram shown in Figure 2.10, either through the β phase or peritectically. Depending on processing conditions and alloy composition, it is even possible that two peritectic reactions could occur [3]. Small differences in the Al concentration can result in different solidification microstructures.

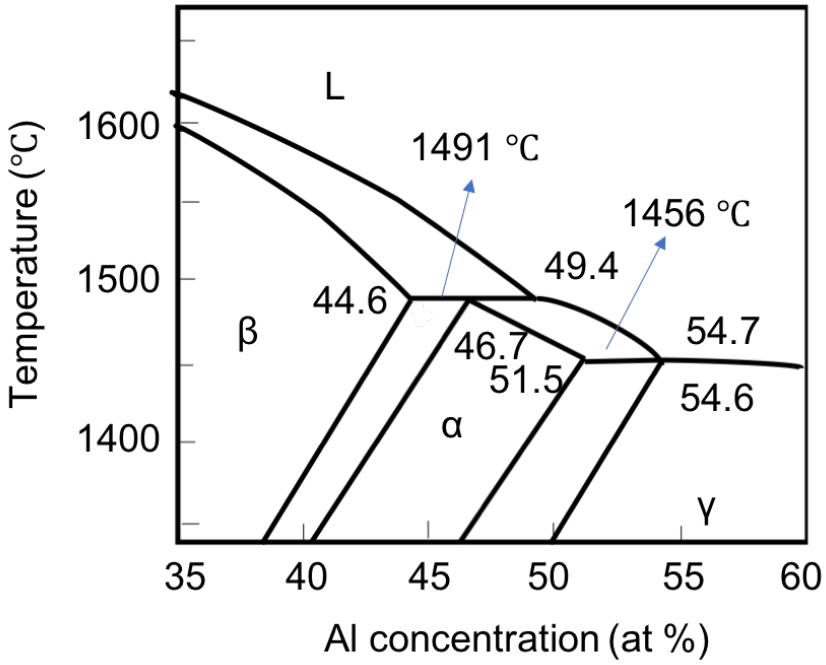

Figure 2.10: Section of the binary Ti-Al phase diagram [3].

If the Al content is less than <45 at.%, TiAl solidifies via β phase. The pathway can be tracked as L → L+ β → β → β + α → α → α+ γ. The solidification path for TiAl with Al concentrations of 45-49 at.% is L→ L+β → *L* + β +α→ L+ α →α → α +γ → α_2+γ. As a result, α phase is formed peritectically, along with dendrites. In situations where Al at.% is >50%, α phase is formed first followed by peritectic reaction. L+ α → γ [3, 16, 17].

2.4.1 Rapid solidifications

The term rapid solidification is normally applied when cooling rate is greater than 100 °CS^{-1}. During solidification of TiAl if the cooling rate is very high (>300 °CS^{-1}) a non-equilibrium volume fraction of α_2 phase will be formed along with other retained phases, either disordered α or β phase [3,18]. In cases with <300 °CS^{-1} solidification rate, massive transformation of existing α phase to fine and feathery γ phase, takes place. Primary ultrafine α+ γ lamellar microstructures with enhanced properties can be produced by aging or heat treatment of these non-equilibrium samples. Additive manufacturing (AM) technologies for metal manufacturing, characterised by ultra-fast cooling has gained recognition now and hence many researches currently focus on microstructural development at very high cooling rate, 10^3 -10^8 °CS^{-1}.

2.4.2 Solid-state transformations

In TiAl alloys, the phase transformation process during rapid solidification often occur far from thermodynamic equilibrium and are governed by complex heat transport and diffusion processes, that depend on the solidification conditions [3]. Final microstructure and texture are influenced by different solid-state transformations after the solidification process. Different microstructural evolution and precipitation reactions are observed in TiAl alloys, with respect to the processing route and alloy composition. Variation in cooling rate influences the solid-state transformations. In the following sections massive transformation and lamellar transformation are discussed.

2.4.2.1 Massive transformations

Massive transformation is a discontinuous composition- invariant phase transformation, behind a migrating reaction front. Short - range diffusion is needed for it. α phase undergoes massive transformation to form γ structure, when cooling rate is higher. The cooling rate for massive transformation should be fast enough to prevent formation of primary lamellar structure [19]. Massive transformation gives rise to a fine and feathery microstructure. Initial α grain and resultant γ grain possess different orientations. There is a need for further investigations, to obtain a better understanding about massive transformations. It is observed that γ phase produced as a result of massive transformation is unstable and will be transformed into α_2 and γ phases, which are stable, on further aging. Figure 2.11 shows a schematic illustration of the feathery massive gamma phase.

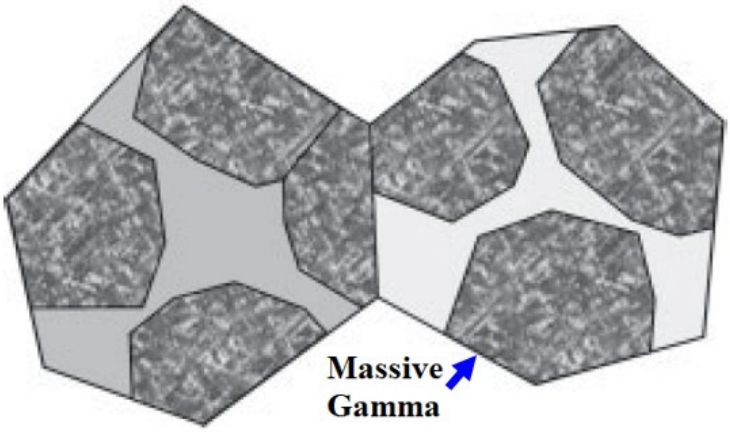

Figure 2.11: Schematic illustration of the feathery massive gamma phase [3].

2.4.2.2 Formation of $\alpha_2+\gamma$ lamellar structure

For the formation of $\alpha_2+\gamma$ lamellar structure from single phase α field, Denquin & Naka postulated two reactions [20, 21].

$$\alpha \rightarrow \alpha + \gamma \rightarrow \alpha_2 + \gamma$$

$$\alpha \rightarrow \alpha_2 \rightarrow \alpha_2 + \gamma$$

Eutectoid formation mechanism of lamellar TiAl structure is a topic of ongoing debate. In the above steps eutectoid reactions do not take place, instead ordered **γ** precipitation from α or α_2 phases occurs. The resultant microstructure formed by both of these paths mentioned above, are so similar that the nucleation and growth process are deemed to be the same. The precise formation mechanisms of α + γ lamellar microstructure is not extensively studied for ternary TiAl alloys.

The formation of lamellae is diffusion controlled. A minimum of 80 °C of undercooling is required for the nucleation of γ and it grows through the diffusion mechanism. Tetragonal fcc γ needles are formed within hcp α grains and that is the first step. Growth of γ needles continues through long range diffusion and remaining α is ordered to α_2 lastly.

Shockley partial dislocation movement was postulated by Denquin et al. [20], as the transformation mechanism causes α lamellae transformation to γ lamellas. Lamellae formed

will be having {111}γ//(0001)α_2 and <110]γ//<1120>α_2 Blackburn orientation relationship. Tetragonality in the γ and hexagonal α_2 makes {111}γ and plane (0001)α_2 non- parallel and hence, incoherent phase boundaries are formed. Cooling rate bears an important role in lamellar formation. Different cooling rate leads to the formation of various lamellar morphology and it is inter-related to diffusion. If cooling rate is high, atoms become less mobile and the diffusion becomes slow, causing sluggish lamellar growth and as a result, fine lamellae are formed. With slow cooling rate, lamellae get enough time to get thickened and sparse γ nucleations are also observed.

2.4.2.3 Refinement of lamellar microstructure

Duplex microstructures have better room temperature ductility and tensile properties, but their fracture toughness and creep resistance are poor. The scenario is just opposite for coarse-grained fully lamellar microstructure. Recently, Fine-grained fully lamellar (FGFL) microstructure is reported to improve the mechanical property balance in γ -TiAl alloys [3, 22].

To refine the microstructure and to obtain desired mechanical properties, extensive researches have been done. The fine-grained lamellar structure with grain size <50 μm shows best combination of strength and ductility [22]. Extensive thermo-mechanical processing or grain refinement by minor alloying or their combinations are researched in order to produce FGFL microstructures. Lamellar thickness variation with different cooling rate is shown in Figure 2.12 [23].

In TiAl alloys, ~0.5 – 1 μm lamellar spacing could be created by controlled furnace cooling whereas fast cooling in air causes a finer lamellar spacing of ~ 50 - 75 nm. Alloy composition, heat treatment method, temperature, and cooling rates affect lamellar colony size, thickness, spacing and lamellar orientation. Since diffusion rate gets increased and other phases are not there to inhibit the α grain growth, lamellar grain size will be increased when heat treatment time and/or temperature in the single-phase α field is increased [3, 6].

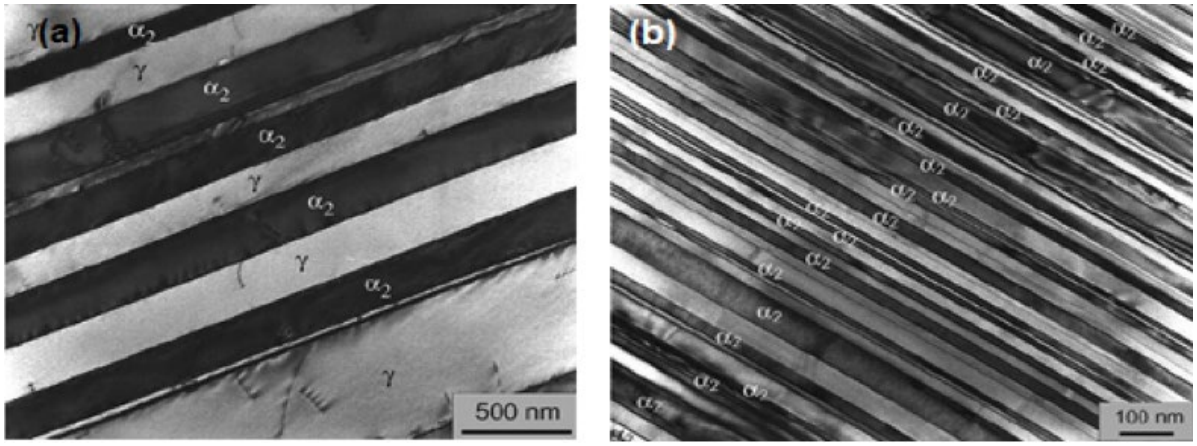

Figure 2.12: TEM microstructures of TiAl showing lamellar thickness variation (a) furnace cooled and (b) air cooled [23].

The important aim of alloy design strategy is to achieve refined-colony/ultrafine-lamellar microstructures in two phase near gamma alloy. Cast TiAl alloys grain size can be refined by adding boron. Alternative approaches are by quenching and subsequent ageing of massive transformed gamma in upper (α+β) region, which results in fine lamellar microstructure. This process may result in quench crack. When grain size of the fully lamellar microstructure is reduced from 1200 μm to 52 μm, the strength and ductility increase drastically from ~380 MPa and 0.8% to ~520 MPa and 3.8% respectively [24, 25].

2.5 Heat treatment

Regions in the phase diagram which are important for heat treatments and microstructural control includes,

• The high temperature (α+β) two-phase field

• The α single-phase region

• The (α+γ) two-phase region bounded by the α transus line ‘Tα' and the γ solvus line

• The α_2+γ two-phase field.

Manufacturing method and cooling rate determine the microstructure of as-cast materials. When cooled to room temperature from liquid during different manufacturing methods, materials will have to go through different regions of phase diagram and the microstructure of

the end product also will be different. Alloy composition also has significant influence on the microstructure and phases present in the as-produced materials. Since Cr and Nb has a role in forming and stabilizing β, small amounts of β phase may be formed when cooling commercial TiAl alloys like Ti-48Al-2Cr-2Nb [3, 26]. At times, the end product will not be having any of the desirable properties and it becomes necessary to alter the microstructure with the aid of treatments like hot isostatic pressing (HIP), heat treatment or hot working. Temperature of heat treatment is dependent on time of holding, composition of alloy and rate of cooling.

Hot Isostatic Pressing uses heat and high pressure to refine the microstructure of the as fabricated parts. Microstructural homogenization and removal or reduction of porosity from manufactured parts can be achieved by HIPing. To effectively remove the pores, HIPing temperature needs to be high enough to take TiAl parts to α+γ phase field [27]. To restrict the temperature related microstructural changes like recrystallization, grain growth and phase transformations, higher pressure is tried with reduction of temperature. Based on the requirement of final microstructure and properties, the temperature and pressure setting for HIPing is altered.

2.6 Alloying of TiAl

Alongside microstructural development, alloying of titanium aluminides is a major factor that influences strength and ductility of the material. As it can be seen in Table 2.3, alloying leads to different generations of TiAl alloys [3, 28, 29].γ TiAl alloys with potential engineering applications are multicomponent alloys that usually contain 44 to 49 at.% aluminium and up to 10 at.% of other elements like Mn, Cr, Nb, V, Mo, B etc. By occupying the aluminium site, these elements decrease the c/a ratio of the γ phase, making Ti-Al covalent bond weak. This will increase the deformation and thereby room temperature ductility is increased. Addition of β stabilising elements shifts the (β+α) two-phase field of phase diagram to low temperatures and drags the (β+α)/α phase boundary to high aluminium concentration side. Disordered β phase present, will limit the α grain growth during heat treatment and will be transformed to ordered B2 phase at lower temperatures [28]. Small fraction of ordered B2 phase present at grain boundaries of γ, further reduces grain growth during heating and increases ductility [3].

2.6.1 Effect of Alloy elements

The Table 2.2 enlists different elements that are studied in TiAl system and their expected effects on properties.

Table 2.2: Effect of Alloy elements on TiAl [3].

Element	Reported Effects
Al	Affects ductility by altering the microstructure. The optimum ductility is at the range of 46-49 at. %. Reduces fracture toughness but increases oxidation resistance.
B	Addition of ~ 0.5 at.% refines grains
C	Doping increases creep resistance but decreases ductility. Improves strength by dispersion or precipitation hardening.
Cr	β stabilizer. Additions of 1-3 at.% increases the ductility.
Fe	β stabilizer. Increases fluidity but susceptibility to hot cracking is more.
Mn	Additions of 1-2 at.% increases the ductility. Reduces oxidation resistance. Shifts the $(\alpha_2+\gamma)/\gamma$ to the titanium side and decreases Aluminium content of γ phase.
Mo	Improves ductility and strength of a fine-grained material; also improves oxidation resistance.
Nb	In minor additions, increases oxidation and creep properties, if added between 5%-10% high temperature strength increases
Si	Increases fluidity, reduces susceptibility to hot cracking, refines cast microstructure and improves oxidation resistance. Addition of 0.5-1 at.% Si improves creep resistance.
Ta	Oxidation and creep resistance improves but susceptibility to hot cracking increases

V	1-3 at.% addition increases the ductility of duplex alloys. Shifts the $(\alpha_2+\gamma)/\gamma$ to the titanium side and decreases Al content in the γ phase.
W	Greatly improves creep and oxidation resistance.

2.6.2 Silicon in TiAl Alloys

Much of the initial development in TiAl based alloys achieved progress in terms of ductility enhancement but lagged behind on creep resistance [30]. In response to this, research into additional alloying identified Si as a major provider of creep enhancement. Dislocations were seen to be low by pinned silicide precipitates at lamellar interface and improves the creep resistance.

When Si addition done in minor proportions below 1%, the ζ -Ti_5Si_3 phase precipitates and improves the high temperature properties of -TiAl alloys. Figure 2.13 shows ζ -Ti_5Si_3 phase precipitation (the submicron bright contrast phase) during aging treatment of Ti-47Al-2Zr-0.3Si alloy at 900 °C and 1000 °C [31].

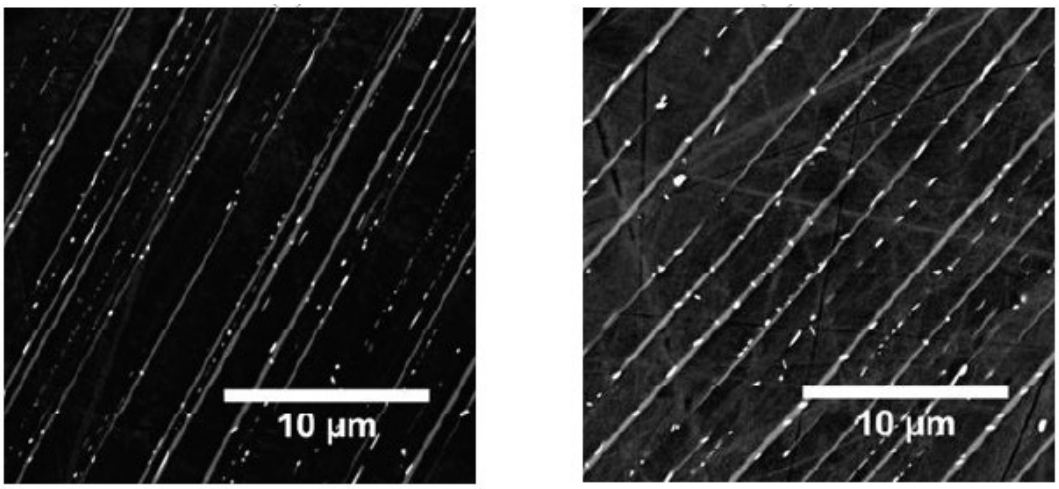

Figure 2.13: Precipitation ζ -Ti_5Si_3 phase. at (a) 900 °C and (b) 1000 °C [31].

2.6.3 State of the Art TiAl Alloys

Since few years, TiAl alloy development and microstructure development has gained more attention, for the betterment of their performance. Many researches in this domain led to the

formation of four state-of-the art alloys which are having excellent properties. The properties and compositions are compared in Table 2.3 [3, 11, 13]. For specific applications different elements are used for alloying, according to the suitability of the outcome. The composition of popular alloy systems can be generalised as:

Ti- (42-49) Al – (1-10) Nb, Ta – (0-4) X – (0-1) Y – (0-1) Z

Where X= Cr, Mn, Ta, V, Mo; Y= W, Hf, Zr; and Z= C, B, Si, N

Alloy additions bring alterations in the binary phase diagram. Figure 2.14 shows the effect of Nb addition on the phase diagram. Increasing Nb content increases the eutectoid and melting temperature, decreases transus temperatures of α and β and shifts them to higher Aluminum concentrations side.

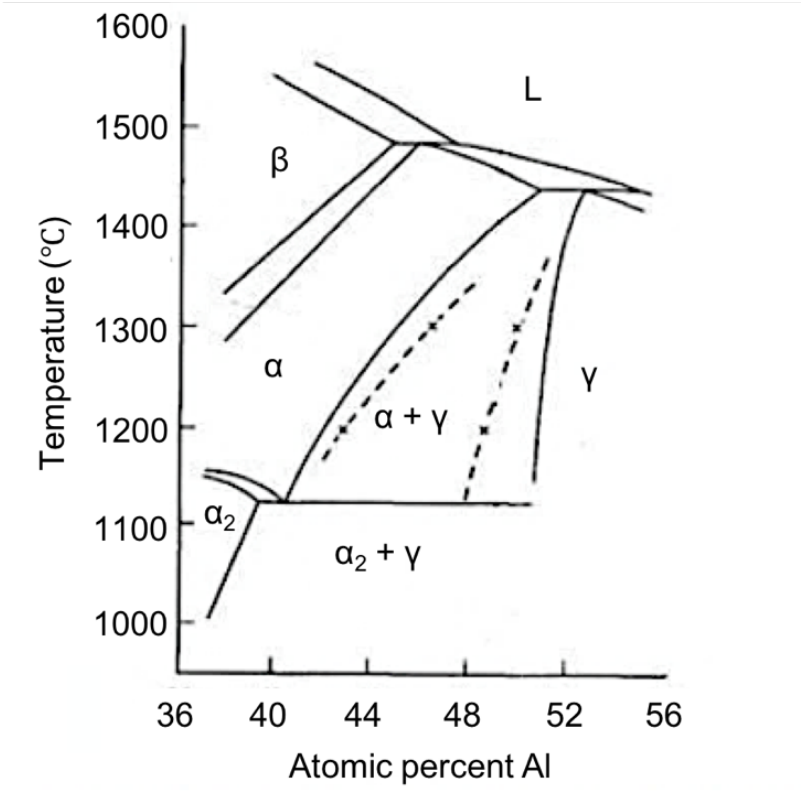

Figure 2.14: Ti-Al binary phase diagram with the dotted lines showing the phase lines changes if Nb is added [3].

“X” elements increase ductility and Cr 2% is the most popular among them. Nb and Ta improve creep properties and oxidation resistance and, in most cases, >2% Nb is added. If Nb concentration is low, oxidation and creep resistance are increased and at higher concentrations, Nb improves high temperature strength [32]. Conventional alloys mainly consist of two subcategories, which are first- and second-generation alloys. Binary alloys with minor element addition along with variable aluminium content are classified as alloys of first generation, whereas second generation alloys contain minor elemental addition, mostly < 5 at.%. Ti-48Al-2Cr-2Nb and Ti-45Al-2Nb-2Mn are the most investigated alloys in last few years, of which Ti-48Al-2Cr-2Nb is γ-TiAl alloy mainly used for aerospace engines.

Designing of alloys is mainly for the purpose of mechanical property improvement. Ductility is observed to be higher for $\alpha_2 + \gamma$ duplex alloys with an aluminium concentration closer to 48 at. %, whereas their performance is not satisfactory when it comes to high temperature strength, oxidation and creep resistance, especially above 700 ºC. As a solution to this, 3rd and 4th generation alloys are developed with 5-10 at.% elemental addition. 3rd and 4th generation alloy families are: massive transformed, high Nb and β- solidifying alloys. Massively transformed alloys, if appropriately heat treated in the $\alpha + \gamma$ region produces very fine microstructure with balanced good properties. Popular examples for 4th generation alloys are Ti46Al8Nb and Ti46Al8Ta. High niobium alloys possess improved creep and oxidation resistance, along with high temperature strength. Nb improves these properties, especially at concentrations >5 at.%. β- solidifying alloys have increased potential for grain refinement of cast structure and they possess balanced mechanical properties when heat-treated. The most popular alloys under this class are the TNM alloys [32, 33].

Table 2.3: Different generations of commercial TiAl alloys [3].

Alloy Name	Composition (at.%)	Alloy Strengths
General Electric, USA: 48-2-2	Ti-48Al-2Cr-2Nb	Ductility, fracture toughness and oxidation resistance
Plansee, Austria: γ –MET	Ti-45Al-(5-10) Nb	High temperature strength, creep, fatigue and oxidation resistance
GKSS Research Center, Germany: TNB Alloy	Ti-(45-47) Al-10Nb	High temperature strength, creep and oxidation resistance
Martin Marietta Laboratories, USA: XD^{TM} TiAl	Ti-45Al-2Mn-2Nb-0.8B	Ductility, high temperature strength, stiffness, creep and oxidation resistance

2.6.4 Ti-48Al-2Cr-2Nb

γ TiAl, owing to their desirable mechanical properties, can be counted as a potent replacement for many materials, which are currently used in high temperature applications. Ti-48Al-2Cr-2Nb, the titanium-based alloy with 48 at.% Al, 2 at.% Cr and 2 at.% Nb, has gained more recognition in engineering field. Cr increases the ductility whereas Nb enhances the oxidation and creep resistance, making 48-2-2 alloys, easy to process [34].

2.7 Thermal Exposure and Microstructure Stability in TiAl Based Alloys

Solidification and heat treatments described in sections 2.4 and 2.5 respectively, involve cooling from liquid phase, single phase α or α+γ phase field, to room temperature. Depending on the cooling rate, different microstructures, phases and phase compositions/fractions are obtained. If non equilibrium situation exists, system will undergo different solid-state transformations, when exposed to high temperatures and approaches equilibrium. Number of experimental and theoretical studies are available to understand the lamellar instability mechanisms in TiAl [35, 36]. In these investigations both coarsening and decomposition are observed in primary lamellar structure which are completely out of equilibrium.

2.7.1 Continuous coarsening (CC) of lamellar structure

Eutectic or eutectoid reactions lead to the formation of lamellar microstructures. In order to attain thermodynamical equilibrium, the system tries to minimise total energy and various driving forces prompt lamellar plates for compositional adjustments. Similarly, TiAl alloys with lamellar microstructure exhibit mainly two instability mechanisms namely continuous and discontinuous coarsening. These differs based on spacing of lamellae and their morphological perfection [37, 38].

Continuous coarsening is one among the mechanisms, in which interface area is reduced by means of coarsening. The source of instability in case of continuous coarsening is mainly internal faults such as ledges, edges and curved interfaces, by which the initial lamellar structure tends to be unstable [35]. Continuous coarsening of the fully lamellar microstructure in Ti-48Al alloy occurs when aged above 1150 °C (α+γ) field [38, 39]. During continuous coarsening the diffusion of solute atom happens along the faulted lamellar interface. Figure 2.15 shows effect of temperature on the coarsening of lamellar microstructure after heat treatments i.e., CC in FeAl intermetallic compound during heat treatment at 1000 ºC. As it is clearly evident from the image, longer aging induces more coarsening [38].

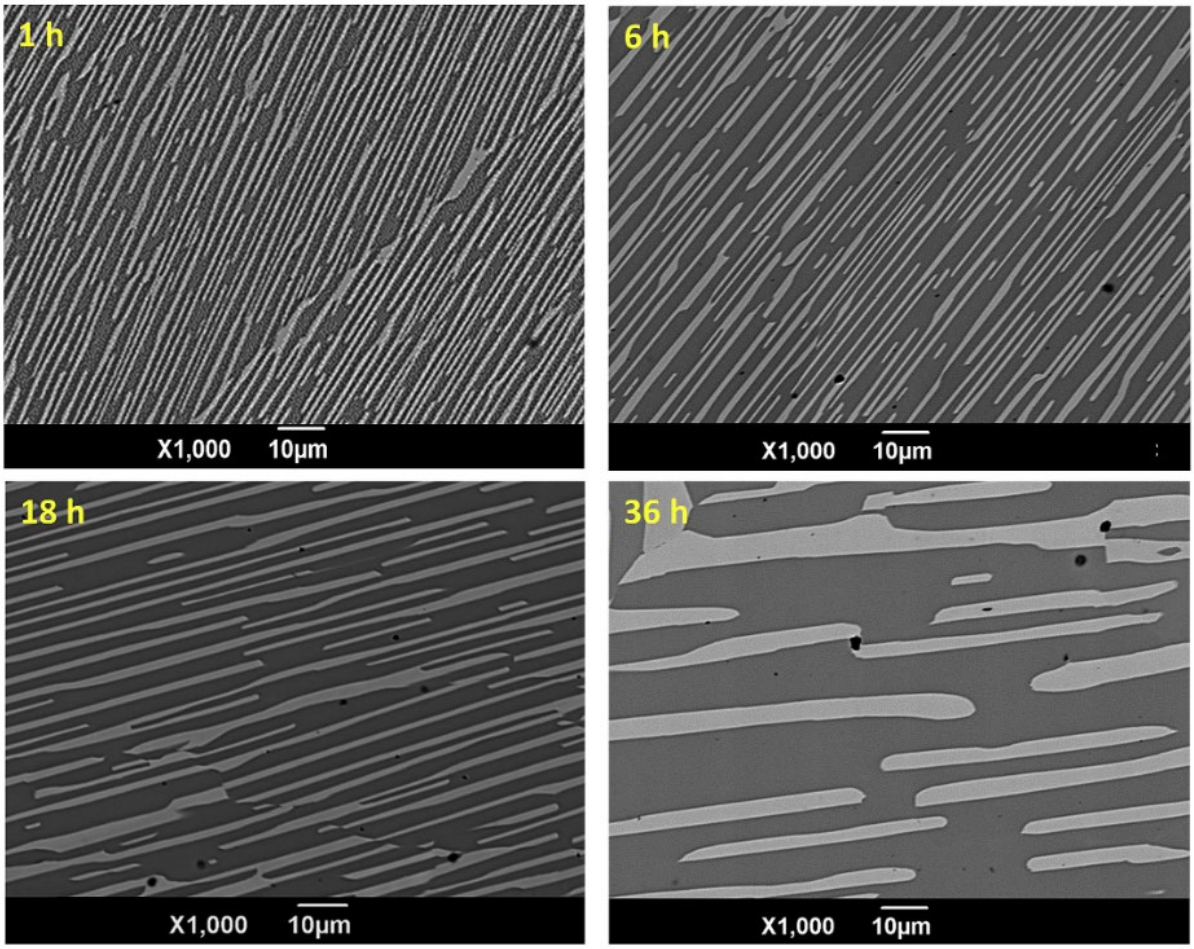

Figure 2.15: Continuous coarsening of the lamellar FeAl- $FeAl_2$ microstructure [40].

2.7.2 Discontinuous coarsening (DC)

Discontinuous coarsening is the reaction by which the primary fine lamellar structure gets coarsened and gives rise to a product, which is entirely different in microstructure. Chemical and morphological non equilibrium is observed to cause the DC. A schematic representation of DC is shown in Figure 2.16. Where supersaturated α' in fine primary microstructure is replaced by coarsened lamellar structure.

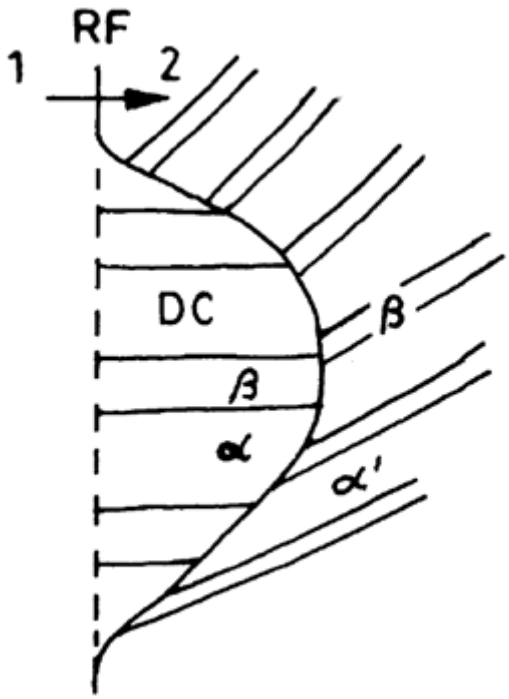

Figure 2.16: A schematic representation of discontinuous coarsening across the migrating RF in a binary system.

Livingston and Cahn [41] while investigating on thermal stability of Co-Si, Cu-In and Ni-In aligned eutectoid alloys, observed significant discontinuous coarsening via grain boundary migration along with continuous coarsening. Figure 2.17 shows SEM micrograph where DC is taking place which replaces fine primary structure by a coarsened lamellar colony. The progress of coarsening reaction varies with temperature and spacing of lamellae. With higher temperatures or finer lamellar spacing, coarsening increases. [42].

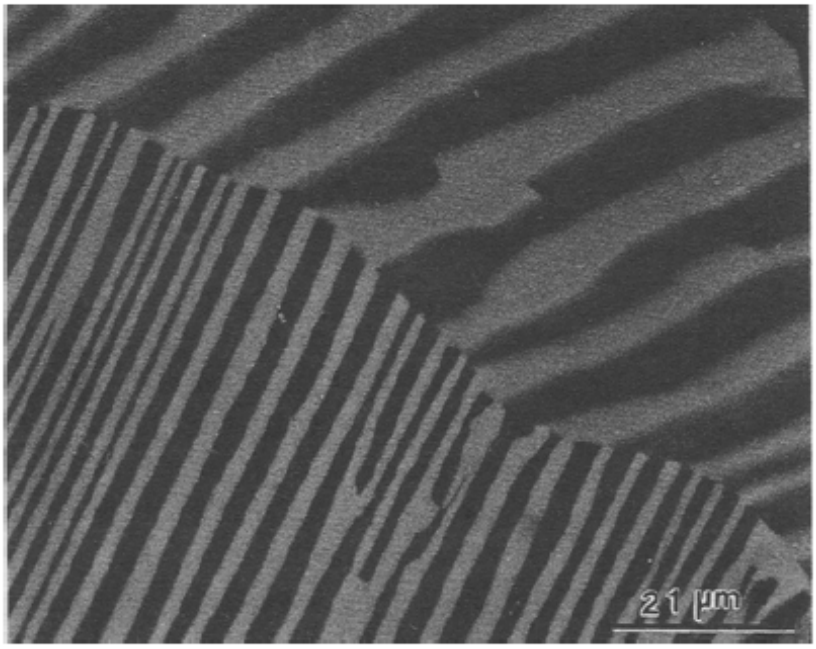

Figure 2.17: SEM showing DC [42].

2.8 Manufacturing of TiAl based Alloys

Despite attractive properties of titanium aluminides, their widespread use is limited because of difficulty in conventional manufacturing and the need of machining afterwards. Advanced manufacturing technologies and alloy design are found to be successful in making TiAl components with required quality. However specially designed post-processing make the process, time and cost inefficient. So, advanced near-net shaping manufacturing technologies are developed for TiAl, in which the requirement for post-processing is minimal.

2.8.1 Conventional manufacturing

Investment casting, powder metallurgy (PM) and ingot metallurgy (IM) are the common conventional methods used to fabricate TiAl parts. In powder metallurgy, advanced methods like spark plasma sintering and explosive reaction synthesis are found to be successful in producing TiAl components [3, 43].

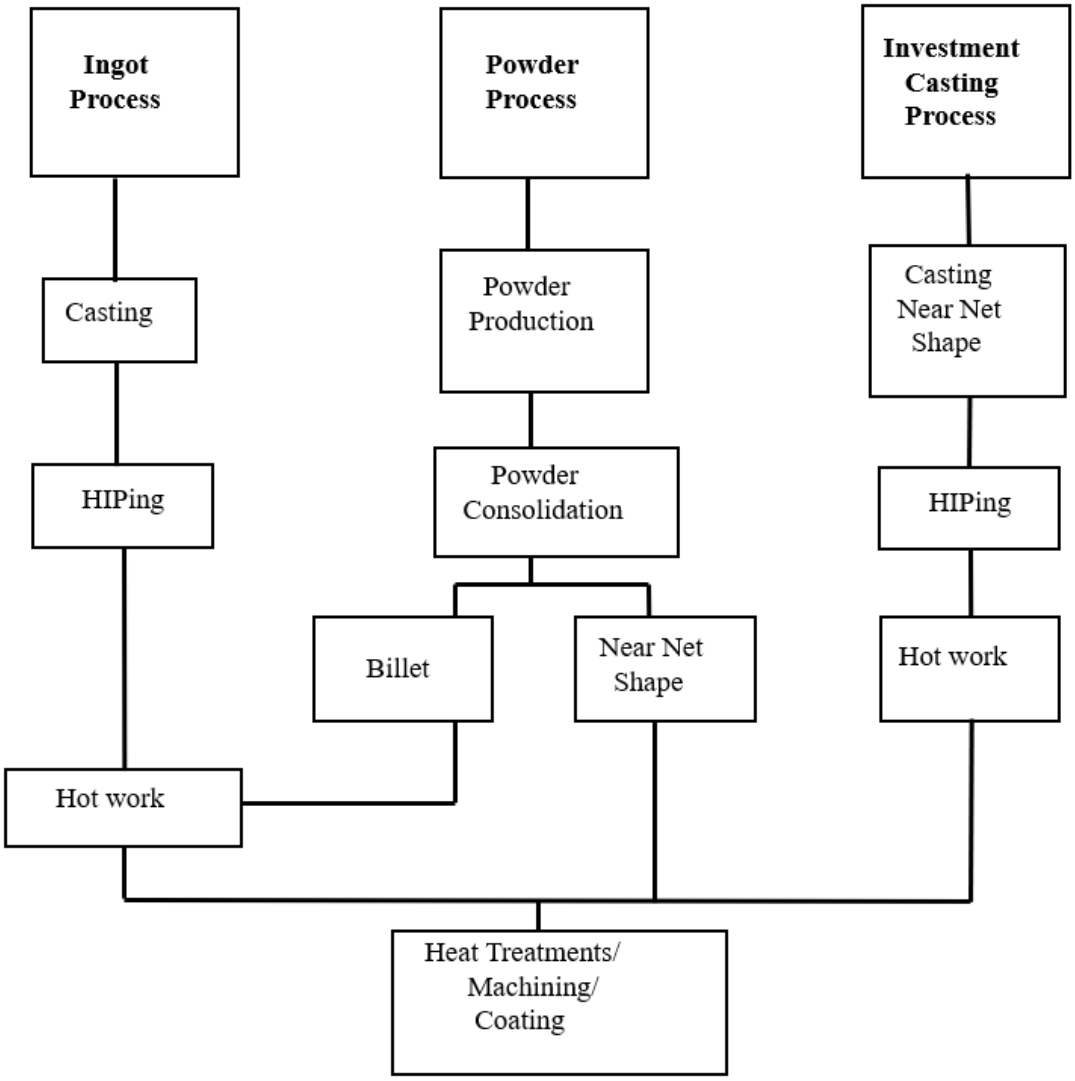

Figure 2.18: Conventional processing methods for γ-TiAl based alloys.

A general outline of conventional manufacturing routes for γ -TiAl based alloys is demonstrated in Figure 2.18. The investment casting, ingot metallurgy and powder metallurgy combined with thermo-mechanical processing has made broad range of tailored microstructures to achieve a balanced property profile. TiAl is very reactive and difficult to contain and that is the main problem faced while casting. Compositional inhomogeneities, segregation of alloying elements and thermal crack associated with residual stress are common issues in conventional manufacturing. In general, cast microstructure can be rough, with coarse lamellar structure and large colony size.

But the necessity of post-processing and machining to further optimize properties does significantly increase processing costs. Recent entry of Additive Manufacturing (AM) made it

possible to produce TiAl parts with desired mechanical properties using minimal post processing [44]. Optical micrograph of cast and AM processed TiAl samples are shown in Figure 2.19. AM microstructure is much finer and more uniform than that of conventionally processed samples. Industry and research communities believe that development of AM processes and microstructural modification is the need of the hour, in case of TiAl.

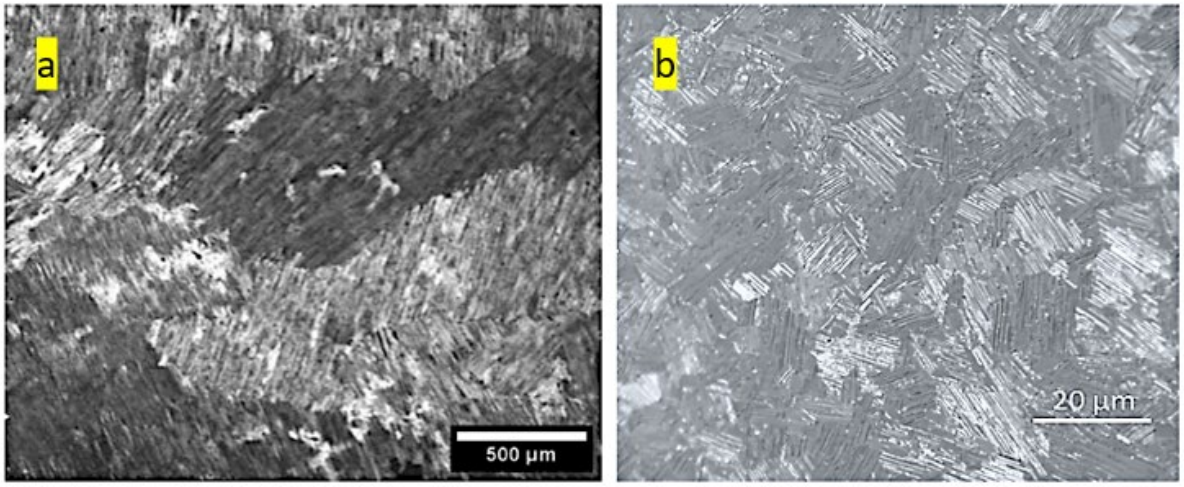

Figure 2.19: Optical micrograph of (a) cast and (b) AM processed TiAl samples [3].

2.8.2 Additive Manufacturing (AM) of Metals

Over the past 20 years, additive manufacturing (AM) has evolved from 3D printers used for rapid prototyping to sophisticated rapid manufacturing of metals and ceramics, which can create components directly from powder without tooling. AM methods differ from subtractive methods, such as milling or turning, where material is removed from the work piece. In AM, part is being created by the incremental addition of material rather than the incremental subtraction of material. Additive Manufacturing (AM) is a broad term for different methods of fabricating articles layer by layer, based on a computer file. Other names are Rapid Manufacturing (RM), solid free form fabrication (SFF) and Layer based manufacturing or in public language 3D-printing [45, 46]. Metal AM processes use melting or joining solid-state, in order to consolidate the feedstock into a dense 3D part. The principle of all additive manufacturing techniques is very similar. The energy source in AM for metals can be a laser or electron beam. Energy input must be high enough to melt the metal or alloy and join powder layers. The main benefit of additive manufacturing is the possibility to create complex

geometries. AM systems for metals can be classified to two main groups: powder fed systems (direct energy deposition process), powder bed systems, as shown in Figure 2.20.

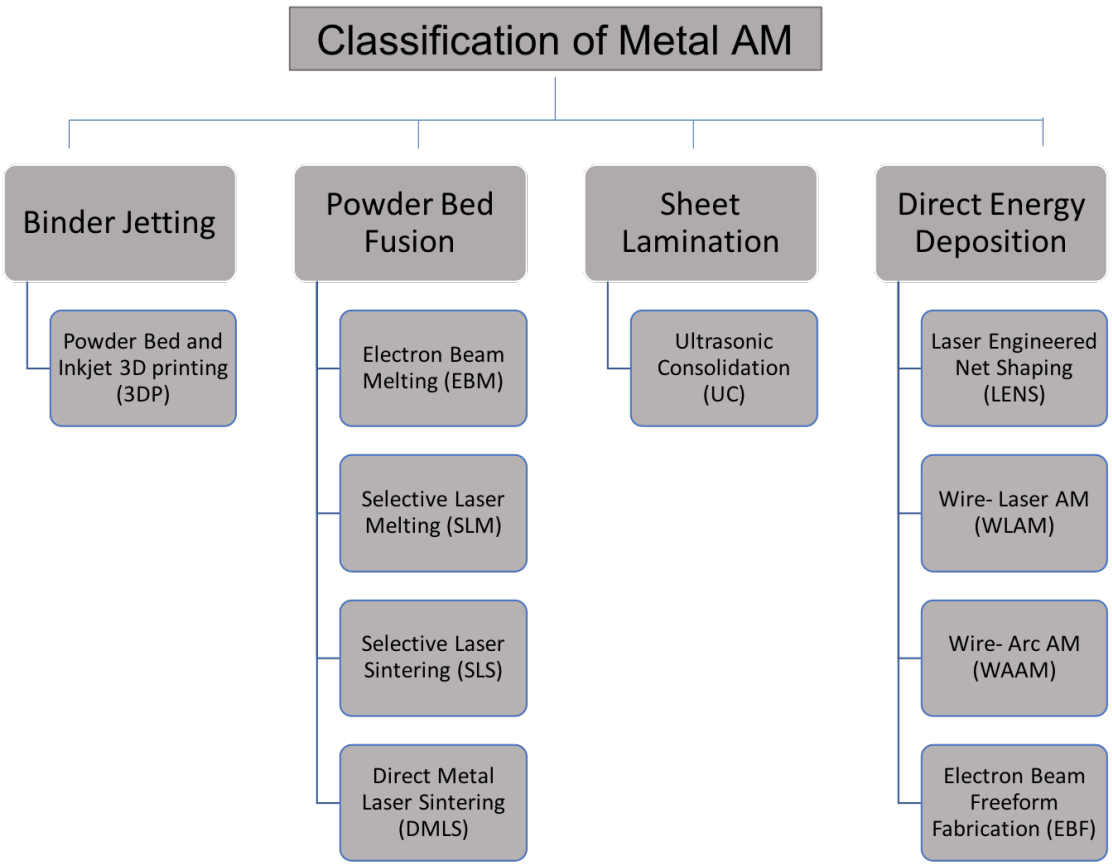

Figure 2.20: Different additive manufacturing processes.

2.8.2.1 Powder Bed Systems

Energy sources used in powder bed fusion technologies are laser or electron beam. A substrate plate of similar alloy composition as that of powder is used for mechanical support and to guarantee good heat dissipation. In First step, a measured quantity of powder is uniformly spread across the build platform. In a second step, the high energy beam selectively scans and melts the powder layer based on the computer file. Next lowers the building platform for a distance of layer thickness and the new powder layer is distributed to repeat the process till the desired part is manufactured. Remaining unmelted powder is collected and reused. The most popular ones among powder bed metal 3D printing technologies are electron beam melting (EBM) and selective laser melting (SLM). A brief description of powder bed process is given in Figure 2.21 [46, 47]. The metal powder is either fed by a hopper or provided by a reservoir

next to the work area and a thin layer of metal powder is spread in the platform using a roller or a rake blade. Then selectively applies the laser or electron beam according to the design and again, the powder is spread. This cyclic process is repeated till the part is fully built.

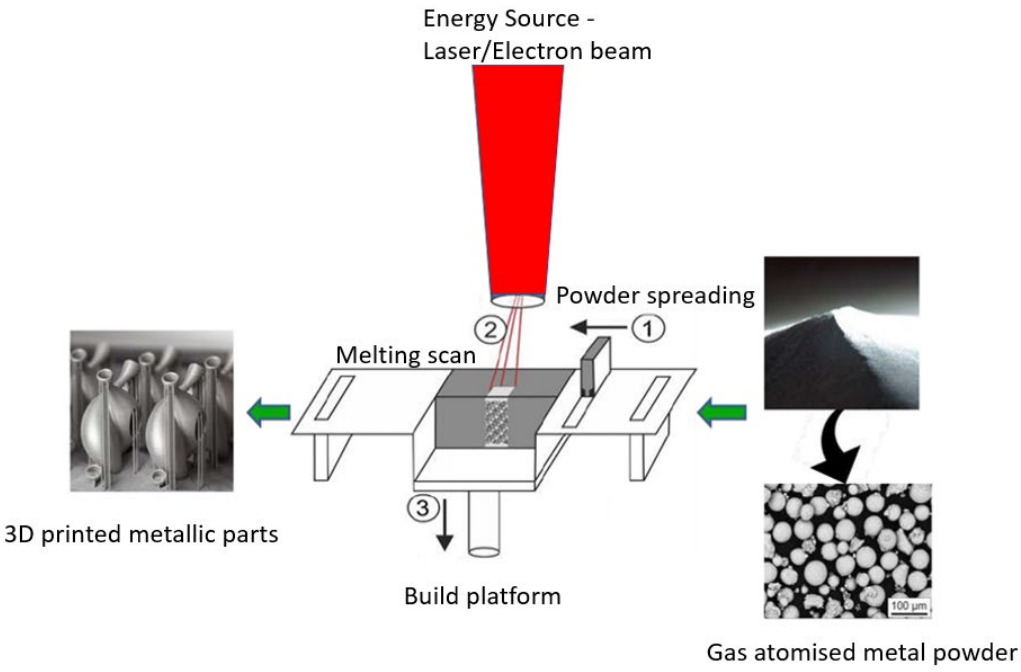

Figure 2.21: Schematic of powder bed process: (1) metal powder feeding (2) Selective melting of powder bed layer (3) lowering of the platform and adding next layer.

2.8.2.2 Selective laser melting

Selective Laser Melting (SLM) is the powder bed AM process in which high-power laser like Nd: YAG lasers are used as energy source. The process features a considerable number of parameters which need to be optimized, to get defect free components. Parameters that determines the final properties of the component can be divided into three as: powder characteristics, laser parameters, and processing variables. Even the smallest compositional variation or process fine tuning affect overall properties of the samples. Selective laser Melting (SLM) and Selective Laser Sintering (SLS) are commonly employed in laser-based AM. In SLS only surface melting of the powder occurs, but in SLM complete melting of the powder is accomplished. Literatures have shown that SLM has the potential to melt the metal powder completely. The high energy laser beam which strikes on metal powder gives the energy for melting. Recent developments of high-power laser also enable SLM to process different

metallic materials, such as steel, titanium, nickel, copper, aluminium, and tungsten alloys. The main application of SLM and EBM technologies are in bio-implants, aircraft components and in automobile applications.

SLM employs characteristic high temperature gradients and rapid solidification, thereby causing non-equilibrium phases and microstructures. Processing parameters like focal offset distance, scanning speed, energy density and layer thickness for each material are selected judiciously for controlling the microstructure in as fabricated samples.

Laser based powder bed processes do often cause a lot of residual stresses in the produced articles. They are often performed in a cold atmosphere and the laser beam has a very small focal diameter which provides fast heating and cooling. The rapid heating and cooling create high residual stress and chance of thermal crack in some of the alloy systems, which are prone to crack. There was an idea of reducing these residual stresses by using an elevated chamber temperature during the build process. Pre-heating of the workspace for powder bed laser processes with infrared heater was developed in the early 90's in order to conduct process at high temperature [48]. This technique is however less popular mainly because of the need for equipment modifications and its associated complexities [5]. Another option is EBM which has the capability of printing metal at high substrate temperature or build temperature upto 1100 ºC [49].

2.8.2.3 Electron beam melting

Electron beam melting (EBM) is a comparatively novel AM technology introduced in 2001 by Arcam AB, Sweden. It is categorized as powder-bed fusion metal AM technology, in which components are fabricated by layer by layer addition of metal powders. High energy density electron beam is the heating source, which melts subsequent layers of metal powder and fuses layers to get metal parts with nearly full density. Since electrons can get affected by atmospheric gases, EBM process is operated in a vacuum chamber. Due to high build temperature during EBM, stress induced cracks are minimal. It allows fabrication of complex parts, according to the 3D geometries directly given as input, making the process simple to plan. High energy efficiency and low operation cost makes EBM one of the most promising manufacturing methods. Currently, EBM is successfully used in materials, including Ti6Al4V, Inconel 625 superalloy, cobalt (Co)-based superalloy, and TiAl alloy [50], which have wide

applications in medical implant, automotive and aerospace industries. More details about EBM manufacturing is discussed in Chapter 4.

2.8.2.4 Direct Energy Deposition (DED) Process

Laser engineered net shaping (LENS) and direct metal deposition (DMD) are categorized as DED processes [51, 52]. A focused beam or an electric arc is used here to fuse feedstock by layer-wise melting. The layer thickness ranges 0.1 to a few millimeters. They can be subclassified based on material feedstock into powder-fed systems and wire-fed systems. Powder-fed AM systems are advantageous in the repair of worn or damaged structures.

Lasers in combination with powder feeding is the most common deposition process. A schematic of laser metal deposition process is shown in Figure 2.22. Powder is continuously fed through a nozzle, directed at the deposition spot where it is melted by the laser beam. Powder is transported with a gas to force the deposition to the right place and making it possible to add material at non horizontal surfaces. Nozzle can be a coaxial powder feeder that is integrated in the laser beam head or an external single nozzle powder feeder.

Powder fed deposition processes make it possible to create gradient objects by regulating the scanning and powder feeding speed. Separate nozzles and powder depots offer the possibility for in situ alloy mixing and fabrication of gradient materials. In this way, powder fed process enables making of objects with ductile core and hard, worn resistant surface [52].

The microstructure in laser-based deposition processes and laser-based powder bed processes are similar in many aspects. Microstructure is very fine due to high cooling rate.

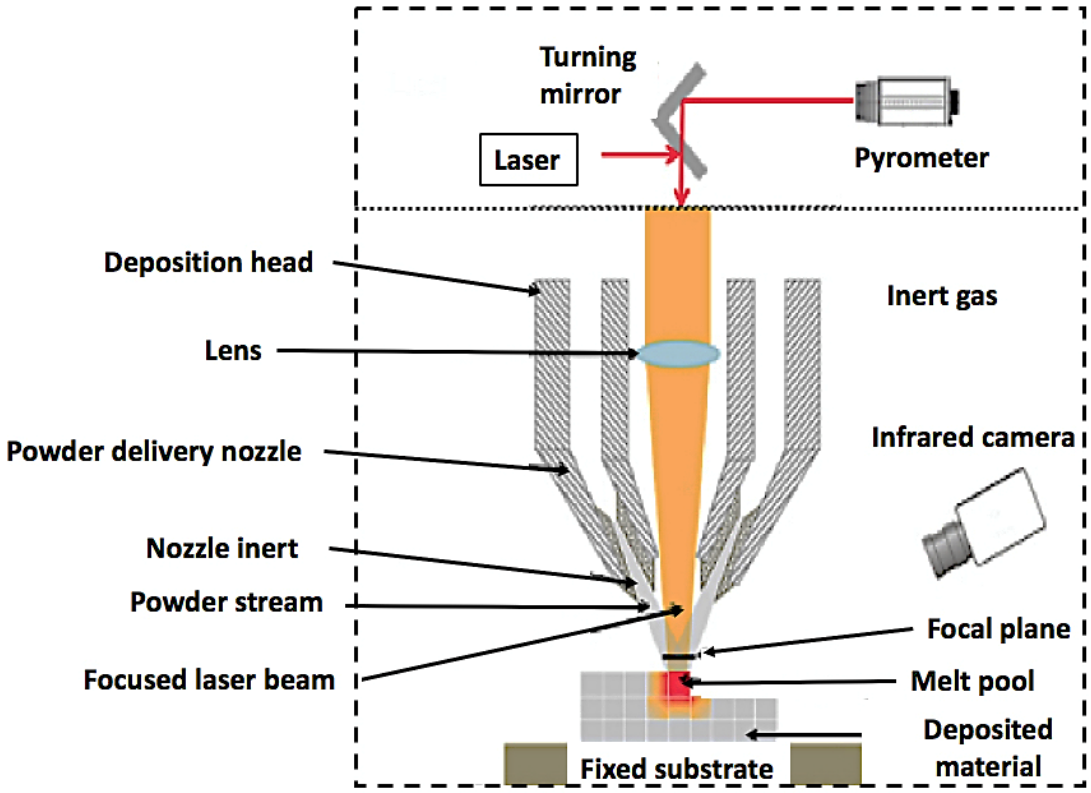

Figure 2.22: Schematic of Laser Metal Deposition (LMD) process [52].

2.8.2.5 LENS Technology

Laser Engineering Net Shaping (LENS) is commercialized and distributed by Optomec. The Optomec LENS system consists of a four-copper nozzle assembly through which metal powder is injected. Powder falls into a melt pool produced by a high-power laser source. Specifically, a powder feedstock controls the mass flow of powders that are introduced to an argon gas that carries elemental and/or elemental blends of powder through the deposition head that expels these powders onto the focus of the laser beam. The laser source (Nd: YAG or Fiber Optic CO_2) simultaneously liquefies the metal powders and locally creates a melt pool on the substrate fixed to a X-Y motion control stage. The liquefied powder is then introduced to the local melt pool and is rapidly solidified as the beam raster along X-Y plane based on design file. After each layer, the deposition head is moved along the Z – direction creating successive layers of the component until completion [52,53].

2.8.2.6 Comparison of different AM techniques: SLM vs EBM vs LENS

A direct comparison of AM techniques is given in Table 2.4. Both EBM and SLM are powder bed based additive manufacturing processes whereas LENS is a powder fed process. Powder bed-based processes are very similar in principle, but the main difference is the energy source and associated supporting arrangements. In EBM, accelerated electrons are moving in a high vacuum atmosphere and in some cases, mild helium flow is provided for better process stability. These provisions make EBM machine a complex one [5].

Table 2.4: Comparison of AM techniques [45].

Characteristics	**EBM**	**LENS**	**SLM**
Energy Source	Electron beam	Laser	Laser
Energy absorption	Limited conductivity	Limited absorptivity of laser	Limited absorptivity of laser
Scan speed	Very fast, magnetically driven	Lesser speed	Lesser speed, limited by inertia
Powder pre-heating	Use electron beam (about 1000 ºC)	Room Temperature	Use infrared heaters (about 200 ºC)
Atmosphere	Vacuum	Argon Inert gas	Inert gas
Surface Finish	Moderate	Moderate	Excellent
Materials that can be processed	Metals	Polymers, metals and ceramics	Polymers, metals and ceramics

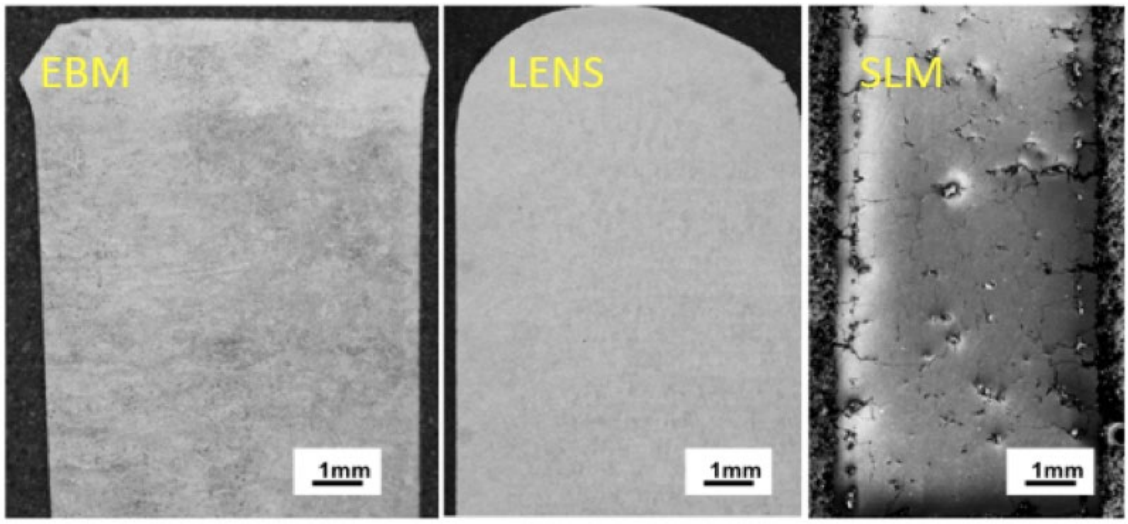

Figure 2.23: A direct comparison of AM techniques in TiAl manufacturing.

Optical image shown in Figure 2.23 is the section of TiAl sample along build direction. In SLM because there is no pre heat, the material which are prone to thermal cracking is difficult to process. Even though in LENS there is no preheating, but the continuous application energy will retain some heat and will cause some buildup of temperature in the printed sample. The high strength materials Titanium and Nickel-based superalloys (e.g. Inconel) are commonly used in AM techniques. The reason is that there is a specific interest in using this technique for these materials. Using AM for expensive materials that are hard to machine is extra beneficial since there is great economic benefits and time savings. Laser, electron beam and plasma arc can probably process most metals, but it requires some research to tune the process for each material. Therefore, the primary focus is to process attractive materials.

The powder can be blended with alloying elements to reach desired properties. Powder deposition processes have more possibilities since it can use multiple nozzles with different material to change the chemical composition in the material in the same part [45].

2.8.3 General summary of previous work - Additive manufacturing of TiAl

AM has gained considerable attention in TiAl manufacturing. EBM, SLM and LMD has been tried for TiAl printing. Even though SLM is the leading technology in metal AM, it is not so popular in TiAl manufacturing mainly because of the severe cracking in as fabricated samples, mainly due to the lack of preheating in SLM. In case of LENS, because of the continuous beam application there is heat accumulation and temperature build up in the printing sample, which

will be beneficial for avoiding thermal cracks to an extent. The possibility of printing at high temperature makes EBM, the most viable AM technique for difficult to print materials like intermetallic TiAl alloys. Compared to Nickel super alloys and Ti-6Al-4V, additive manufacturing of TiAl is been less explored. Recently some researches were done in AM of TiAl alloys using SLM and EBM. Li et al. made an investigation on TiAl manufacturing by SLM and observed that microstructure predominantly consists of α_2 phase. Effect of SLM process parameters on mechanical properties is also documented in that study. Unlike conventional processing, AM processed TiAl has a fine and homogeneous starting microstructure, which is an important advantage to achieve an ultrafine lamellar structure which shows better combination of properties.

The earliest attempt to manufacture TiAl structural component by EBM has been done by Cormier et al. [54], but because of the non-optimised AM conditions the aluminium loss were in excess and not much details on the microstructural aspects are available. Murr et al. [55] and Schwerdtfeger et al. [56] studied aluminium loss during the process and indicated the possibility of adjusting the microstructure during the EBM process

Biamino et al. [57] attempted producing full density near net shaped TiAl parts with tensile properties both at room and high temperatures. They have fabricated prototypes of hollow turbocharger turbines and studied the compositional variation in EBM process. Figure 2.24 shows the tensile properties of EBM TiAl sample in as- fabricated state. General Electric (GE) has done considerable work in additive manufacturing of TiAl, but very limited information on the process is available to research community [4].

In 2012 Avio proposed a process development for high Nb -TiAl alloys, which includes two types of thermal treatments. One was to obtain coarser FL microstructure with good properties and the other to produce fine duplex structure with better fatigue resistance. High Nb alloy was also studied by G. Baudana et al. [44], in order to investigate about their mechanical properties. In that work, the as-built condition microstructure reported as feathery massive gamma structure and after heat treatment it becomes lamellar colonies with grain size ~ 100 μm and a lamellar fraction around 40%.

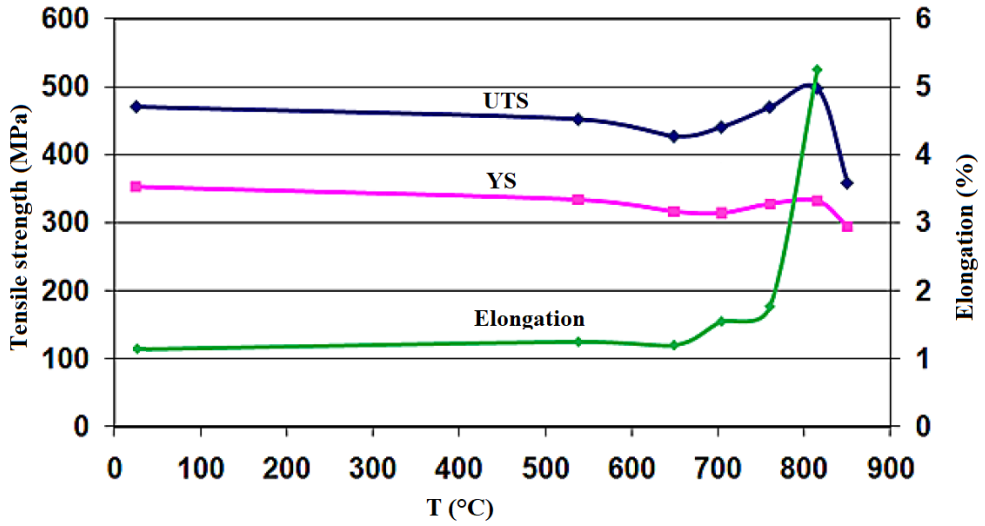

Figure 2.24: Tensile properties of as fabricated Ti-48-Al-2Nb-2Cr alloy in EBM [57].

Todai et al. [58] and Muhmad et al. [59] reported layer-wise microstructural evolution in TiAl EBM. Results obtained at different angle θ between EBM-building directions and testing direction are shown in Figure 2.25.

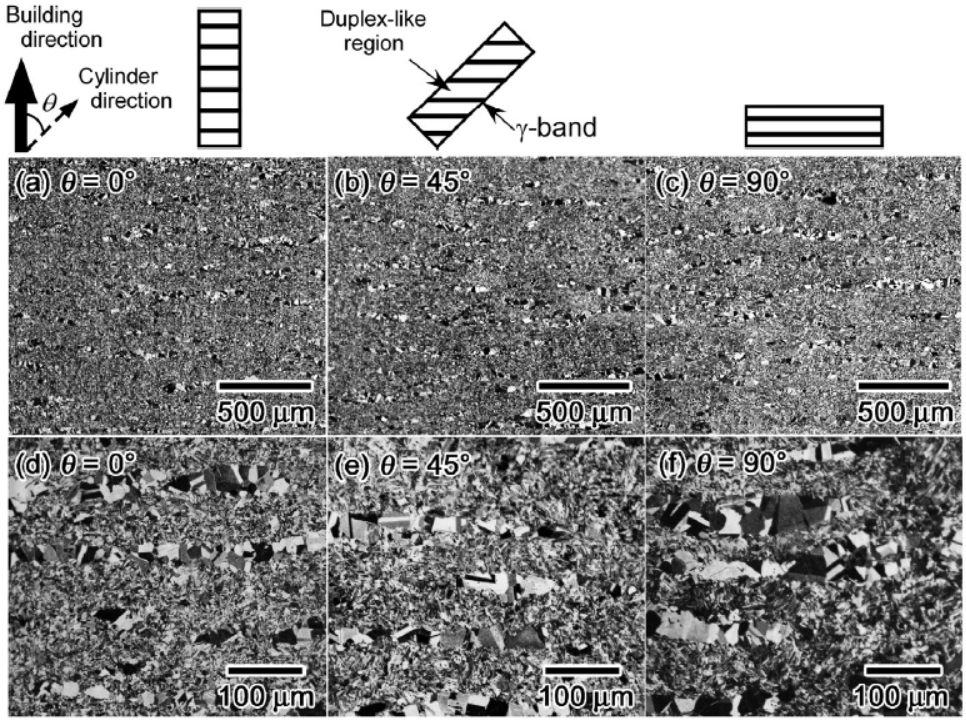

Figure 2.25: Layered microstructure observed in TiAl manufactured by EBM, as per literature [58].

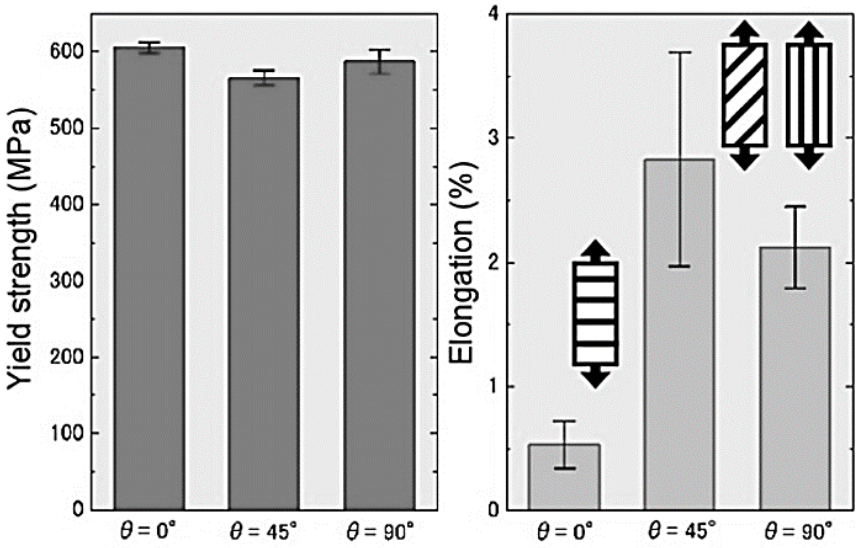

Figure 2.26: Mechanical properties studied along different directions with respect to banding [58].

Mechanical properties studied along different directions with respect to banding is shown in Figure 2.26.

Although microstructural evolution offers a clear link between the process scheme and the resulting mechanical properties, a systematic study that relate AM process and microstructure is yet to be done. All microstructural observations and the possibility of using unique characteristics of AM, mainly the in situ heat treatment conditions still need to be explored further. It can be thus concluded that various EBM process parameters significantly affect the resultant microstructure of TiAl, making assumptions on possibility tailoring desired microstructures by varying process parameters. The relation between process parameters, microstructural evolution and mechanical properties is to be explored further, to broaden the knowledge about the performance of TiAl in AM

2.8.3.1 Alloy powder for AM process

Today, metals are the fastest growing and promising segment of 3D printing. The significance of metal powder rheometry in EBM/SLM processes has become widely accepted. Generally, gas or plasma atomized powders are preferred for additive manufacturing. After production,

powders can be characterized according to various standard techniques used for spherical materials. Metal powders used in AM should have:

- Spherical shape to ensure good flow and a high packing density,
- Particle size usually below 20-150 μm depending on machine type and surface finish
- Optimized particle size distribution
- Controlled chemical composition

Slotwinski et al. [60] discuss the need of scientific study and standardised characterization methods in the ASTM for metal AM powders. Properties of the powder should be closely matched to the application and the machine to be used, for example, in powder bed process, where powder rolled under pressure and it behave differently compared other AM process.

It has been shown in literature that two powders that have the same particle size distribution and chemical composition could have different dynamic behaviour [61, 62]; hence nonstandard practice in metal powder metrology may be resulted in unexpected results. It is preferred to not depend upon single measured powder properties.

Spherical powder with suitable particle size is needed to obtain dense product. During processing, powders perform differently with varying particle size. Smaller sized powder melts faster than higher sized ones.

2.8.3.2 Alloy design specific to AM

For optimisation of mechanical properties and performance of TiAl alloys, many researches are being carried out nowadays. Enhancement of overall performance can be achieved by controlling the microstructural evolution or by alloying. The alloys which are used in additive manufacturing is same as that used in conventional manufacturing and that may not be the best way. Since it leads to the formation of a microstructure that is not in equilibrium, Ti-48-2-2 may not be the ideal alloy composition for additive manufacturing of TiAl. This leads to the necessity of novel alloy designing with more compatibility with the characteristic environment of additive manufacturing process.

2.9 Summary

Due to low density and excellent high temperature properties, γ-Titanium Aluminide intermetallics are considered as ideal candidates for applications in automobile and aerospace industries. Considering binary TiAl alloys, 48% aluminum region in the $\alpha_2 + \gamma$ segment exhibits most desirable properties, among them fully lamellar and duplex microstructures are more significant in technical and commercial aspects. However, their lower ductility and fracture toughness makes them difficult to process. Alloying and post-manufacture machining significantly improves the mechanical properties, but the process is expensive.

Refinement in their microstructure brings out huge enhancement of properties and so, TiAl manufacturing and ways to influence its microstructural evolution, is studied extensively in last decade. Using conventional manufacturing processes, it is hard to get TiAl parts with desirable properties in required geometry, at acceptable cost. AM methods, especially near-net shape technologies are helpful in this regard. Poor formability of γ-TiAl is overcome using AM, which are well known for materials which are difficult to process. EBM, SLM and LMD are most popular among them. For fabricating γ-TiAl components, EBM is considered to be the most promising method, as it excludes cracking due to thermal induced stress. Reference data is scarcely available on Ti-48-2-2 additive manufacturing, which is one of the most popular TiAl alloy.

The non-equilibrium condition of the TiAl microstructural evolution during AM and further solid-state transformations and microstructural instabilities need to be addressed. To know the influence of thermal cycling and characteristic printing conditions in AM, on microstructural evolution is critical for producing desired microstructure with respect to the property requirement. Alloy development specific to AM also deserves to be investigated further. Alloy development and design specific to AM are growing sectors of additive manufacturing.

Chapter 3: Research Problems

Depending on the process condition, heat treatment and alloy composition, a wide range of microstructure can be created in a TiAl system. Additive Manufacturing (AM) process allows formation of complex microstructures, as the process involve rapid solidification and repeated in-situ cyclic heating. It was observed that solidified microstructures on EBM printing conditions are very fine and out of equilibrium, strongly influenced by the process parameters and cooling conditions. There are studies which portray the TiAl microstructural variations from duplex to lamellar structure in EBM. But differentiation of primary lamellar structure formed through solidification from the lamellar structure formed after coarsening, is not yet addressed. Due to the absence of differentiation and detailed microstructural analysis on different solid-state transformations (SST), the effects of SST on the microstructural evolution and properties of EBM/ LENS manufactured TiAl has not been completely explored.

Looking forward, there are several topics, which require further investigation. All the microstructural observations in the AM fabricated TiAl samples are not systematically studied. Behaviour of material at AM environment, variation of microstructure with different AM processing conditions, also require further investigation. Unique characteristics of AM especially that of EBM, and its effects on microstructural evolution, are not fully understood. Commercially available TiAl 48-2-2 is designed and optimised for the conventional manufacturing process and may not be best suited for AM. This also needs to be addressed in further research. To exploit the unique characteristics of AM and achieve better outcomes, specific alloy modifications for AM need to be considered, along with optimisation of machinery. Main motives of this research are fabricating quality TiAl samples using EBM/LENS process and studying the effect of process scheme on its morphology and properties. Another important goal was to investigate the solid-state transformations during TiAl manufacturing. Accordingly, the objectives of the research can be outlined as follows.

Objectives

The objectives of the research can be outlined as follows.

1. To stabilize and optimise the TiAl printing in EBM and LENS machines. EBM/LENS process development for new alloys is not straightforward. Series of process recipe changes and hardware adjustments are required even for achieving process stability.

2. To understand how the uniformity of microstructure is varied along the build direction of intermetallic TiAl alloy, under different process conditions of EBM and its improvements.

3. To systematically analyse the in-situ cyclic heat treatment and associated solid-state transformations (SST) - Discontinuous coarsening (DC) and β phase formation, in EBM and its influence on the microstructural evolution of TiAl. Since deposited metal is subjected to thermal cycling for most of its building time in AM, this must affect the non-equilibrium primary microstructure formed at high cooling rate, final microstructure and mechanical properties, making this study particularly important.

4. To compare the TiAl microstructural evolution in EBM Vs. LENS and try alloy modification specific to AM, mainly for EBM – Si addition and its effect on Discontinuous coarsening (DC) during fabrication of TiAl.

Chapter 4: Materials and Experimental Procedures

This chapter includes description of the feed powders, experimental methods and sample preparation used in this research. To print TiAl samples, electron beam melting (EBM) and laser engineered net shaping (LENS) technologies were used. Processing conditions and microstructure development were investigated in detail. Microstructural analysis was carried out using different characterisation tools, as outlined in this chapter.

4.1 Material

The precursor in this study is gas atomised spherical powder with the nominal chemical composition Ti-48Al-2Cr-2Nb supplied by ARCAM, Sweden. The powder size distribution ranges from 40μm to 140μm, which is determined by a laser particle size distribution analyser. The powder is mostly spherical, with satellites of smaller sizes attached to powder particles. The details of characterisation of as received and recycled powder is discussed in chapter 5.1.

Alloy powder for EBM or AM in general, should meet quality standards connected with health and safety guidelines. So, for the safe handling and to prevent powder fire, oxygen passivation was done during gas atomisation to 0.12%. Powder is required to be free flowing, which means that powder should be spherical, with minimum amount of satellites. For this study, a gas-atomisation technique method was used to produce pre-alloyed powder with the required characteristics and quality. The standard Ti-48Al-2Cr-2Nb powder was used for most of the printing. After the microstructural study, alloy modification specific to EBM process was done, specifically for the microstructural refinement. The powder used for the customised composition Ti-47.5 Al-2Cr-2Nb 0.5 Si was gas atomised at TLS –GmbH (Germany).

As-received powder was sieved to get specific powder size distribution in the range (63-140 μm) for the EBM. No powder specifications were available as reference for the customised composition, and different powder size distributions were sieved and experimented on for optimisation.

4.2 Powder recovery and recycling

The Powder recovery system (PRS) was used to recycle the non-melted or sintered powder from the EBM machine. Ti-48Al-2Cr-2Nb powder was used as a blasting medium, to break up sintered blocks of powder from the previous build. After recovering the powder from the PRS, sieving is done using a 150 µm mesh and used again for printing. The oxygen analysis showed a minimum pick up of oxygen in the recycled powder. Figure 4.1 shows the interior of powder recovery system (PRS) used for this study.

Figure 4.1: Inside view of powder recovery system (PRS).

4.3 Processing

The additive manufacturing, sample preparation, and analysing of the samples was mainly performed at Lab 22, CSIRO Manufacturing, Clayton, Australia. Both powder bed and blown powder process methods were used to make the TiAl samples. Powder bed melting was carried out using the Arcam A1 electron beam melting (EBM) machine and the blown powder process, using Optomec MR 7 LENS machine.

4.3.1 Arcam - Electron Beam Melting (EBM) Process

Electron beam melting (EBM) is a relatively new AM technology, first commercialized by Arcam AB, Sweden in 2001. In the EBM process thin layers of powder are melted and joined according to a CAD model. Figure 4.2 shows the EBM machinery used in this study. Figure 4.2a is the Arcam AB EBM machine at CSIRO, Figure 4.2b is interior of machine and Figure 4.2c is machine interior, when printing is being done.

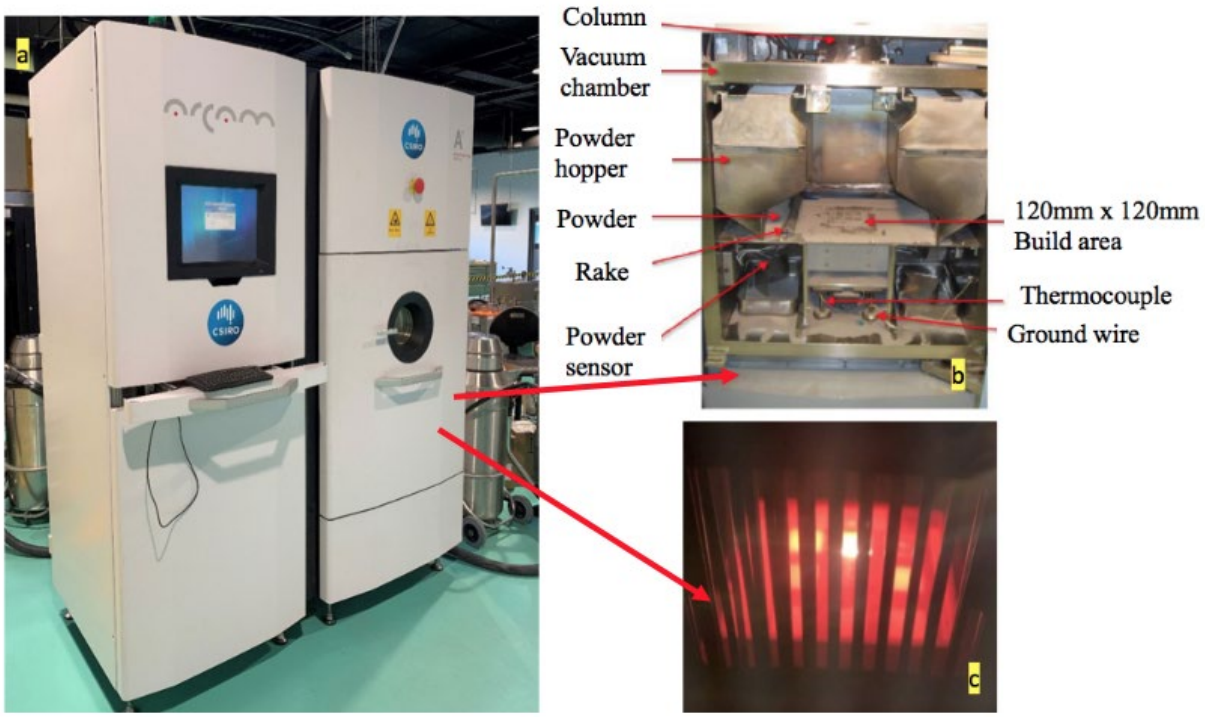

Figure 4.2: EBM machinery (a) shows the Arcam AB EBM machine at CSIRO (b) interior of machine (c) interior when printing is being done.

A schematic of ARCAM EBM machine is shown in Fig.4.3. In EBM the heat source is an electron beam. Thin layers of powder are melted and joined according to a CAD model. Electrons emitted from a heated tungsten filament which is placed in a grid cup, then accelerated through the gun by applying a high voltage of 60 kV between the cathode and the anode.

Electrons are magnetically focused and directed to the powder bed as shown in Figure 4.3. This magnetic control allows very fast deflection of the electron beam in the powder bed. The beam diameter is about 0.1 mm [57], and the beam current is in the range 1–50 mA. In the chamber, spherical metal powder, of size 50-100 μm is distributed and forms a thin layer of range 50-200 μm by a raking mechanism. The electron beam selectively scans the powder layer based on the CAD file and consolidates the chosen areas into dense solid parts. Before melting, first the powder bed is scanned at a high speed in order to preheat the powder to a sintered state. This preheating will slightly sinter the particle together and provide necessary conductivity for further melting process, where the beam scans at high energy input and lower speed. Then a new layer of powder is spread on top and the beam selectively scans the added layer. The process is repeated until all layers are consolidated to form the required component.

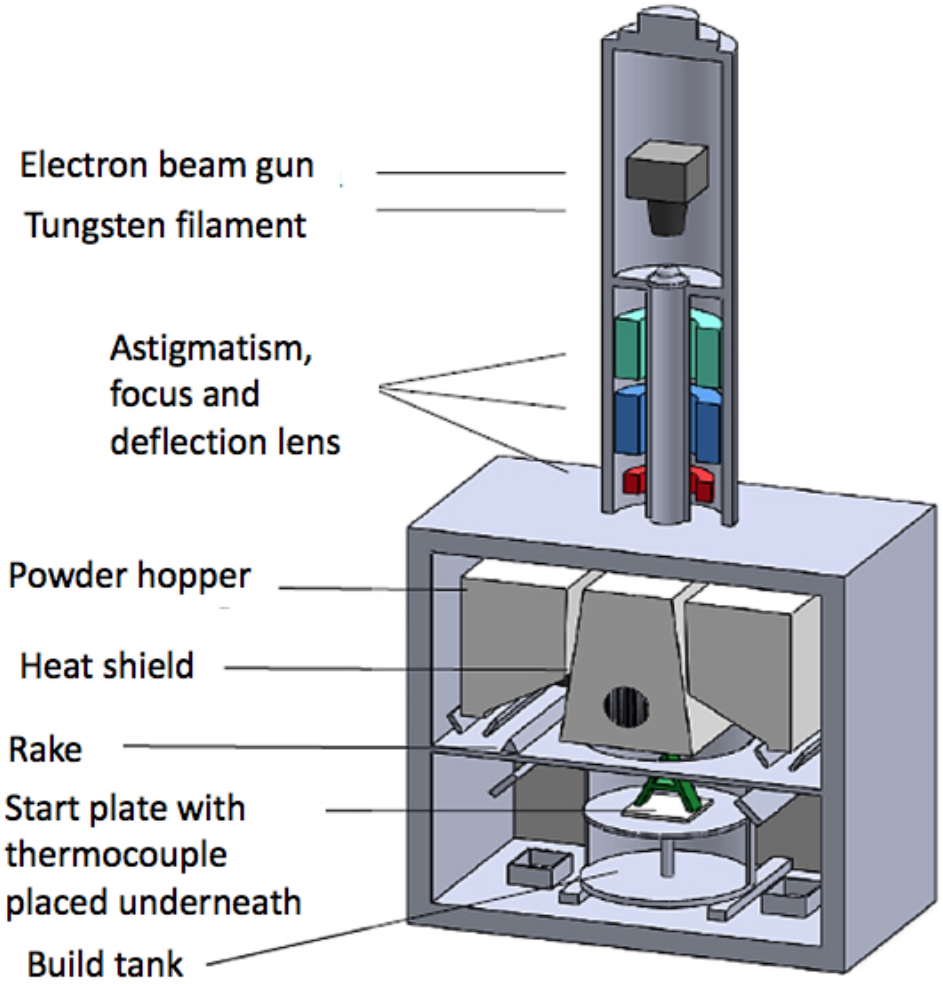

Figure 4.3: A schematic of ARCAM EBM machine [63].

EBM can be compared with SLM, another powder bed process in order to understand the process better. Rafi et al. (2013) made a comparison between the microstructural and mechanical properties of Ti6Al4V parts produced EBM (Arcam S400) and DMLS (EOS M270) [64]. The materials tested were made in the as built condition without any post-processing such as grinding or heat treatment. They found out that the EBM process delivered ductile material with tensile strength comparable to the same material in cast and annealed condition, while SLM delivered a more brittle material with higher strength and fatigue limit than EBM. This is because the EBM process has a longer cooling time which gives a softer material. They also observed that the surface finish was smoother for the SLM sample, which they explained to be due to a characteristic of EBM process, which runs with thicker layers and with a larger powder size. The effect of the pre-heating is the major difference between SLM and electron beam, giving different microstructure and material properties. The main aim of preheating cycle variation was to maintain the build temperature. If temperature is coming down from the set value, preheating cycle were increased. The entire printing process takes place under vacuum environment. Normally the pressure inside the A1 machine during the printing process is ~10^{-2} Pa in the vacuum chamber and 10^{-4} Pa in the electron gun. During Titanium alloy printing, a small pressure of helium gas is filled in the vacuum chamber to avoid arc trip due to charge build up.

According to Brandl et al. [65] one of the benefits with running the AM process in vacuum is that post-processing such as Hot Isostatic Pressing (HIP) can close remaining porosity with a very good result. Pores in material made by AM-processes in inert gas contain remains of the gas and are therefore more difficult to close. Table 4.1 depicts the technical aspects and specifications of Arcam A1 machine.

Table 4.1: Technical aspects and specifications of Arcam A1 machine [63].

ARCAM A1 Technical Data	
Maximum build size	200x200x180 mm (W x D x H)
Surface finish (vertical & horizontal)	Ra25/Ra35
Beam Power	50–3000 W
Beam spot size (FWHM)	0.2 mm – 1.0 mm (continuously variable)
EB scan speed	up to 8000 m/s
Build rate	55/80 cm^3/h (Ti6Al4V)
No. of Beam spots	up to ~100
Cooling	Active (He gas assisted)
Power supply	3x400V, 32A, &7KW

4.3.2 Optomec- Laser Engineered Net Shaping (LENS) Process

Laser engineered net shaping is one of the LMD additive manufacturing processes that can produce near-net shape components from metallic powder. The LENS system uses a 750-Watt continuous wave Nd-YAG laser that is focused on the substrate by a six-inch focal length

convex lens. The interaction of the laser with the substrate produces a melt pool that is used to liquefy and consolidate the feedstock powder. Situated around the focusing lens are four powder delivery nozzles, that direct the feedstock powder to the melt pool on the substrate surface via argon carrier gas. Figure 4.4a shows the MR-7 Optomec LENS machine used in this study and Figure 4.4b shows the LENS printing process.

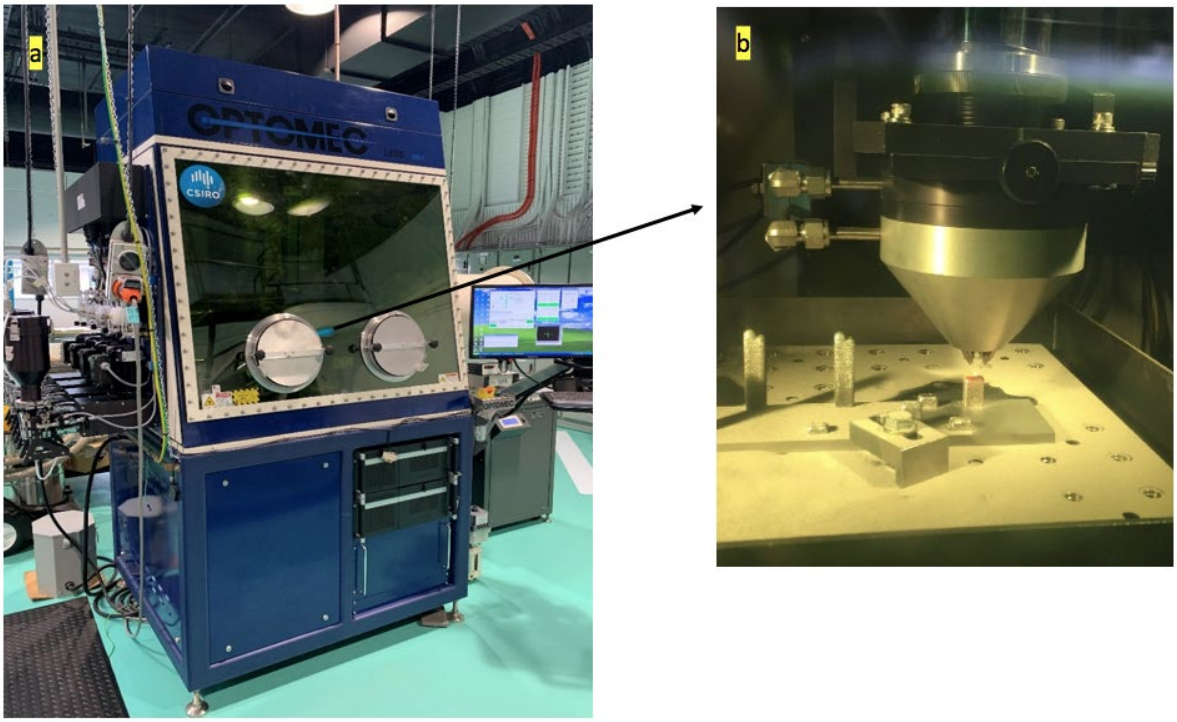

Figure 4.4: Optomec MR-7 machine used for TiAl printing (a) Optomec machine used in this study (b) LENS printing process.

A schematic of the Optomec LENS system is shown in Figure 4.5. The focusing lens, powder flow nozzles, and x-y motion stage are all enclosed in a glove box that operates in argon environment. The glove box allows manual manipulation of the substrate before and after deposition, without exposing the substrate and deposit to an oxygen-rich environment. The oxygen content inside the glove box is carefully controlled to a level of approximately 12 ppm. Oxygen control is important for Ti alloys because of its high reactivity to oxygen. Oxidation can cause brittleness and may lead to premature cracking of deposited samples.

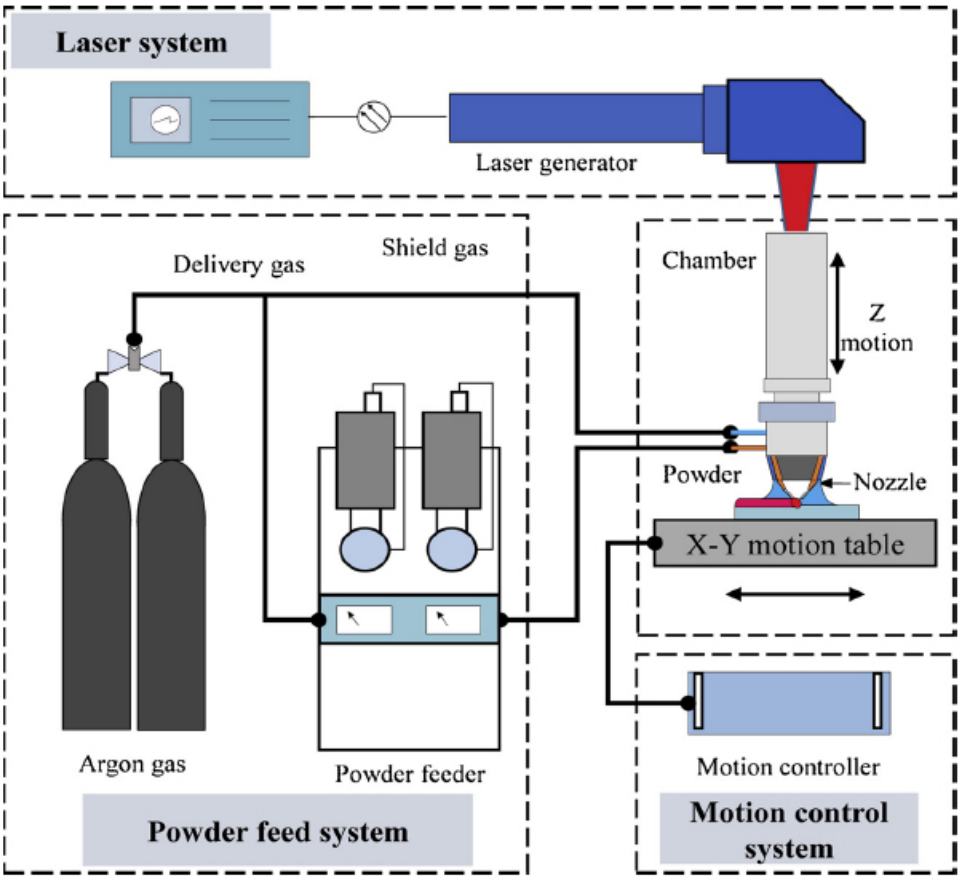

Figure 4.5: Schematic of the Optomec LENS system [66].

The laser deposition process contains many variables that can affect the quality of the deposition, and these variables include the laser power, travel speed of the x-y stage, powder flow rate, hatch spacing (distance between individual passes on one 2-D layer), layer thickness, and standoff distance of the head unit [66, 67]. Variations in these parameters significantly influences the processing conditions, and thereby the microstructure of the deposition. For example, increasing the traverse speed of the x-y stage gives rise to accumulated heat and leads to increase of temperature in the sample being built [5]. The standard LENS setting is with the nozzles set 9.5 mm off the build plane, with the focusing lens set in such a way that the laser is focused about 3.81mm below the build plane (Optomec call this the buried distance), giving a spot diameter about 500 μm [66]. This is basically three turns down of the focusing ring, which has a thread pitch of 1. 27mm. When the system is set to have the focus on the deposition plane, the spot size is 260 μm. Tests were conducted with the laser defocused 3.81mm above

and below the deposition plane which doubled the laser beam diameter to 520 μm. Table 4.2 describes the technical specifications of MR-7 Optomec machine.

Table 4.2: Technical specifications of MR-7 Optomec machine [66,68].

LENS MR-7 Technical data	
Process chamber dimensions	300 x 300 x 300 mm
Motion Control	XY linear table motion Z gantry motion Additional Axis Optional rotary dividing head All axes under full CNC control
Positional accuracy	± .25mm
Linear resolution	± .025mm
Motion velocity	60 mm/s
Deposition rate	Up to 100 g/hrs.
Gas purification system	Unit maintains O_2 level ≤10 ppm
Lasers	500W or 1kW IPG Fiber Laser
Dual powder feeders	Each feeder holds up to 2 liters of powder Gradient capability Optionally up to four feeders

In general, the as-deposited TiAl microstructure consists of macroscopic banding which corresponds to the height of the deposited layers, as shown in Figure 4.6. The continuous and

cyclical reheating produces a coarse microstructure in remelted areas and a finer microstructure in non-remelted areas, forming a layered or banded macrostructure [69].

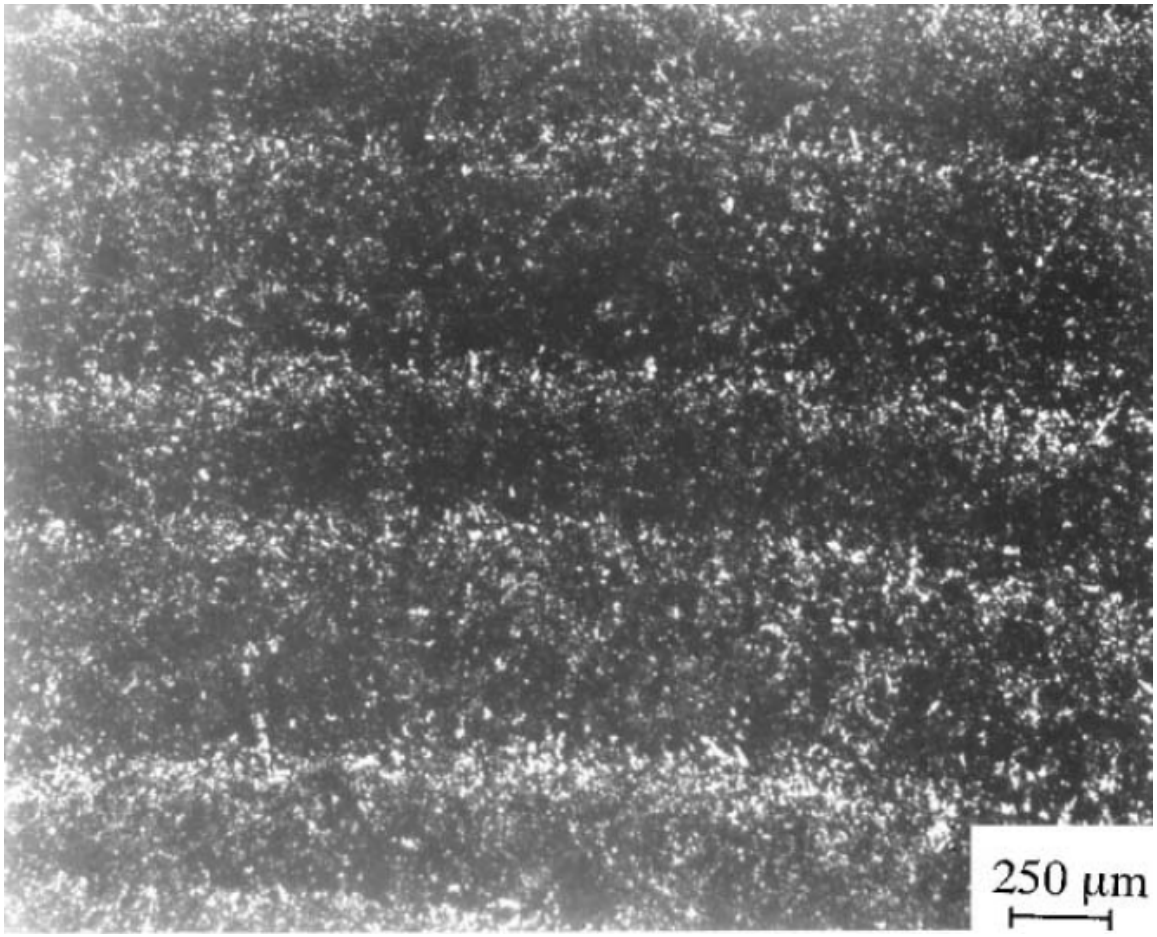

Figure 4.6: The as-deposited TiAl microstructure consisting of macroscopic banding, which corresponds to the height of the deposited layers [69].

4.4 Heat Treatment

TiAl samples were cut from as fabricated LENS and EBM processed cubes using a diamond wheel cutter. Small sliced pieces along build direction (X-Z) were kept in quartz tube. Using a glass blowing lathe, the quartz tube was sealed for heat treatment, to avoid oxidation and other contamination during heat treatment.

To avoid diffusion of Si from the quartz tube into the sample in furnace, direct contact between the sample and the quartz tube was prevented by wrapping the sample with tantalum wire. The tubes were evacuated with vacuum system, and finally back filled with 25 kPa of argon before

they were sealed. A box furnace was used for the heat treatment. Once the sample tube was ready, a furnace was preheated to the desired temperature, and samples were kept at temperature based on the heat treatment plan, followed by either furnace or air cooling.

4.5 Microstructural characterization, physical measurements and mechanical testing

Metallographic analysis of AM samples was done using different characterisation methods. Optical microscopy (OM; Olympus Essential), scanning electron microscopy (SEM; Zeiss Merlin), X-ray diffraction (XRD; Bruker D8 Advance X-ray Diffractometer), transmission electron microscopy (TEM; FEI Tecnai F20 TEM) were used to examine the microstructure of as-built and heat treated Ti-48Al-2Cr-2Nb samples. Image analysis was done using Olympus essential and Image J software.

4.5.1 Sample preparation

As fabricated TiAl samples were cut using a high-speed silicon carbide cutter. Solid samples were hot mounted in polyfast conductive resins resin in a Struers CitoPress-10/-20 hot mounting machine. A temperature of 170°C and a pressure of about 300 bar was applied during hot pressing. Water cooling was used to obtain efficient cooling. Samples were ground using grit papers starting with 400, 600, 1000, 1200 and 4000 grit size. Finally, polished samples were obtained by using colloidal silica (SiO2) based oxide polishing suspensions (OPS-1 μm) with some addition of ammonia. As fabricated samples, after metallographic preparation were etched in modified Krolls reagent for 5 seconds.

4.5.2 X-ray diffraction (XRD) Analysis and Rietveld refinement

Identification of phases and calculation of phase fractions were done using XRD plots in the as fabricated and heat-treated samples. A Bruker D8 Advance X-ray Diffractometer operating under CuKα radiation equipped with a Lynx Eye detector was employed to get XRD patterns. Samples were scanned over the 2θ range 5° to 130° with a step size of 0.02°.

Analysis of the collected XRD data done using the Bruker XRD search match program EVA4.2. Crystalline phases were recognized using the ICDD-JCPDS powder diffraction database. Quantitative Rietveld analysis of the XRD patterns from TiAl powder samples and solid TiAl sample after EBM/LENS were carried out by fitting of the whole diffraction pattern using Bruker TOPAS V5 suite.

For Rietveld analysis, starting parameters were the parameters from the nearest match phases in the ICDD-JCPDS powder diffraction database. Spherical harmonics preferred orientation function used to correct the relative peak intensities. Background signal was described using a combination of Chebyshev polynomial linear interpolation function and 1/x function [70]. Cell parameters, vertical sample displacement, peak full width at half maximum, and scale factor were all refined. For weight percentage values, the error ranges were calculated on the basis of three estimated standard deviations as calculated by TOPAS.

In the Rietveld method, the weight fraction (wt.%) of the of the crystalline phases α_2, γ and β are calculated using Hill and Howard relationship (4.1) [70].

$$W_\alpha = \frac{S_\alpha (ZMV)_\alpha}{\sum_{j=1}^{n} S_j (ZMV)_j} \qquad (4.1)$$

Where,

• S_α is the Rietveld scale factor for phase α_2

• ZM is the mass of the unit cell contents,

• V is the volume of the unit cell, and

• n is the number of phases in the analysis.

The Rietveld method relies on the assumption that all phases in the sample are crystalline and have been included in the analysis.

4.5.3 Optical microscopy

As fabricated samples after metallographic preparation, were etched in modified Krolls reagent for 5-10 seconds. Optical microscopy used to analyse lamellar colony boundaries and uniformity of microstructure along the build direction, for which lower magnification preferred.

4.5.4 Scanning Electron Microscope (SEM)

SEM was extensively used in this study. Secondary (SE), InLens and back scattered (BSE) mode of electron detection were used in FEI Zeiss Merlin scanning electron microscope. Examination different phases, morphological variations, grain size, coarsening, and other microstructural observations were done using SEM, mainly in BSE mode. Samples were prepared as described in the 4.5.1 Voltage of 10 KeV- 20 KeV with 2.5 nA spot size used for image capturing.

4.5.5 Energy dispersive X-ray spectrometry (EDS)

Energy dispersive spectroscopy (EDS) was used to identify elements present within the samples. Samples for SEM imaging were also analysed using EDS. In SEM when electrons strike the sample surface, it will produce X-rays from it. The EDS system used was AZTEC, manufactured by Oxford Instruments Pty. Ltd using their X-Max Extreme Silicon Drift Detector (SDD) detector (spatial resolution ~1μm), linked with Zeiss Merlin SEM. An accelerating voltage of 10 -15 kV, spot sizes of 2 and working distance (WD) of 8.5 were used for EDS analysis. Measurement counts maintained at 10^4 to get tolerance level below 2%. The spectrum quantified and the results were taken as semi-quantitative and trends compared. Composition and distribution analysis of elements, mainly Ti, Al, Nb, Cr and Fe were done. Major use of the analytical electron microscopy was to obtain a qualitative microchemical analysis of α_2, γ and β phases along the build direction.

4.5.6 Focused ion beam (FIB) technique

FIB (focused ion beam) technique was employed to cut 100 nm thin TiAl samples for TEM study. As fabricated TiAl samples were prepared as described in 4.5.1 Figure 4.6 depicts different steps during FIB technique.

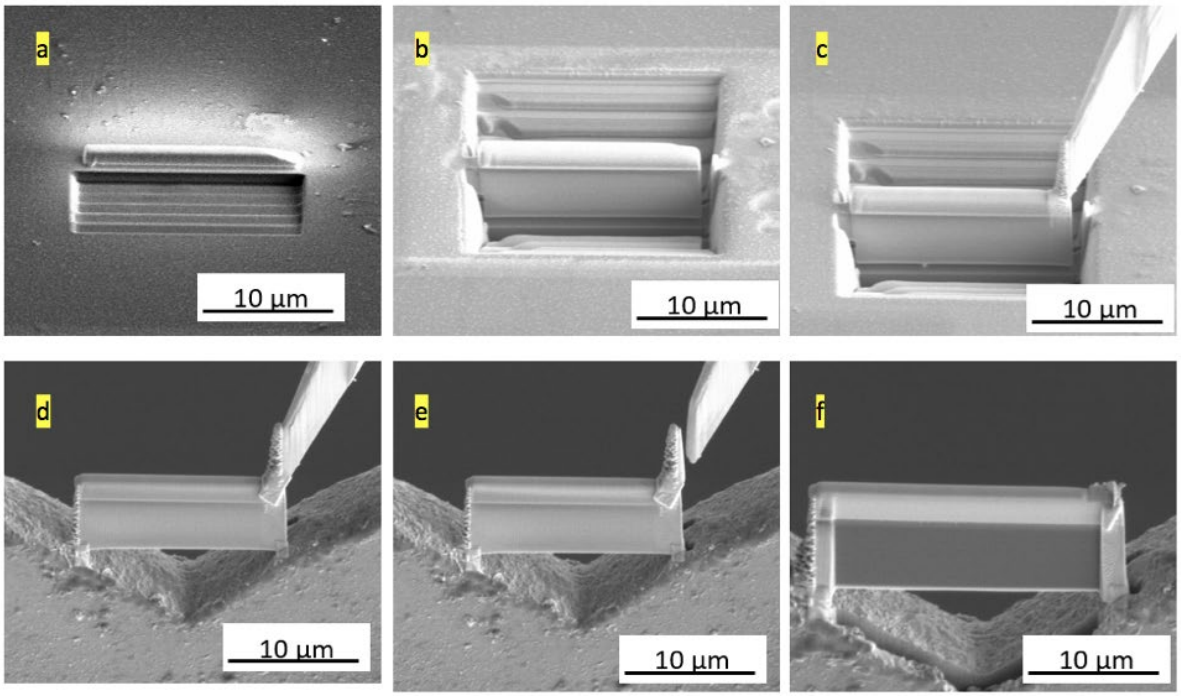

Figure 4.7: SEM images of FIB Lift out (a) Platinum deposition in 22 µm length (b) Cutting of stair step trenches in sample (c) Sample lift out using tungsten needle after cutting (d) Fixing of sample in Cu grid using Pt deposition (e) Separating the tungsten need.

4.5.7 Transmission electron microscope (TEM) investigation.

TEM was used to confirm the presence of beta phase and to study the fine primary lamellar structure. FEI Tecnai F20 TEM with EDAX system was used. Thin FIB lift out samples were used for TEM study. Both bright field imaging and dark field imaging were used to identify the fine features such as fine lamellar colonies and beta precipitates.

Selected area electron diffraction (SAED) pattern's ring diameter and distance between spots were measured to calculate d-spacing. Crystal structures were identified by comparing d-spacing.

4.5.8 Electron Back Scatter Diffraction (EBSD)

EBSD was carried out on FEI Nova Dual Beam FIB SEM equipped with oxford instruments symmetry EBSD detector. Samples were prepared using the standard polishing procedure outlined above. After a first set of polishing, etching and OPS polishing was repeated 3-4 times

to get a deformation free surface. Grids of 320 × 500 points were taken using a step size of 100nm, at an accelerating voltage of 10kV. 70̊ specimen tilt was given for EBSD detection

4.5.9 Integrally Coupled Plasma-Optical Emission Spectrophotometer (ICP-OES)

ICP OES can determine the composition in ppm level. It was used to measure the elemental composition of alloy powder accurately. Metal alloy samples were analysed in order to determine their Al, Cr, Fe, Nb, Ni and Ti concentrations. Samples for chemical analysis prepared by Microwave digestion in Teflon beakers with 10ml of 1:1 HNO_3 and 0.5ml of 48% HF by warming on a hotplate. Resulting solutions were diluted as required and measured by ICP-OES for major requested elements. Certified single element solutions were used to prepare calibrations and certified multi-element check solutions were used to check accuracy of calibration. LECO – TCH600 system was used to measure the oxygen pick up during the process

4.5.10 Differential Scanning Calorimetry (DSC)

DSC analysis was done on NETZSCH STA 449F1 instrument. As fabricated samples weighing ~20 mg were used for DSC analysis. Overnight purging with Ar was done to prevent any contamination. The heating rate was varied from 5°C/min – 50°C/min. Samples were heated to 1500 °C to find the phase transformation temperature.

4.5.11 Particle size analyser

Particle size distribution analysis of the as received and recycled powder from EBM and LENS machines were done using Malvern master sizer 3000µ. The technique uses a laser that passes through a powder dispersed solution, the particles then scatter the laser beam and then the diffraction obtained is dependent on the size of the particles. Based on the scattered laser beam diffracted intensity, the size distribution and median diameter of the TiAl powder is calculated.

4.5.12 Vickers micro Hardness

Hardness measurement was done on samples made at different printing conditions. The Hardness test was a quick and easy way to get some idea about the mechanical properties of materials. Vickers hardness tests were done using a Micromet 2100 Microhardness tester by applying a normal load of 300g for 10 seconds. Flat samples were prepared. The average

hardness value was calculated from 20 repeated hardness tests for each sample. A quick approximation of the yield strength was calculated from microhardness using the empirical relationship between microhardness and yield strength as shown [71].

$$\boldsymbol{\sigma_y = \frac{H_v}{3}}$$

H_v is HVx9.81 MPa.

4.5.13 Lamellar colony size and lamellar thickness measurement

Image analysis was done on the sets of 20 SEM BSE micrographs at 1000X magnification on each layer position and average lamellar colony size was calculated. The measurement was done by highlighting the edges of lamellar colony boundary as shown in Figure 4.8, and measuring the area fraction using ImageJ software [72]. The image analysis process followed the standard sequence as follows: 1. Global scale set based on micrograph scale bar 2. Background removal 3. Threshold to produce binary image isolating the relevant features and 4. 'Area fraction measurement' to get average area of lamellar colonies.

In SEM-BSE images for TiAl Samples, dark regions indicate the γ phase and the bright regions correspond to the α_2 phase. Thickness measurement of (α_2 + γ) laths were done by a line intercept method using BSE images. It is acknowledged that this method may not be an accurate way of determining the true lath thickness, since it does not ensure that the laths are edge-on. Also, the orientation of lamellar colonies can alter the actual thickness of lamellae. Still, the lamellar thickness calculation sheds light on the qualitative differences between samples, at different AM conditions.

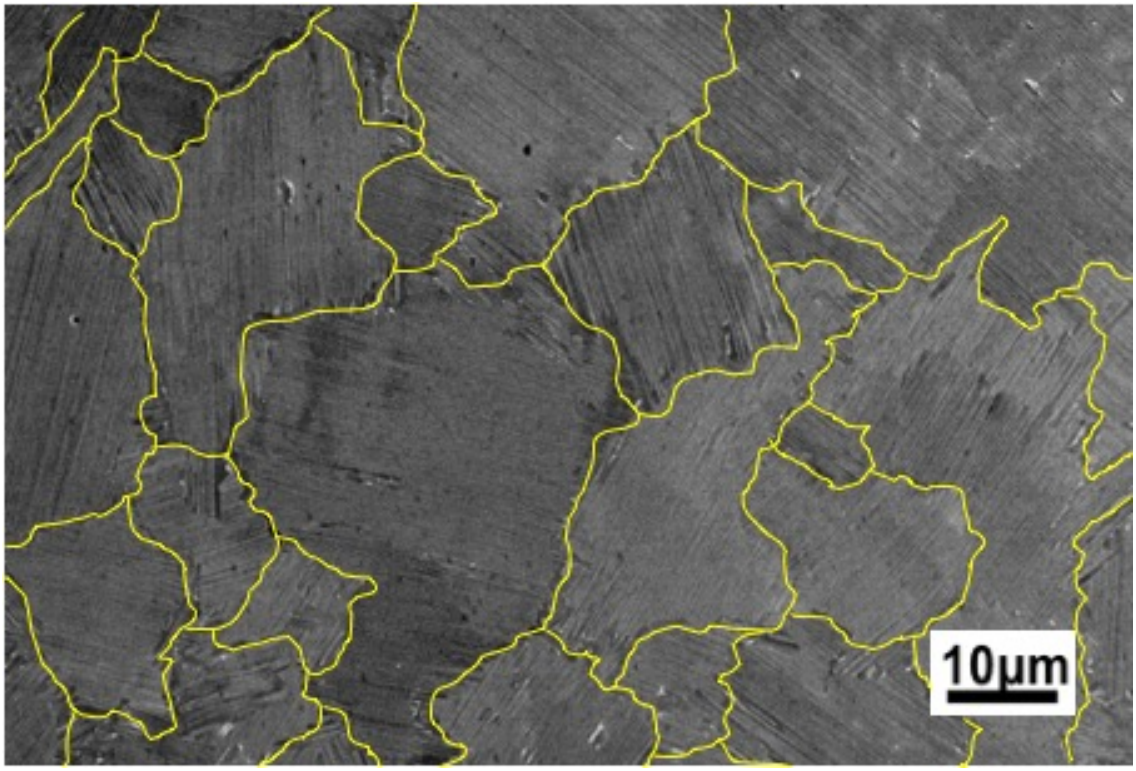

Figure 4.8: TiAl SEM image showing highlighted lamellar colony boundary, for ImageJ analysis.

Chapter 5: Preliminary characterisations of feed material and EBM process stabilization and optimisation for TiAl

Fabrication of materials like TiAl alloys which are not widely employed in additive manufacturing, requires a systematic approach to develop an ideal process scheme. This chapter demonstrates optimum printing conditions developed in EBM, for fabrication of TiAl samples with near full density and minimal defects. Preliminary characterization of the as-received and recycled powder are discussed first and then process stabilisation and optimisation of EBM are discussed briefly.

5.1 Preliminary characterization of the feed material: Gas atomized TiAl powder

Powder characterization includes many different aspects such as chemical composition, surface morphology, particle size distribution, related powder density (bulk and tap density), flowability and satellite distribution [62,73]. These will directly affect the powder layer quality and final quality of the product. Variations of the same features in recycled powder also studied, along with oxygen pick up during the printing process.

5.1.1 Chemical composition of the as-received and recycled powder

The target composition of the processed materials was Ti-48Al-2Cr-2Nb. Due to the high temperature during the process and the vacuum environment in EBM, evaporation of aluminium was observed during the EBM.

The chemical composition (by ICP analysis) of the starting powder and recycled powder used in EBM is shown in Table 5.1. LECO analysis showed minimal pick up of oxygen due to the high-vacuum environment in Arcam A1 machine.

Table 5. 1: Chemical composition of Ti-48 Al-2Cr-2Nb Powder (In At.%).

Sample	Al	Cr	Nb	Ti	O
TiAl – As-received powder	47.7 ± 0.4	1.4 ± 0.1	1.7 ± 0.1	48.9 ± 0.4	0.27 ± 0.01
TiAl – 1 Run	47.5 ± 0.4	1.5 ± 0.1	1.8 ± 0.1	48.9 ± 0.4	0.30 ± 0.01
TiAl – 10 Run	47.1 ± 0.4	1.6 ± 0.1	1.7 ± 0.1	49.2 ± 0.4	0.32 ± 0.01
TiAl – 15 Run	47.1 ± 0.4	1.5 ± 0.1	1.7± 0.1	49.3 ± 0.4	0.35 ± 0.01

5.1.2 Particle size distribution of Powder

An appropriate Particle Size Distribution (PSD) gives a better packing density, which is critical for process stability. Figure 5.1 shows the PSD of the Ti-48Al-2Cr-2Nb powders. The specified PSD for Arcam A1 process was 40-140 μm. D_{50} of as-received powder is 87 μm.

The PSD of recycled powder also been studied and after couple of runs in the EBM machine, PSD is improved mainly because of the removal of satellites and fine particles in Powder recovery system (PRS), but recycling may become difficult after several cycles of printing, due to sintering of particles and presence of impurities.

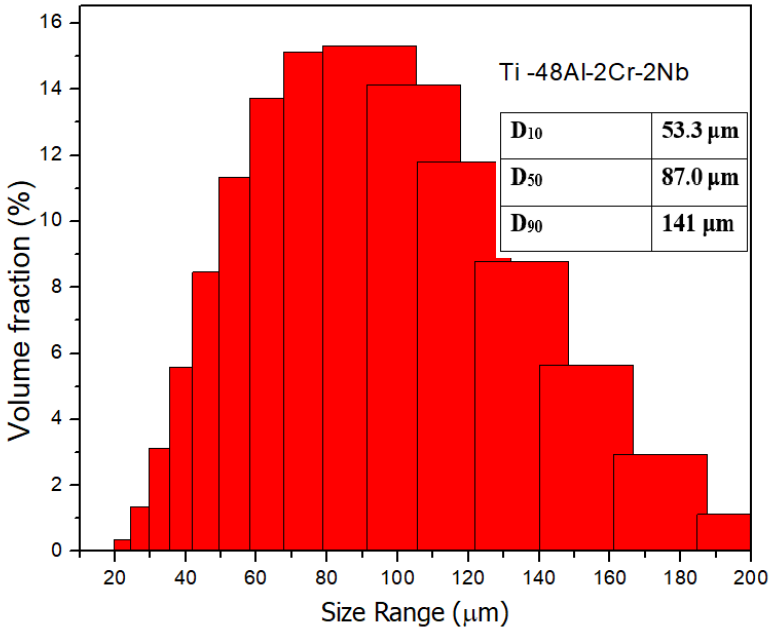

Figure 5.1: PSD of the as-received Ti-48Al-2Cr-2Nb powder.

5.1.3 SEM analysis of as-received powder - Microstructure and size distribution

Ti-48Al-2Cr-2Nb powder was observed by scanning electron microscopy (SEM). SEM micrographs revealed spherical powder of size ranging between 50-140 µm, as shown in Figure 5.2. Many particles could be observed to be sticking onto the surface of the processed powder, which are called satellites. Some gas porosity was also observed. In some powder particles, holes are visible. In cross section it appears as spherical pores. Argon entrapment during the gas-atomisation process is very common, leading to gas porosity, typically spherical in morphology, as observed in this study [74].

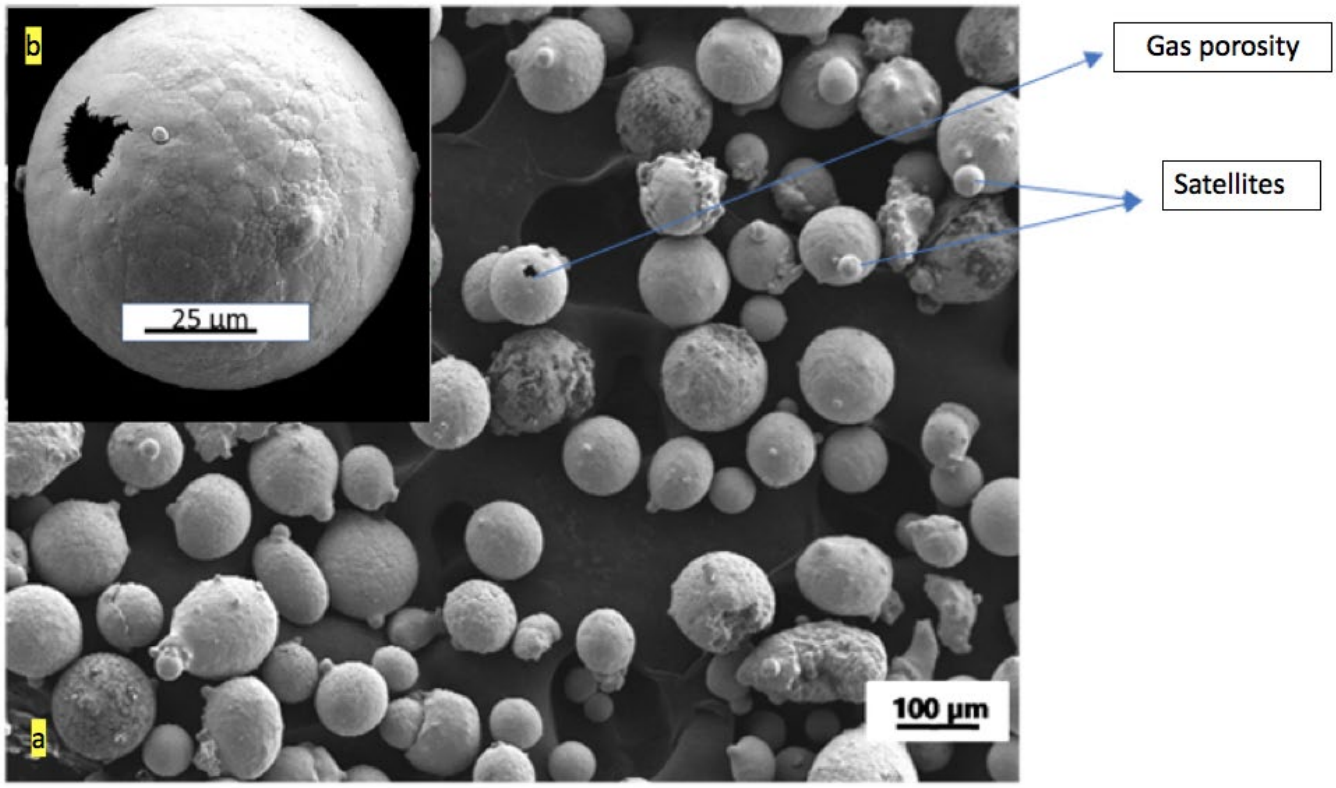

Figure 5.2: SEM images of Ti-48Al-2Cr-2Nb alloy powders. (a) as received powder (b) magnified single particle showing surface morphology.

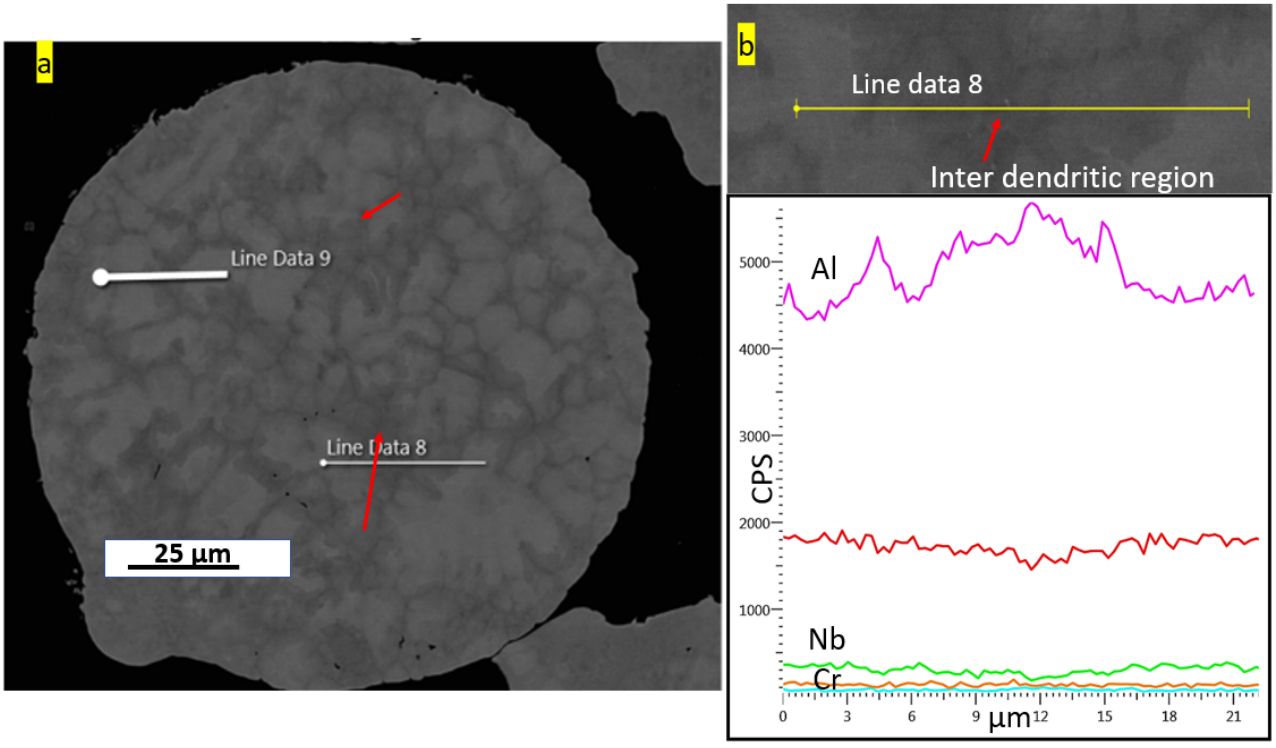

Figure 5.3: Cross section of TiAl powder shows (a) dendritic structure (b) The Al segregation at inter dendritic region is pointed by arrows.

In Figure 5.3, the cross section of the powder is shown. Due to rapid solidification, microstructure was dendritic in morphology. EDS line analysis showed aluminium enrichment in inter dendritic region.

5.1.4 Flowability

The flowability of as-received powder and recycled powder after each run, measured according to ASTM B213-03. Flowability values are enlisted in Table 5.2. The critical flowability in Arcam A1 machine was around 24-26 s/20 mm^3 [48]. An ideal flowability and packing density is required to achieve good densification in the final parts. Ideal flowability is also required to achieve a constant layer thickness and it has a strong influence on the powder layer forming process and hence, on the uniformity of the built-up components. Spherical particles with fewer satellites show better flowability and are preferred for EBM [64].

Table 5.2: Flowability of as-received powder and recycled powder after each run.

Powder	Flowability (s/20 mm^3)
As-received	28 ± 0.5
1-run	26 ± 0.5
10-run	24 ± 0.5
15-run	24 ± 0.5

5.1.5 Hausner ratio

Hausner ratio (HR), is the ratio of tapped density to apparent density of metal powder. HR value indicates the flowability and spread of powder during raking. HR value less than ≤ 1.25 is considered to be as ideal flowability for EBM process but HR greater than > 1.40 is not recommended [48]. The table 5.3 shows the apparent density, tap density (1000 taps) Hausner ratio (HR) of as-received and recycled Ti-48Al-2Cr-2Nb powder.

Table 5.3: Apparent density, tap density and Hausner ratio of as-received and recycled powder.

Powder batch	Apparent density (g/ cm^3)	Tap density (g/ cm^3)	Hausner ratio (HR)
As-received	2.25	2.72	1.21
1-run	2.31	2.66	1.15
10-run	2.31	2.68	1.16
15-run	2.25	2.48	1.1

Tapped and bulk powder density was measured based on ASTM D7481-09 and apparent density, according to ASTM B212-99.

5.2 EBM process development

Printing process was performed at high temperature, making process stability critical for fabrication of successful component. Different stages/ challenges faced are discussed here.

5.2.1 Build temperature

Build temperature was maintained at 1000 ºC by preheat I and preheat II. The average heat input and the layer time are the main factors in maintaining the temperature. Table 5.4 shows the preheating parameters used for TiAl manufacturing in this study and the energy density was calculated based on the Equation 5.1.

To maintain the temperature at required setting during printing, beam current and number of preheating cycles were varied. 5-15 cycles were repeated depending upon the temperature loss. If temperature dropped from the set value, preheating cycle was increased. As process was

manually adjusted, process parameters were selected manually during the entire printing and so, preheating cycles were also adjusted according to the temperature feedback, concurrently with the process. Main aim of preheating cycle variation was to maintain the build temperature.

Table 5.4 : Preheating parameters for TiAl manufacturing.

	Average Beam current (mA)	**Scanning speed (mm/s^1)**	**Line offset (mm)**	**Average energy density (J/mm^2)**
preheat I	24	10000	0.2	0.65
preheat II	26	8000	0.2	0.8

The substrate temperature profile as a function of the time is depicted in Figure 5.4, showing three stages. These stages are preheating the stainless steel (SS) substrate to 1100 ºC, second stage was build temperature during printing and the last stage, cooling down after the printing. Cooling can be assisted by helium gas, if high cooling rate required. Figure 5.4 and 5.5 shows two different build temperature conditions, 950 ºC and 1050 ºC respectively. After reaching the set build temperature the preheating continued for 30-40 minutes, that was for sintering the powder below the start plate. During the build process there was a slight dip in the temperature, which stabilized at around 50 ºC lower than the set temperature.

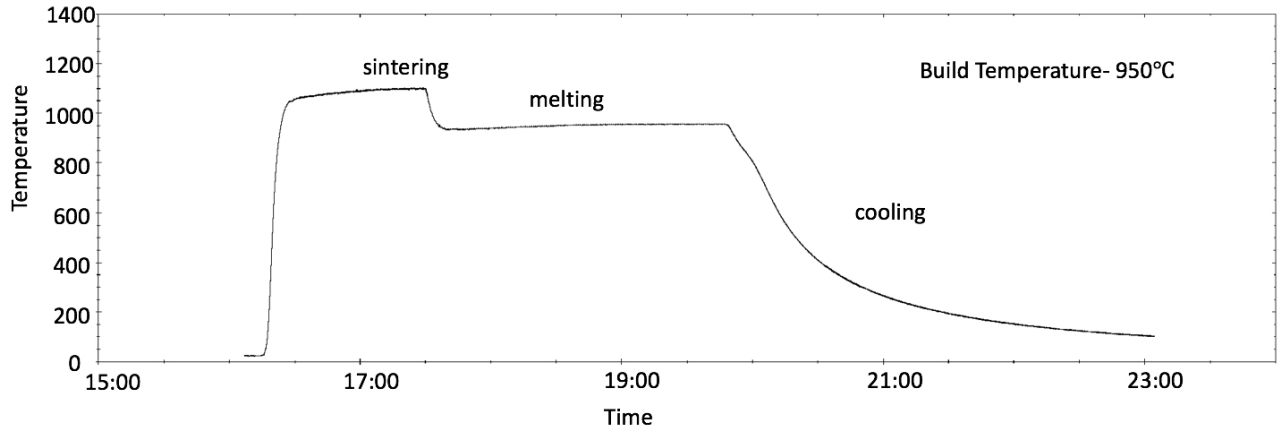

Figure 5.4: Printing at 950 °C build temperature.

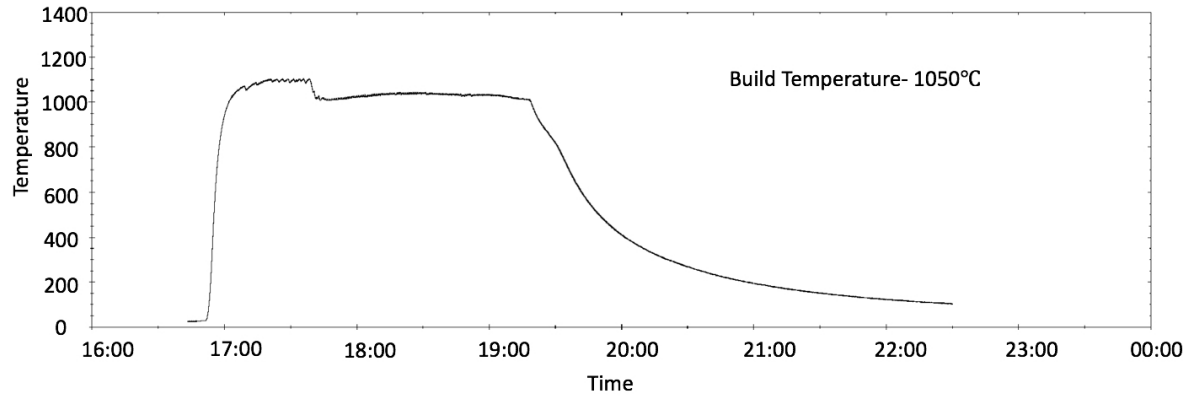

Figure 5.5: Printing at 1050 °C build temperature.

As depicted in Figure 5.5, lesser number of arc trips were observed during printing at 1050 ºC. If preheating cycles are not optimised properly, it may cause over sintering at higher build temperature.

5.2.2 Powder Quality Deterioration during EBM Processing

Prevention of charge build up is an important aspect to be considered when printing TiAl samples by EBM. Sintering enhances powder conductivity, thereby reduces the possibility for charge build-up and makes melting smoother. Sintering needs to be done cautiously, as quality of sintering significantly affects the outcome of the process.

Figure 5.6 shows SEM micrographs of powder from the build platform at different preheating conditions. Figure 5.6a shows loose powder from powder bed before preheating, where particles are well separated. 5.6b shows properly sintered powder, just enough to make powder bed. Sintering is just to connect the powder, not melt. 5.6c and 5.6d depicts over sintered condition where powder particles are melted and fused together like a scale, forming a coalescence. When recycling TiAl powder, the over sintered one is difficult to recycle [64].

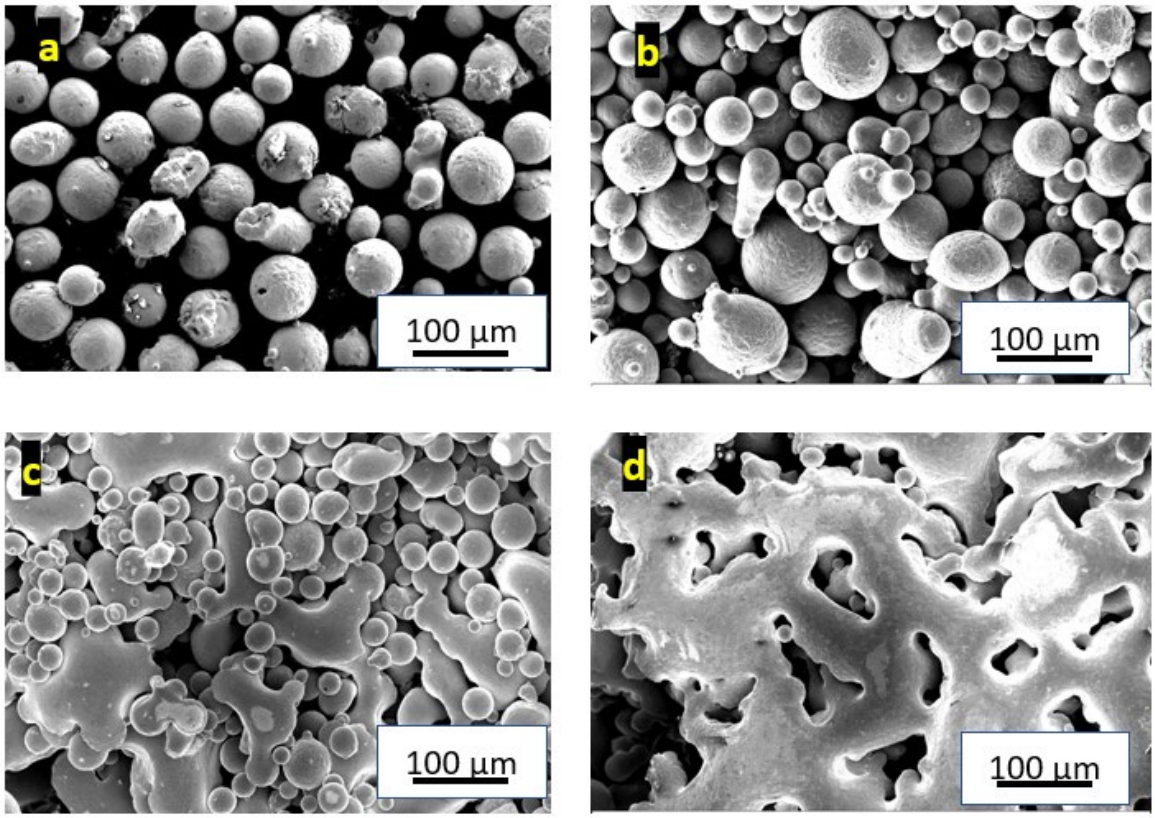

Figure 5.6: Powder morphology at different sintering conditions during preheating. (a) loose powder from powder bed (b), sintered powder, just enough to make powder bed (c), more sintered powder and (d) over sintered powder.

Rather than increasing the preheating current, maintained high temperature was more effective and beneficial for avoiding arc trip and optimum sintering. To achieve stable printing, lots of pins were included in build file along with specimens. Pins were printed using same parameters as that of samples. Using pins was intended to give more heat input to the powder bed, so that proper sintering and maintenance of temperature in the powder bed could be achieved. Pins of 1mm radius were included in CAD design, covering samples uniformly in the powder bed as shown in Figure 5.7, the build after cleaning from PRS.

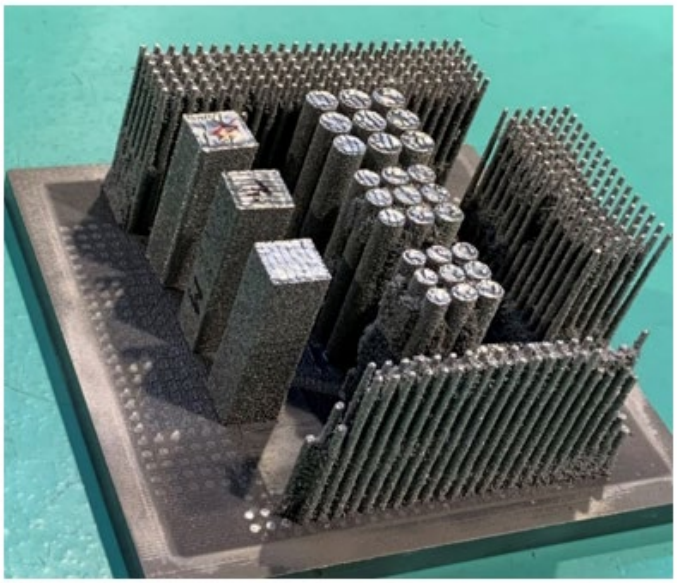

Figure 5.7: Build after cleaning from PRS.

5.2.3 Samples printed at different AM conditions

Figure 5.8 shows the morphology of different samples printed at different EBM conditions. In Figure 5.8a the sample printed at low energy level is shown, exhibits heavy porosity. Figure 5.8b shows excessive balling due to instability in melt pool. Balling was also observed with powder oversintering. Sample in Figure 5.8c, printed at higher ED and exhibits bulging due to excessive heat. Figure 5.8d shows optimal sample, with minimum defects.

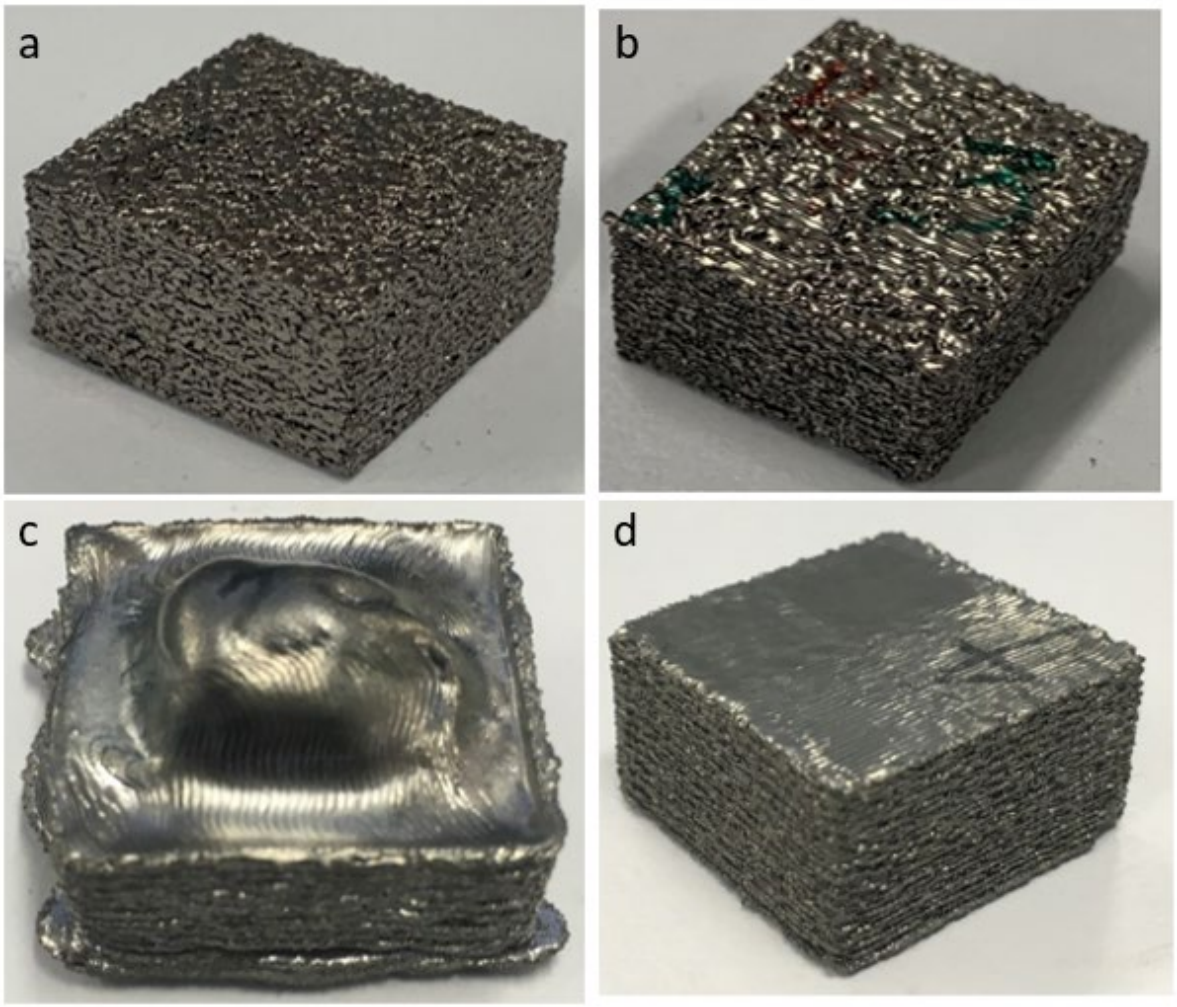

Figure 5.8: Sample showing (a) porosity (b) balling (c) bulging and (d) optimised.

Properties of additively manufactured parts are dramatically influenced by process stability, process parameters, scanning strategy and raw material characteristics. Many investigations have been conducted and focused on process parameter optimization for getting samples with minimal defect or required quality [64,75]. In the current study mainly lack of fusion is observed due to insufficient energy input; and bulging and segregation occurred due to high energy input. This can be reduced by selecting area ED between 2-8 J/mm^2.

5.2.4 Defects in EBM Samples

Different processing issues can create defects in the material, some of which observed in current study are listed below.

- Gas porosity in EBM TiAl samples is caused by entrapped argon gas in the powder during the gas atomisation process and this cannot be completely avoided.
- For low energy input, successive scan tracks cannot fully re-melt the solidified layer, and large pores - lack of fusion appear between layers. By increasing the heat input, the lack of fusion can be minimised.
- Low energy input also causes un-melted powder particles, which are visible in between layers.
- High energy input causes less stable and superheated melt pool, resulting in evaporation of volatile element like aluminium and bulging of the solidified layer. Spattering and segregation due to Al evaporation was also observed

Spatter ejection may also lead to regions of porosity. Unlike lack of fusion, spattering is mainly caused by too much energy application [64]. Visual observation and optical microscopy are often used to quickly assess the quality of as-built or sectioned EBM specimens in terms of geometrical accuracy and the presence of noticeable defects. Figure 5.9 shows the section view of defective samples. Mainly defects oberved are lack of fusion, gas porosity, non-melted powder particles and inclusion of sintered scales. Figure 5.9a shows lack of fusion, which occurs in between layers. For proper bonding between layers along build direction, atready solidified layer should be remelted when electron beam is applied. Insufficient remelting leads to lack of fusion, with larger pores with sharp tips and sometimes they may be connected with other defects forming a big channel of defect. Figure 5.9b exhibits gas porosity carried from the metal powders. These are uniformly distributed in sample and most of the times gas pores are smaller than other defects. Figure 5.9c shows inclusion of sintered scales trapped inside the melt pool, during higher heat input. Figure 5.9d shows non melted powder particles distributed in between layers. This is mainly observed in low energy samples.

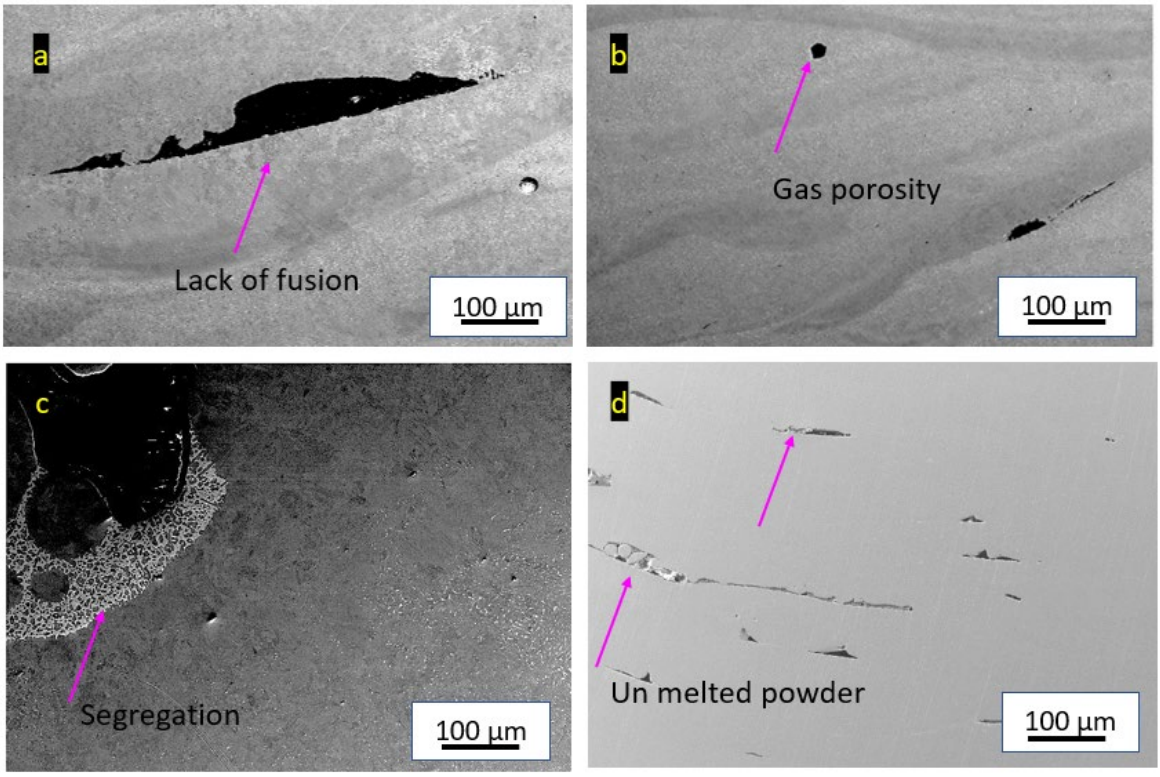

Figure 5.9: Section view of defective samples, showing (a) lack of fusion (b) gas porosity (c)inclusion of sintered scales and (d) non-melted powder particles.

5.2.5 EBM process stabilization and controlling the bed temperature profile.

For EBM manufacturing using newer alloys, process strategy development requires a complicated sequential adjustment of parameters, using a trial and error method. 3 trials of each parameter combinations were done. There was enough quantity of powder in the hopper for 3 continuous trials, and the powder consumption was very less since samples printed were very small, 20*20*10 mm. Moreover, the composition analysis after post- print powder recovery throughout the experiment did not show much variation and there was negligible oxygen pickup because of the high vacuum environment in EBM build chamber, as shown in Table 5.1. This may also necessitate a modification of machinery. Process must be stabilised first, by developing appropriate processing themes, prior to original printing. Then process optimization is needed, in accordance with the microstructural and property requirements. In case of comparatively newer alloys like TiAl, EBM manufacturing does not have a fixed model or previous knowledge based on literature, compared to conventional manufacturing techniques. This makes process stabilisation more significant in EBM.

The main challenges during TiAl printing were charge build ups in powder while applying the electron beam and associated arc trip, which is termed as . Arc trip caused powder to repel each other and caused powder cloud, and it was kind of powder explosion, which contaminated the column and thus process stopped.

Smoking is considered to be due to poor sintering of the powder, which results in failure of adequate electrical conductivity [76]. The temperature profile shown in Figure 5.10 depicts the temperature fluctuations in the build platform, because of the continuous arc trips while stabilising the process. When arc trip occurs, temperature in the column increases due to the spattered hot powder at column. When hot metal powder reaches the column due to excessive smoking and explosion of powder, temperature in the column increases [76].

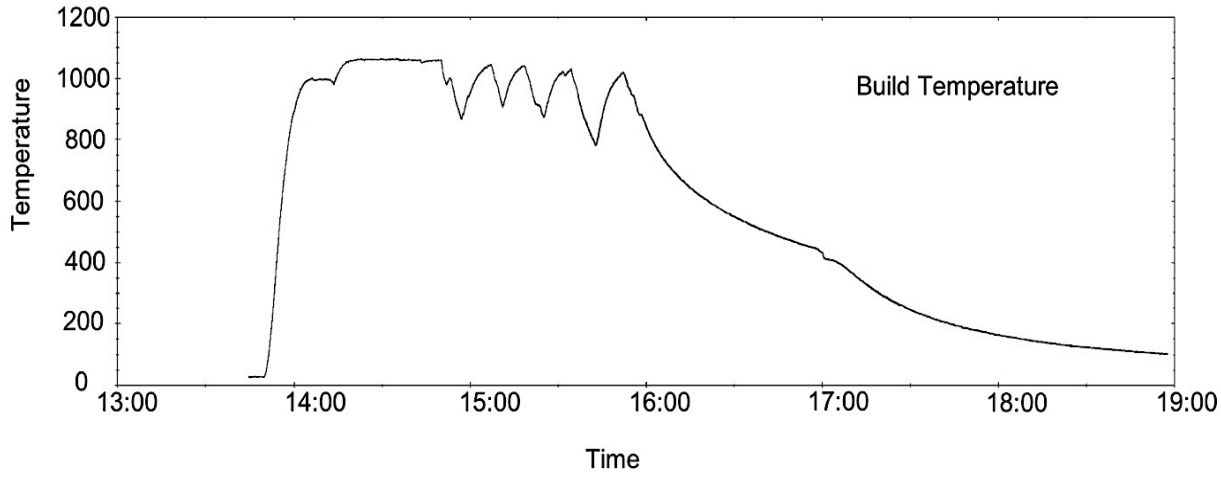

Figure 5.10: Temperature profile during arc trips.

If arc trip is not controlled, build temperature drops down mainly because of multiple pauses. If temperature goes below 800 ºC printing cannot be done for TiAl. In this study arc trip was effectively controlled and this was achieved by following these methods, which are enlisted below.

1) Heating of the build plate was done, to above 1000 ºC and held it there for 30-40 minutes to sinter the powder below and surrounding the start plate. Thus, effective conduction of the charge accumulation was possible. It was also found to be effective, keeping high conductive metal blocks below the start plate so that charge accumulation was prevented.

2) Maintaining high temperature was done by controlling excessive thermal loss, mainly by radiation. Extra aluminium foils were used along with heat shield so that Al foil reflected the radiation back to build area and it was quite effective. Providing more amount of powder below the start plate and sintering it well before printing also significantly reduced the temperature loss by conduction. Smaller start plate (150 mm) found to be more effective and used throughout the TiAl printing. These hardware experimentations helped to stabilize the process to a greater extent.

3) Pre-sintering of TiAl powder was performed, to give enough bonding and continuity for better charge drain out. Care was taken not to over sinter the powder bed, which affects the recyclability of the powder. The schematic (Figure 5.11) representing the degree of sintering, correlated with the SEM micrographs of sintered powder (Figure 5.6). In Figure 5.11a, powder is not sintered enough, and this can cause arc tripping. Figure 5.11b represents properly sintered condition, where necks are formed in between powder particles, at those points where the particles are in contact.

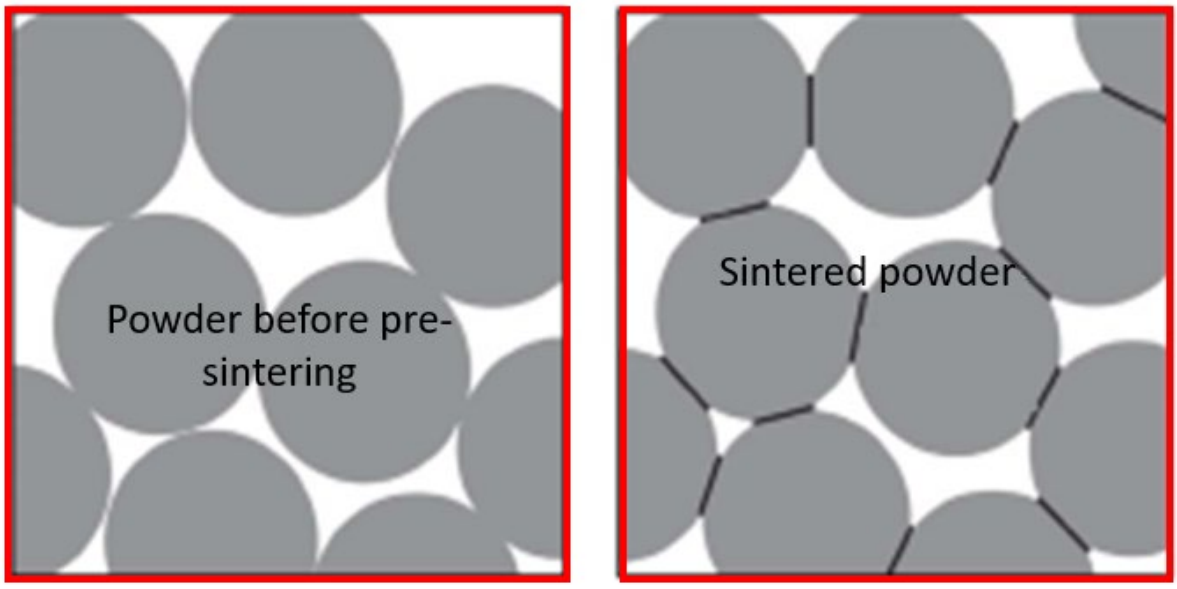

Figure 5.11: Schematic of sintering of powder during EBM process.

Sintering is needed just to connect the powder; excessive surface melting is not desirable. In case of over sintering of powder, scales from excess sintering can get trapped inside the melt

pool. This leaves inclusions in samples, forming defects and cause cracking. Also, scales can affect raking and disturbs top layer spreading. This can occur in optimised samples as well.

Appropriate build temperature and sintering requirement varies with different alloys. Also, it varies for same alloy, with different powder characteristics. For example, the TiAl powder with more satellite particles was quite difficult to get sintered and caused excessive arc tripping, leading to process stoppage [76].

Once the process is stabilized, the next challenge was the process optimisation, in order to obtain printed parts with desired properties and minimal defects.

5.3 Process optimization: Influence of EBM parameters on Microstructure & Integrity

Proper selection of process parameters is inevitable, in order to fabricate samples with desirable qualities and minimal defects. Two types of porosity are mainly observed during EBM- one is due to lack of fusion between interfacial layers and the other is spherical porosity due to porosity in powder. Porosity of powder is formed during gas atomization and processing, which is shown in Figure 5.2. As a result, gas gets entrapped during powder deposition and is carried to the sample, forming porosity in sample, which is difficult to remove. Lack of fusion pores are formed due to inadequate heat input and can be eliminated by appropriate input of energy. Lack of fusion pores are normally observed between melt pool boundaries and have more detrimental effect on fabricated parts [64, 74]. Defects due to balling or liquid spheroidization are influenced by various metallurgical mechanisms including molten pool behavior and wettability of the melt pool, which are dependent on energy input [64]. Thus, appropriate ED, achieved by optimization of process parameters can significantly eliminate defects and produce quality build. Optimisation of EBM process recipe includes optimising several process parameters like electron beam current, scan speed, focus offset, hatch spacing, line order and build temperature.

The scanning strategy used in this study is schematically represented in Figure 5.12a. Samples were fabricated by ‘snake’ scanning strategy where electron beam was moved in a zig zag manner, followed by a change of 90° after each layer. Line offset is highlighted in the picture. Line offset was selected in such a way that proper overlap of melt pool occurs, as shown in Figure 5.12b.

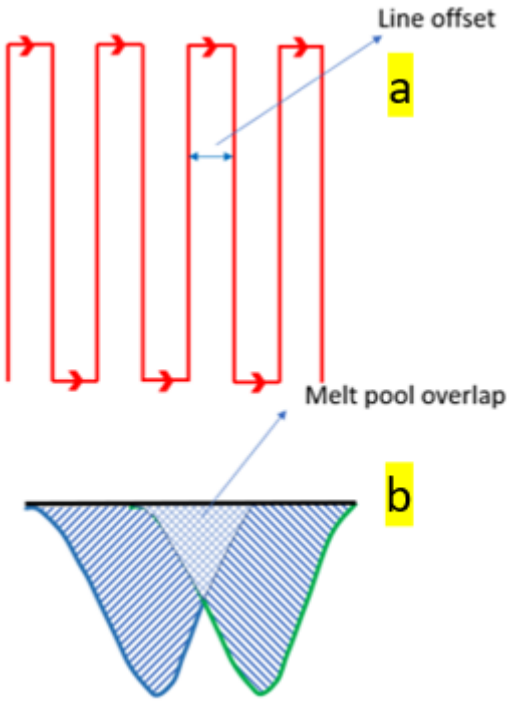

Figure 5.12: Schematic of scanning strategy (a) Line offset (b) melt pool overlap.

Energy density (ED) is decided by the electron beam voltage, beam scan speed, beam current, and hatch distance. The Area ED was calculated as per equation 5.1 [59].

$$\boldsymbol{ED} = \frac{\boldsymbol{UI}}{\boldsymbol{v}\, \boldsymbol{L_{off}}} \tag{5.1}$$

Where ED is energy density, U - accelerating voltage, I - beam current, v - scanning speed and L_{off}– line offset or hatching distance.

Arcam provides Level 1 operation training, standard configuration of machine and basic process scheme for standard materials. ARCAM process themes which are specified as speed function doesn't provide data about the individual parameters. Speed function is an algorithm-based process parameter combination. The lower the speed function, higher will be the ED and vice versa. Automatic power calculation selection will enable speed function and controls the combination of speed and beam current based on the material and geometry of the sample.

In this study, manual parametric selection in A1 Arcam equipment was done for better understanding of the effect of different AM conditions. Developing the optimum parametric

combination was challenging with titanium aluminide, as there is limited or no data about the effect of different parameters on the process optimisation and microstructural development.

In the initial experiments, due to the uncertainty about the quality of print, random levels of energy inputs, based on literature and Arcam reference were selected. Keeping the acceleration voltage at 60 kV and the build chamber temperature at 950 °C, the beam scan speed varied from 400 mm/s to 2400 mm/s. The beam current varied from 4 mA to 20 mA (as limited by Arcam). Line offset for all the sample were 0.2 mm.

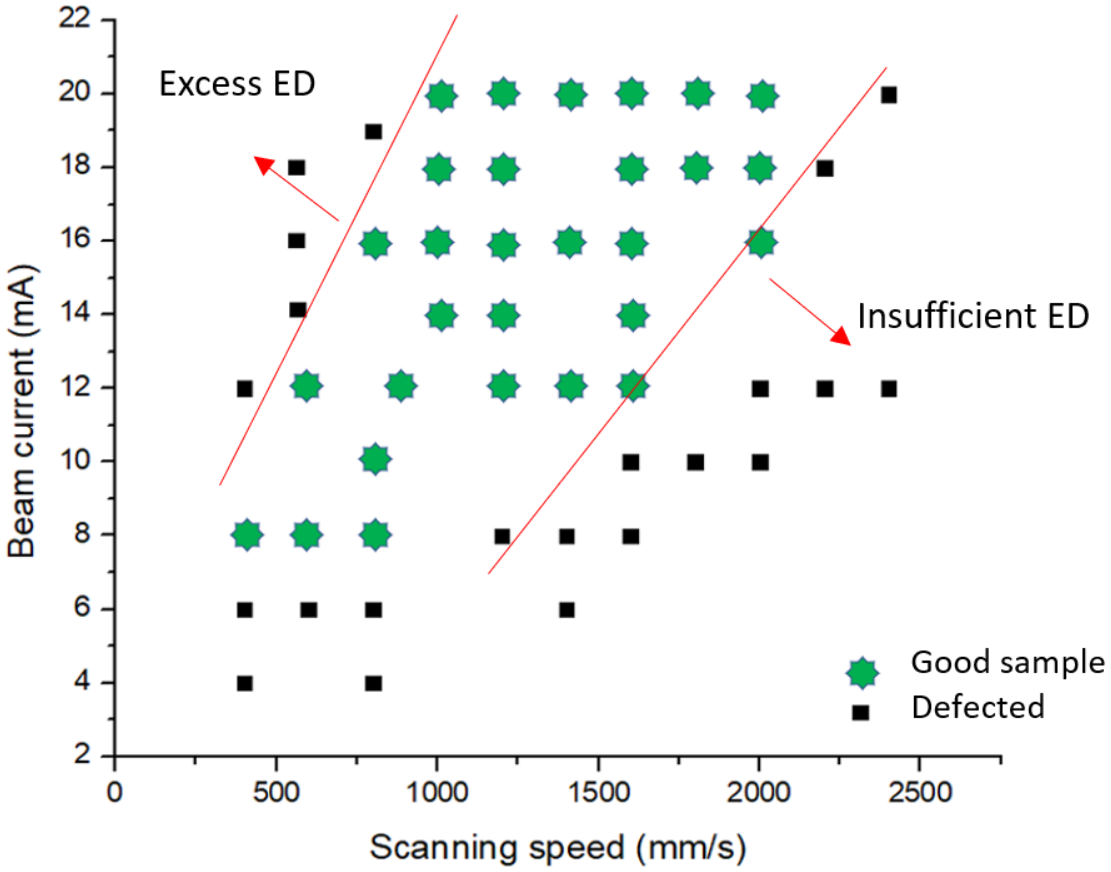

Figure 5.13: Samples at different process combinations, for selecting samples for microstructural study along build direction.

After a sequence of experiments, ED for getting samples of required quality was identified to be ranging in between 2-7 J/mm^2. Visual observation and optical microscopy were often used to quickly assess the quality of as-built or sectioned EBM specimens in terms of geometrical accuracy and the presence of noticeable defects such as lack of fusion, delamination and swelling, which are attributed to the use of insufficient or excess energy. This subjective

assessment was mainly used to select upper and lower energy values in the process window in Figure 5.13, to print samples of required quality. Three samples printed per condition and microstructural study showed identical microstructural evolution.

Chapter 6: Effects of additive manufacturing parameters on microstructural evolution and uniformity of EBM processed TiAl

Morphological features and mechanical properties of alloys printed by additive manufacturing depend on the processing conditions. This chapter presents the results and discussion of a study along the build direction on how ED and layer thickness affect the microstructural development and uniformity of TiAl that are manufactured using ARCAM A1 EBM machine.

6.1 Results

6.1.1 EBM process recipe for H, M and L samples

Deposition parameters used in this study are shown in Table 6.1. Initial trials were done to get required quality samples with minimal defects. H, M and L represent high, medium and low energy samples used for comparative study respectively and Table shows corresponding ED values. Higher beam current was selected for deeper melt pool and better HAZ distribution. The objective for this process parameter selection was better in situ heat treatment and so set the power (beam current) maximum recommended by equipment supplier and varied speed, which directly affects ED. Microstructure of as-fabricated sample was studied along build direction, using different characterisation tools.

Table 6.1: EBM process recipe for H, M and L samples

No	Replicates	Beam Current (mA)	Scanning speed (mms^{-1})	Line offset (mm)	Energy Density (J/mm^2)
H	5	19	950	0.2	6
M	5	19	1400	0.2	4
L	5	19	2400	0.2	2.3

6.1.2 Microstructure of as fabricated sample at different Energy inputs

Figure 6.1 shows low magnification optical image, which exhibits proper bonding between layers. Porosity was high in medium and low energy samples. In high energy samples, porosity observed to be largely closed by high ED. Porosity measurement was done in mid-section (YZ) along the build direction. The Optical microscopy was used to qualitatively compare different sample.

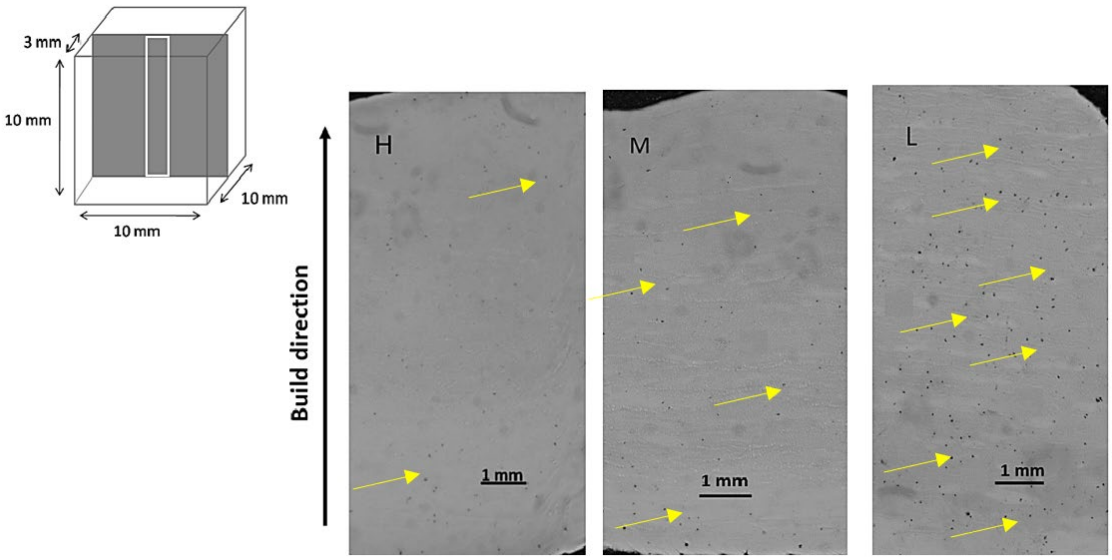

Figure 6.1: Optical micrograph showing porosity (yellow arrow) of H, M and L samples in build direction.

In general, layer by layer melting and re-heating leads to a banded macrostructure along the build direction. The optical images of etched H, M and L sample is shown in Figure 6.2. High energy sample exhibited uniform microstructure. Heavy banding was observed in medium and low energy samples.

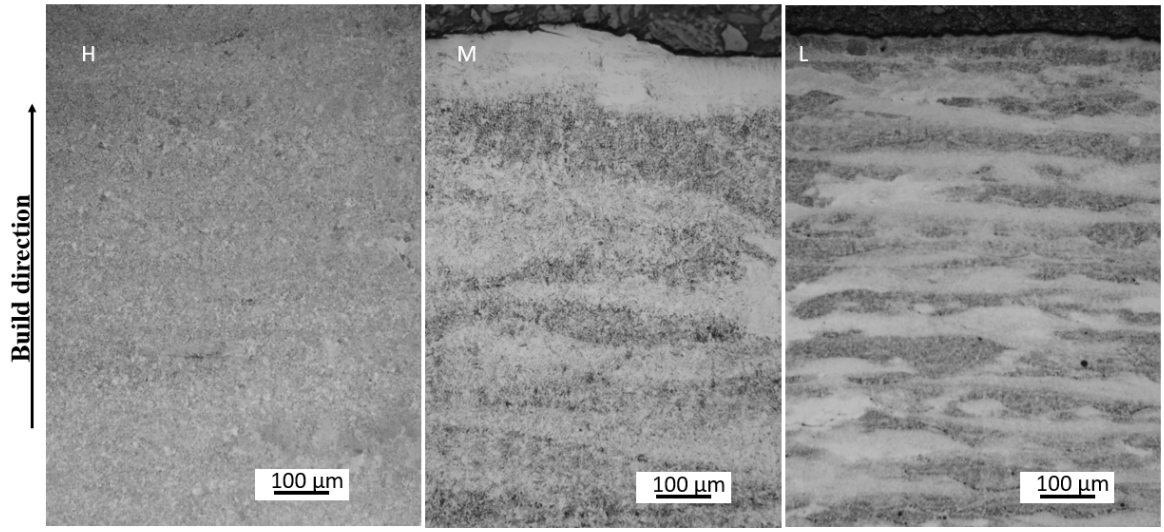

Figure 6.2: Optical images of etched H, M and L sample shows heavy banding in medium (M) and low energy (L) samples.

Microstructure from the middle region of sample in build direction (X-Z) was studied. Duplex microstructure was observed with medium energy whereas towards higher energy, lamellar microstructure was observed. The low energy sample showed feathery massive gamma structure and had micro cracks.

Microstructure of high energy sample is shown in Figure 6.3. Lamellar microstructure was observed in high energy input and was uniform along build direction, as shown in Figure 6.3a. β phase was observed in high and medium energy sample, highlighted in Figure 6.3b and average lamellar colony size was 40-50 µm.

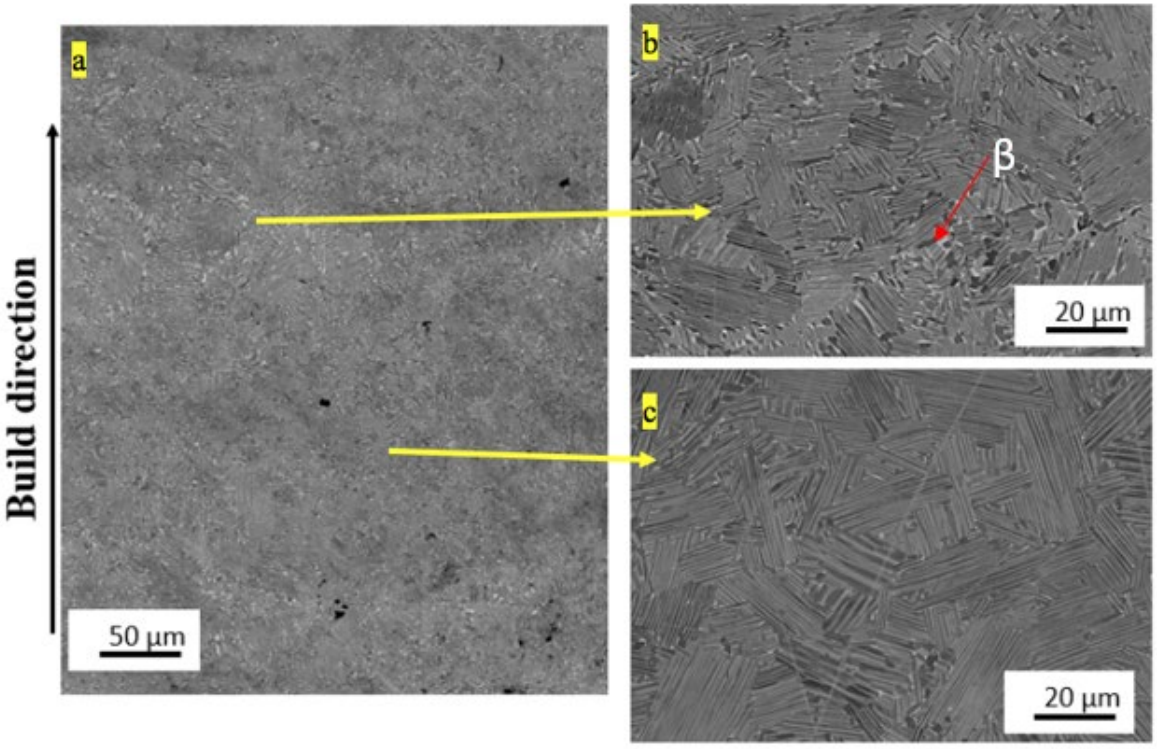

Figure 6.3: Microstructure of high energy (H) sample.

Figure 6.4 shows microstructure of sample printed at medium energy. Lamellar colonies with gamma grains are shown in Figure 6.4a. Microstructure exhibited banding along the build direction and β phase was seen in bands, as shown in Figure 6.4b. Lamellar colony size was 20-30 µm as observed in Figure 6.4c, which is lower than that of high energy samples.

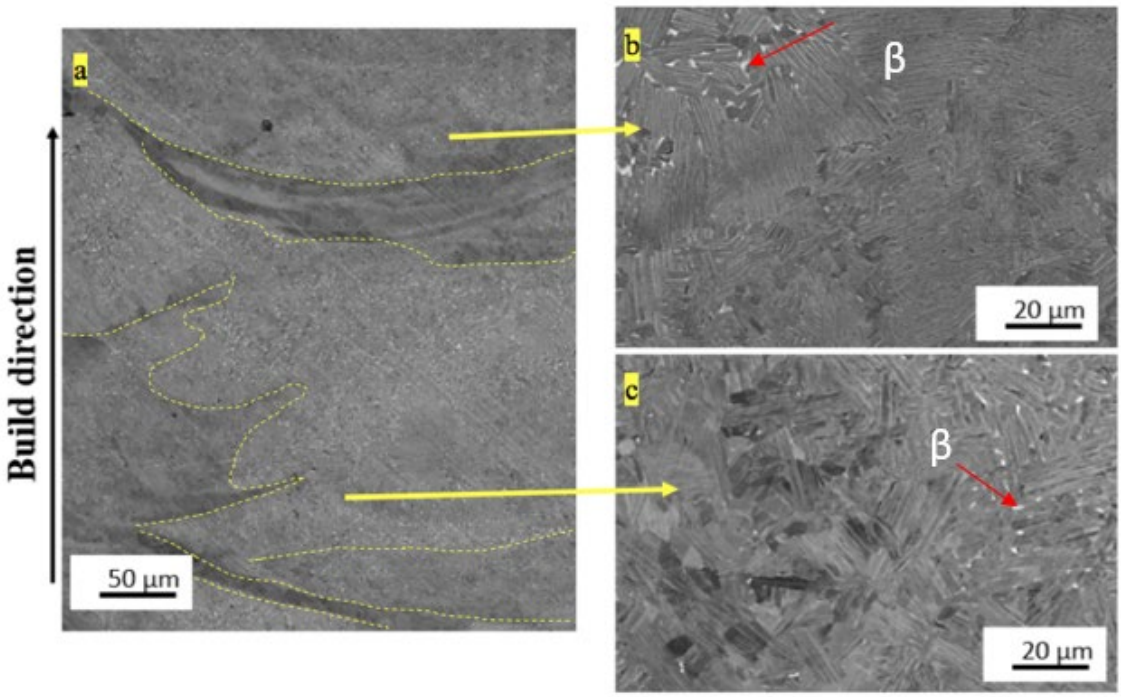

Figure 6.4: Microstructure of medium energy sample.

Microstructure of low energy sample is shown in Figure 6.5. In Figure 6.5a, underdeveloped lamellar microstructure with massive grains are observed. Heavy banding is observed along build direction, in Figure 6.5b. β phase was less, lamellar colony size was 20-30 µm, as seen in Figure 6.5c.

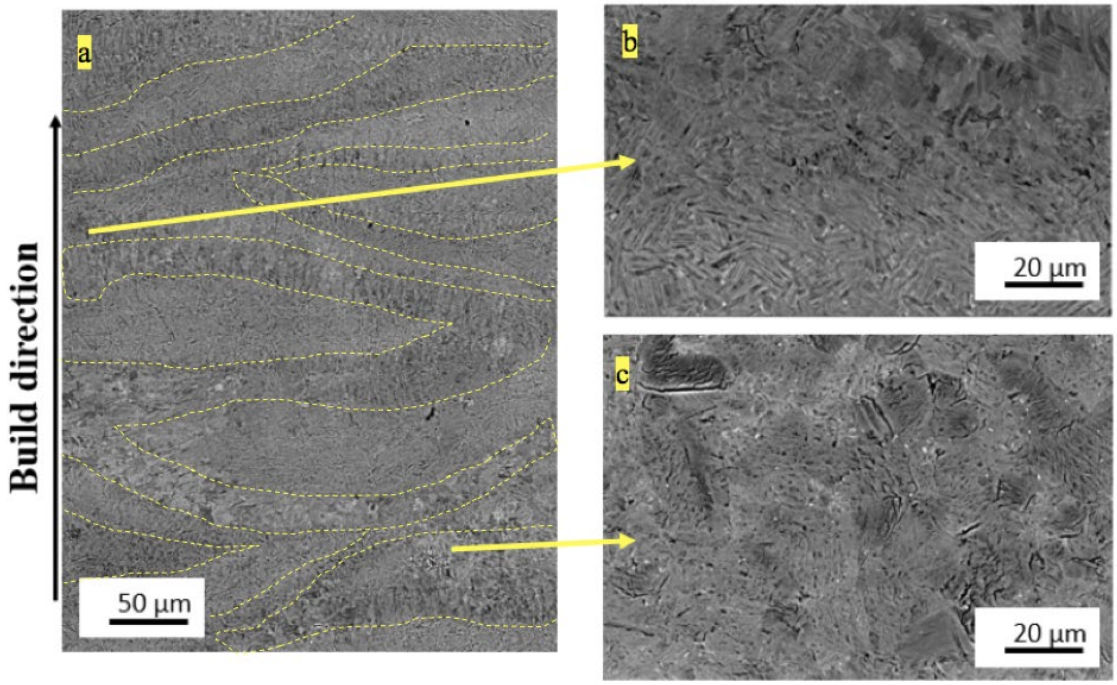

Figure 6.5: Microstructure of low energy sample.

The lamellar structure from H, M and L samples are shown in Figure 6.6. As shown in Figure 6.6 a, the lamellar formation was much more complete in high energy sample, α_2 and γ lamellae were well developed. Lamellar interface was observed to be straighter and continuous. Individual lamellae in medium energy sample were observed to be less developed, compared to high energy samples. Discontinuity observed in interfaces, as in Figure 6.6b. Figure 6.6c shows underdeveloped lamellae in low energy sample. Interfaces were observed to be much more discontinuous than medium energy sample and were broken.

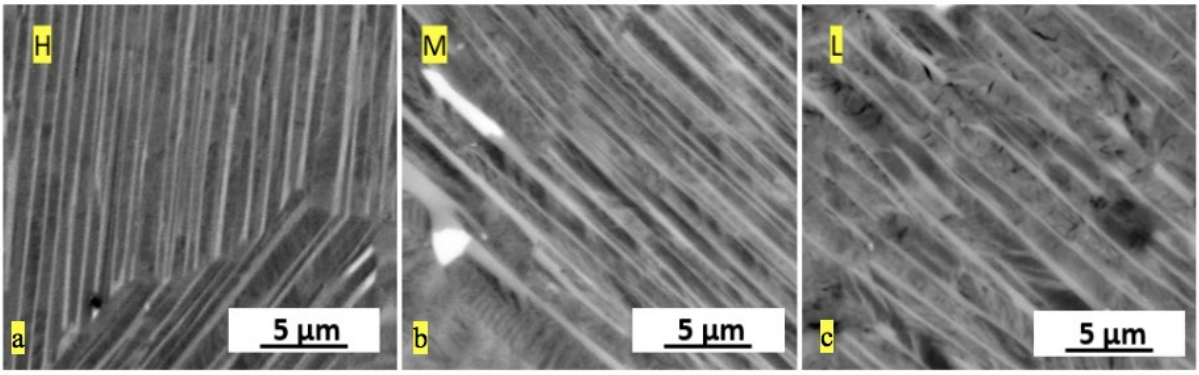

Figure 6.6: SEM micrographs (a), (b), (c) shows the lamellar structure from high, medium and low energy samples, respectively.

6.1.3 Phase constitution

XRD patterns from the central portion of H, M and L samples are shown in Figure 6.7. XRD analysis shows the variation of phase fractions. Composition of as-fabricated samples consists of α_2 and γ phases.

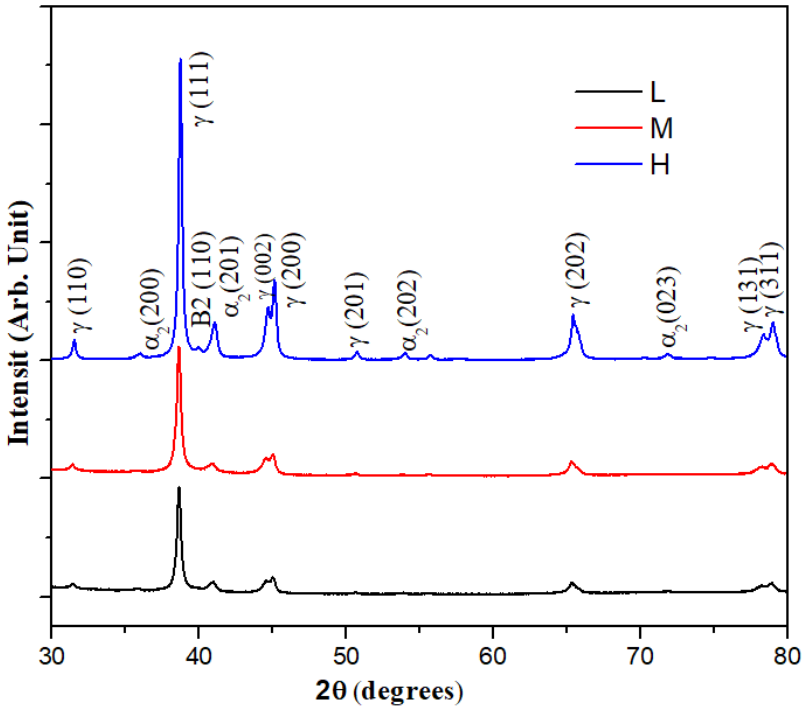

Figure 6.7: XRD patterns from the central portion of H, M and L samples.

Phase fraction values obtained from XRD analysis are shown in Table 6.2. By comparing the peak intensities, α_2 -phase fraction decreased with increasing ED. Presence of weaker β peaks in high and medium energy samples indicated the existence of β phase.

Table 6.2: Phase fraction (wt.%) values obtained from XRD analysis.

Sample	**γ**	**α_2**	β
H	88 ± 1	9 ± 0.8	3 ± 0.4
M	83 ± 1	15 ± 0.8	2 ± 0.4
L	78 ± 1	21 ± 1	1 ± 0.2

6.1.4 ICP analysis of H, M, L samples

The chemical compositions of powder and EBM fabricated samples are presented in Table 6.3. Chemical analysis of samples using ICP/ LECO showed a minimal pick up of oxygen because of the high vacuum environment during EBM printing in Arcam A1 machine. Aluminium evaporation of 2.54% and 2.17% was observed in H and M sample respectively. There was no significant Al evaporation from low energy sample.

Table 6.3: Chemical analysis of samples using ICP/ LECO (At.%).

Sample	Al	Cr	Nb	Ti	O
TiAl - Powder	47.7 ± 0.4	1.4 ± 0.1	1.7 ± 0.1	48.9 ± 0.4	0.27 ± 0.01
EBM- High energy	45.2 ± 0.4	1.6 ± 0.1	1.8 ± 0.1	51.1 ± 0.4	0.32 ± 0.01
EBM- Medium energy	45.9 ± 0.4	1.5 ± 0.1	1.7 ± 0.1	50.5 ± 0.4	0.31 ± 0.01
EBM- Low energy	47.5 ± 0.4	1.4 ± 0.1	1.7 ± 0.1	49.1 ± 0.4	0.31 ± 0.01

6.1.5 Bottom microstructure - substrate dilution

As seen in Figure 6.8, microstructural characteristics in SEM micrograph was different in bottom layers of the samples up to 500-600 μm, due to the formation of Ti -Al -Fe phase.

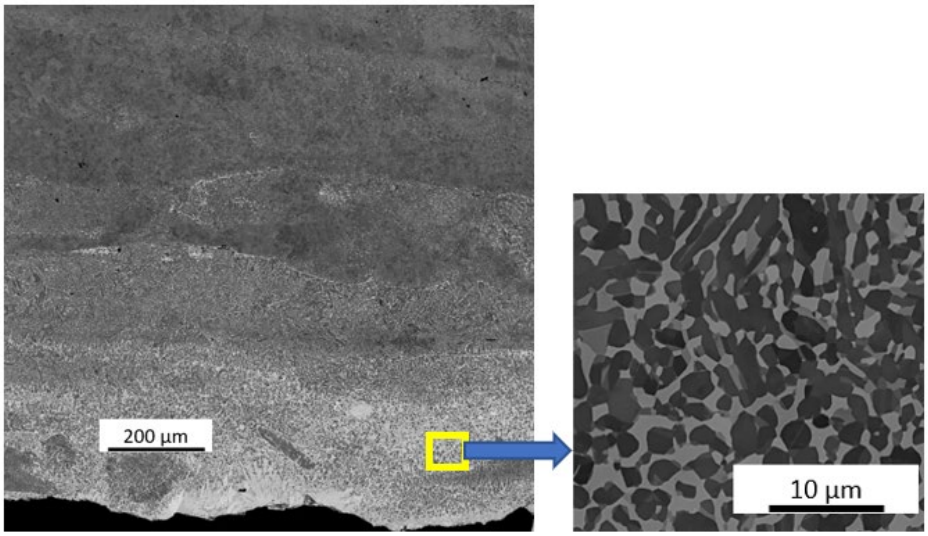

Figure 6.8: SEM micrograph showing microstructure in bottom layers of H sample.

EDS mapping of H sample exhibited Fe and Ni segregations, as shown in Figure 6.9. Approximate elemental composition in the Fe enriched region is shown in Figure 6.10 and ~17.8 at.% iron was identified.

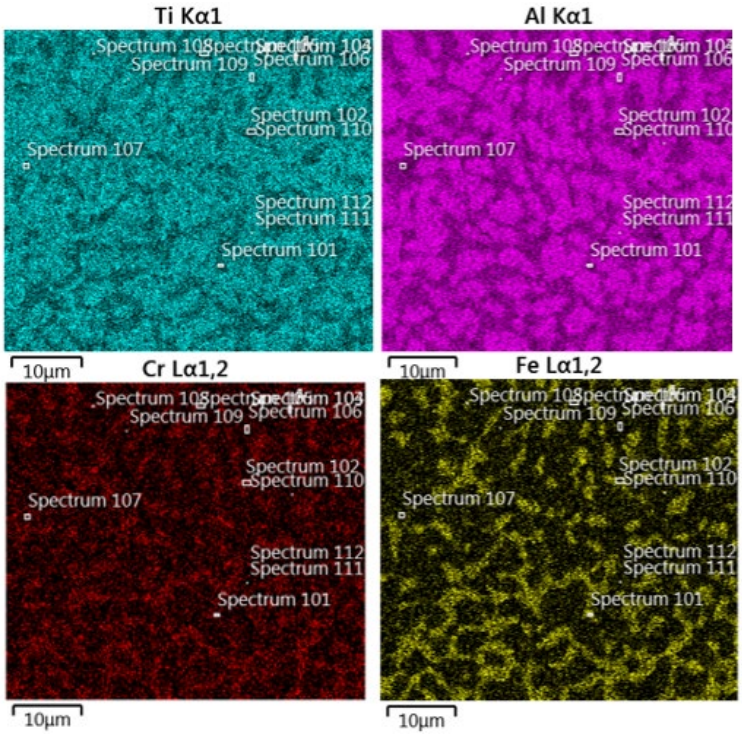

Figure 6.9: EDS elemental mappings of H sample- exhibiting Fe, Ni and Cr segregation.

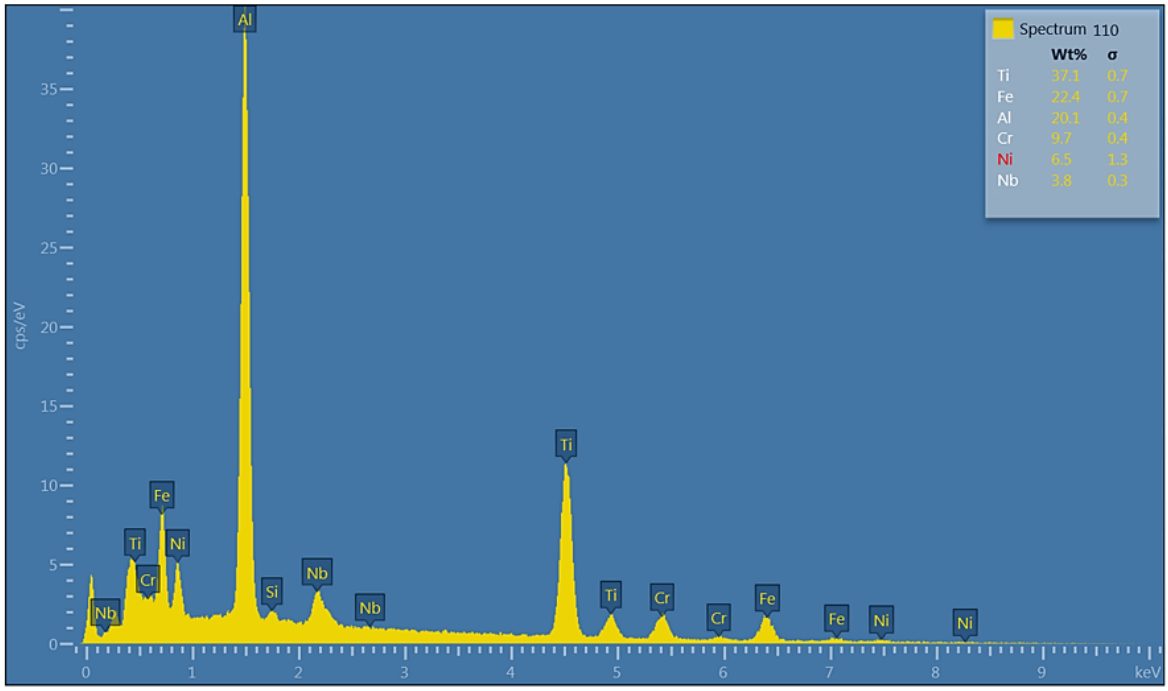

Figure 6.10: Approximate EDS elemental composition in the Fe enriched region.

From the EDS X-ray analysis, The approximate composition of the Fe segregated region in At.% is shown in Table 6.4.

Table 6.4: Approximate EDS elemental composition in the Fe enriched region.

Element	At.%
Ti	34.2
Fe	17.8
Al	32.9
Cr	8.4
Ni	4.9
Nb	1.8

The line EDS analysis from the bottom layers along the build direction showed Fe diffusion up to around 600-800 µm, as shown in Figure 6.11.

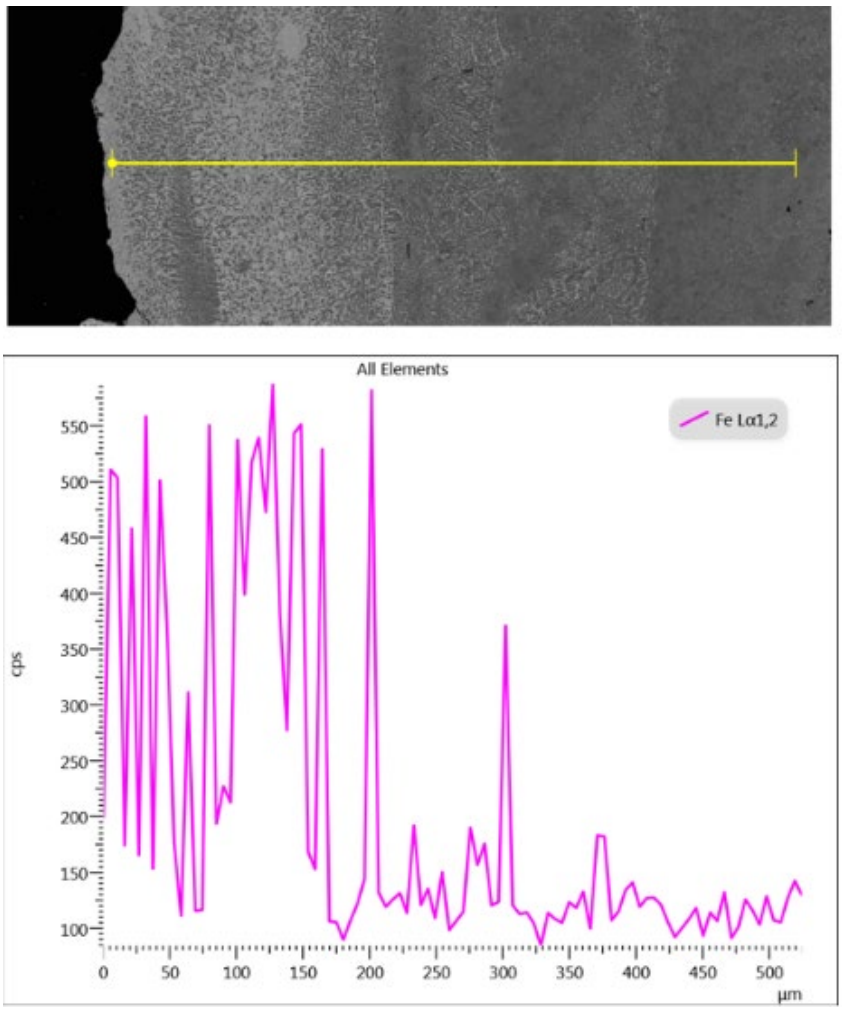

Figure 6.11: Line EDS analysis of bottom layers in H sample, along the build direction showing Fe compositional changes.

6.1.6 Microstructure of Low energy sample (L) at different layer thickness

Heavy banding was observed in M, and L samples. To study the effect of layer thickness, low energy sample was printed at layer thickness of 90 µm and 70 µm. As seen in Figure 6.12, banding was comparatively low in samples printed with 70 µm layer thickness.

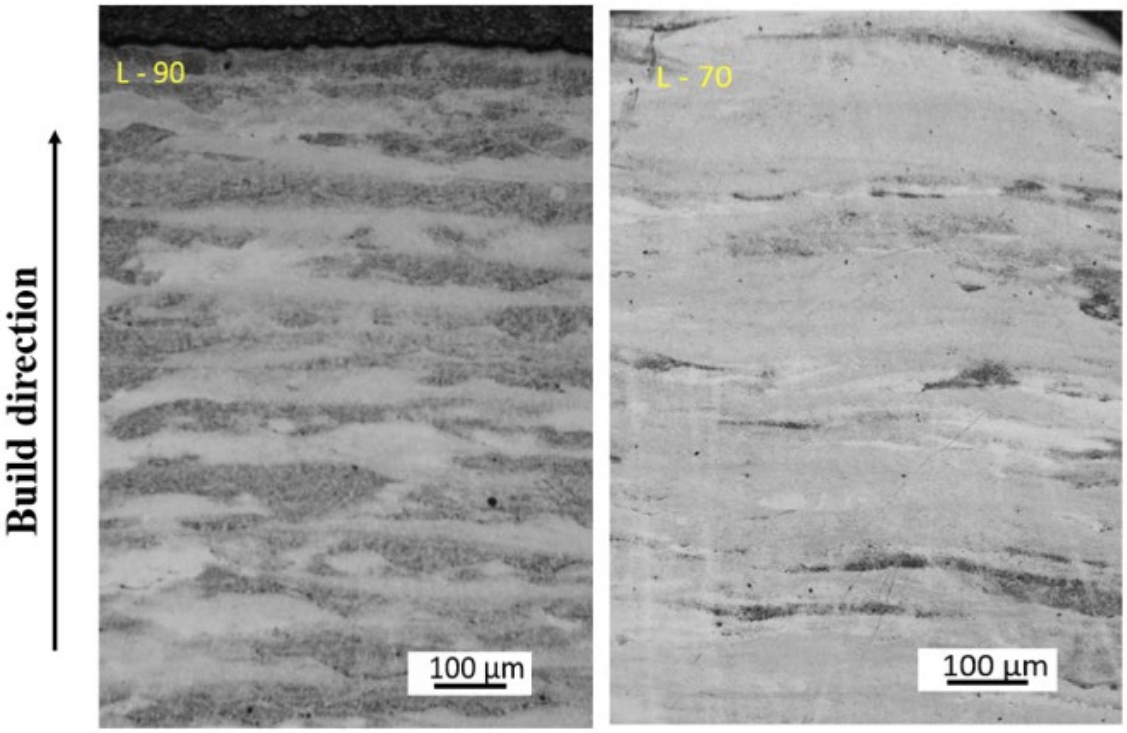

Figure 6.12: Variation of uniformity with layer thickness- in low energy samples.

High magnification SEM BSE micrographs of low energy samples printed at layer thicknesses of 90 µm and 70 µm are shown in Figure 6.13. With reduction in layer thickness, lamellar fraction was increased, and microstructure became more uniform.

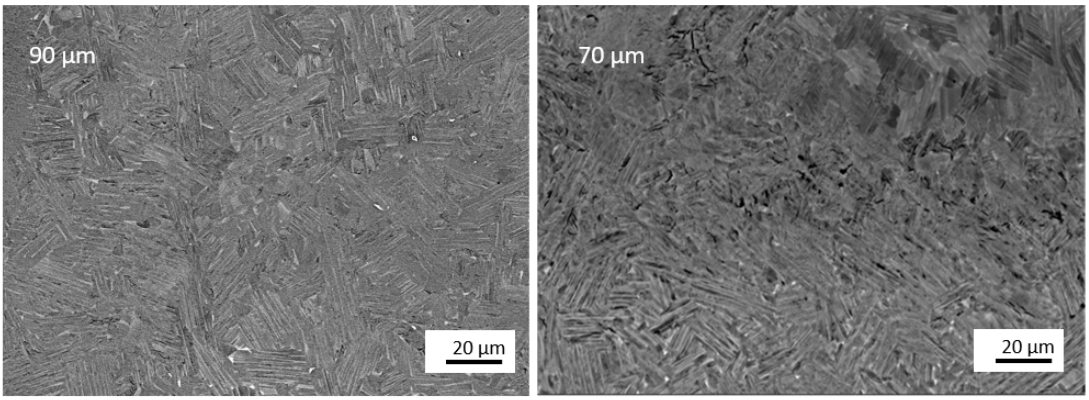

Figure 6.13: SEM BSE micrographs of low energy samples printed at 90 µm and 70 µm layer thickness.

6.1.7 Comparison of microhardness – H, M, L samples

The hardness variations along the build direction in H, M and L samples are plotted in Figure 6.14. All three samples showed higher hardness values at top layers. The surface hardness of TiAl samples printed at different energy inputs during EBM, varied approximately from 460 to 320 HV. Samples produced using a high energy input showed consistently higher hardness than those produced using lower energy input.

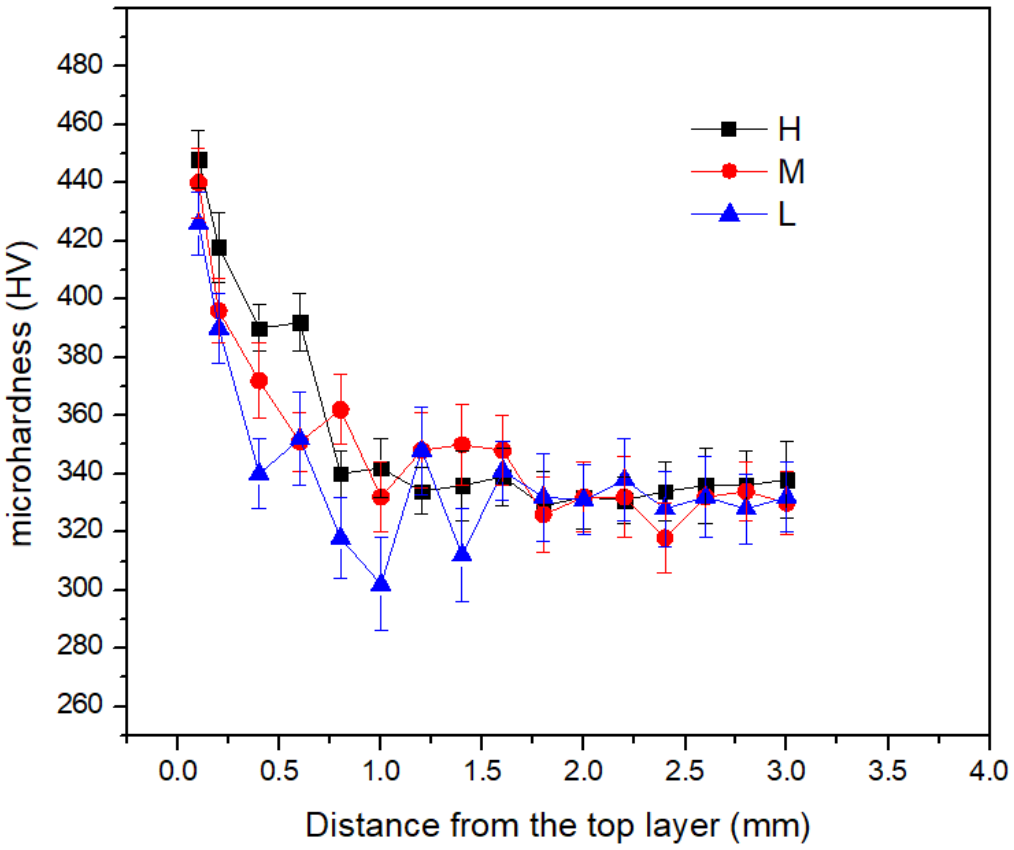

Figure 6.14: Microhardness distribution of high, medium and low energy samples at different distance from the top surface to 3 mm depth.

6.2 Discussion

In EBM, all the optimised parameter combinations will not deliver the same microstructure. It varies with change in parameters. Main factor that influences the microstructure and the process uncertainty is the cooling rate. Cooling rate is an indirect factor in EBM process, which is affected by directly controllable factors like heat input, melt pool temperature and layer thickness etc. Thus, the effect of these variables can be viewed through their influence on microstructure.

6.2.1 Microstructural variation due to difference in energy density

During the printing process, energy input significantly influences final quality of the printed part. It directly affects the microstructural evolution and influences metallurgical bonds at bottom layers. When the energy input is not sufficient, there can be lack of bonding between layers. However excessive energy can cause bulging and distortion of the part. So, energy input is the single most critical parameter that directly and indirectly affect the final performance of fabricated part.

Among high (6 J/mm^2), medium (4 J/ mm^2), and low (2.3 J/ mm^2) energy samples, Figure 6.2 (b) and (c) shows non uniform microstructural development along the build direction, at medium and low energies respectively. There was an increase in β -phase with increasing ED in the investigated samples. The discussion about beta formation is included in chapter 7.

Microstructural evolution can be significantly affected by the variation of heat input, principal factor being the cooling rate. The materials processed in EBM experience very high cooling rate, of 10^3-10^6 °CS^{-1} [5, 77]. Cooling rate primarily depends upon energy input, melt pool temperature and temperature gradient. At higher energy input, the melt pool size and the heat affected zone will be larger, and the associated cooling rates will be lower due to lower thermal gradient and heat dissipation [5, 69, 78]. With the lower cooling rate, the phase transformation sequence is $L \rightarrow \alpha \rightarrow \alpha + \gamma \rightarrow \alpha_2 + \gamma$, which forms the lamellar colonies. From literature it is reported that the formation of lamellas is diffusion-controlled mechanism [3, 20]. As soon as the γ start to nucleate, it grows through the diffusion mechanism. As cooling rate increases the diffusion becomes slower as the mobility of the atoms decreases. When the diffusion becomes slow, the growth of the lamellas will decline. At lower heat input, the melt pool and heat affected zone is smaller and there will be very high thermal gradient which will lead to high

cooling rate, which results in superfine microstructure is obtained [5,63, 69]. The featureless feathery microstructure in L and M sample is assumed to be massive gamma formation.

Generally, with increase in ED, colony size observed larger, as seen in Figures 6.3, 6.4 and 6.5. 52% rise in colony size was observed with an increase of ED from 4 J/mm^2 to 6 J/mm^2. The average colony size with different ED values is plotted in Figure 6.15. Even though the error bar is overlapping, there is a trend of increase in colony size from low energy sample to higher energy sample. Compared with conventional processed TiAl, colony size is smaller for EBM printed samples [5]. This is because of the rapid solidification and microstructural refinement associated with EBM. Lamellar colony size is a critical morphological characteristic for attaining the optimum mechanical properties.

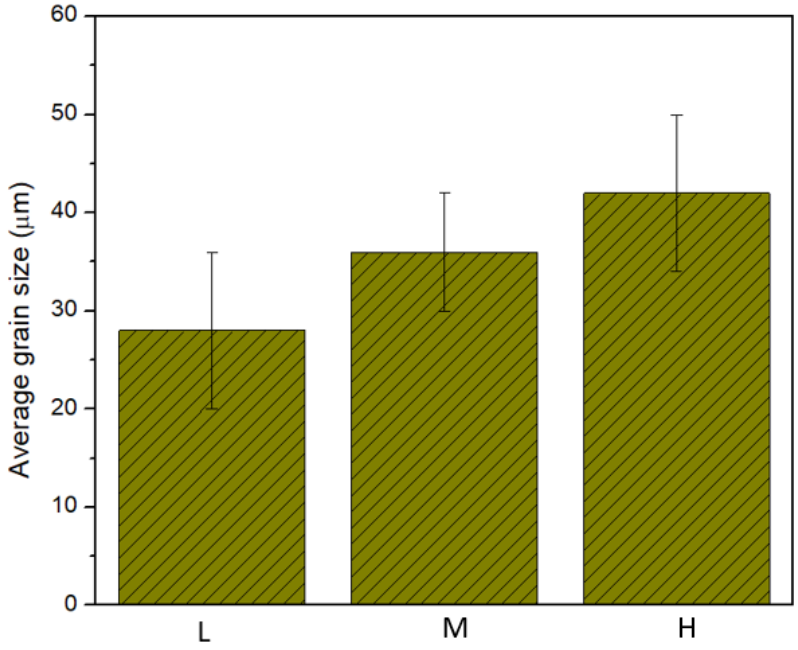

Figure 6.15: Bar diagram showing average colony size with different energy density values.

The variation of uniformity in H, M and L sample can be explained based on geometrical dilution and heat affected zone during the layer wise melting in EBM process.

6.2.2 Effect of energy density on geometrical dilution

Dilution is considered as a process taking place across the boundary of deposited layers, caused by the intermixing of deposited powder layer with already solidified bottom layers or substrate

[79]. The geometrical dilution for high energy sample is depicted in Figure 6.16. Better metallurgical bonding can be obtained by a good dilution, but excess dilution leads to melt pool instability and balling effect. So, it is important to control the dilution during the process of material deposition.

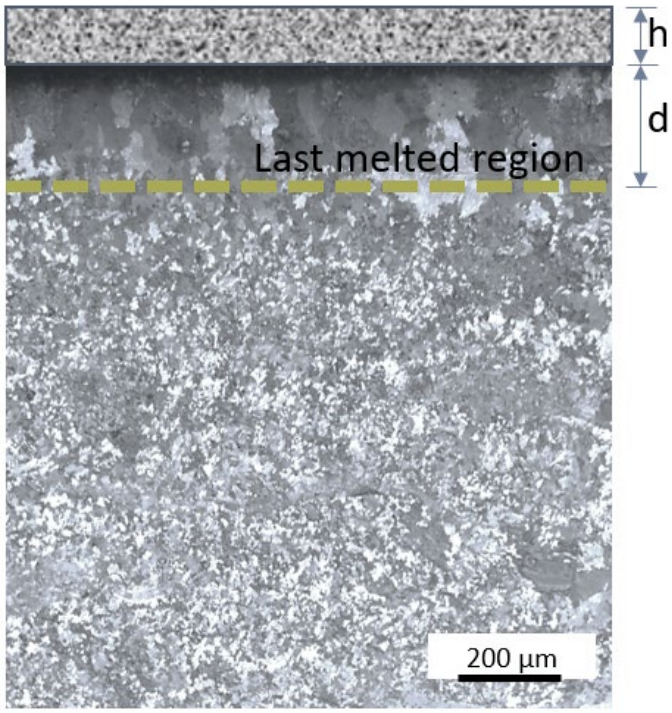

Figure 6.16: Geometrical dilution for high energy sample, where d denotes melt pool depth and h denotes layer thickness.

The dilution (D) can be calculated by Equation (6.1) [79].

$$D = \frac{d}{h+d} \tag{6.1}$$

Where d is melt pool depth and h, layer thickness. Approximate value of d can be obtained from SEM of the last melted region in build the direction. Dilution is directly proportional to the ED, as seen in Figure 6.17. Low dilution can cause lack of fusion or delamination between layers. In case of first deposited layers the dilution is between deposited material and stainless steel (SS) substrate. Dilution is reduced when the intermixing between the deposited material

and the substrate is low. Compared to conventional welding process, the dilution in EBM process is less due to smaller layer thickness and faster beam interaction time.

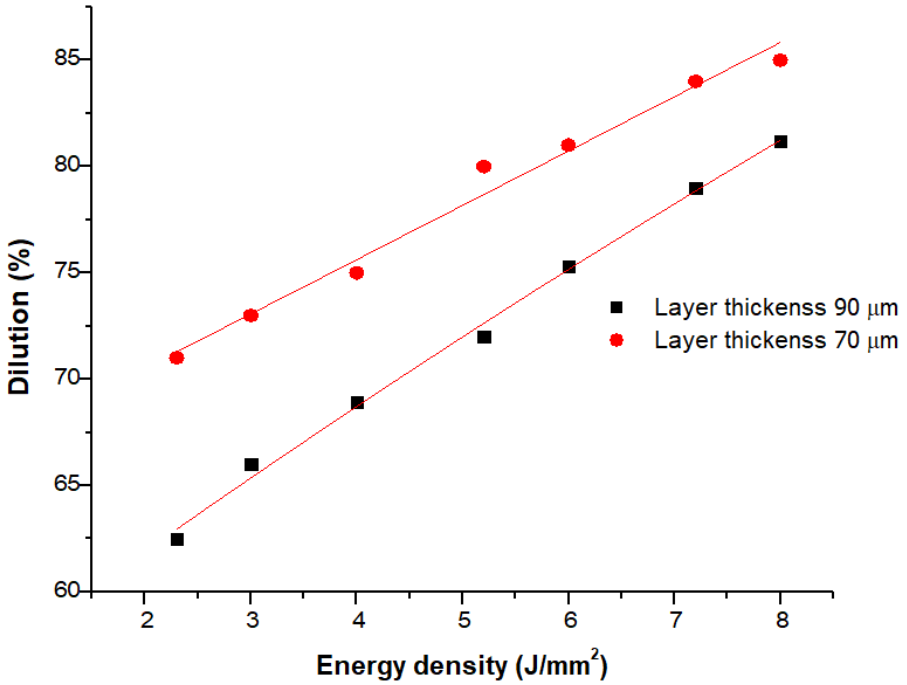

Figure 6.17: Effect of energy density on geometrical dilution.

6.2.3 Fe diffusion due to substrate dilution

SEM and EDS analysis of the interface between substrate and material, revealed the segregation of iron and nickel, as shown in Figure 6.9. It concludes that substrate melts during the deposition of first few layers. It is also noticed that melting is higher when higher energy beam is delivered. So, it is important to remove the diluted region from the sample. During TiAl fabrication stainless steel was used as substrate plate. Alloy mismatch between the deposited material and the stainless-steel plate can be helpful for removing fabricated parts from the base plate without much difficulty. Inserting 1-2 mm support pins or support structures upon the stainless-steel start plate, also will be beneficial in avoiding substrate dilution and unexpected microstructures.

6.2.4 Temperature profile and associated heat affected zone (HAZ) during EBM of TiAl and the effect on microstructural evolution.

During thermal cycling of EBM manufacturing, solidified layers are re melted and then in situ heat treated during successive application of heat input on top layers. Mechanism of loss of heat from melt pool is varied throughout the process. Initially heat loss is by radiation, from top. With increasing build height, main heat loss mechanism is changed to conduction, from powder bed and start plate [56]. In the current study the accurate measurement of the thermal history such as temperature and temperature gradient during EBM has not been carried out mainly because of the difficulty in temperature measurement. Therefore, precise interpretation of the complex microstructure of TiAl sample to the thermal history is difficult.

MATLAB simulation used to qualitatively differentiate the HAZ variation with ED or layer thickness. Modified Rosenthal equation for a moving heat source with a Gaussian profile was used for calculating the temperature distribution [80]. MATLAB simulation is shown in Figure 6.18.

$$\triangle \boldsymbol{T}_{(xyz)} = \frac{2\alpha\beta p}{\kappa\pi^{3}/_{2}} \int_{0}^{t} \frac{exp\left[-2\frac{(x+v_b t)^2+y^2}{{D_b}^2+8\alpha t}-\frac{z^2}{4\alpha t}\right]}{\left(\sqrt{\alpha t}.a{D_b}^2+8\alpha t\right)}.\boldsymbol{dt} \quad (6.2)$$

Where, power P = I*V (I-beam current, V- beam voltage), κ- thermal conductivity, α- thermal diffusivity, β- efficiency (0.8) parameter, Vb- beam speed, Db- electron beam diameter

Process parameters for H and M samples used along with constant voltage of 60 kV. Beam diameter was taken as 100 μm. The thermal conductivity and diffusivity obtained from TiAl diffusivity chart [81] at 1000 °C. The build temperature was 1000 °C and β values for EBM are reported in the range 0.8-0.9. Efficiency parameter (β) is a commonly used factor to account for energy losses during beam/material interaction. For electron beam processing (not exclusively for EBM) β values between 0.6-0.9 are reported [77, 82, 83]. For laser beam processing, the beam diameter is a well-defined process parameter [5], which can be adjusted as required. On the other hand, for EBM, beam diameter is not something that readily can be measured and it is controlled by the focus offset. Db which was derived from literature data, used to calculate the beam diameter for all the temperature calculations for this work [57].

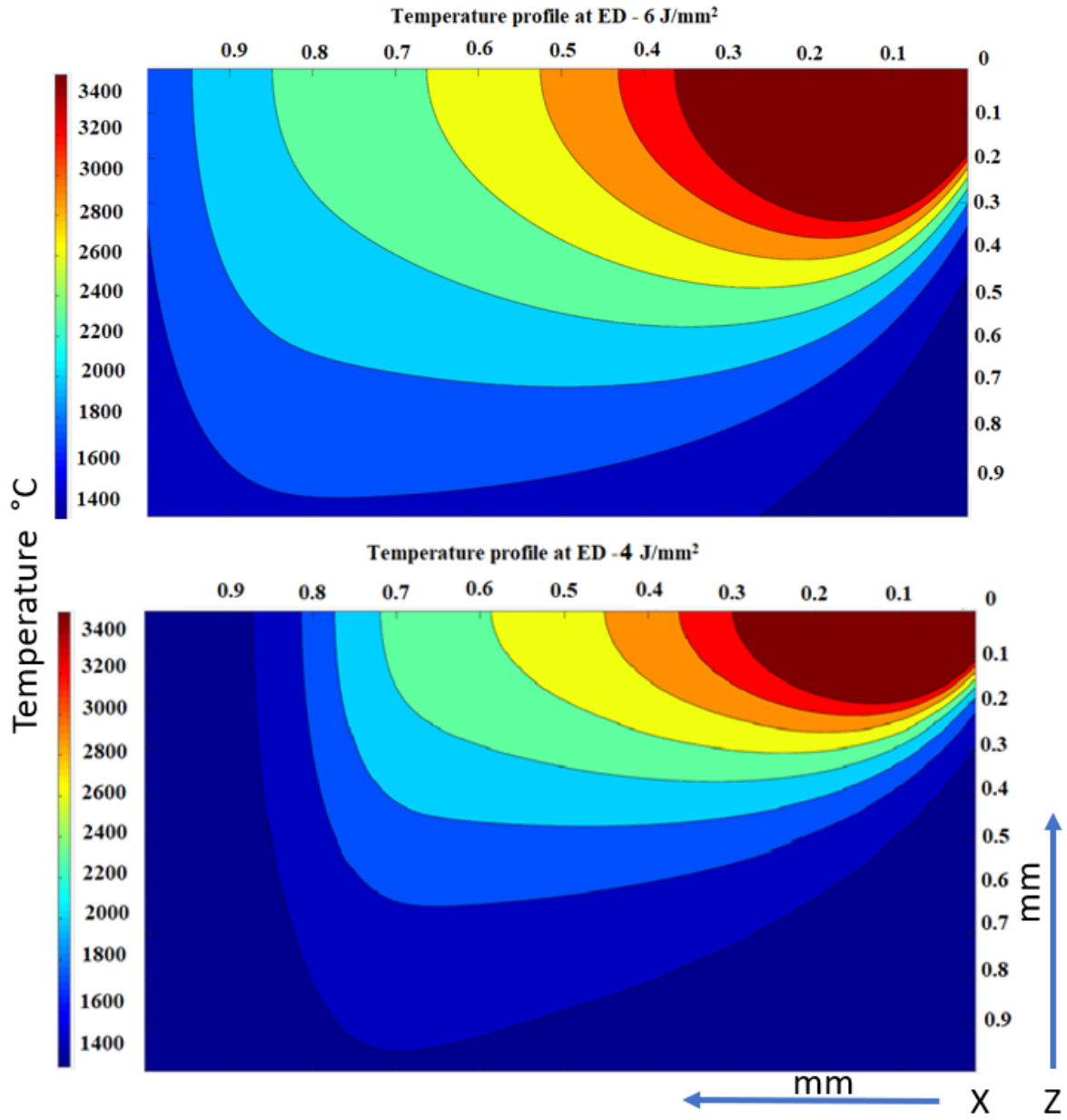

Figure 6.18: MATLAB simulation- HAZ variation with ED.

Based on the numerical analysis, melt pool size and heat affected zone progressively increased with ED. Figure 6.18 shows the temperature distribution during EBM printing in H and M sample. At higher heat input the number of bottom layers reheated to single phase alpha field or (α+γ) is more, which directly influences solid-state transformations and associated microstructural change, eventually leads to better uniformity.

6.2.5 Effect of layer thickness on uniformity

As layer thickness is increased, more energy is provided to melt more volume of material. Additionally, a larger layer thickness increases electron backscattering and energy loss due to beam-powder interactions. It can be hypothesized that preheat and post heat times would need to be increased to compensate for the added requirement of heating more thermal mass. Also as shown in Figure 6.19, schematic of the HAZ (heat affected zone) has a wider reach with lower layer thickness, making the solid-state transformation more effective and provide better uniformity in the build direction.

Also, as layer thickness increases, more powder is needed to be sintered prior to melting, in order to prevent smoking and reduce spatter ejection. The limit observed during the printing experiments using EBM was 70- 100 µm. The upper and lower limits of the workable layer thickness of powder bed mainly depend on particle size distribution. The loss of geometric resolution also decreases with increasing layer thickness, and a balance with process time must be made. Towards the lower side, the particle size distribution is a critical factor to consider. In the currently used powder with D_{50} 87 µm, layer thickness less than 70 µm resulted in quite unstable powder bed. In the current study the variation of layer thickness from 90 µm to 70 µm in low energy sample resulted in a considerable improvement in uniformity. High energy samples are expected to give better uniformity, but aluminium evaporation is a major challenge in increasing the ED. So, layer thickness variation is one way to achieve better uniformity without increasing the ED and Al evaporation issues.

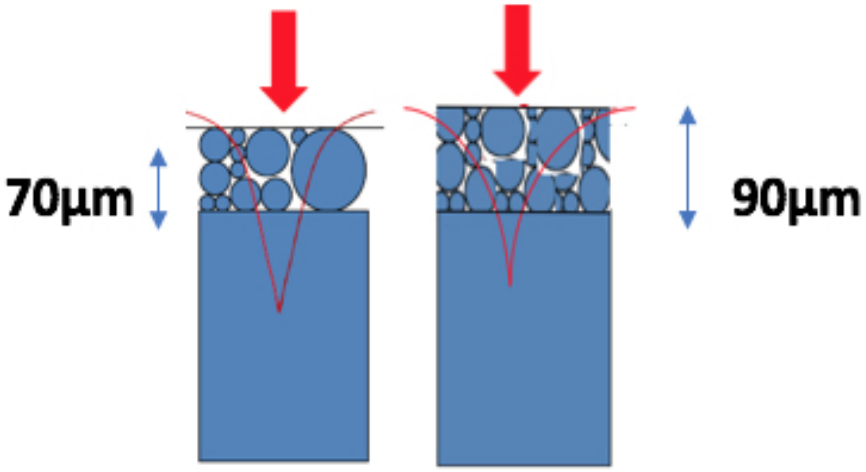

Figure 6.19: Schematic of heat affected zone, with variation in layer thickness.

6.2.6 Energy density and Aluminium loss

Significant decrease in aluminium (~3 at.%) composition was observed in samples fabricated with higher ED, due to vaporization. Murr et al. and Korner et al. [55, 56] also made similar observations while fabricating γ-TiAl by EBM at higher ED. The aluminum loss in H, M and L samples is shown in Table 6.3. The maximum aluminium loss is observed in high energy sample. Even in that case, the solidification path is through α+γ region, based on the phase diagram. But there is a shift of path towards lower aluminum concentration, which changes the kinetics and transformation temperature of the phases and have considerable effect on phase fraction and equilibrium of the microstructure. If there is further excess aluminum evaporation than these three samples, there can be shift of solidification path to Ti-rich region, and pass through β single phase field, leading to formation of β phase. The phase fraction of H, M and L samples were not in agreement with equilibrium phase diagram. During rapid solidification, the α ordering to α_2 is easier than α→γ transformation and resulted in nonequilibrium high phase fraction of α_2 in all samples. The change to equilibrium state was more achieved in high energy sample, because of comparatively more effective in situ heating.

6.2.7 Effect of energy density on microhardness

The surface hardness of TiAl samples printed at different energy inputs during EBM, is varied approximately from 460 to 320 HV, with an average of 341 HV in the core of the sample, showing similar findings as that of prior researches [84]. Microhardness values along build direction is plotted in Figure 6.14. Higher energy sample showed highest hardness values and that can be attributed to the lamellar microstructural morphology. On the other hand, low energy sample showed irregular pattern for hardness, due to the heavy banding.

6.3 Summary

Effect of ED and layer thickness on microstructural evolution and uniformity of EBM processed TiAl samples were studied. Microstructural development, morphological variations and uniformity were studied with high, medium and low energy level.

Changes in beam speed directly affect the energy input, in EBM manufacturing. Only higher energies lead to lamellar microstructural formation, whereas low energy input provides duplex

microstructure. There is a trend of increase in colony size from low energy sample to higher ED sample.

Geometrical dilution is directly proportional to the ED. Dilution is relatively high in TiAl samples printed using higher energy input and is comparatively less for low energy samples.

High energy input reduces porosity; on the other hand, it also causes Al evaporation. The appropriate ED provides quality product, with optimised microstructure, better uniformity and negligible porosity.

Chapter 7: Investigation of in-situ cyclic heat treatment and solid-state transformations (SST) in TiAl processed EBM.

Formation of the primary TiAl lamellar structure in EBM and different solid-state transformations during in situ thermal cycling are systematically investigated in this chapter. The initial TiAl microstructure after solidification in EBM is at non-equilibrium condition. Two types of microstructural changes were observed mainly.

a) Discontinuous Coarsening of primary α_2 /γ lamellar structure (PLS)

b) Dissolution of α_2 lamellae by $\alpha_2 \longrightarrow \beta + \gamma$ phase transformation

Discontinuous coarsening is the prominent solid-state transformation mechanism. Its effect on microstructural evolution is investigated by tracking the layer-wise microstructural changes along build direction, using systematic characterization. Effect of EBM process parameters on DC is studied and the driving forces for DC are briefly discussed. The second solid-state transformation observed in EBM process is the precipitation of β phase, through dissolution of α_2 lamellae. The beta formation is influenced by preheating condition and thermal cycling of EBM manufacturing.

7.1 Results

7.1.1 Sample for DC study

As discussed in the previous chapter, Ti-48Al-2Cr-2Nb samples were printed at low, medium and high energy input conditions. Of these groups, samples printed at high energy input showed better uniformity and lamellar formation and were selected to study the microstructure in detail. All samples used in this chapter were printed at a higher ED of 6 J/mm^2. A cuboidal TiAl sample fabricated by EBM is shown in Figure 7.1. The characteristic microstructural evolution studied along build direction (highlighted section). Layer by layer manufacturing method and high rate of cooling during the EBM process are the main influencing factors for the characteristic microstructural pattern of the as-printed Ti-48-2-2.

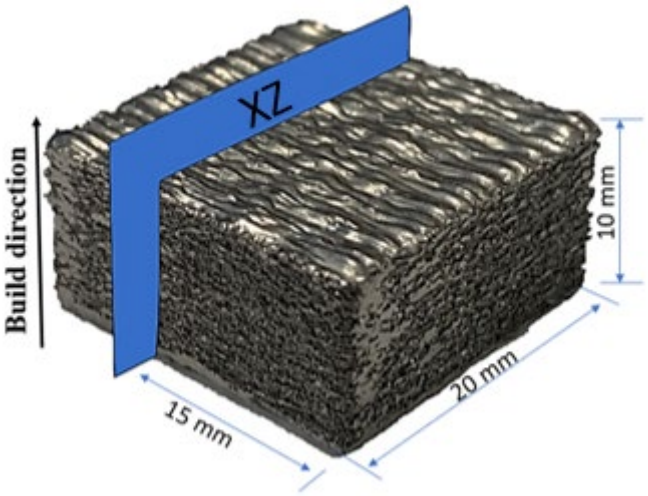

Figure 7.1: Cuboidal Ti-48Al-2Cr-2Nb samples fabricated by EBM, section along the build direction- for the microstructural study.

7.1.1.1 Phase constitution and microstructure

The microstructure of as fabricated sample from different regions in x–z plane is displayed in Figure 7.2. Macrostructure shows quality build with minimal defects and proper remelting and fusion between layers along the building direction. The microstructural analysis of the top surface in as-fabricated sample along the build direction revealed a fine primary lamellar structure (PLS) composed of randomly oriented lamellar colonies made up of alternate plates of α_2 ($D0_{19}$) and γ ($L1_0$). Figure 7.2(a) is optical image of etched section of the highlighted region in Figure 7.1. The magnified view of etched sample from top, middle and bottom regions are shown in Figure 7.2(b), (c), (d) and high magnification BSE images in Figure 7.2(e), (f) and (g) respectively. Figure 7.2(e) shows fine primary lamellar structure, where light coloured α_2 plates and dark γ plates are arranged as alternate ribbon-like lamellae, forming colonies with an average colony size of 130 μm. Average interlamellar spacing was about 90 nm. Interfaces were well developed and straight. Figure 7.2 (f) shows microstructure in the middle portion, where near lamellar colonies with coarsened lamellae are seen. Colony size was observed to be smaller in size compared to top layers. Figure 7.2(g) shows the microstructure in bottom layers, showing a near lamellar structure with more amount of γ phase, unlike upper layers. Interlamellar spacing was increased and colony size was reduced, compared to the PLS and middle portion. Lamellar colony size of dominant microstructure varied in the range 40 – 60 μm.

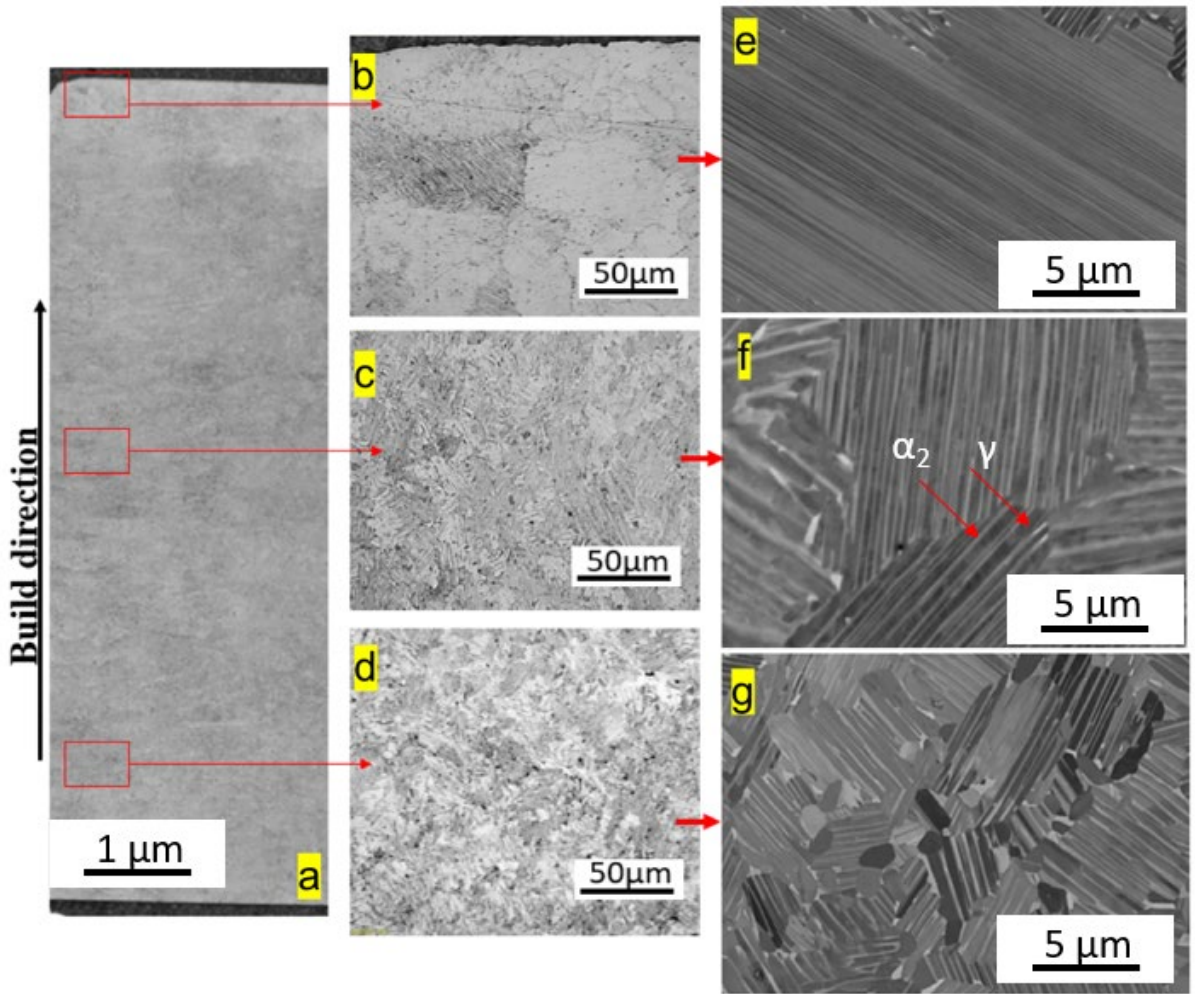

Figure 7.2: The microstructure of as fabricated sample- from different regions in x–z plane. (a): Optical image of etched section of the highlighted region in Figure 7.1. (b): Magnified view of etched sample from top region, (c): Magnified view middle region, (d): Magnified view of bottom region. (e): High magnification BSE image from top region, shows fine primary lamellar structure (f): High magnification BSE image from middle region, near lamellar colonies with coarsened lamellae are seen (α_2 and γ are highlighted); (g): High magnification BSE image from bottom region, shows near lamellar structure with more amount of γ phase**.**

7.1.1.2 Primary lamellar microstructure (PLS)

SEM micrograph of primary lamellar structure is shown in Figure 7.3. The PLS contained grains with increased colony size, thin grain boundary and fine lamellae. This attributes to more interfacial area and as a result, high interfacial energy. The PLS have different lamellar orientation and were distinguishable from adjacent grains. Inset shows magnified image of PLS, where stable and straight interfaces is the most significant feature.

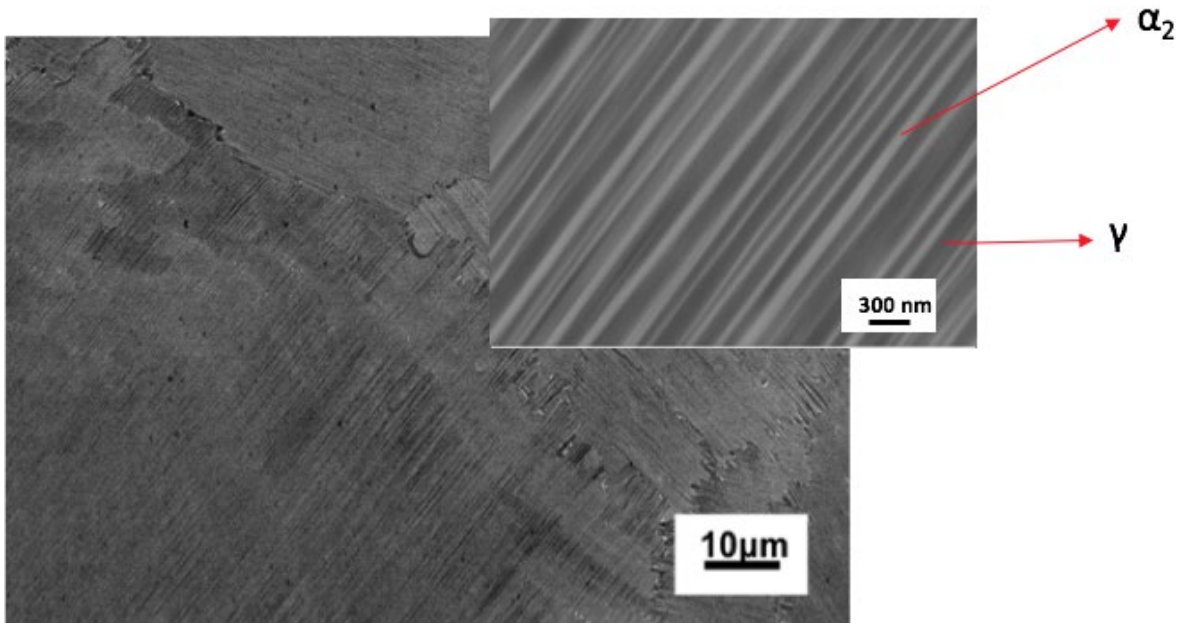

Figure 7.3: SEM image of primary lamellar structure, inset shows fine α_2 and γ lamellae.

TEM analysis as shown in Figure 7.4, clearly reveals that primary lamellar interfaces were stable and straight.

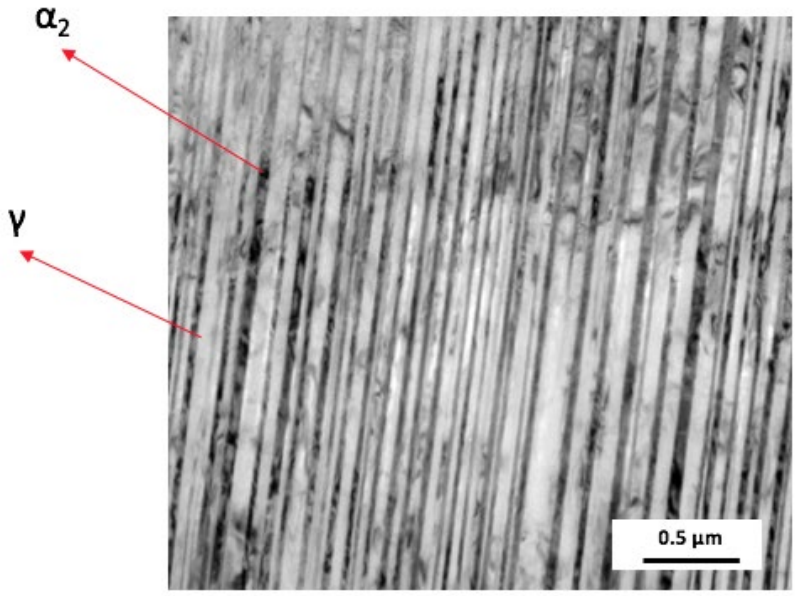

Figure 7.4: TEM analysis reveals stable and straight primary lamellar interfaces.

7.1.2 Cyclic in-situ heating and resultant microstructural changes

Cyclic in situ heating, which is a unique characteristic of EBM printing, produces significant microstructural changes in various layers, in the build direction. The sequential microstructural changes are depicted in Figure 7.5. Figure 7.5(a) is an optical image showing microstructure of the high energy sample sectioned along the build direction, displays a uniform microstructure with minimal defects. Figure 7.5(b-f) shows the sequence of microstructural changes upon cyclical heating during EBM.

Figure 7.5(b) shows the PLS microstructure with fine lamellae. Figure 7.5(c), Figure 7.5(d), Figure 7.5(e) and Figure 7.5(f) show the microstructure in 4^{th}, 6^{th}, 8^{th} and 12^{th} layer respectively and a sequential microstructural change could be tracked. A secondary coarse lamellar structure started nucleating, which later grew into adjacent grains, consuming primary cells as seen in. As cyclic heating progressed, initial fine lamellae was coarsened and the colony size was reduced. In bottom layers microstructure is near lamellar or duplex. The growth of gamma phase and beta phase were observed in bottom layers. β phase could be seen as white spots in Figure 7.5 (f). Sequential microstructural changes in layers along build direction tracked by SEM images is shown separately in Figure 7.6.

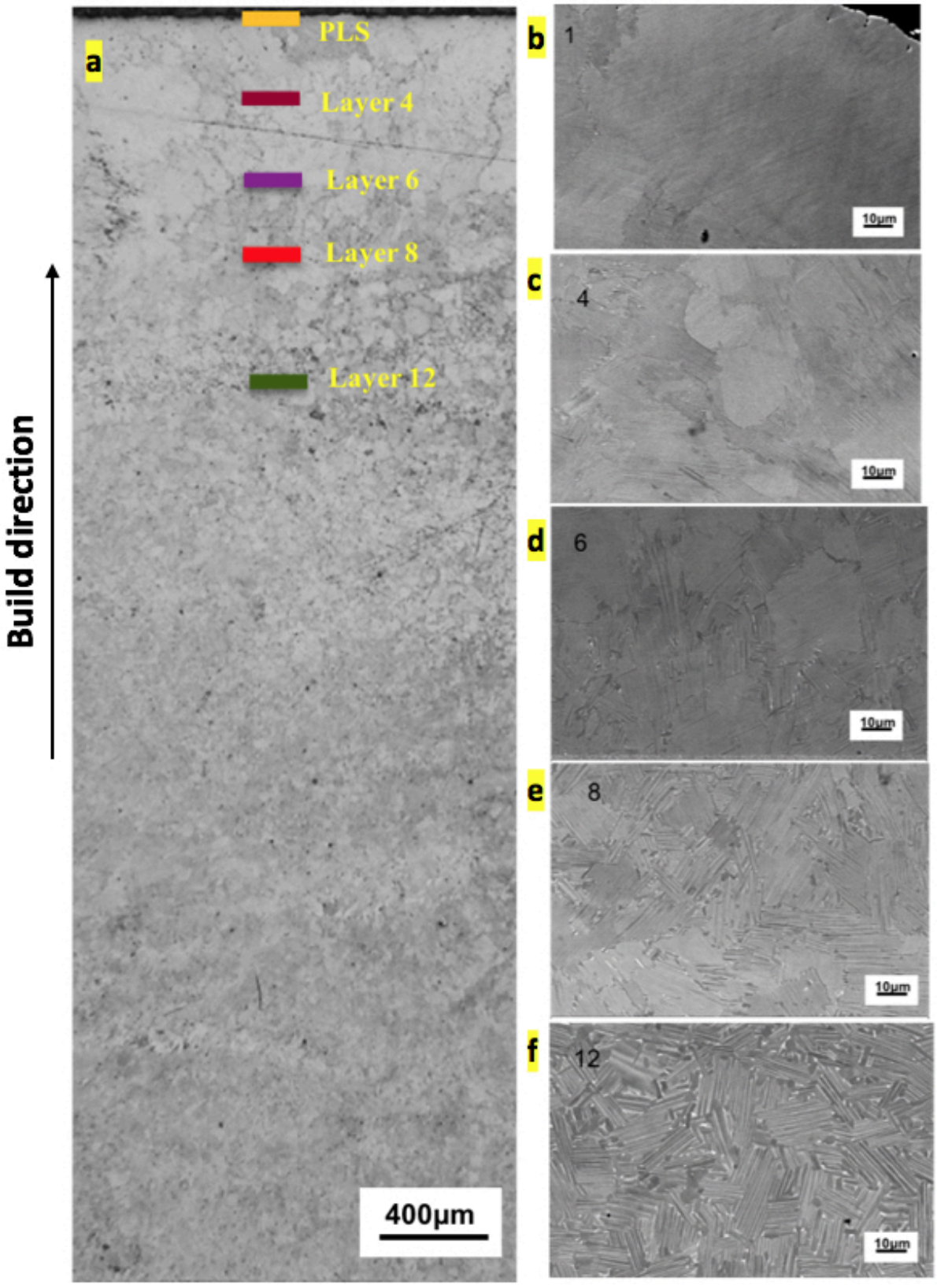

Figure 7.5: Sequential microstructural changes observed in various layers, in build direction. (b) SEM micrograph shows the PLS microstructure with fine lamellae. (c), (d), (e) and (f) show the SEM micrograph of 4th, 6 th, 8 th and 12 th layer respectively.

Figure 7.6a represents microstructure of 4th layer. As shown in figure, heat input and consequent melting during EBM process initiated the formation of coarse nuclei in PLS matrix, at lamellar termination points and colony boundaries. Nucleation is highlighted by an arrow in Figure 7.6a. These nuclei, as highlighted by arrows in Figure 7.6b (microstructure of layer 6), exhibited dissimilar orientation than that of the initial lamellar colonies. They extended into nearby grains, became coarsened small colonies and then grew within neighboring grains. During successive cyclic heating, these coarsened colonies got enlarged, and further nuclei formed within the primary structure. During each heat cycle, the process was repeated. As the number of cycles increased, the phase fraction of coarsened lamellae colonies was also increased, which is visible in Figure 7.6c (microstructure in 8th layer). γ phase fraction was increased and colony size was reduced. Fine lamellae of PLS became coarsened lamellar structure. Towards the 11th cycle of heating, the initial PLS microstructure entirely got replaced, as observed in Figure 7.6d (12th layer microstructure). Lamellae got coarsened, inter lamellar spacing was increased, with a reduction of colony size at an average of 61% and a coarsening ratio of 14 at the 12th layer compared with PLS. Along with increased phase fraction of γ phase, β phase formation was also observed in high energy sample.

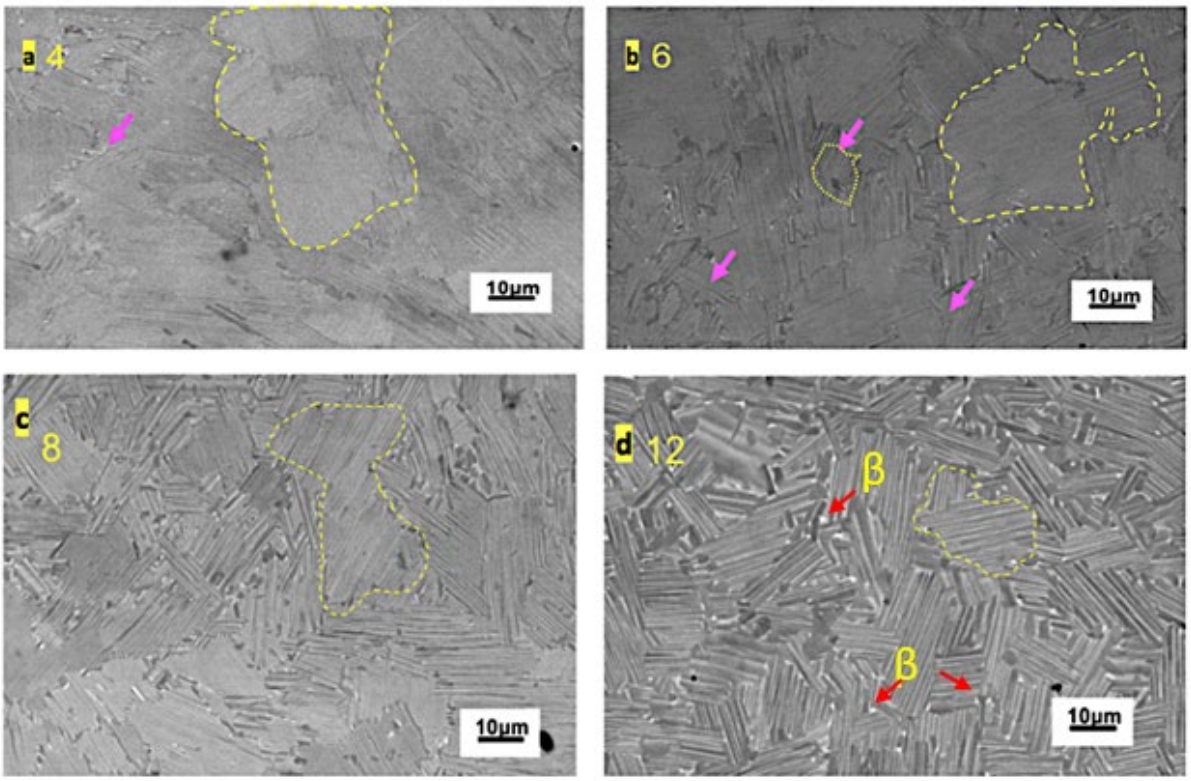

Figure 7.6: SEM micrographs showing microstructural changes in various layers. 7.6 (a), (b), (c) and (d) show the SEM micrograph of 4th, 6th, 8th and 12th layer respectively.

To support the coarsening observation in bottom layers, 8 layers were deposited in a selected area of the top last melted region in a TiAl sample, as picturized in Figure 7.7

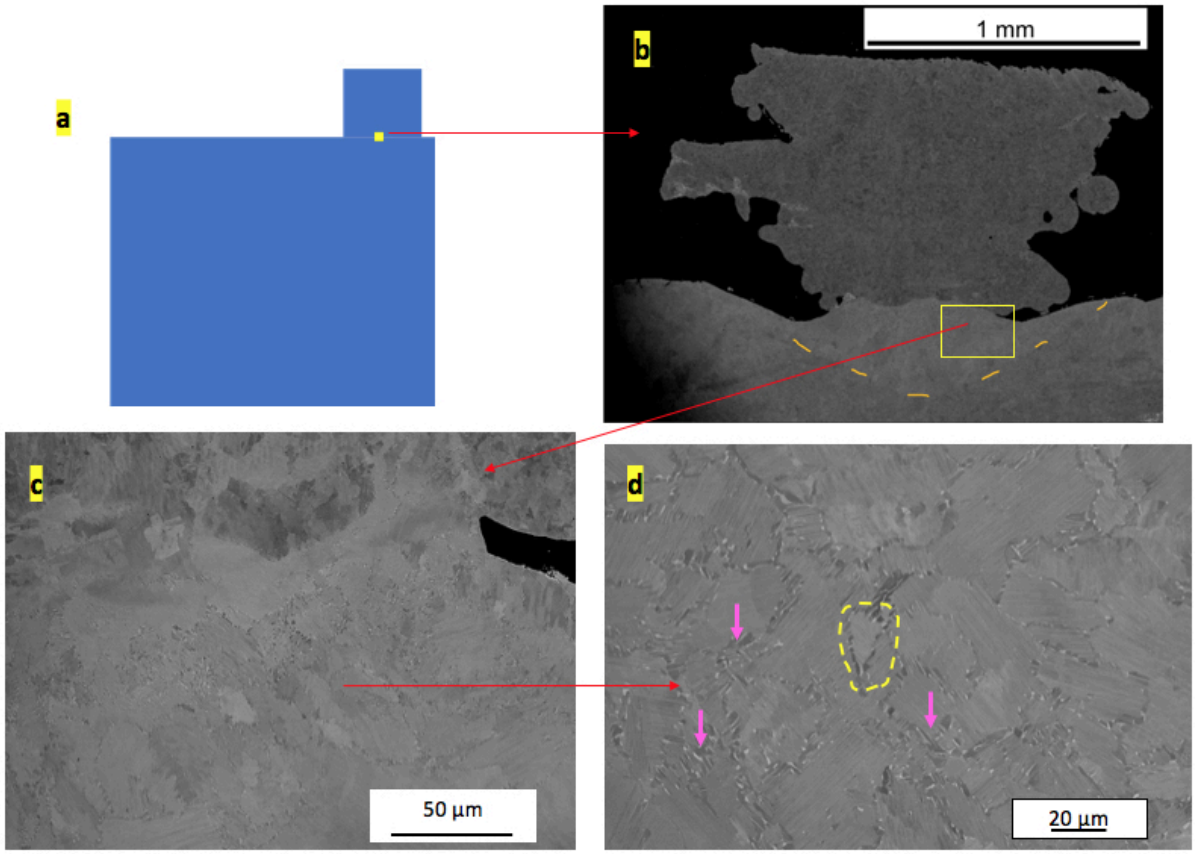

Figure 7.7: Images showing coarsening reaction observed in TiAl sample due to top layers. (a): Schematic diagram of the sample printed. (b): SEM micrograph of neck area, highlighted in the image (c): shows the SEM micrograph of the top layer of cube. (d): SEM micrograph showing formation of coarsening nuclei and coarsening of primary fine lamellae (highlighted in image).

Figure 7.7a is the schematic diagram of the sample printed. 8 layers printed at the top PLS layer of main block, using a different ED as represented in Figure 7.7 b. Neck area, highlighted in the image, showed the microstructural change in the top layer of the cube due to the 8 layers above, as seen in Figure 7.6c (after 8 cycles of heating). Magnified view of the neck area is seen in Figure 7.7 (d). Coarsening nuclei observed (highlighted with arrows in the Figure 7.7(d)) as expected and coarsening of primary fine lamellae is clearly visible (highlighted in image). After layer wise analysis, more lamellar width for γ is observed below the 8^{th} layer, indicating higher coarsening rate for γ than that of α_2. The 8-layer experiment also suggests that

around 8-10 layers are required for a nearly complete transformation of primary to secondary lamellar structure. While doing this experiment, it was easy to trace exact position below 8 layers. Additionally, 8 layers with different energy input were deposited over the high energy sample. At higher energy 8-layer deposition only, significant DC observed.

7.1.2.1 XRD Analysis

To study the microstructural development and phases formed during EBM process, XRD patterns of as fabricated sample were taken from different layers and analysed. After each layer XRD analysis, it is grounded and polished to bottom layer by 100 µm. The layer depth measurement was done using Vernier calliper. The XRD patterns from the top layer (which is considered as layer 1 in this study) to layer 10 are shown in Figure 7.8, reveals that the as-printed sample was made up of γ and α_2 phases. Characteristic planes of γ (110), (111), (200), (202), (311) and α_2 (200), (201) and (202) are clearly visible. It should be noted that α_2 phase fraction decreased, when moving down in build direction.

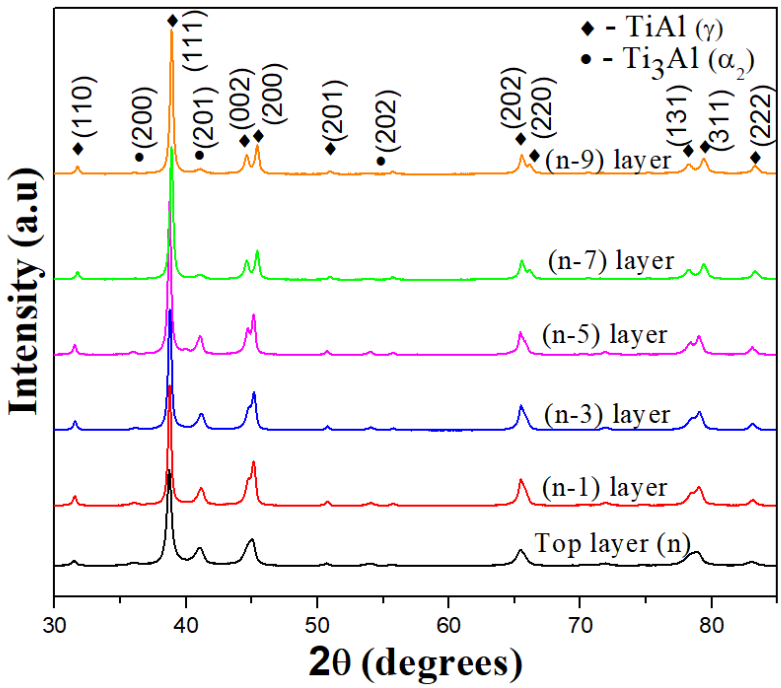

Figure 7.8: XRD analysis in various layers of TiAl EBM sample, reveals characteristic planes of γ (110), (111), (200), (202), (311) and α_2 (200), (201) and (202).

XRD analysis from the middle of sample (ED - 6 J/mm$^{2)}$ printed at build temperature 950 ºC and 1050 ºC was done. The weak (110) β peak was detected at 2θ angle of ~39.9°, revealing the presence of β phase, as shown in Figure 7.9. The low intensity β peak denoted very small

β phase fraction. When printing condition changed from 950 ºC to 1050 ºC, the beta phase fraction increased, from 3.5% to 8%.

The growth of beta phase was observed in bottom layers, which were under in situ annealing due to preheating comparatively higher time than top layers. XRD studies of layers along build direction showed an increase in beta phase reaction in bottom layers. The increased presence of beta phase is highlighted with red arrow in SEM, as shown in Figure 7.6 (d) and 7.15.

SEM-BSE quantitative analysis revealed an average lamellar colony size of 46.6 µm and β phase fraction of about 3-7 vol.%. Another important observation was the increased presence of β phase at lamellar colony boundaries (LCB). This was not observed in PLS.

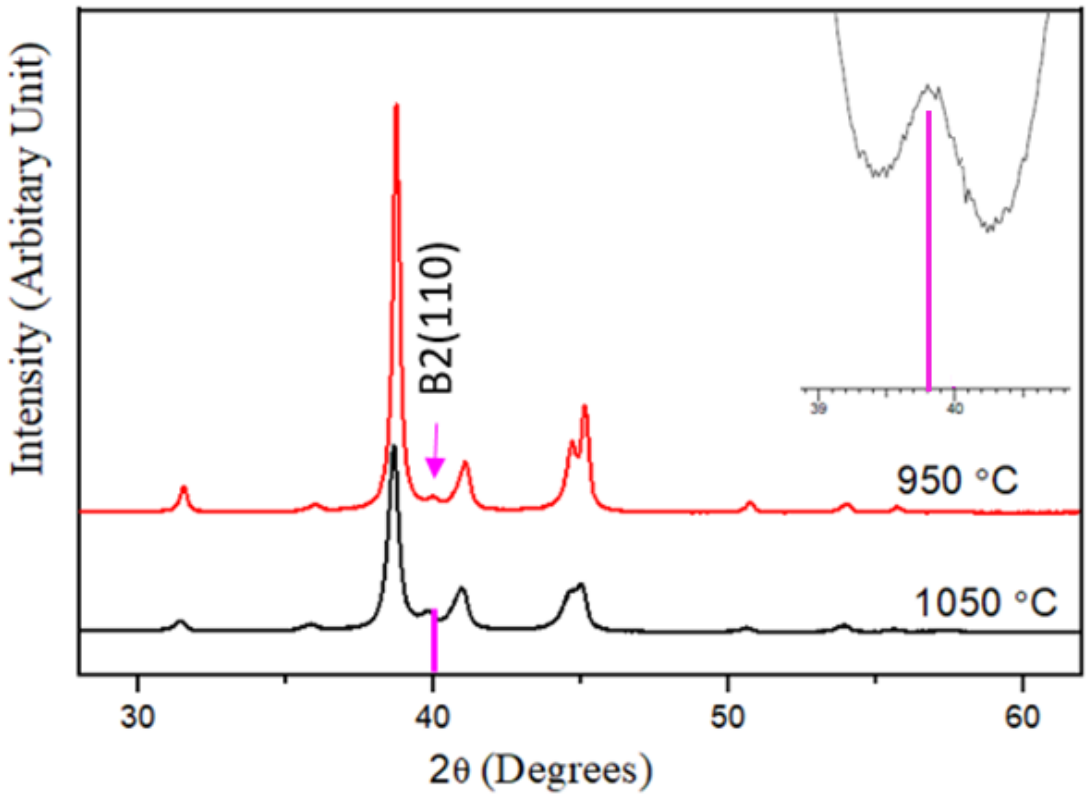

Figure 7.9: XRD analysis from the middle of sample (ED - 6 J/mm2) at printing condition (a) 950 ºC and (b) 1050 ºC. Weak (110) β peak detected at 2θ angle of ~39.9°.

Table 7.1 shows the computed phase fraction values of different layers along the build direction. α_2 fraction reduced from 26% at PLS to 10% at 10^{th} layer. At the same time, an increase in fraction of γ phase was also observed. γ phase showed an increase by 15% from PLS (layer 1) to layer 10.

Table 7.1: Variation of the phases fraction (wt.%) in layers along build direction.

Layer from top	γ	α_2	β
Layer 1	73 ± 1	26 ± 1	1 ± 0.2
Layer 2	79 ± 1	20 ± 1	1 ± 0.2
Layer 4	80 ± 1	19 ± 0.8	1 ± 0.2
Layer 6	83 ± 2	15 ± 1	2 ± 0.2
Layer 8	86 ± 2	12 ± 1	2 ± 0.2
Layer 10	88 ± 1	10 ± 0.8	2 ± 0.2

7.1.2.2 Chemical composition – EDS analysis

Elemental analysis using EDS along the layers, from top layer to 8th layer showed variation of aluminium concentration in α_2 and γ phases. As the layer gets more thermal cycling, Al concentration in α_2 got reduced from around 45 at.% (in layer 1) to 39 at.% (in layer 8), became closer to equilibrium. At the same time in γ phase, there was no much variation in Al concentration during coarsening. Figure 7.10(a) shows optical image of high energy sample cross section, with layers marked. Figures 7.10(b), 7.10(c), 7.10(d) and 7.10(e) shows lamellae in layers 1,4,6 and 8 respectively, where EDS analysis was conducted. Aluminium concentration in α_2 shows a gradual reduction and approaches close to equilibrium 39% in the studied TiAl alloy. After reaching close to equilibrium, there was no further significant change towards bottom layers. γ lamellae did not show much variation. This gradual change of aluminium content in layers is plotted in Figure 7.10(g). Corresponding EDS-XRD spectra is given in Figure 7.11. Figure 7.11(a), 7.11(b), 7.11(c) and 7.11(d) shows EDS-XRD spectra of layers 1,4,6 and 8 respectively, showing a similar observation as above.

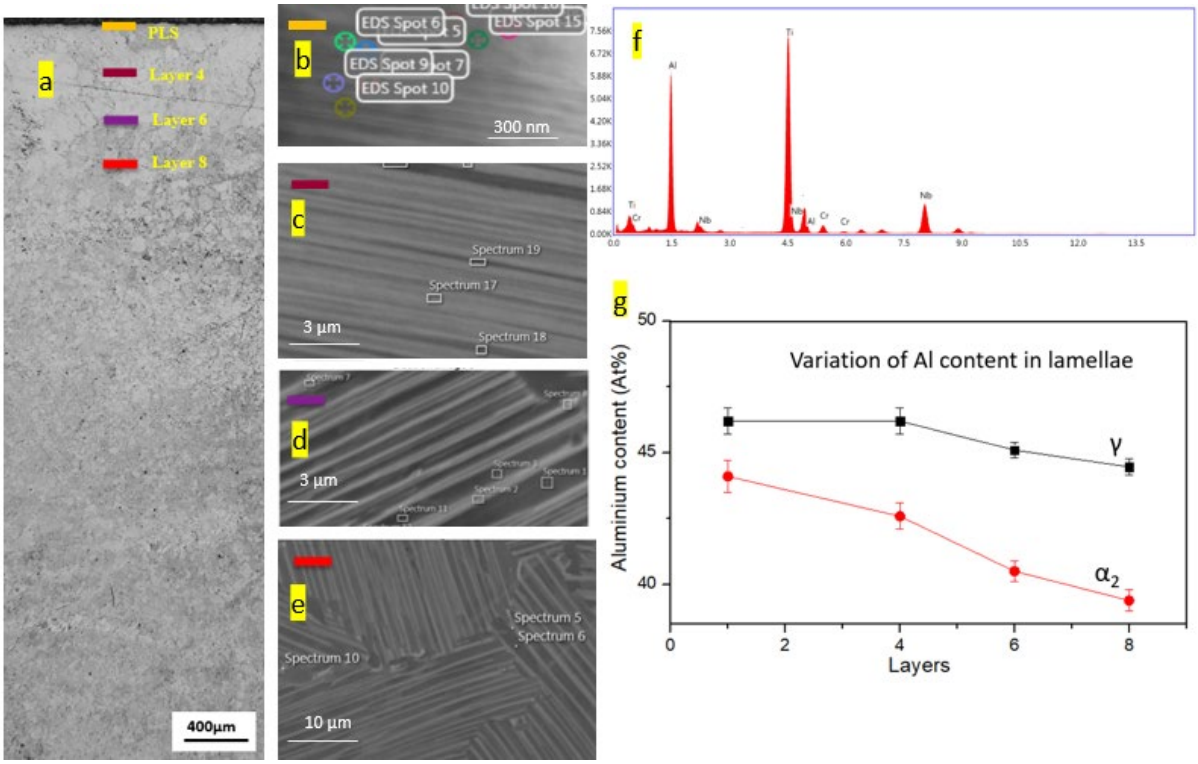

Figure 7.10: Elemental analysis using EDS along 1 to 8 layers. (a): Optical image of high energy sample cross section, with layers marked. (b), (c), (d) and (e) shows lamellae in layers 1,4,6 and 8 respectively, where EDS analysis was conducted. (g): Gradual change of aluminium content in layers is plotted.

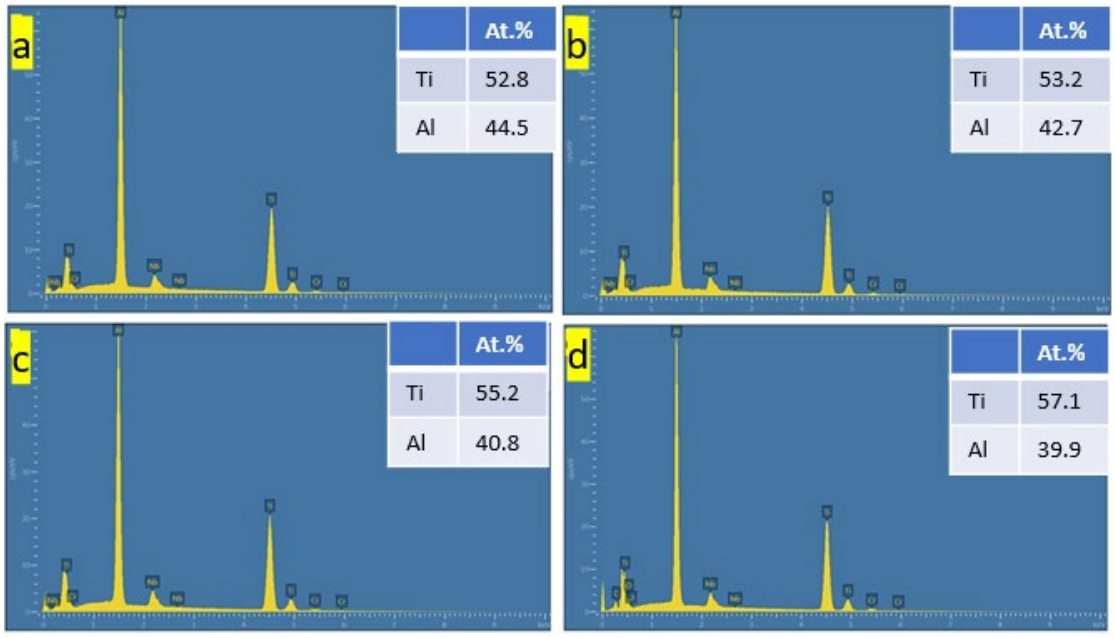

Figure 7.11: EDS-XRD spectra of layers 1,4,6 and 8. (a), (b), (c) and (d) shows EDS-XRD spectra of layers 1,4,6 and 8 respectively, showing a gradual decline in Al concentration in α_2 towards bottom layers, without much variation in γ lamellae.

7.1.2.3 Differential scanning calorimetric (DSC) curve for TiAl EBM printed sample

It is essential to understand the phase transformations and chemical reactions in Ti-48Al-2Cr-2Nb samples, to study the effect of in situ heat treatment. Thus, optimisation of the final microstructure becomes possible, by selecting suitable in-situ heating condition. The top layers from as fabricated sample were heated in an Ar environment at 20 °C/min heating rate in DSC and the heat flow was plotted. Figure 7.12 shows DSC curve of EBM fabricated TiAl sample. Observed 3 major peaks and their corresponding phase transformations can be studied from the TiAl phase diagram. Table 7.2 shows the expected phase transformations corresponding to 1,2 and 3 peaks. There were some peaks starting between 800-900 °C, but it was merged with the peak 1 and not considered for this study. Negligible mass change was observed in this test.

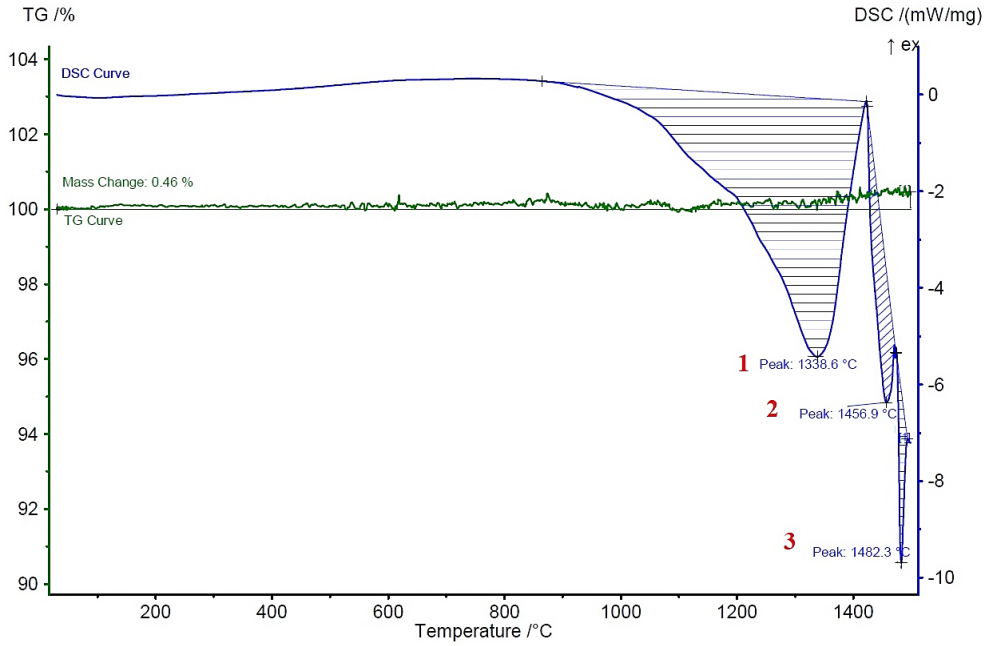

Figure 7.12: Differential scanning calorimetric curve of TiAl sample, observed 3 major peaks.

Table 7.2: Expected phase transformation corresponding to 1, 2 and 3 peaks of DSC.

DSC peak	Temperature (°C)	Phase transformation
1	**1338.6**	$\alpha + \gamma \rightarrow \alpha$
2	**1456.9**	$\alpha \rightarrow \alpha + \beta$
3	**1482.3**	$\alpha + \beta \rightarrow L + \beta$

7.1.2.4 Microstructural changes in top layer during cyclic heat treatment

When cyclic heat treatment using electron beam was given to top layers inside the EBM machine in an attempt to produce similar effects as that of in-situ heating, nucleation was observed. Figure 7.13 shows microstructures obtained at various stages during cyclic heating experiment. Build temperature was maintained at 1000 ºC and the last deposited layer cyclically reheated 3 times with decreasing energy input. The process parameters for reheating experiments are given in Table 7. 3. The ED was calculated based on the Equation 5.1.

Table 7.3: Reheating parameters for top layer heat treatment

	Average Beam current (mA)	**Scanning speed (mm/s^1)**	**Line offset (mm)**	**Average energy density (J/mm^2)**
Reheat I	30	10000	0.3	0.6
Reheat II	20	10000	0.3	0.4
Reheat III	10	10000	0.3	0.2

Figure 13 (a) shows PLS microstructure in top layer. Top layer after one cycle of heat input, showed nucleations arising randomly at primary lamellar colony boundaries and lamellar terminations as observed in Figure 7.13 (b). Nucleations are highlighted by arrows in the image. Further heating cycles produced more nucleations, along with growth of earlier formed nuclei, as shown in Figure 7.13(c). Microstructure obtained after 3 cycles of heating is shown in Figure 7.13(d). Nucleations observed to be increasing and as highlighted, growing DC colonies could be observed. Further heat cycles would be needed for PLS, to be completely replaced by SLS.

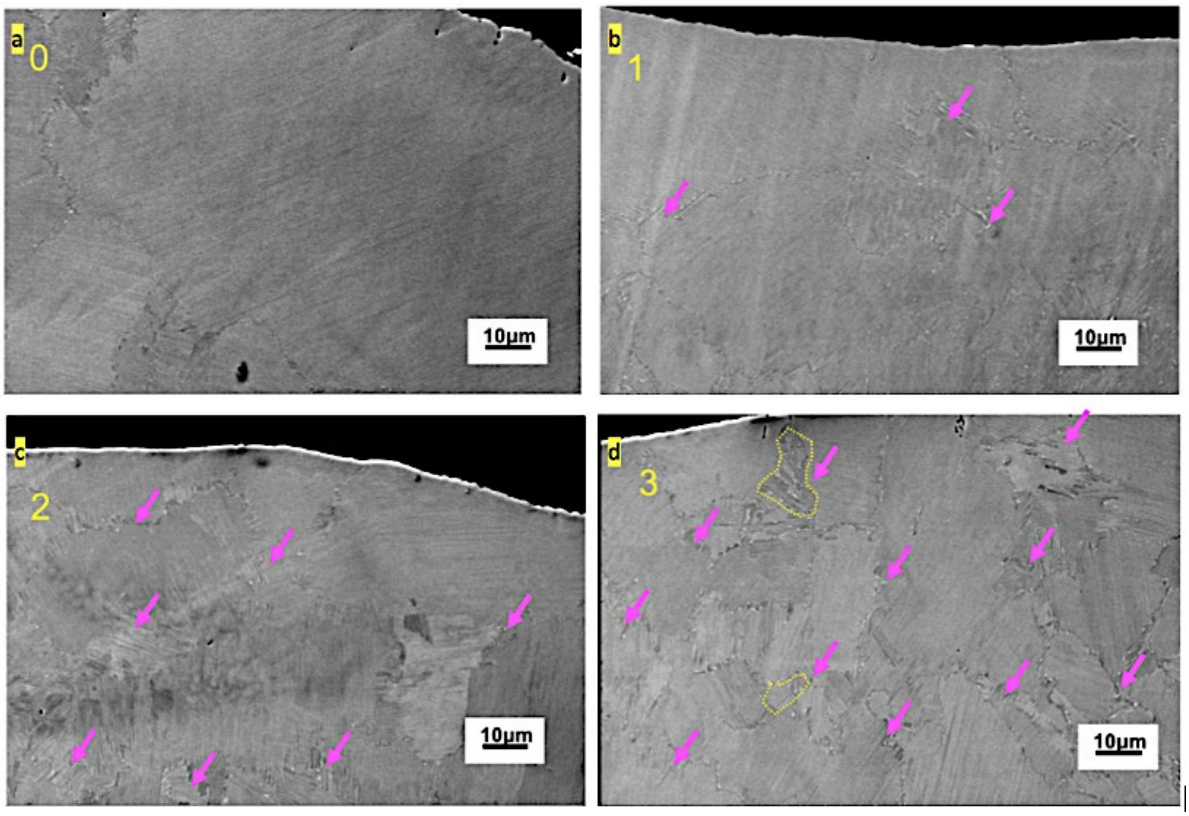

Figure 7.13: SEM micrographs of cyclic heat treatment in ARCAM. (a): PLS microstructure in top layer. (b): Top layer after one cycle of heat input, showed nucleations arising randomly, as highlighted by arrows. (c): Further nucleations produced by more heating cycles. (d): Microstructure obtained after 3 cycles. Increasing nucleations, growing DC colonies highlighted.

Whereas during the heat treatment, when samples were kept at 1300 °C for 2 hours, there was no DC. Figure 7.14 shows the microstructure after this heat treatment. This proves that the formation of DC nuclei was not a result of holding at high temperature, but that of cyclic heating.

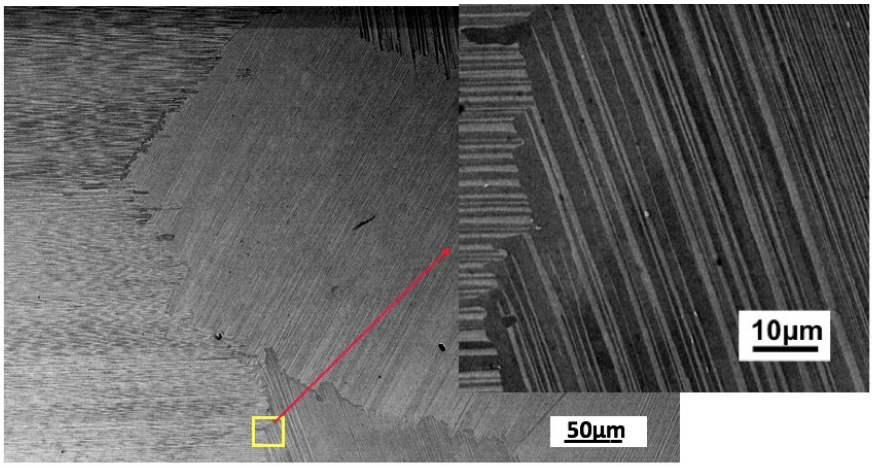

Figure 7.14: SEM micrograph of top layer after heat treatment, where samples were kept at 1300 °C for 2 hours.

7.1.3 β Phase during TiAl EBM process

As fabricated TiAl microstructure from the middle of the sample at ED 6J/ mm^2 is shown in Figure 7.15. Presence of β phase within lamellar colonies and at grain boundaries could be identified in SEM-BSE image of the middle portion. The supersaturated α_2 laths found to be decomposed into equiaxed gamma grains and β phase. The magnified view from the selected region clearly exhibits various phases formed.

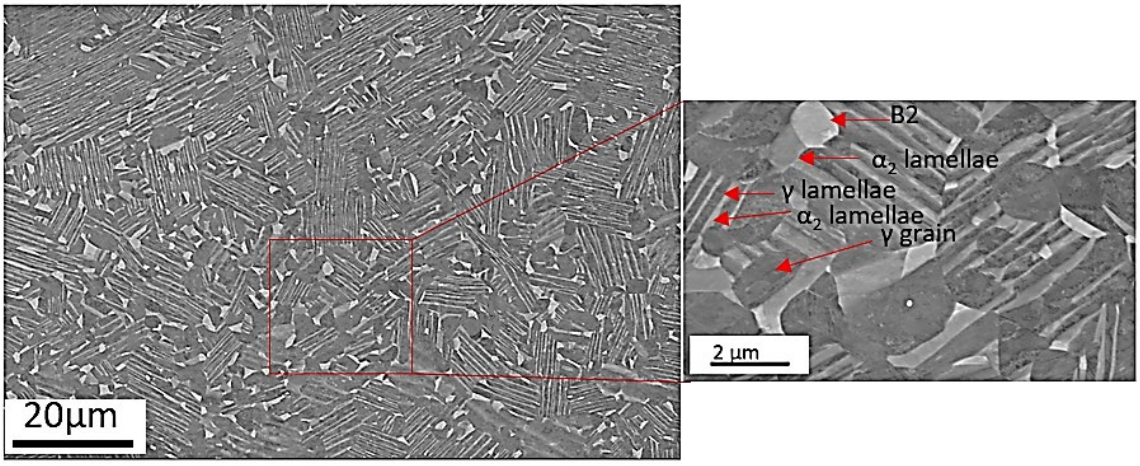

Figure 7.15: SEM analysis in middle layers of high energy EBM TiAl sample, showing beta phase.

TEM analysis done to confirm the presence of β phase. In high energy sample. Fig 7.16 a demonstrates bright field TEM image, where beta phase is observed as dark precipitate. Cr segregation was observed in TEM EDS analysis, shown as highlighted region in Figure 7.16

b. SAED patterns of [111] zone axes from dark precipitate shown in Figure 7.16 c confirmed presence of ordered β phase.

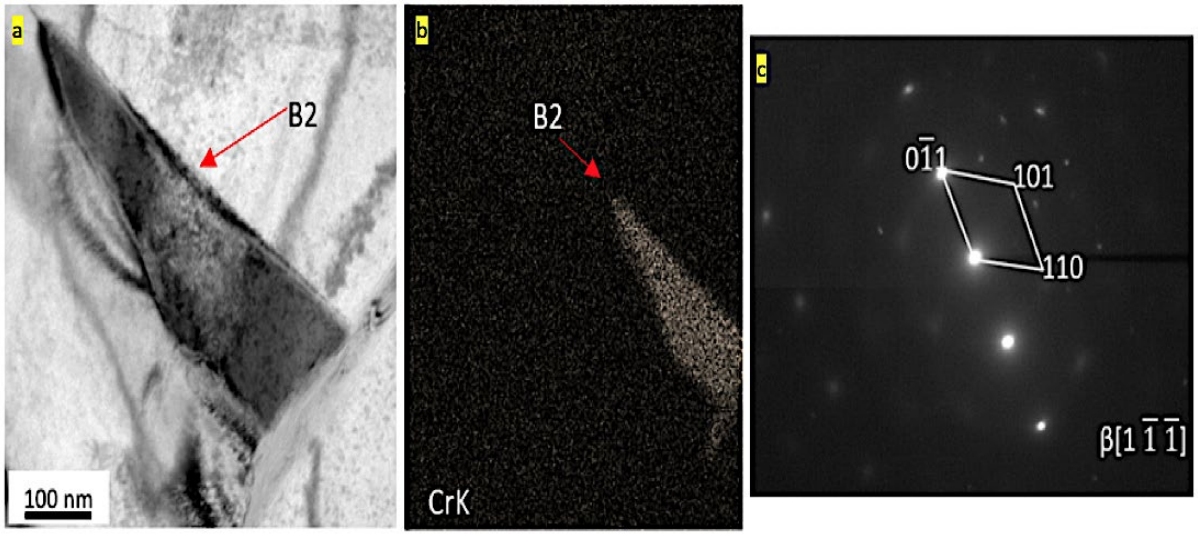

Figure 7.16: TEM analysis in middle layers of high energy TiAl samples, confirming presence of beta phase. (a): Bright field TEM image, beta phase is observed as dark precipitate. (b): TEM EDS analysis showing Cr segregation, as highlighted. (c): SAED patterns of [111] zone axes, show presence of ordered β phase.

The SEM - EDS mapping shows Cr segregation in bright contrast region. This leads to the postulation that beta phase formation is attributed by the segregation of chromium. Figure 7.17 shows EDS mapping of samples. Cr segregation was observed, as highlighted in image. In beta region aluminium depletion was also observed as highlighted in the EDS map. The EDS elemental composition from the bright contrast region is shown in Table 7.4. Cr enrichment up to 8 at.% was observed.

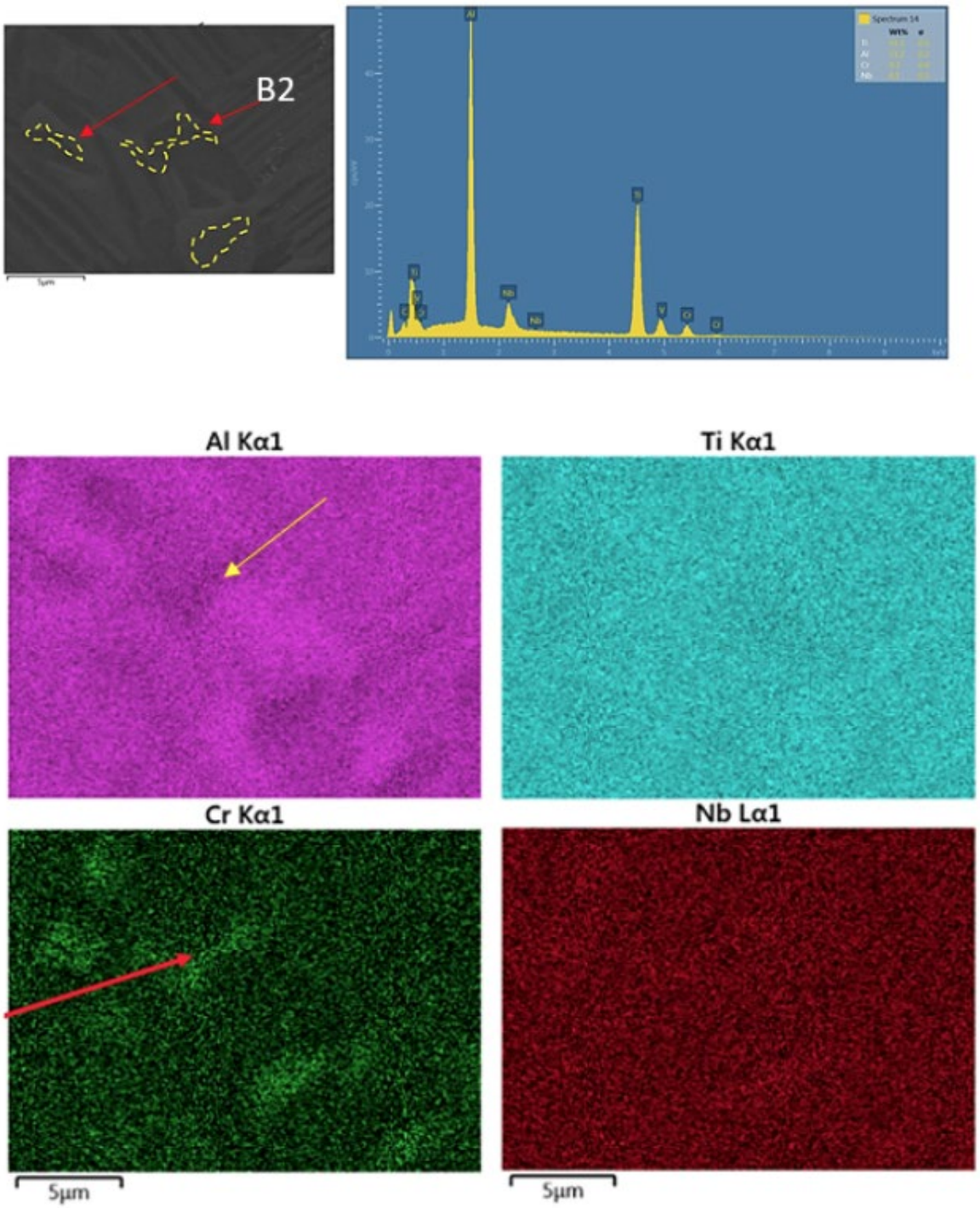

Figure 7.17: EDS mapping shows Cr segregation in β as highlighted in image.

Table 7.4: Relative EDS elemental composition of samples, showing Cr segregation.

Element	At.%
Ti	55
Al	34
Cr	8
Nb	3

7.1.3.1 EBSD Analysis

EBSD analysis was done in centre portions of TiAl samples printed at high energy. Figure 7.18 (a) depicts phase map, which revealed the phase composition showing α_2, γ and β phases. β phase could be observed, are seen as blue dots in the picture. This is a characteristic observation in high energy samples. Phase fraction of α_2 phase is observed to be less than expected. This is because selected EBSD data base did not identify α_2 lamellae. α_2 lamellae are off-stoichiometric in composition, causing lattice parameter variations and are seen as dark colour in phase map. In pole figure, (Figure 7.18 b), randomly oriented lamellar colonies were observed. Columnar growth or texture could not be observed along build direction.

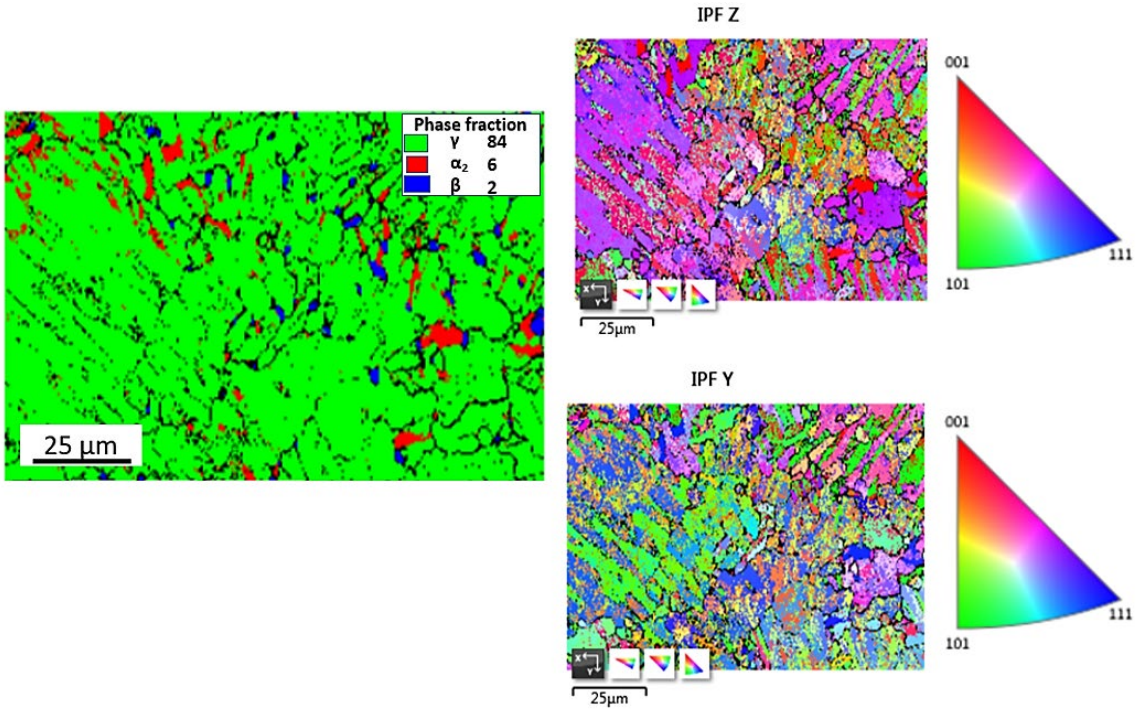

Figure 7.18: EBSD analysis, showing phase composition of EBM high energy samples. (a): Phase map reveals α_2, γ and β phases of phase composition. (b): Pole figure shows randomly oriented lamellar colonies.

7.1.3.2 Grain boundary coarsening

After DC, thick grain boundary and presence of beta could be observed. This grain boundary coarsening observed from PLS to SLS, is shown in Figure 7.19. This is mainly due to the formation of β + γ and its growth during EBM printing at high temperatures, along the lamellar colony boundaries (LCB).

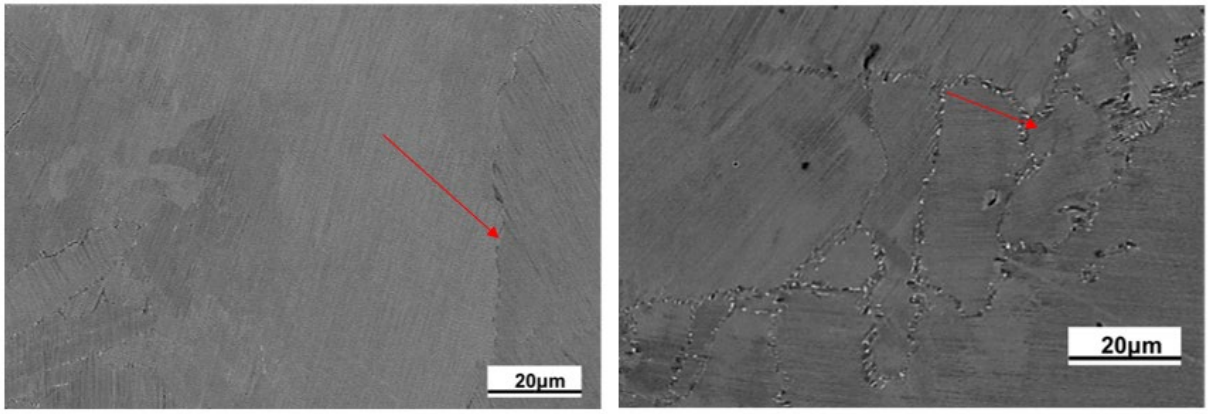

Figure 7.19: SEM micrograph showing grain boundary coarsening from PLS to SLS. Formation of β + γ along the lamellar colony boundaries is highlighted.

7.1.3.3 Effect of build temperature on beta phase formation

Samples with same parametric combination of ED 6 J/mm^2 were printed at build temperatures of 950 ºC, 1000 ºC and 1050 ºC. Figure 7.20 shows SEM analysis of samples printed at 950 ºC, 1000 ºC and 1050 ºC. XRD Analysis shown in Figure 7.9 revealed an increase of beta phase with pre heat temperature, from 3.5% at 950 °C to 8% at 1050 °C.

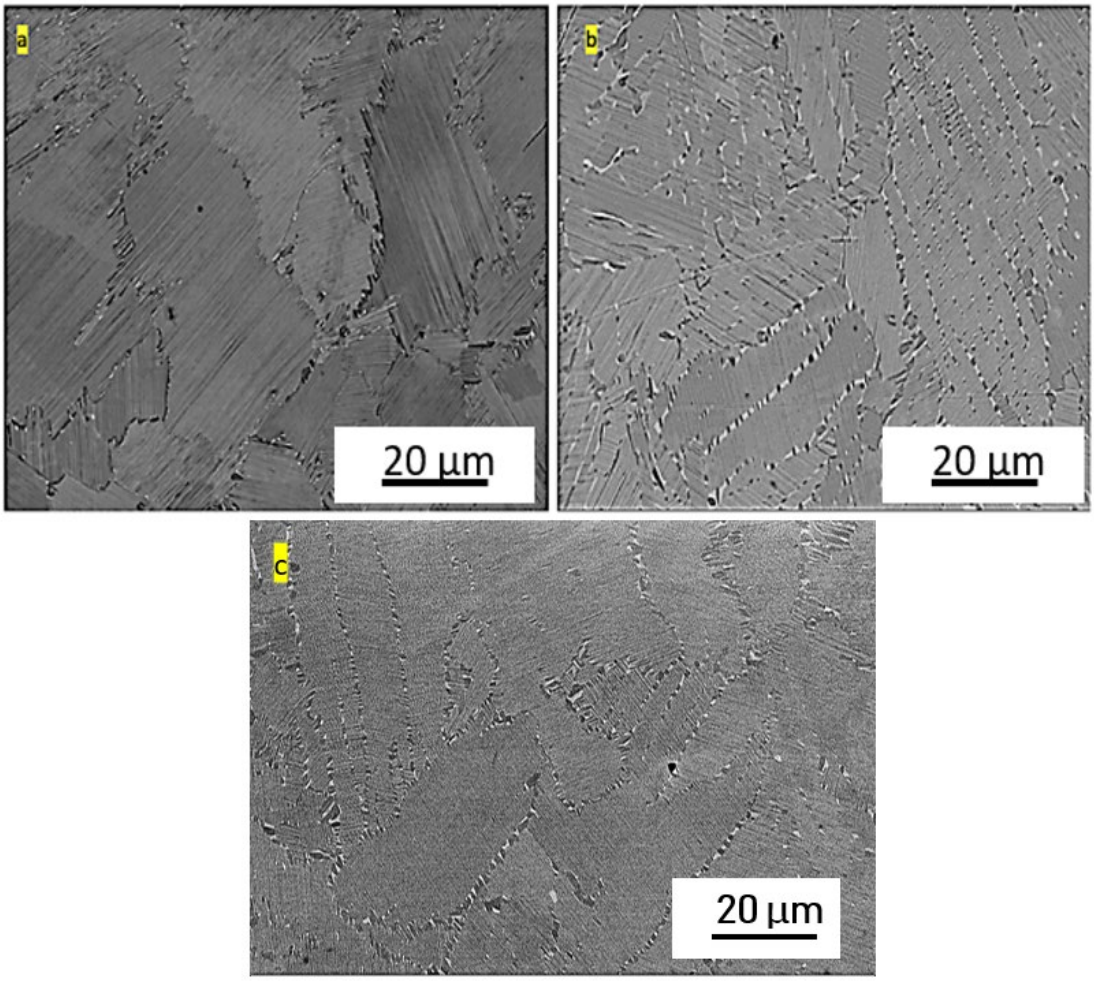

Figure 7.20: SEM analysis of samples printed at same parametric combination of ED 6 J/mm2 and different build temperatures. (a): printed at 950 °C and (b): printed at 1050 °C and (c): printed at 1000 °C.

7.1.3.4 Heat treatment of TiAl primary lamellar structure

Heat treatment was done in such a way that samples were kept at high temperature for one hour. The SEM images of heat treated PLS at 800 °C, 900 °C and 1000 °C are shown in Figure 7.21 (a-d). Dissolution of PLS to γ and beta was observed at 1000 °C. This observation could

not be made in other temperatures. Corresponding XRD analysis of PLS, heat treated at 1000 °C was done, which revealed substantial increase of β phase. This observation proved critical association between beta formation and the preheating condition or build temperature, in as fabricated EBM samples.

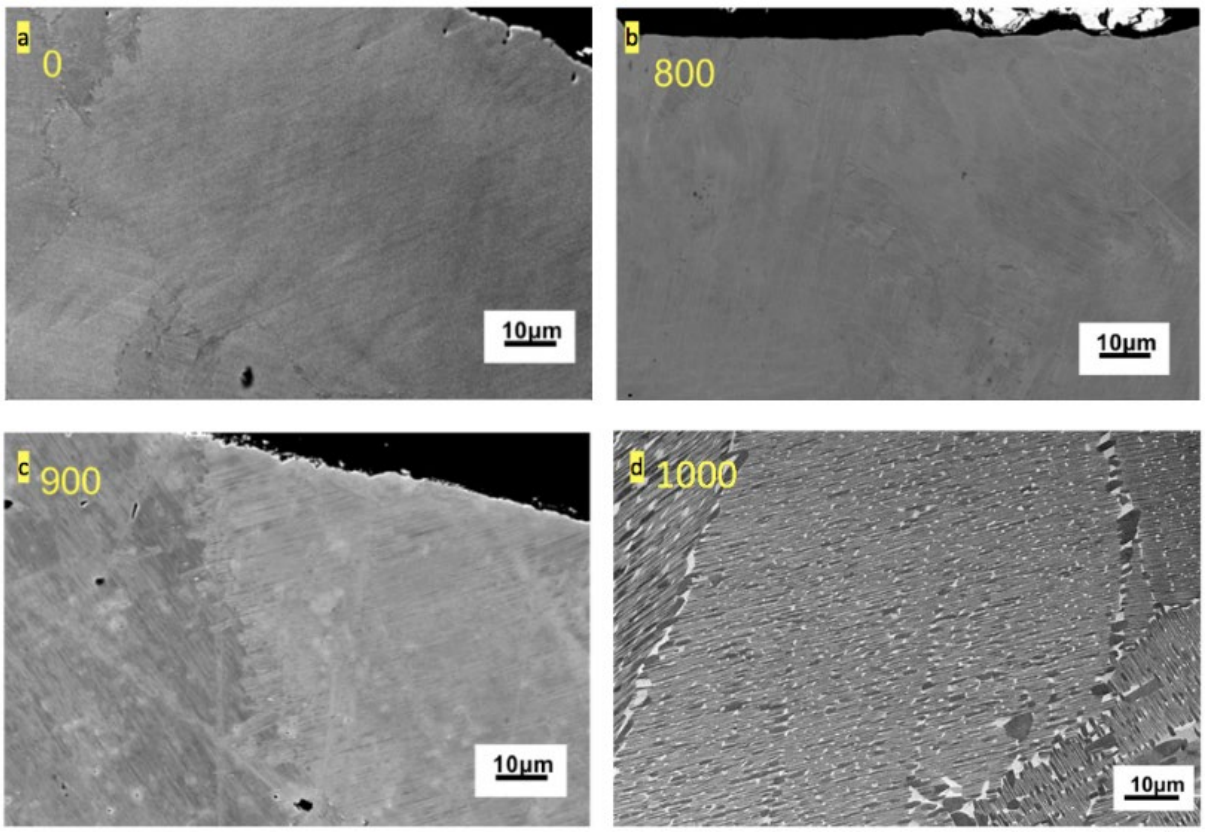

Figure 7.21: SEM micrographs of heat treated PLS at 800 °C, 900 °C and 1000 °C. (a): Shows initial PLS microstructure, (b): Shows no much variation, (c): Shows indication of segregation, (d): Shows beta formation in PLS.

7.1.4 Mechanical properties

7.1.4.1 Hardness measurement

Since colony size reduced and lamellar thickness increased due to the observed coarsening reaction, mechanical properties were affected. The micro hardness profile shown in Figure 7.22 represents the average hardness of layers along the build direction. In PLS the hardness value was ~450 HV and it gradually decreased towards bottom layers.

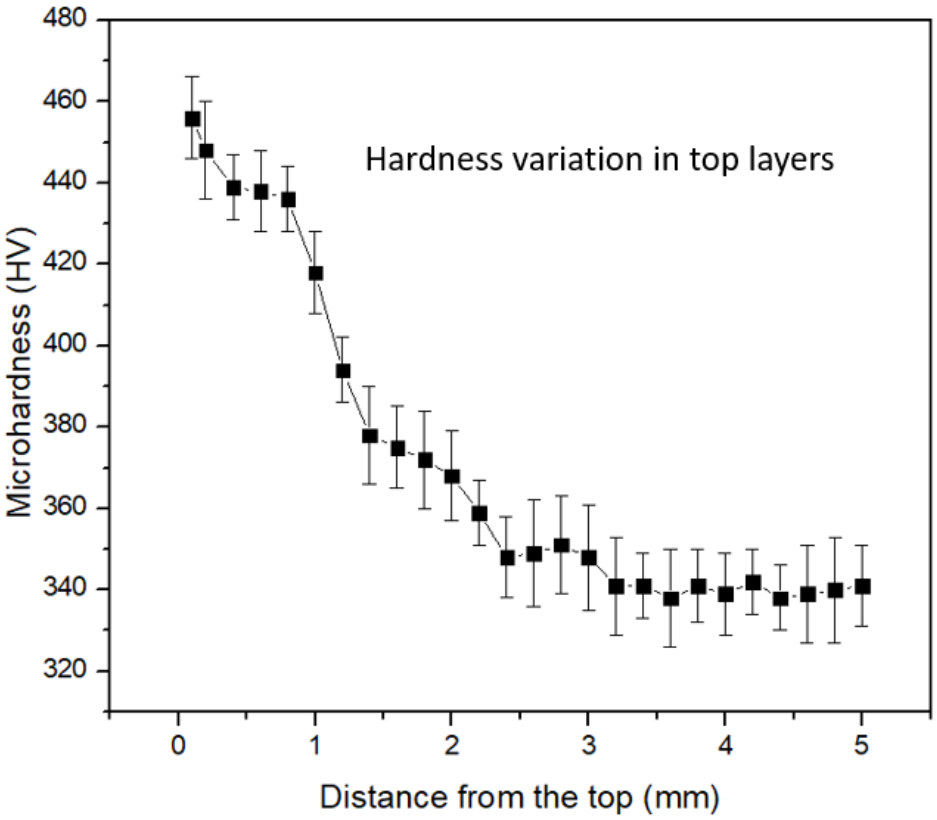

Figure 7.22: Microhardness profile in various layers of EBM TiAl sample, along the build direction upto 5mm from top.

7.2 Discussion

7.2.1 Discontinuous coarsening (DC) during EBM and effects on microstructural development

Rapid solidification during EBM results in the formation of a primary lamellar structure, which is far from equilibrium and possess high energy. To alleviate the excess energy and to attain equilibrium, system undergoes solid-state transformations, among which discontinuous coarsening is of particular interest. Discontinuous coarsening is a grain boundary migration reaction characterized by a moving reaction front (RF) [85]. This is a lamellar coarsening mechanism which replaces primary microstructure and leaves coarsened lamellar colonies with different orientation and composition. Growing DC colony consumes primary lamellae and same matrix is reorganized. Product of primary reaction, denoted as primary lamellar structure

(PLS) here, is entirely replaced by a secondary lamellar structure (SLS), of near-equilibrium composition, without alteration in crystal structure. This reaction is capable of introducing chemical and morphological modifications which are responsible for significant changes in the microstructure, composition, and properties.

Symbolically DC can be represented as:

$$(\alpha_2 + \gamma)_{fine} \rightarrow (\alpha_2 + \gamma)_{coarse}$$

Continuous coarsening normally occurs through the diffusion along lamellar interface, preferably takes place at lamellar defects [85, 86]. In as fabricated EBM sample, primary lamellar structure is having very fine lamellar structure. Both α_2/ γ and γ/ γ interfaces of EBM PLS are observed to be very stable and straight. This makes the diffusion along the stable lamellar interface quite difficult and the easy channel for diffusion becomes lamellar ending and grain boundary. So, discontinuous coarsening becomes more dominant mechanism of lamellar coarsening in the case of Ti-48-2-2 during EBM manufacturing.

Figure 7.23 illustrates the microstructural evolution of PLS during cyclic in-situ heating. After the cyclic exposure of heat, which is intrinsic to electron beam melting, the initial microstructure undergoes DC and is gradually replaced by a secondary lamellar structure. The complete replacement of PLS by SLS is depicted below.

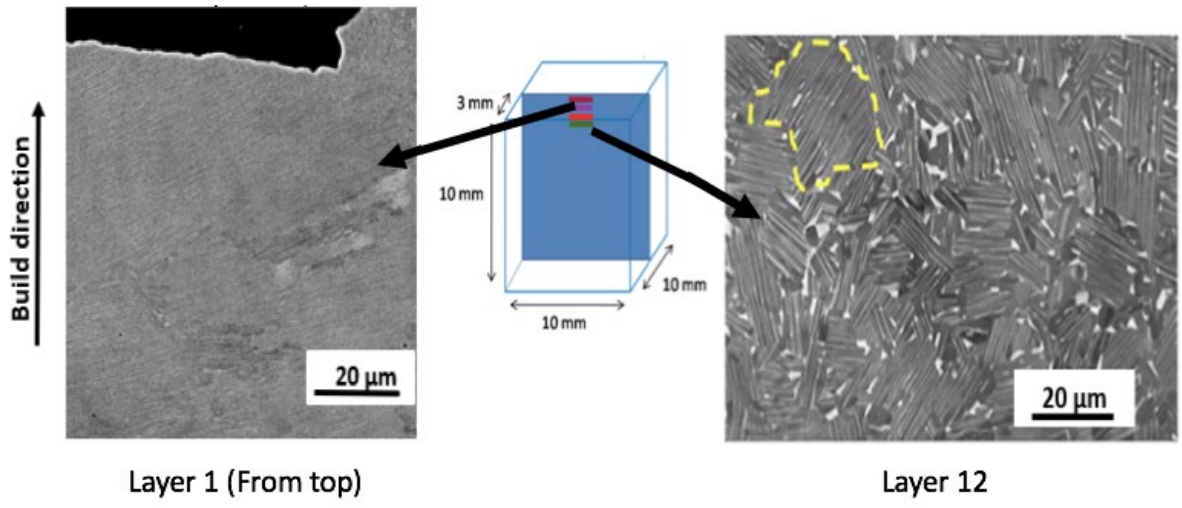

Figure 7.23: SEM micrograph shows microstructural evolution of PLS during cyclic in-situ heating.

7.2.1.1 Driving forces for DC

A sequential change in regard to composition and morphology can be tracked in various layers during the course of EBM, which is identified as discontinuous coarsening. Subsequent heat cycles cause coarsening of initial fine lamellar microstructure, in such a way that after several heat cycles, a coarser structure completely replaces the initial structure. Major driving forces responsible for this characteristic microstructural evolution are identified in this section.

Based on the experimental results it can be qualitatively concluded that driving force for discontinuous coarsening is the combined effect of chemical free energy due to non-equilibrium condition and interfacial energy change of PLS. This can be expressed as [87]

$$\triangle \boldsymbol{F} = \triangle \boldsymbol{G_I} + \triangle \boldsymbol{G_C} \tag{7.1}$$

Where $\triangle F$ is driving force for DC; $\triangle G_I$ and $\triangle G_C$ are interfacial energy change and chemical free energy change respectively.

7.2.1.2 Interfacial energy as a driving force for DC

Kaya et al. [88] proposed that solidification leading to narrow interlamellar spacing as observed in this study, causes an increase in the interfacial energy. Every system has a normal inclination towards reduced free energy state. As per Livingston and Cahn's theory [89], reduction of this excess interfacial energy can be achieved by reduction of interfacial area. To reduce the interfacial energy, coarsening takes place. Through straight stable interfaces, diffusion will not be permitted. Instead, grain boundary migration will be taken place. So, grain boundary migration mechanism, which is termed as discontinuous coarsening becomes the preferred mode to reduce the interfacial energy. Newly formed DC grains has high lamellar thickness as expected, and results in decreased interfacial area.

The interfacial energy change $\triangle G_I$ can be expressed as [87, 89]

$$\triangle \boldsymbol{G_I} = \boldsymbol{2\sigma_{\alpha 2\gamma}\left(\frac{1}{\lambda_2}-\frac{1}{\lambda_1}\right)V_m} \tag{7.2}$$

Here, $\sigma_{\alpha 2\gamma}$ is α_2/γ interfacial energy per unit area ($\sigma_{\alpha 2\gamma}$ = 0.274 J/m^2) [90, 91]. λ_1, λ_2 are inter lamellar spacing before and after coarsening, respectively. V_m is the atomic molar volume,

calculated using lattice parameters measured from XRD, V_m = 1.02745 x 10^{-5} m^3/ mol. Average interlamellar spacing observed in primary lamellar structure is ~90nm. After coarsening, average interlamellar spacing becomes ~1.6 µm.

Considering colonies, after first cycle of DC reaction, coarsening ratio is 5.5 for PLS, (interlamellar space changed from 90 nm to 0.5 µm) and interfacial energy change is ~51.4 J mol^{-1}. During second cycle of DC, if earlier formed DC cell further undergoes DC reaction, forms a DC sub cell with a coarsening ratio of 2, (interlamellar space changed from 0.5 µm to 1 µm), then interfacial energy change will be ~5.6 J mol^{-1}. Hence the driving force for a DC cell to accommodate another DC cell will be approximately 10 times lesser than that of primary lamellar structure as shown in Figure 7.25 bar chart. Hence PLS continues to form DC cells on further thermal cycling and gets completely replaced by DC coarsened lamellar colonies.

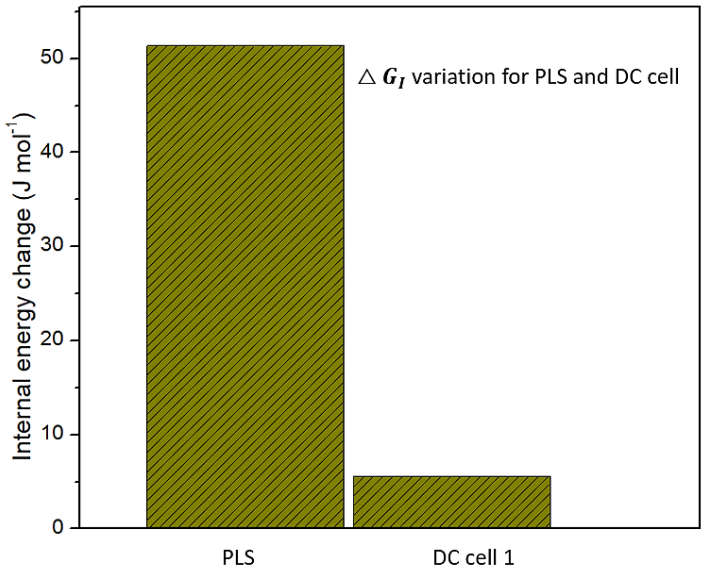

Figure 7.24: DC driving forces comparison for PLS and a DC cell.

7.2.1.3 Non-equilibrium chemical composition as a driving force for DC

The excess chemical energy and consequent instability of the primary lamellar structure is also a major driving force for DC reaction. Generally, alloys with less variation in the α_2/γ phase fraction from equilibrium are considered to be thermally more stable. For T-48Al-2Cr-2Nb alloy, the α_2 phase fraction in the primary lamellar structure is found to be higher than other layers, as evident from Table 7.1. This is attributed by the characteristic high cooling rate during the EBM process.

The equilibrium phase fraction of α_2 in Ti-48Al-2Cr-2Nb is ~6 % [3]. The sample contains α_2 phase composition of 26% in PLS and is clearly out of equilibrium. This excess of chemical free energy due to non-equilibrium phase fraction is one of the major driving forces for the coarsening observed. The XRD analysis on layers in the top region as shown in Table 7.1, clearly reveals a gradual transition in phase composition of α2 towards equilibrium. At around 10^{th} layer, α_2 phase composition becomes 10, which is closer to equilibrium. This observation is plotted as in Figure 7.26.

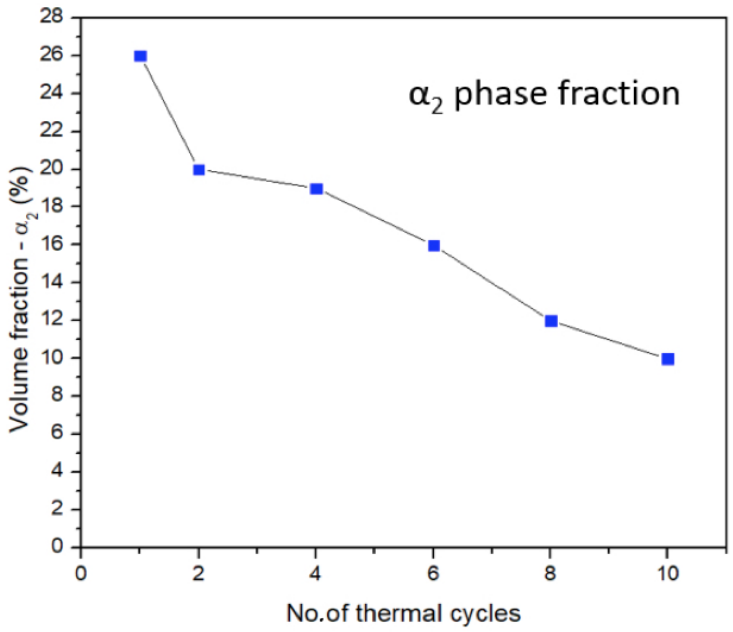

Figure 7.25: α_2 phase fraction variation in top layers along the build direction.

Phase fraction of α_2 and γ phases calculated by SEM image analysis, also shows a similar trend as in XRD observations. This is plotted in a bar diagram, as shown in Figure 7.26. A decrease in α_2 phase fraction is observed, from layer 1 to layer 10. As evident in XRD plot, sample contains α_2 phase composition of around 30 in PLS and is clearly out of equilibrium. After cyclic heating and associated DC reaction, phase fraction of α_2 reduces and becomes closer to equilibrium value i.e., 6.

Along with high phase fraction of α_2 in top layers, supersaturation of aluminium in α_2 is also clearly evident from the EDS analysis of α_2 lamellae along build direction. Fournelle first stated that the solute supersaturation after solidification is an important driving force for DC [92]. Soon after solidification, the solute concentration is far from equilibrium. $\triangle G_C$ calculation is

difficult due to the non-availability of exact phase diagram for ternary TiAl alloy. Local chemical compositional change due to the very dynamic nature of melt pool and aluminium evaporation during EBM process also makes the $\triangle G_C$ calculation difficult.

The average Al composition of phases in various layers was analysed and is observed that α2 in PLS is super saturated with Al and has non-equilibrium chemical composition in lamellae. During cyclic heating events, α_2 gets rearranged, Al gets ejected and solute rearrangement occurs. Thus, Al concentration decreases in α_2 and PLS moves towards equilibrium resulting in a more stable structure. To support this argument, EDS analysis (Figure 7.10) shows supersaturation of aluminium in primary lamellar structure and it gradually reduces to equilibrium concentration of 39(at.%) in secondary lamellar structure. Interdiffusion of aluminium can be considered as major impulse for DC reaction in Ti-48-2-2 alloy during EBM.

Together with aluminum supersaturation, high-phase fraction of α_2 makes PLS highly unstable. After DC, the solute content and phase fraction approaches more towards equilibrium state, proving the argument of chemical counterpart in DC driving force.

7.2.1.4 Grain boundary migration

If there occurs a difference in energy level between neighbouring colonies, a pressure gradient arises, which leads to the migration of grain boundaries. Reduction of energy takes place by forming DC nuclei and grain boundary migration into lamellar colony with higher energy. As per the postulations by Livingston and Cahn, normal force applied by lamellae, at grain boundaries can be calculated by [89]:

$$\boldsymbol{F_T} = \frac{2\sigma_{\alpha 2\gamma} Sin^2\boldsymbol{\theta}}{\boldsymbol{\lambda_1}} \tag{7.3}$$

$\sigma_{\alpha 2\gamma}$ gives interfacial energy, λ_1 denotes the inter-lamellar space, $\boldsymbol{\theta}$ gives angle between colony boundaries and lamellas.

Orientation difference in lamellae across grain boundaries, makes the colony boundary under differential pressure [93]. This in turn results in grain boundary migration and DC. Microstructural analysis done, correlates with the hypothesis. Figure7.27 shows Lamellar colonies, LC-1 and LC-2 are oriented at right angles to each other, and the reaction front in both discontinuous coarsening reactions, DC-1 and DC-2, grows into lamellar colony 1, outlining the grain boundary migration well.

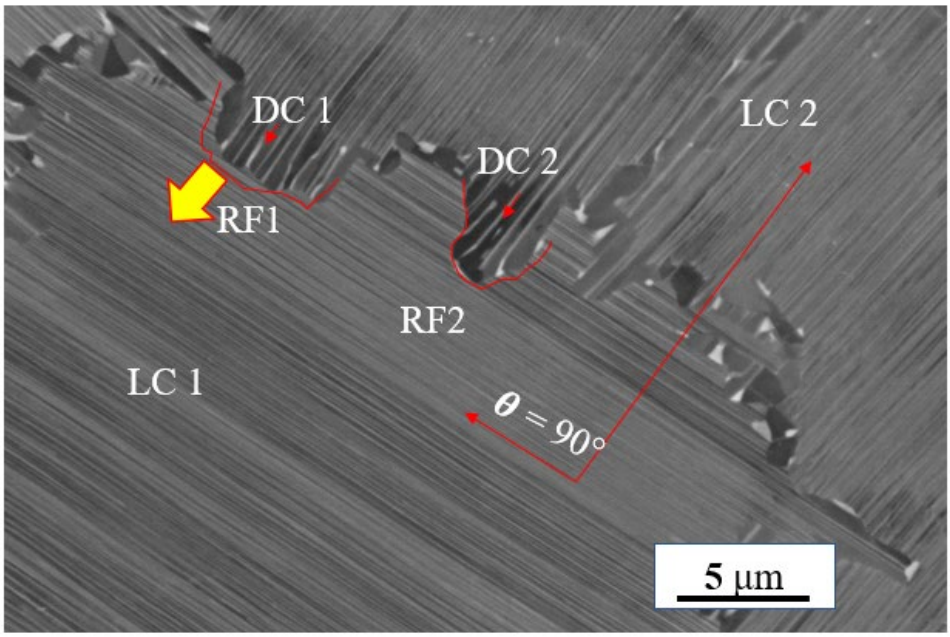

Figure 7.26: SEM image showing grain boundary migration in PLS which are at 90 degrees angulation.

Although the lamellar orientation causes relative pressure set up on the grain boundary, correlation could not be formed between DC nucleation and lamellar orientation. Cyclic heating leads to a greater number of defects and these defects. These defects can act as nucleation for DC along the colony boundary and inside the colony. Figure 7.28 shows DC development in lamellar colonies which are at different angulation than 90 degrees.

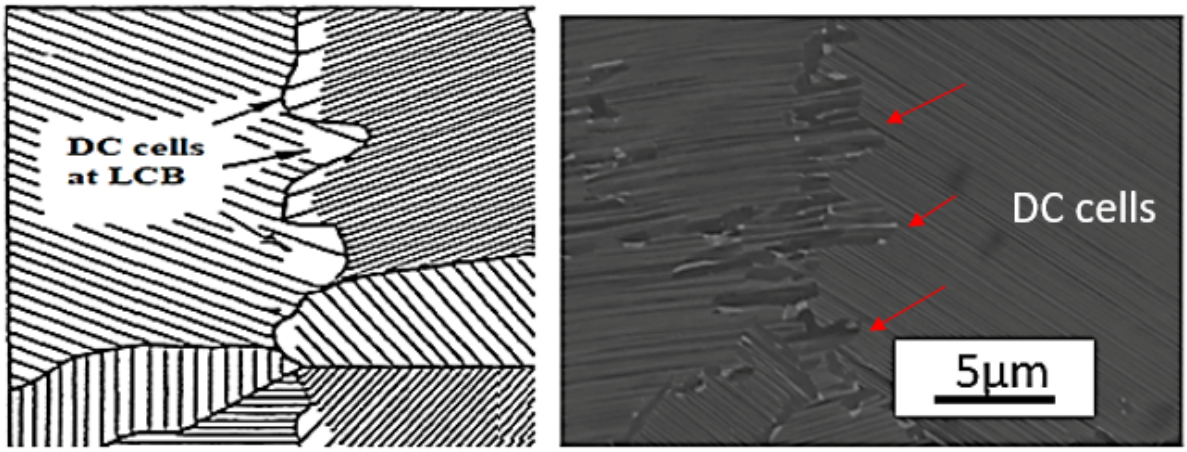

Figure 7.27: Schematic showing the DC development, shows comparison with SEM micrograph.

7.2.1.5 Effect of in-situ cyclic heating on DC reaction

It was reported in literature that, DC observed in TiAl alloys during cyclic heat treatments in the (α+γ) phase-field. In works done by Yang et al. [94], cast samples were solution heat treated in the single phase α region and then quenched. Repeated cyclic heating of this quenched TiAl in the furnace with short holding time, led to discontinuous coarsening.

During successive cyclic heating in EBM process, sequence of temperature cycles with peak value close to the melting point (decreasing in intensity with every additional layer) initiates DC reaction. DC nuclei are formed at the original colony boundaries and within original colony grains. Lamellar orientations in cells are different from those in adjacent grains. In the next cyclic heating, these nuclei extend into nearby grains, become coarsened small colonies and grow at the expense of primary cells. During each consequent heat cycle, these coarsened colonies grow, and new DC nucleation occur simultaneously, within the primary structure. DC takes place concurrently at primary lamellae and at the newly formed coarsened DC cells as well. However, due to the finer lamellar arrangement, DC is predominantly occurring at primary lamellae. This is schematically represented in Figure 7.29. This process repeats and as number of cycles increases, the phase fraction of coarsened lamellae colonies also increases. When the original FL structure was completely replaced by the DC structure, the lamellar spacing became large. Thus, further DC appeared difficult. Figure 7.32 shows a schematic representation of DC reaction.

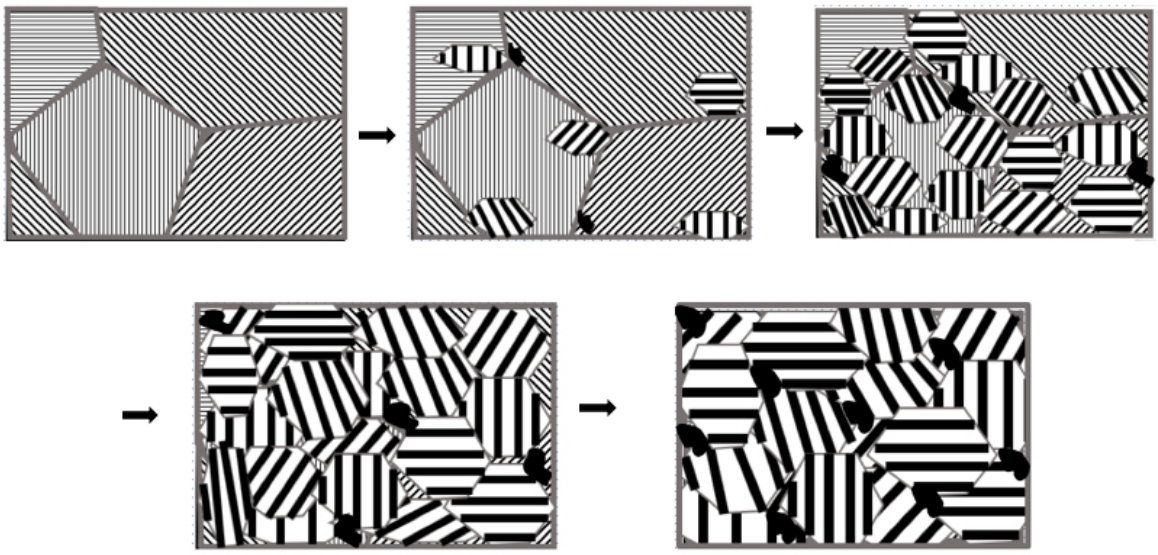

Figure 7.28: Schematic representation of DC reaction in TiAl during EBM

In order to interpret and explain the solid-state transformation during the in-situ heat -treatment at EBM, schematic of the thermal cycles is estimated at a particular point during EBM printing. Numerical analysis was done using modified Rosenthal equation (Eqn. 6.1) [80] for a moving heat source with a Gaussian profile for calculating the temperature distribution. The approximate temperature profile peak intensities are close to melting point and then reducing in intensity in successive layers.

The temperature profile in Figure 7.30 corresponds to the central points of the sample, which gets in situ heat treatment upon the deposition of top layers. Based on the approximate temperature calculations the solidified layer momentarily taken to single phase α and (α+γ) field in the initial thermal cycle peaks. During the first thermal cycle, $\alpha_2+\gamma \rightarrow \alpha$ transformation takes place. Thus, γ phase start to dissolve. But since the rate of heating is high and holding time in α field is short, undissolved γ phase remains. This undissolved gamma can act as nucleation for DC cell during instantly following cooling path. Simulation did not consider the heat transfer by convection. If convection is also considered more temperature peak can be there in single phase α field. A greater number of in situ cycles result in an increased DC, but the cyclic heating effect after a certain number of layers is not significant to advance DC growth. This is either because of the dismissal of driving force for DC or that there is not enough temperature for DC growth.

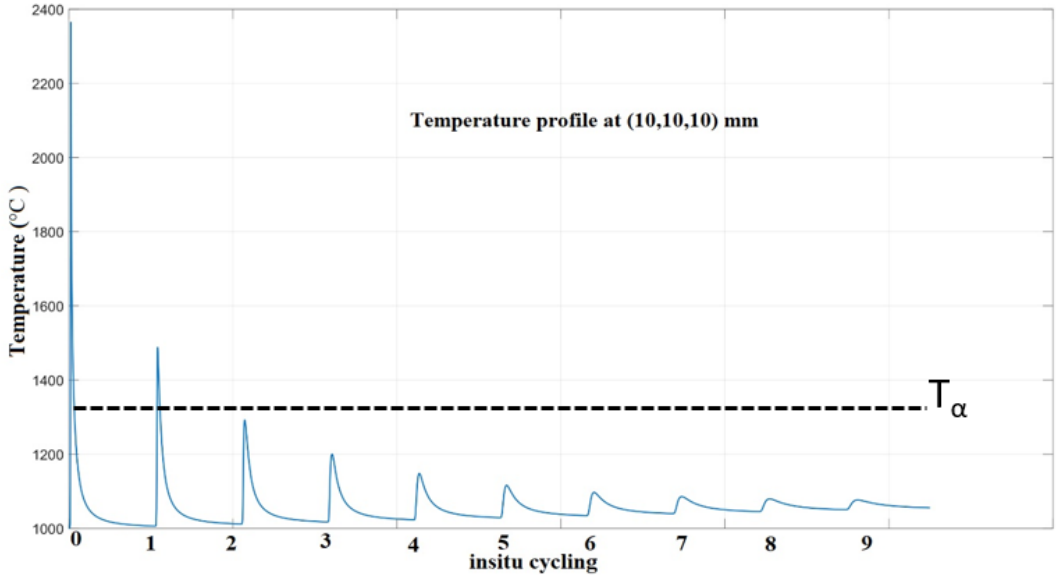

Figure 7.29: Temperature profile of cyclic in situ heating during EBM, by Matlab simulation.

In order to substantiate the in-situ heating effect, the top surface is intentionally heated cyclically using defocused electron beam of known ED. The beam energy selected in such a way that it is not melting the surface and also reducing in intensity in succeeding cycles. The beam parameter for this experiment is given in table 7.3. The heat treatment was done in such a way that it mimics the in-situ heat treatment getting to a particular point in sample by added layers. Peak temperature will be reduced with low energy input [77]. But as there is no option to measure the temperature inside the machine, an approximation based on the Matlab plot was helpful. After each beam application more DC nucleation and growth of DC cells was observed, as shown in Figure 7.13.

It is proven that long-term thermal cycling is prerequisite for DC reaction, rather than thermal exposure at constant temperature. The thermal cycling delivers more driving force for DC as additional α_2 /γ interface free energy is created during in situ cyclic heating. This is attributed to the thermal expansion co-efficient mismatch between α_2 and γ, which creates stresses at interface leading to an increase in interfacial energy.

7.2.1.6 Variation of DC with energy density

Discontinuous coarsening is dependent on energy applied during EBM process. Sample printed with ED 5 J/mm^2 or more showed prominent DC development and growth. For DC transformation to happen primary lamellar formation is inevitable criteria. In low energy sample the primary lamellar formation is incomplete. As we have discussed in chapter 5, medium and low samples are having banded microstructure and in top layers primary lamellar structure formation is incomplete. This is mainly due to higher cooling rate in those samples. In L and M samples, the solidified microstructure tends to be massive gamma. Another point with low and medium energy sample is the lack of enough in situ heating in bottom layers. In Chapter 5 it was explained by lower dilutions with ED and smaller heat affected zone. That was the reason of layered or banded microstructural development and low energy samples.

Another point to discuss is the aluminium concentration change with ED. From ICP analysis, the aluminium concentration of high energy sample is lowest, and this brings the α transus (Tα) temperature lower than low and medium ED samples, as shown in Figure 7.31. This change has an influence during the in situ cyclic heating where peak temperature momentarily reaching Tα. In case of high ED sample there can be more peak temperature values in single phase α field, which in turn intensifies the DC reactions [77, 95].

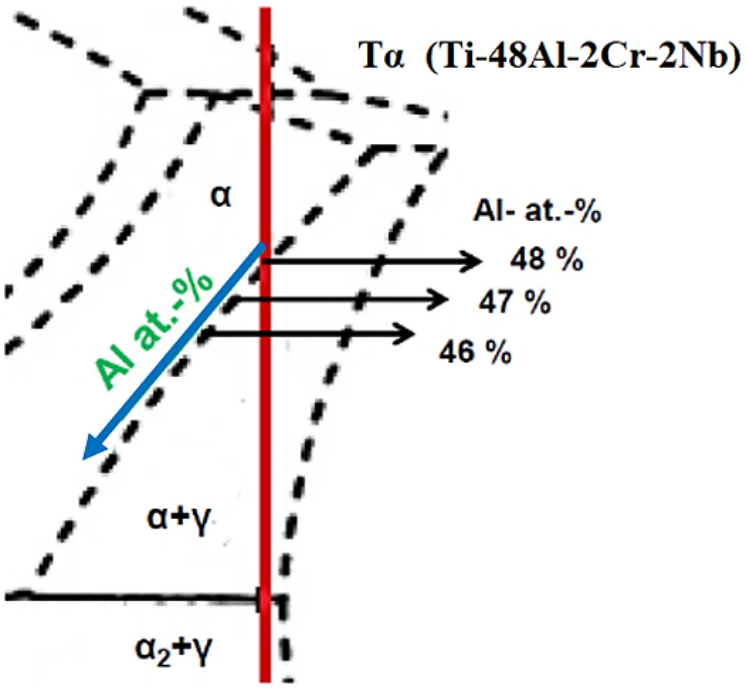

Figure 7.30: Schematic showing effect of energy density on DC [3].

7.2.2 Precipitation of β phase

The second solid-state transformation mechanism observed in EBM process is the α_2 lamellar dissolution, mainly precipitation of β. During EBM process, the high cooling rate results in supersaturation of α_2, creating a non-equilibrium condition, which prompts the system for an α_2 dissolution in order to attain the equilibrium composition. This includes conversion of α_2 to β + γ phase. At 950 °C, precipitation of B2, which is ordered variant of beta (β) phase is reported in TiAl alloys having β stabilizers [96, 97]. As shown in Figure 7.32, presence of an α_2 + γ + B2 region is indicated at this temperature range.

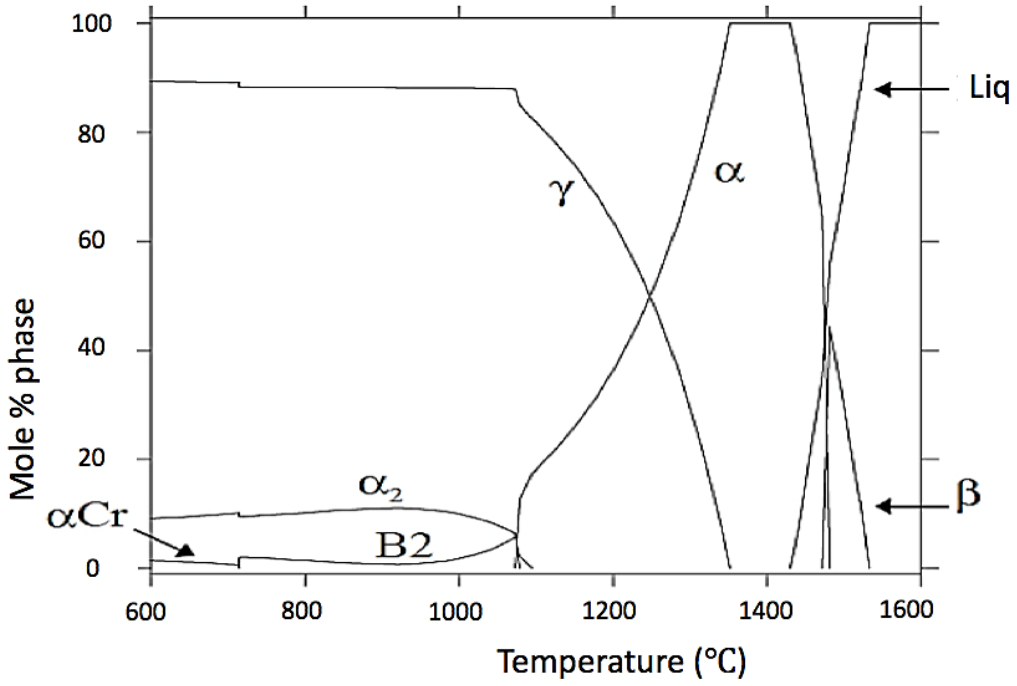

Figure 7.31: Mole % Vs temperature for Ti-47Al-2Cr-2Nb alloy [96].

7.2.2.1 Formation mechanisms - γ + α_2 + β in EBM TiAl

β phase can be formed in two routes in TiAl. Firstly, β phase can be formed as retained beta from high temperature β (through the path β → α+ β → α_2 + γ + β). Second mechanism is through α_2/ α dissolution, (α → α_2 + γ + β). In this study of EBM printed TiAl, β was not observed in primary lamellar structure (PLS). So, the α_2/ α dissolution is the possible mechanism of beta formation in EBM TiAl.

During EBM printing at or above 950 °C, the additional α_2 phase is kept at high temperatures till the build was finished during that time. The β formation in EBM is assumed to be $\alpha_2 \rightarrow \gamma + \beta$ or $\alpha_2 \rightarrow \gamma + \alpha_{2+}$ β. During rapid solidification the α_2 ordering is comparatively faster, but allocation of solute atoms is at non-equilibrium. Volume of chromium and niobium in α_2 is corrected through β precipitation. Another expected beta phase formation route is $\gamma \rightarrow \gamma + \beta$, where excess Cr and Nb of primary γ phase is ejected and forms β phase during in situ aging because of the thermal condition. These two mechanisms are schematically shown in Figure 7.33. In regions where chemical configuration is suitable, β precipitation occurs during printing at 950 ºC or above, since there is enough time and also the energy requirement is met.

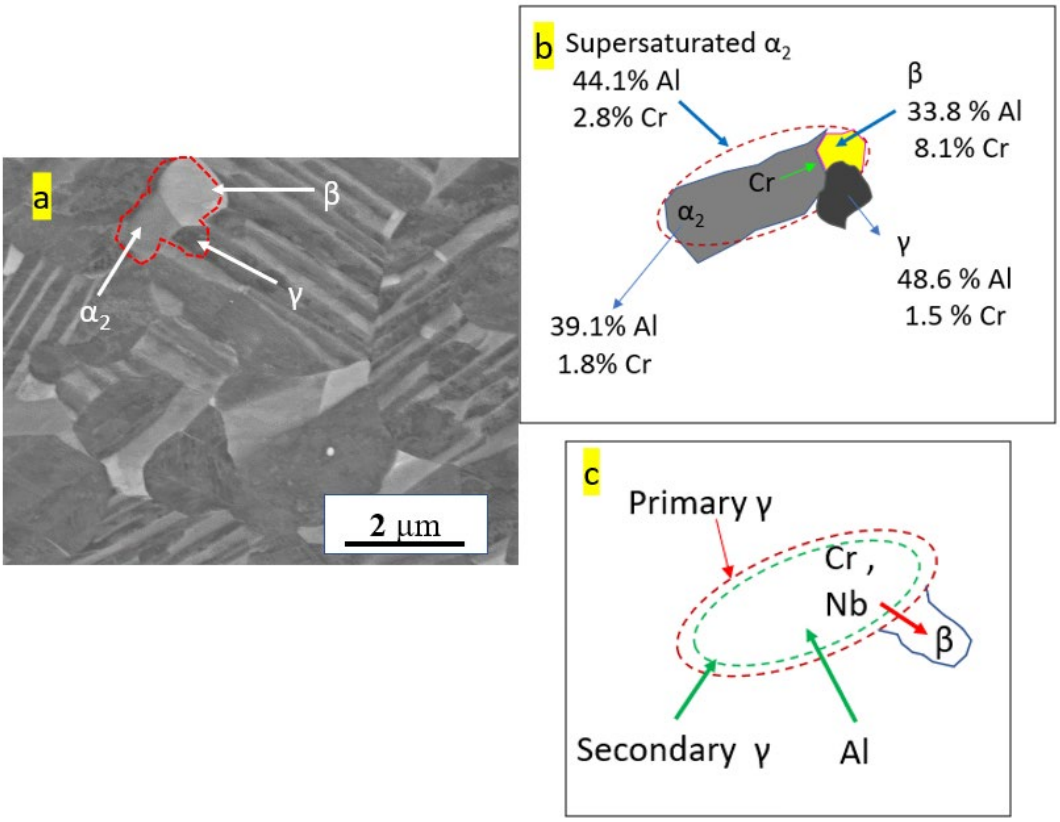

Figure 7.32: Representation of β formation during EBM (a) β phase highlighted (b) schematic of beta formation from α_2 and (c) beta formation from γ.

7.2.2.2 Dissolution of α_2 lamellae

In TiAl, α_2 dissolution to γ and β is mainly influenced by rate of cooling from single phase alpha region. When cooling is sluggish, α gives rise to α_2 + γ lamellar colonies of nearly equilibrium composition. But during rapid cooling as in the case of EBM printing, the phase fraction of α_2 phase is completely out of equilibrium as shown in XRD (Table 7.1). During thermal cycling, removal of excess α_2 is anticipated. β produced at the terminations or inside laths, during α_2 dissolution. This is due to the high solubility of α_2 for chromium than gamma. The partitioning coefficient of Cr in γ /α_2 is around 0.5 when TiAl cooled down from single phase α in air [98]. With high rate of cooling during EBM, γ / α_2 partition coefficient will fall again, resulting in enrichment of chromium to be higher in α_2 than gamma. α_2 of primary lamellar structure contains 44.1% aluminium. α_2 readjusts to attain equilibrium phase fraction by changing to γ phase, but γ cannot contain the entire Cr from α_2, which leads to segregation of chromium and niobium in the vicinity of α_2, as shown schematic, Figure 7.33(b). This in turn gets transformed to β. So, along with γ and α_2, EBM fabricated TiAl contains of β as minor

phase. In second mechanism the excess Cr and Nb from γ can be ejected out and form beta during the in situ aging in EBM that is represented in Figure 7.33(c).

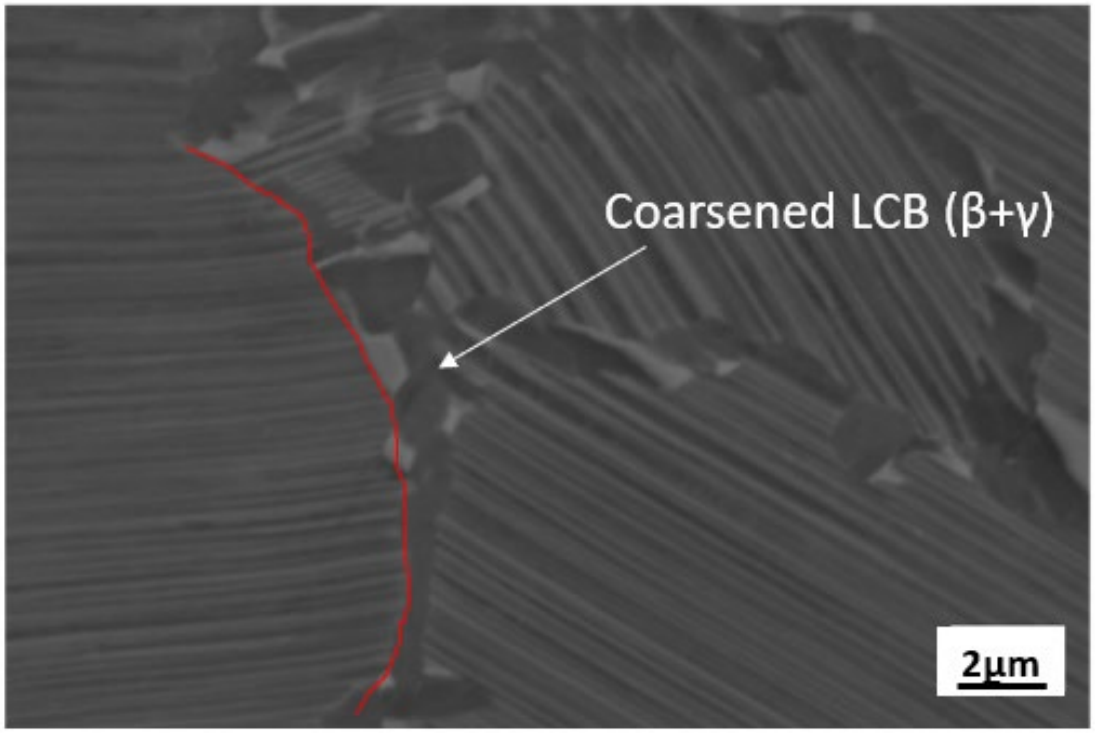

Figure 7.33: SEM micrograph showing LCB coarsening after beta formation.

γ and β precipitation leads to coarsening of lamellar colony boundaries, as shown in Figure 7.34. Coarsening increases with build temperatures and cyclic heating. The beta formation also affects lamellar colony size and discontinuous coarsening. The presence of beta along LCB can restrict the grain growth and in beta rich areas, smaller colony size was observed. Since β small grain can act as a nucleation site for DC cells, DC is also affected by beta formation.

7.2.3 Hardness variation during DC

DC causes a reduction in hardness value which can be related to increased lamellar thickness and decrease in colony size. Also, since α_2 is harder than γ [99], the higher phase concentration of α_2 in upper layers also will contribute to the increased hardness in upper layers. As DC proceeds, α_2 fraction decreases and subsequently hardness decreases.

Upper layers, which contain primary lamellar structure with finer interlamellar space, possess higher values of microhardness. This can be linked to the equation 7.4, showing relationship of the microhardness and the lamellar spacing, which is reported in literature [99].

$$\boldsymbol{H = H_{V0} + k\lambda^{-0.5}} \quad (7.4)$$

where H is microhardness, $\boldsymbol{\lambda}$ is lamellar spacing, H_{V0} and k are constants. Based on this relation, hardness increases with decrease in lamellar thickness. This explains higher microhardness explained in upper layers.

7.3 Summary

Sample made with ED 5 J/mm^2 or more showed prominent discontinuous coarsening. DC during the EBM process of Ti-48-2-2 at build temperature 950 ºC, resulted in a relatively homogeneous composition throughout the sample. DC resulted in coarsened lamellae with smaller colonies. In high energy sample with ED 6 J/mm^2, after getting 10-12 in situ cyclic heat treatment, the primary lamellar structure was completely replaced by coarsened secondary lamellar structure. The average coarsening ratio was found to be 18.6 and around 67% reduction of colony size was observed.

The microstructure of the primary lamellar structure is unstable due to the high interface energy attributed by the fine lamellae and the system tries to decrease the interfacial area in order to reduce the interfacial energy. In addition to that, system tries to reduce excess chemical free energy in PLS by achieving near equilibrium chemical composition and equilibrium phase fractions of various phases. These PLS instabilities cause grain boundary migration and undergoes discontinuous coarsening. Thus, major driving forces for the discontinuous coarsening are provided by these two factors.

In AM process, the temperature of each previously solidified layer can be raised in situ. This "in-situ heat treatment" is unique in additive manufacturing process and can be exploited for modifying the microstructure by influencing the solid-state transformations after deposition.

The second solid-state transformation observed in EBM process is the precipitation of β (ordered β) phase through dissolution of α_2 lamellae. Formation beta phase is influenced by ED and build temperature, showing a linear relationship. The beta formation has a significant influence on the lamellar colony size and discontinuous coarsening. Lamellar colony size found to be reduced in beta rich areas.

Chapter 8: Comparison of TiAl microstructural evolution- EBM versus LENS and Alloy modification specific to AM.

Processing condition in different AM techniques directly impacts the final microstructure of manufactured TiAl parts. Microstructure, in turn, influences the mechanical properties of the material. AM is generally associated with solid-state transformations (SST) and has both positive and negative effects on microstructural and mechanical properties. So, understanding and controlling different SST's in AM is very critical. Chapter 7 discussed in detail about the DC and decomposition of PLS in EBM at different processing themes and observed to have a critical role in microstructural evolution. Information on DC in different AM methods is needed for a better understanding and its control in AM process in general. So, DC studies in LENS will help to understand and control DC in EBM and vice versa. The main objective of this chapter was to compare SST in LENS and EBM and in turn, to understand SST in AM processed TiAl in general. Comparable microstructural development in terms of DC could be observed in high energy samples fabricated by both EBM and LENS and so, those samples were mainly focused. Alloy modification specific to AM was tried, in order to investigate the methods by which DC could be controlled in AM. Results suggested that Si has an effect on DC and no efforts were made to optimise the AM process for the modified alloy.

8.1 Results

8.1.1 Fabrication of nearly dense gamma TiAl samples using LENS

For the stability of LENS process defocused laser beam was used for printing. Figure 8.1 shows single melting tracks from the "fine" focus (about 0.6mm buried below start plate or about ½ a turn of focus adjusting wheel) to positive and negative defocused laser beams. An additional 3 clockwise turns, giving about total defocus about -4.45 mm was applied, which means buried distance was about 4.45 mm in the powder bed. The fine focus set nominally on the build plane will give an extremely high-power density that will lead to plasma, and will basically cause a hole in the substrate. Tests were conducted with the laser defocused 3.81mm above and below the deposition plane, which doubled the laser beam diameter to 520 μm. To guarantee a stable deposition process and good bonding with bottom layers, focus suggested to be below the deposition plane and so, the -3.81mm approach was selected.

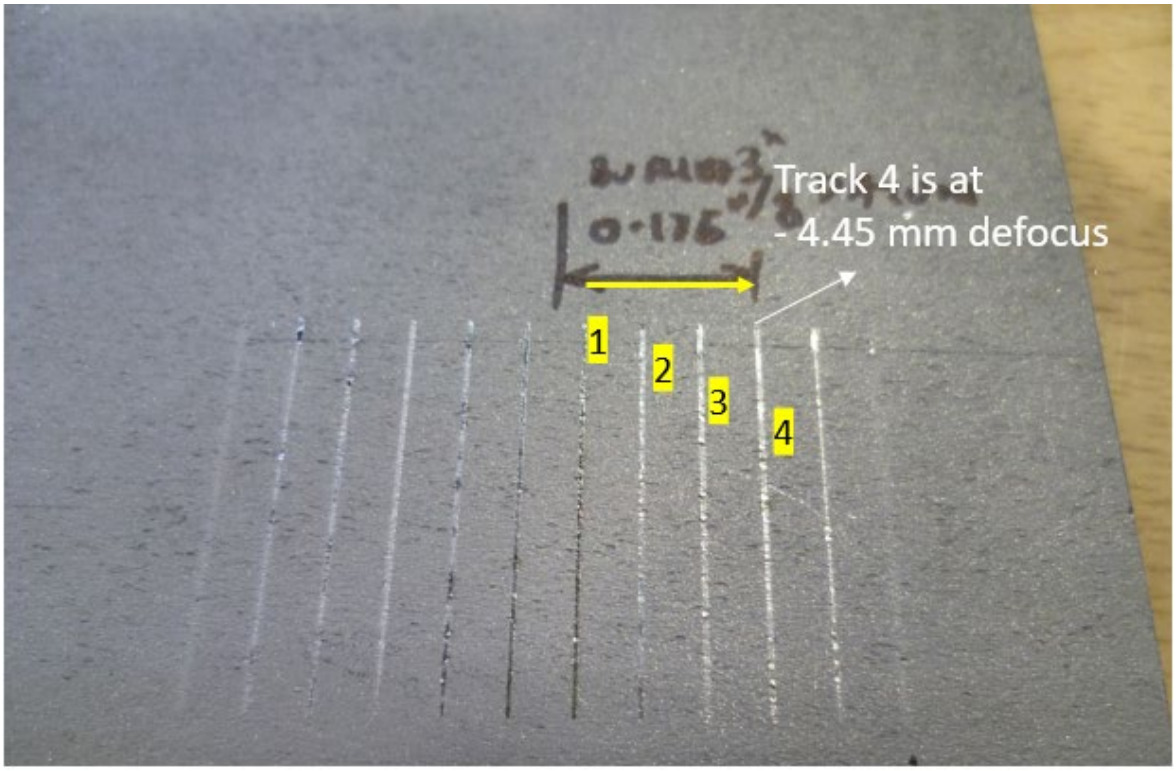

Figure 8.1: Result of LENS focus test for TiAl printing showing focused and defocused single tracks. The marked melt line 4 printed at -4.45 mm defocus (buried distance).

Mainly laser power and scanning speed are responsible for the output quality of LENS printed samples. The deposition parameters used in this study are shown in Table 8.1. These parameters were selected based upon the literature and as suggested by equipment manufacturer. Since EBM samples exhibited characteristic microstructural evolution when high energy was used, LENS samples were mostly printed at higher energy.

Table 8.1: Process recipes used in LENS TiAl printing.

Sample	Laser Power (W)	Scanning speed (mm/sec)	Focus offset (mm)
1	300	15	+ 3.81
2	350	15	+ 3.81
3	250	15	On focus
4	P300	15	- 3.81

5	P350	15	- 3.81

As suggested by the equipment manufacturer, hatch spacing was selected as 280 µm and layer thickness as 280 µm, since the laser spot diameter of the machine was 520 µm at the selected focus setting.

Samples of 6*4*50 mm dimension were deposited on Titanium plate. The schematic of the sample (Figure 8.2) shows build direction and the shaded section shows the plane along the build direction, where microstructural analysis was done.

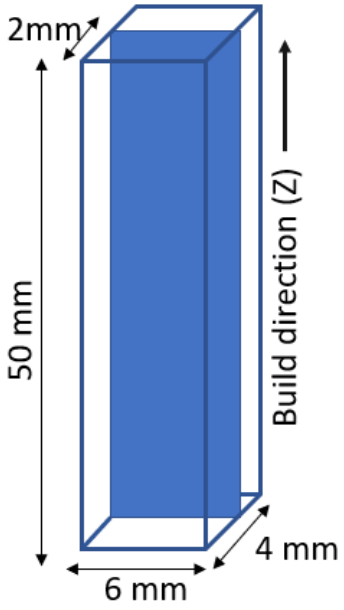

Figure 8.2: Schematic of the sample section which was selected for microstructural study.

8.1.2 Phase constitution and microstructure of as fabricated LENS sample

The microstructure of the as-printed sample was studied along the build direction, using different characterisation tools mainly optical microscopy, SEM and XRD. Optical micrographs of LENS TiAl samples along build direction are shown in Figure 8.3. High cooling rate and track-by-track manufacturing method of the LENS processing are the main influencing factors for the microstructural characteristics of as-printed Ti-48-2-2.

Unlike EBM, substrate heating is not done in LENS, which causes high cooling rate and thereby makes TiAl samples more prone for cracking [5]. A solution to mitigate this issue is by retaining heat in the samples while printing. This can be achieved by the proper geometrical selection for samples, by printing thin samples with smaller cross-sectional area. In this study, sample dimensions in XY plane were kept small, so that, less time will be taken for the laser beam return and that will help more heat to be retained in the sample. Heat accumulation eventually take the sample temperature near the deposition to close-to or above the brittle-ductile transition, thereby cracks can be avoided [68].

The geometry is a critical factor in LENS printing to maximise retained heat in the sample and thus higher temperature and to highlight this effect, samples were printed as shown in Figure 8.3. The microstructure showed significant variation with difference in cross-sectional area. In this study, in the top region, where dimensions were half of that of the main block and where more heat was retained, the microstructure was much more lamellar and well developed, as shown in Figure 8.3 c. Microstructure appears to be fine and feathery for the larger block as shown in Figure 8.3 d, where cross sectional area is more.

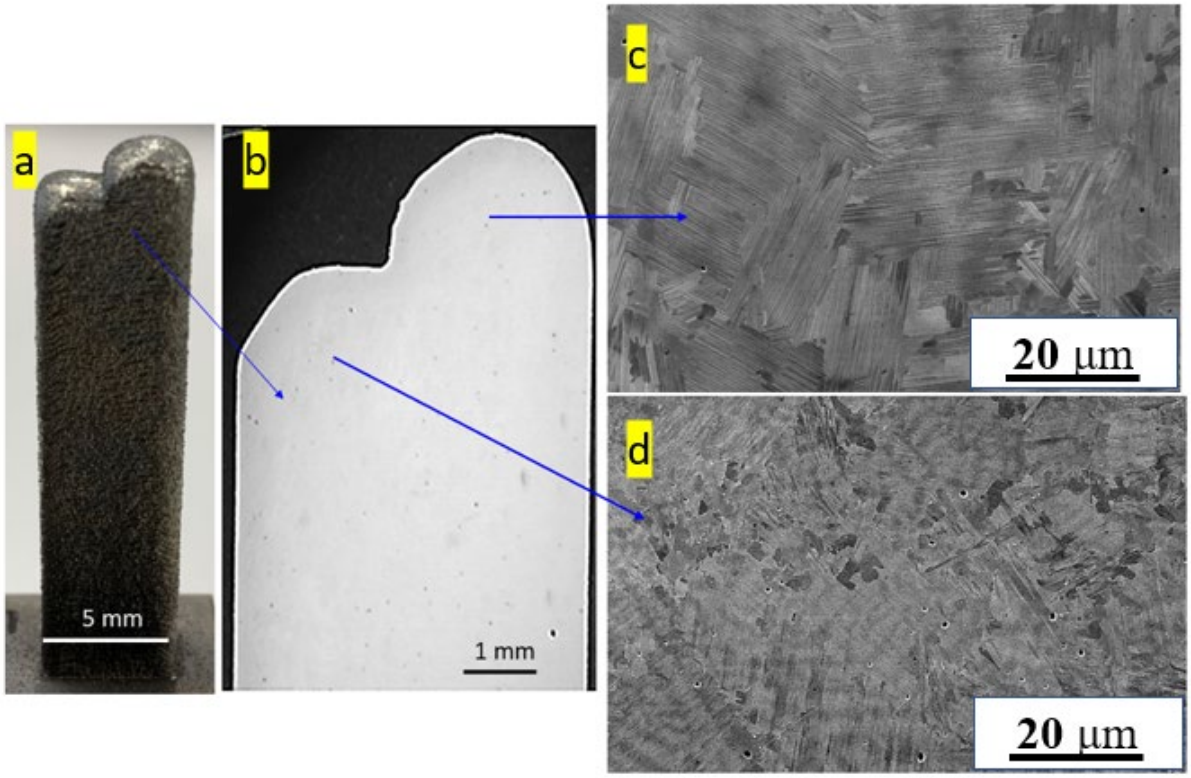

Figure 8.3: Micrographs of LENS TiAl samples (a) as - fabricated sample (b) Optical image from top region (c) SEM image from smaller area and (d) SEM image from larger cross-sectional area.

8.1.2.1 Microstructure at different laser energy input

From Table 8.1, two samples were selected for comparison. Samples P300 and P350 were printed at laser power 300 and 350 W respectively. Both samples were printed at 15mmsec^{-1} scanning speed and focus +3.81mm buried. The higher power sample, P350 showed lamellar microstructure, as shown in Figure 8.4a. P 300, which is the low power sample, showed duplex microstructure, as in Figure 8.4b.

Coarsening was mainly observed in P350 samples and were used for investigating microstructural evolution during LENS. Microstructural observations in LENS high energy samples were comparable with high energy (H) samples printed using EBM, in terms of DC and secondary lamellar formation.

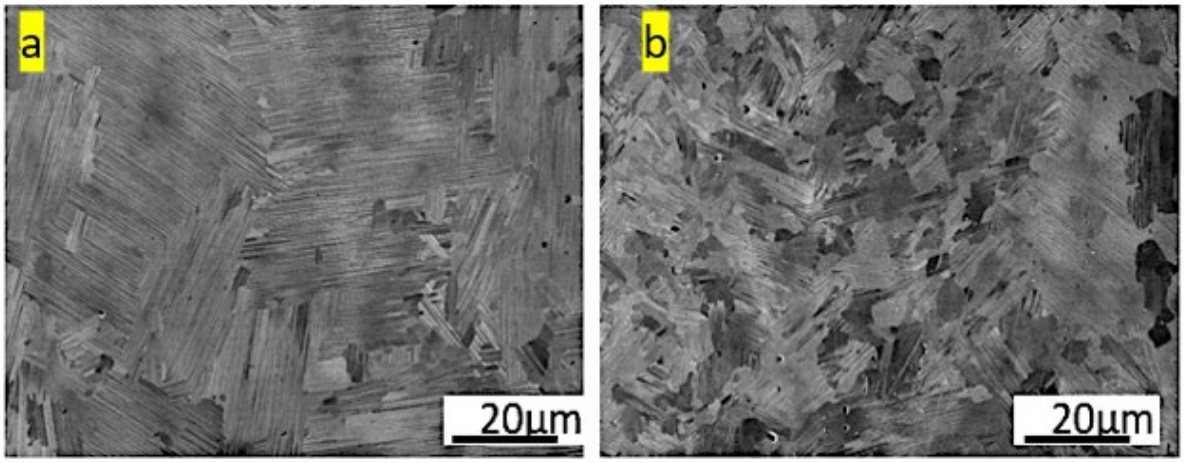

Figure 8.4: SEM micrographs showing comparison between two TiAl LENS samples, printed at different powers (a) P350 (b) P300.

8.1.2.2 XRD

The XRD patterns from the middle of as-printed sample at laser power 300 and 350 W is shown in Figure 8.5. Both samples mainly consisted of α_2 and γ phases. Characteristic planes of γ (110), (111), (200), (202), (311) and α_2 (200), (201) and (202) were clearly visible. There was no indication of the existence of β phase in XRD and SEM analysis. The α_2 phase fraction was observed to be higher in P300 sample, as at lower heat input the cooling rate will be higher and higher cooling rate will leave more α_2 at non-equilibrium condition.

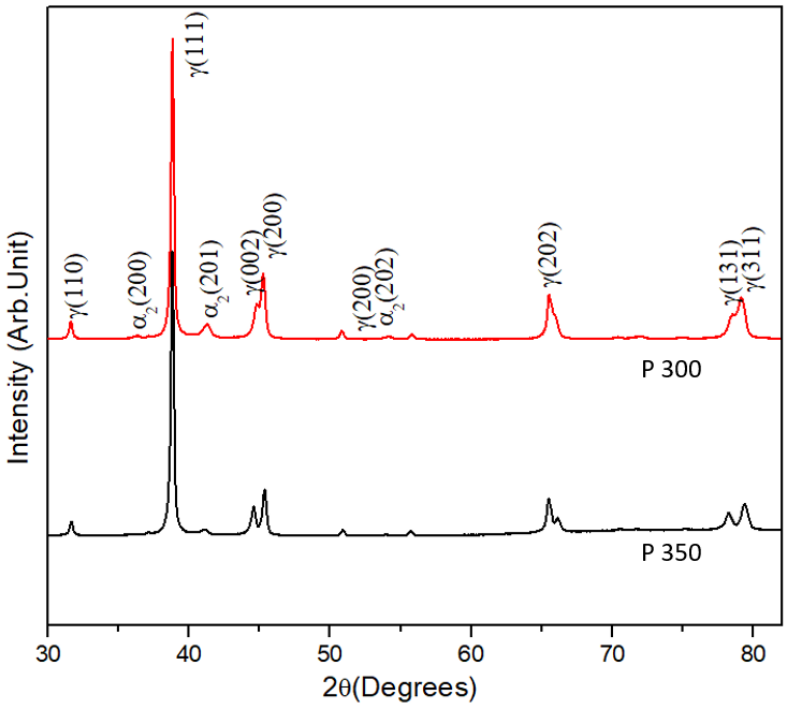

Figure 8.5: XRD patterns from the middle of as-printed LENS samples, printed at laser power 300 and 350 W.

8.1.2.3 EBSD analysis

The EBSD analysis of central portion of P350 LENS sample with band contrast map is shown in Figure 8.6. In the phase map shown in Figure 8.6 (b), the α_2 was not identified by the EBSD detector, mainly due to the off- stoichiometric composition and associated lattice parameter variations. α_2 appeared as black colour in phase mapping. Pole figure (Figure 8.6 c) showed random orientation of lamellar colonies which was similar to the EBSD observation in EBM TiAl sample. In EBSD analysis also, beta phase was not identified, supporting the XRD analysis.

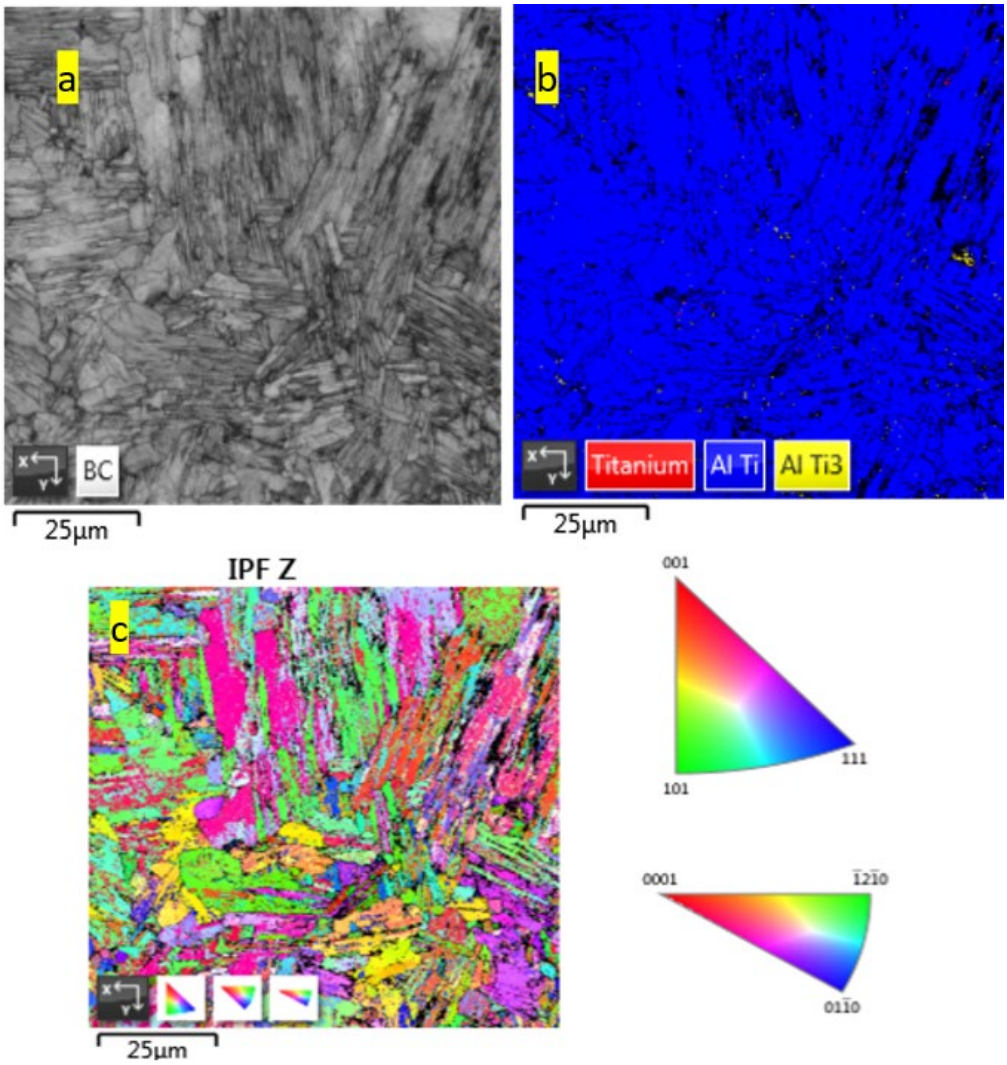

Figure 8.6: EBSD analysis of the central portion of high energy LENS samples (a) Band contrast map (b) Phase map and (c) Pole figures.

8.1.2.4 Chemical composition of as-fabricated LENS sample

The chemical composition (by ICP analysis) of the as-fabricated LENS P300 and P350 samples are shown in Table 8.2. LECO analysis showed minimal pick up of oxygen. Compared to EBM, LENS samples did not show any significant aluminium evaporation, as in case of EBM, the evaporation of highly volatile Al was enhanced by high vacuum environment.

Table 8.2: ICP analysis of LENS TiAl P300 and P350 sample (at.%).

LENS sample	Ti	Al	Cr	Nb	O
P 300	48.8 ± 0.4	47.4 ± 0.4	1.6 ± 0.1	1.8 ± 0.1	0.4 ± 0.01
P350	49.7 ± 0.4	46.7 ± 0.4	1.5 ± 0.1	1.8 ± 0.1	0.3 ± 0.01

8.1.2.5 Primary lamellar structure

The primary lamellar microstructure (PLS) of P350- high energy sample is shown in Figure 8.7. The microstructure showed dendritic morphology similar to the structure observed in gas atomised powder. In the inset the magnified view of PLS is given. The top layer appeared to be solidified dendritically and at inter-dendritic regions, where Al segregation could be observed in EDS line elemental analysis, as shown in Figure 8.7.

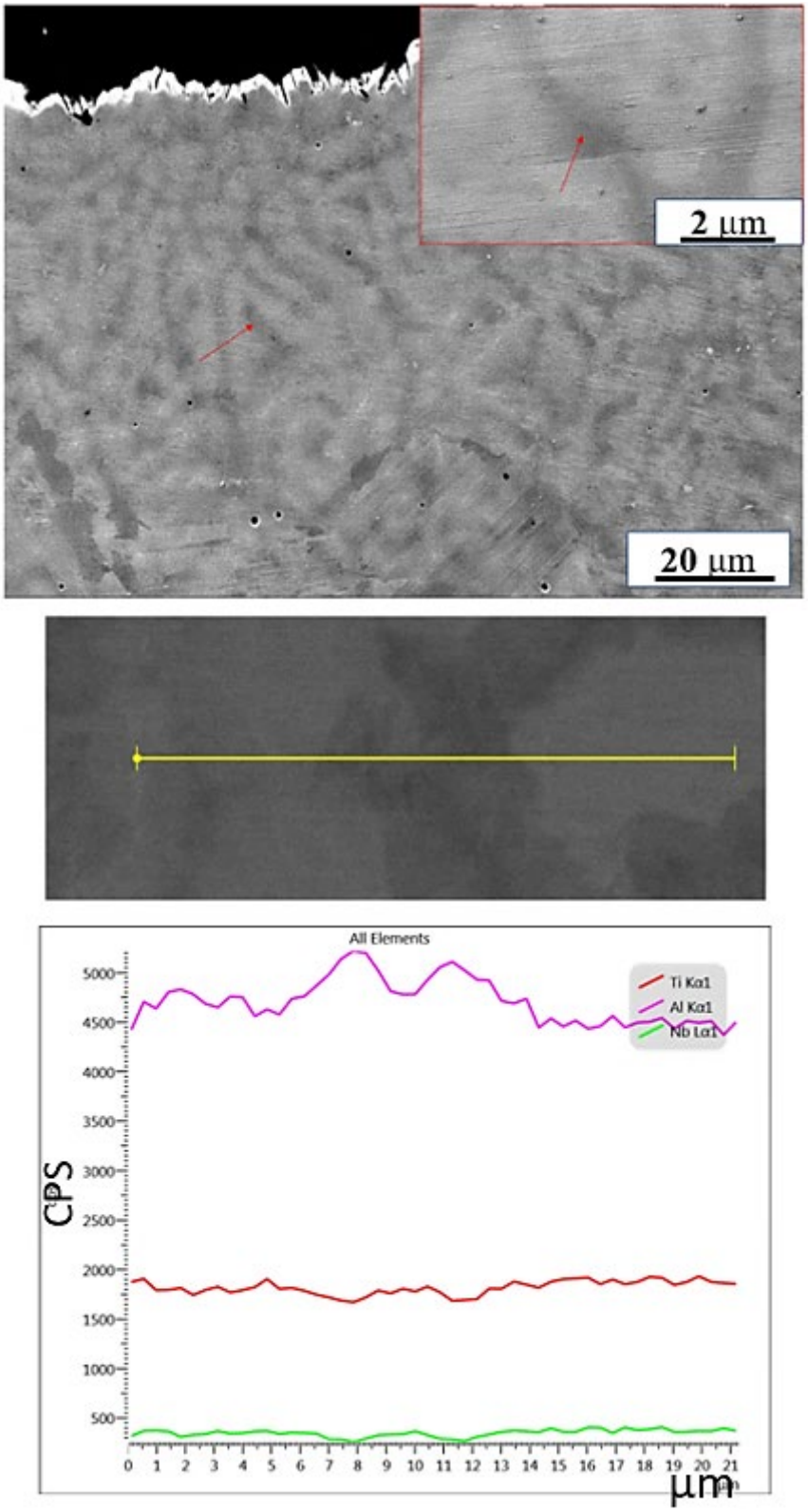

Figure 8.7: (a) SEM images of primary lamellar structure of P350 sample, inset shows high magnified SEM image of PLS. (b) EDS line elemental analysis of LENS samples showing Al segregation at inter-dendritic regions

8.1.2.6 Discontinuous Coarsening (DC) in LENS

Because of thermal cycling, solidified layers in the bottom undergo coarsening. PLS was gradually replaced by secondary lamellar structure (SLS) because of the discontinuous coarsening during printing process. Microstructure from layers 4,6,8 and 12 are shown in Figures 8.8 (a), 8.8 (b), 8.8 (c) and 8.8 (d) respectively.

Figure 8.8 (a) shows primary lamellar structure, being developed from the dendritic microstructure. Figure 8.8 (b) shows two small DC colonies and as shown in Figure 8.8 (c), DC colonies were more prominent and bigger. DC cells are highlighted in the micrograph. In Figure 8.8 (d), PLS was completely replaced by a secondary lamellar structure, after DC.

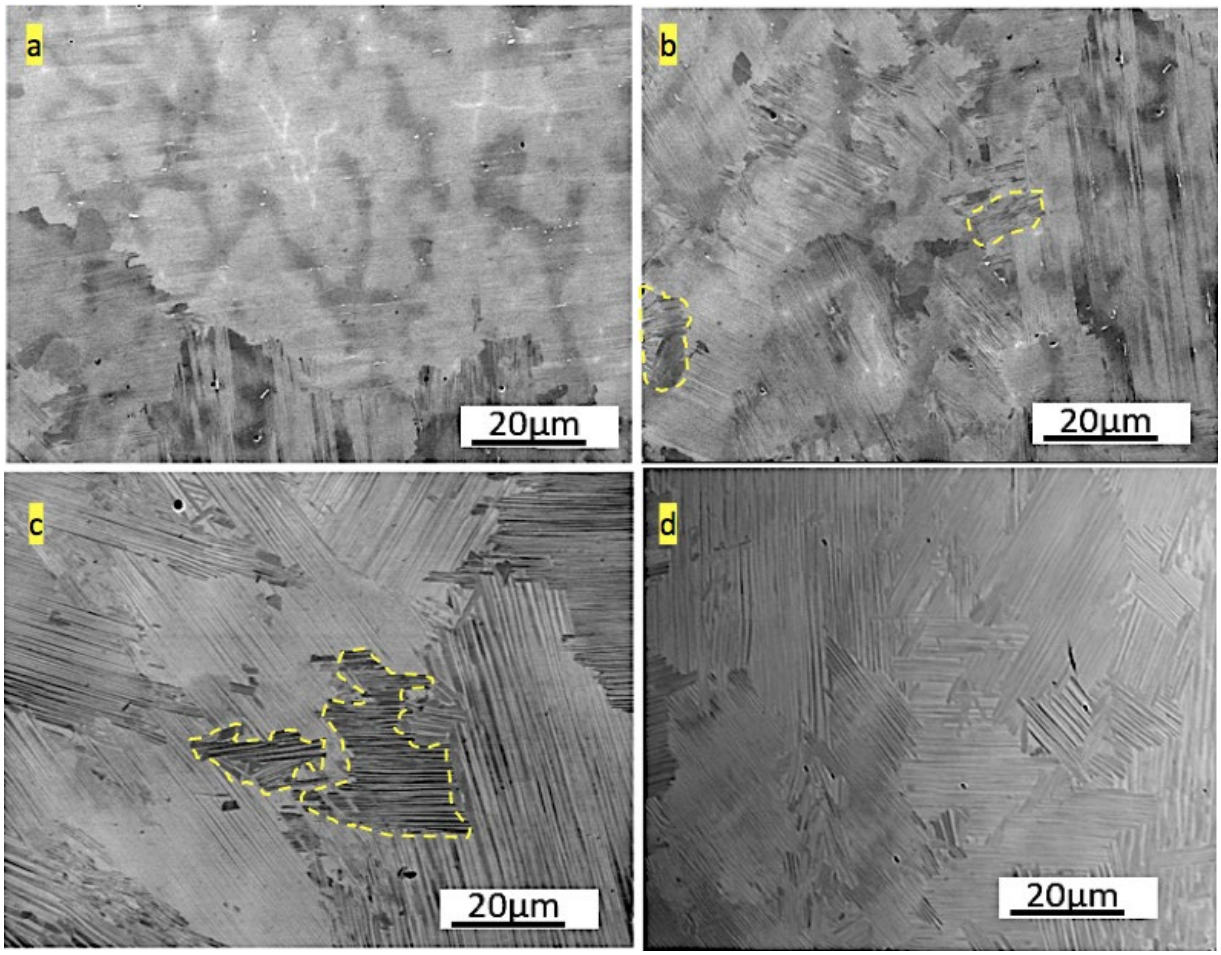

Figure 8.8: SEM images showing discontinuous coarsening in LENS TiAl sample. (a), (b), (c), and (d) shows microstructure from 4,6,8 and 12 layers, respectively.

8.1.3 EBM Microstructure Vs LENS Microstructure

Microstructure from the central portion of as fabricated LENS (P350) and EBM (H) samples were analysed to compare the evolution of DC. In Figure 8.9 (a) LENS sample shows bigger colonies. Lamellar coarsening was observed to be higher in EBM sample, as shown in Figure 8.9 (b). β phase was observed in EBM sample, which could not be seen in LENS sample. Major differences in microstructure are enlisted in Table 8.4.

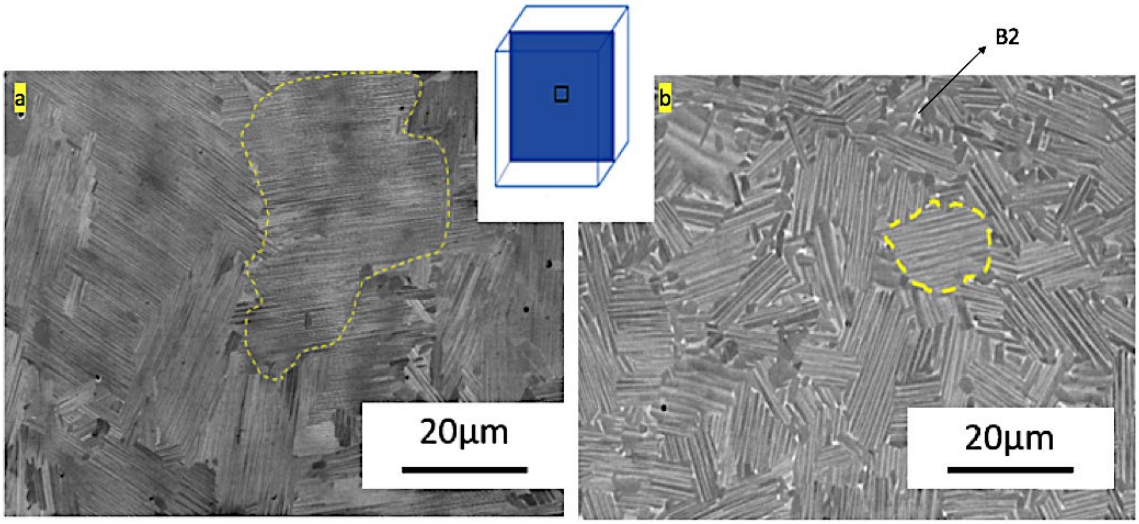

Figure 8.9: (a) and (b) shows SEM micrographs of as fabricated LENS (P350) and EBM (H) samples, respectively.

Table 8.3: Comparison of EBM and LENS fabricated TiAl microstructure.

Microstructural feature	LENS sample	EBM sample
Colony size	Larger	Smaller
Interlamellar space	Finer	Coarser
Presence of beta phase	Absent	Present
Coarsening ratio (r)- α_2	~7	~14.3
Coarsening ratio (r)- γ	~10	~20

Coarsening ratio (r) = Secondary lamellae thickness / Primary lamellae thickness

8.1.4 Effect of silicon addition

The Ti-48Al-2Cr-2Nb powder composition was modified with an addition of 0.5(at.%) Si. Pre-alloyed powder was made by gas atomisation. EBM sample was printed at ED 6 J/mm^2 using Ti-47.5Al-2Cr-2Nb-0.5Si. The top layer microstructure is shown in Figure 8.10(a). DC at layers 4,8 and 12 shown in Figure 8.10(b), Figure 8.10(c) and Figure 8.10(d) respectively. DC was observed to be limited to a smaller extent, in samples printed with modified alloy. Further process optimisation is required to confirm this. With modified alloy, more beta phase was observed as seen in Figure 8.10(c) and Figure 8.10(d). The EBM printing condition was not optimised for new alloy.

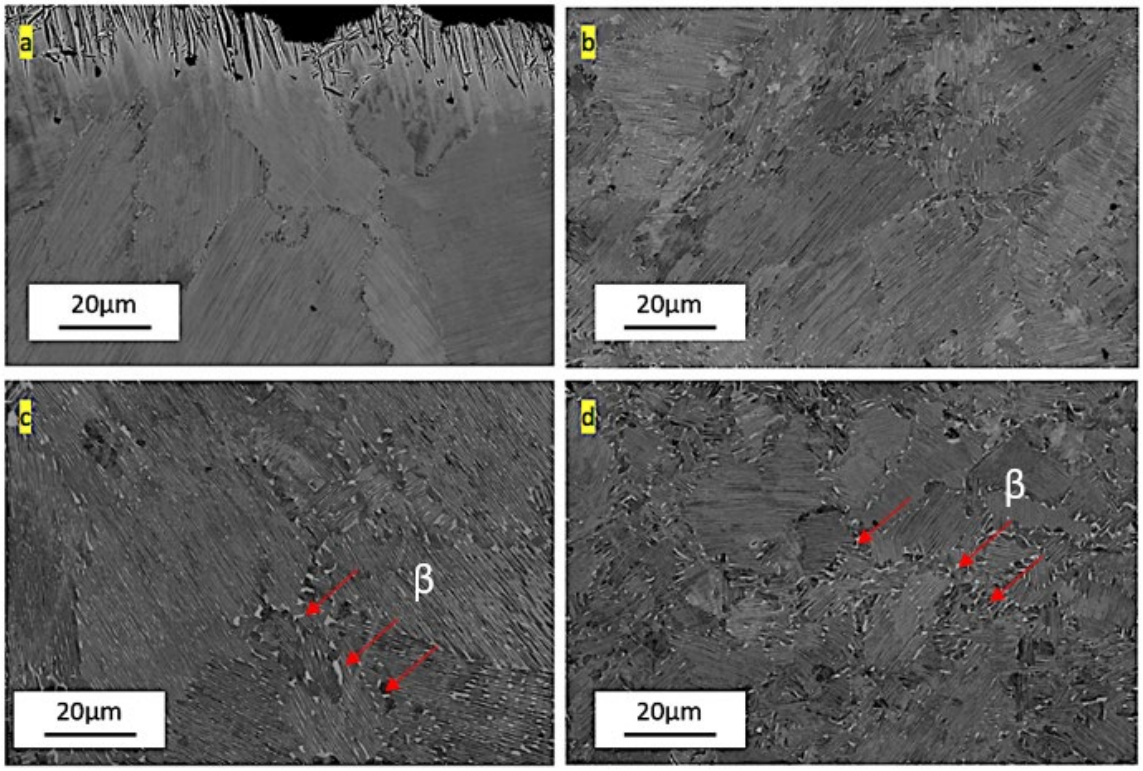

Figure 8.10: SEM micrographs of various layers in EBM sample, fabricated using modified Ti-47.5Al-2Cr-2Nb-0.5Si alloy. (a), (b), (c), and (d) shows microstructure from layers 4,6,8 and 12, respectively.

High magnification SEM BSE images are shown in Figure 8.11. A detailed microstructural study of the modified alloy composition was not done. Presence of Si precipitate and reduced lamellar coarsening was observed, compared to Ti-48Al-2Cr-2Nb alloy. Si precipitates observed in lamellar colonies, are highlighted by arrows in the inset micrograph.

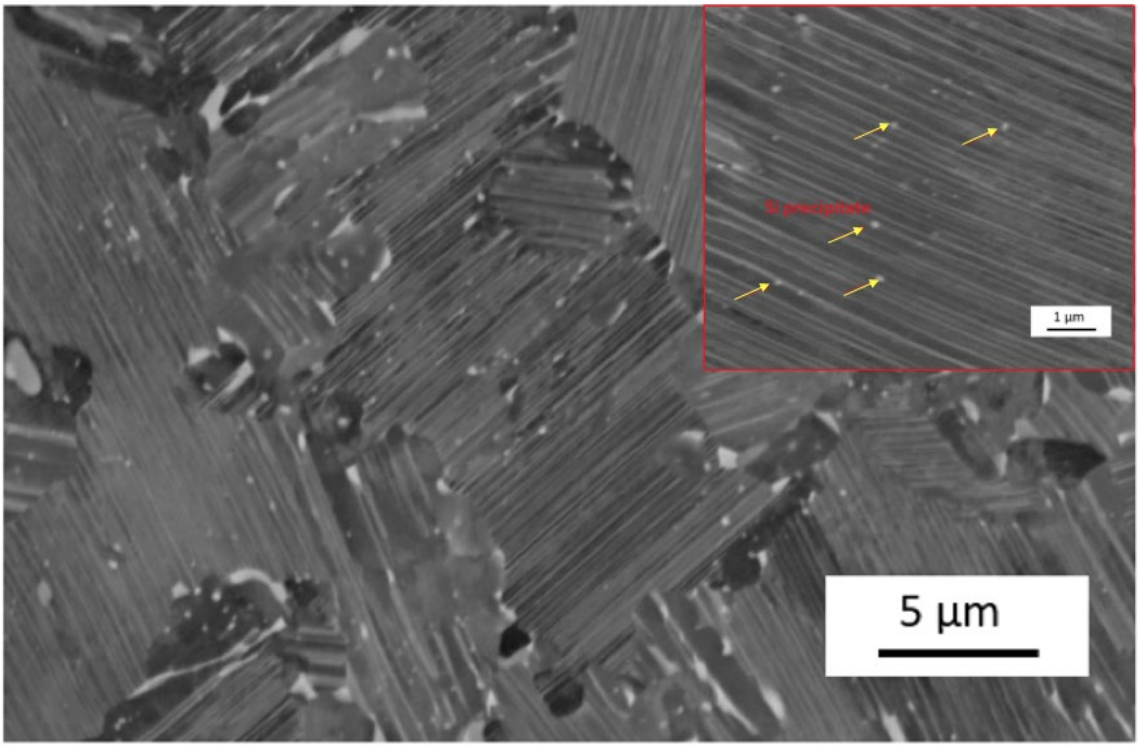

Figure 8.11: SEM BSE image of EBM microstructure, fabricated using modified Ti-47.5Al-2Cr-2Nb-0.5Si alloy. Inset shows Si precipitates in lamellar colonies.

As shown in Figure 8.12, EDS analysis from the precipitate particle showed Si segregation of 4.9 at.%. As this precipitate size is smaller than the resolution of EDS analysis, actual Si % is expected to be much higher.

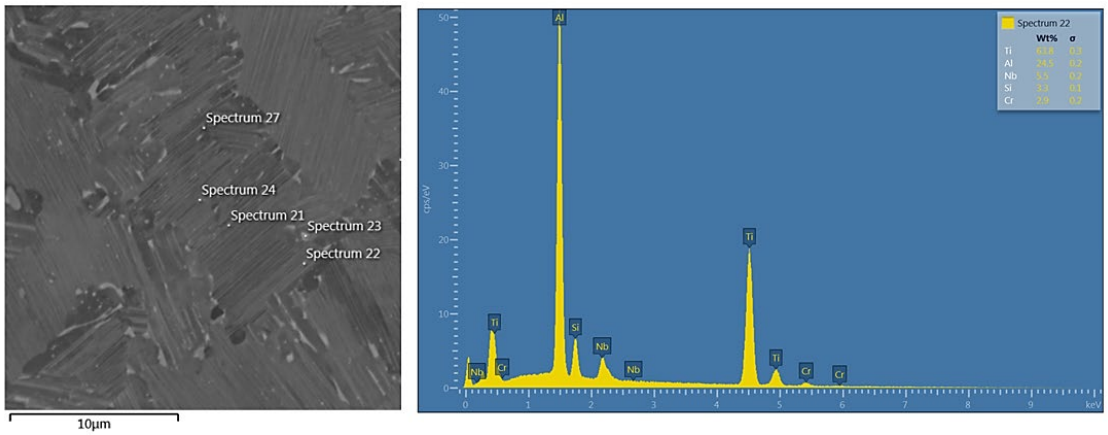

Figure 8.12: EDS analysis of Ti-47.5Al-2Cr-2Nb-0.5Si sample.

8.2 Discussion

8.2.1 Effect of LENS process parameters on microstructural evolution

Variation in scan speed and laser power will significantly influence the cooling rate. So, microstructural development and phase composition are dependent on these parameters. LENS samples showed finer lamellae when compared to EBM, due to the difference in cooling rate. Through downward conduction and forced convection by Argon shield gas flow, heat gets dissipated from melt pool in LENS which makes LENS cooling rate much faster than that of EBM [5]. α_2 phase fraction has a linear relationship with cooling rate. So, α_2 fraction of TiAl was high in LENS process, where rapid cooling is incorporated.

When comparing LENS P300 and P350 samples, the heat input to the P350 sample was higher. It created bigger melt pool and higher melt pool temperature. The relationship of cooling rate and lamellar formation discussed in the chapter 6, could be applied in this condition as well. Lower cooling rate in P350 sample produced lamellar morphology when compared with the duplex microstructure in P300. Characteristic observations could be made in specially designed samples, with small cube on the top of the block. As printing area got reduced in each layer, return time of the laser head to a particular X-Y point was also reduced. This helped to retain some heat from the previous scan and produced an upsurge in melt pool temperature with addition of each layer, until an isothermal temperature was attained at a certain height. This isothermal temperature was closer to or above the ductile-to-brittle transition temperature, which explains minimal cracks in LENS fabricated TiAl samples [5, 68].

As shown in Figure 8.13, red-hot temperature achieved in sample was studied with a schematic of heat affected zone, qualitatively drawn. Arrows in the figure indicates that heat is dissipating in all directions. As observed in the schematic, heat accumulation in upper layers influenced other solidified layers underneath. Solidified bottom layers were expected to take to single phase α phase filed or (α+γ) region [77], causing solid-state transformations.

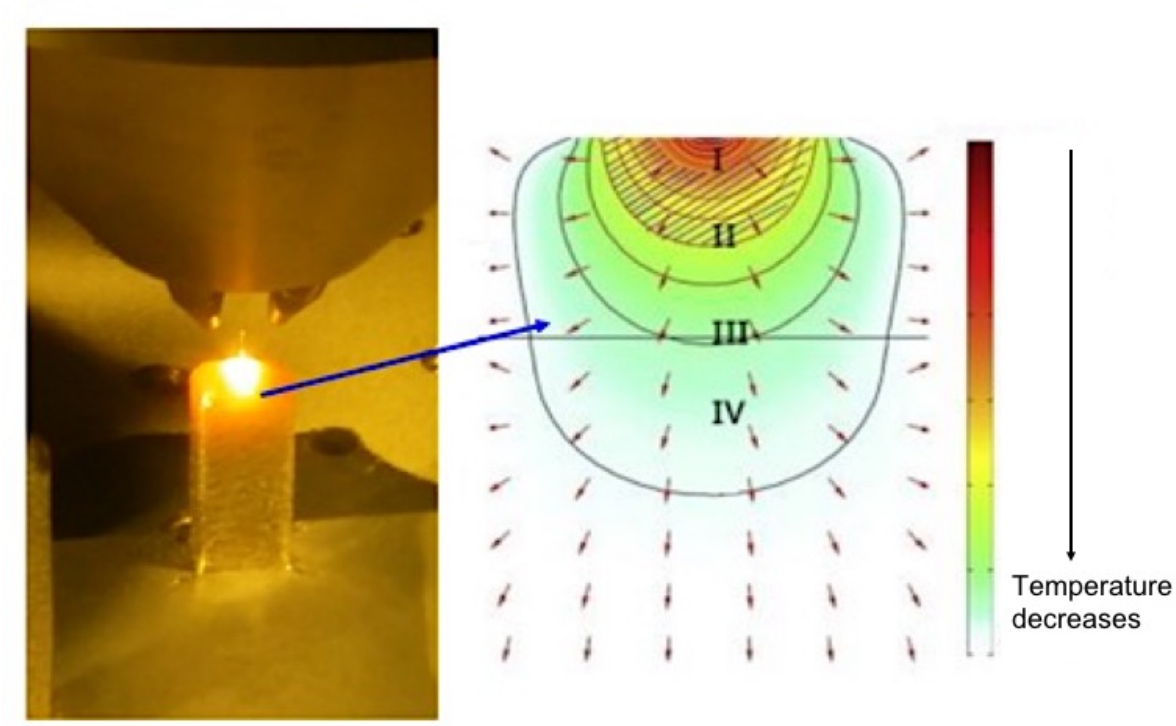

Figure 8.13: Schematic of heat affected zone during LENS process.

8.2.2 Comparison of solid-state transformation in LENS and EBM fabricated samples

Difference in build temperature is the most important factor which differentiates EBM from LENS. EBM build temperature is higher than that of LENS and is almost equivalent to insitu aging being done during EBM printing. If LENS is carried out under higher build temperature and slower cooling situations as in EBM, top layers of LENS samples will show microstructural features more towards nanolamellar structure, than usual dendritic microstructure of LENS, based on G/R ratio. Temperature gradient (G), solidification rate (R) and cooling rate (T) are interrelated in such a way that T= GR, and these can be changed according to the variations in heat input and interaction time. Changes in G/R and GR regulates microstructural characteristics. Increased GR produces fine microstructures on solidification [100]. In case of LENS the temperature gradient (G) and cooling rate (R) is higher than EBM and resulted in finer microstructure [5].

To get higher temperature, sample size should be small so that the heat accumulation can be higher. This possibility was observed in small cube geometry made in LENS. The high laser

power and high scan speed also helped in PLS formation as there was retained heat accumulation and provided some preheating effect. Thus, $\alpha_2 + \gamma$ lamellar microstructure of Ti-48-2-2 could be printed by LENS.

The difference in microstructural development and cooling rate for EBM and LENS process leads to significant difference in morphologies, lamellar coarsening and mechanical properties of samples. Due to higher cooling rate in LENS, the last melted region exhibited dendritic microstructure. After one to two heat cycles, dendritic structure changed to form nanolamellar microstructure. It could be correlated with the study conducted on gas atomised powder by Guyon et. al. [101], where SEM observation of the particle shows the dendritic nature of solidification during atomization. On further heat treatment of gas atomised TiAl powder to 850 °C, it was revealed that the lamellar structure evolution takes place in steps: a nano lamellar transformation occurs first, on further heating it changes to near lamellar or duplex microstructure. A similar observation could be made in TiAl samples fabricated by LENS. The top layers dendritic solidified microstructure changed to primary lamellar and then to secondary lamellar structure during in situ cyclic heating.

On top layer deposition during printing, temperature in bottom solidified layer is expected to be taken to single phase α and α+γ phase region for a short time and then cooled down [77]. The process was repeated during printing, simulating a cyclic heat treatment. The schematic diagram for this treatment is presented in Figure 8.14. During the first stage of treatment, effects of interdendritic microsegregation were removed and the initial alloy microstructure was homogenised. On subsequent cycles, PLS was replaced by a coarsened lamellar structure. Comparison between EBM and LENS manufactured TiAl samples revealed finer lamellar space in LENS samples, with an average of ~75 nm interlamellar space on SEM microstructural analysis. Coarsening in LENS sample was around 35% lesser than that of EBM sample. The higher cooling rate and the lower peak temperatures during thermal cycles in LENS caused these variations.

EBM required a vacuum environment in order to inhibit interaction of electron beam with environmental gas, which was not a requirement in case of LENS. The operational atmosphere for the EBM process is basically a high vacuum of $<10^{-2}$ Pa [5, 102]. Feeding helium to the build chamber during the melting process is beneficial for avoiding the charging of the powder particles. But in case TiAl printing the “He” flow is detrimental to maintain the higher

temperature so only very less “He” flow was maintained. Vacuum environment protected high reactive TiAl from being oxygen contaminated. At the same time, evaporation of highly volatile Al was enhanced by vacuum environment of EBM, producing corresponding observations in microscopy.

In LENS TiAl microstructure, there was no beta precipitation observed. Based on the understanding from literature two reasons are anticipated [59, 97].

(1) Due to Aluminium evaporation, instead of solidifying mainly through the α phase, the solidification pathway is switched to the Ti-rich side of the peritectic reaction and there can be retained β due to rapid solidification in case of EBM. In LENS, ICP analysis showed negligible Al evaporation, which was attributed by argon printing environment. According to the binary phase diagram of Ti–Al, β phase does not exist as an equilibrium phase. On the other hand, in the quaternary Ti–48Al–2Cr–2Nb phase diagram at certain thermodynamic conditions, β phase is reported [97].
(2) It was observed that process temperature also had an important role in the formation of β phase. The high build temperature which was measured at bottom stainless steel plate using a thermocouple attached to it. Preheating conditions in EBM causes in situ aging round ~1000 °C and this aging is causes β precipitation. Increasing preheating or increasing energy density has a secondary effect of increasing the in-situ aging temperature. Studies by Fang et.al. reported that during long-term thermal cycling, the lamellar microstructures tend to undergo significant microstructural degradation, including the coarsening of lamellar colony boundaries and precipitation of the beta particles and with increasing the aging temperature from 900 to 1000 °C the beta precipitation was also reported as increased [98]. β phase formation was not observed in LENS and it was considered to be due to the lack of preheating condition. It is expected that β phase formation can be controlled during EBM, by reducing preheating temperature or by reducing the ED.

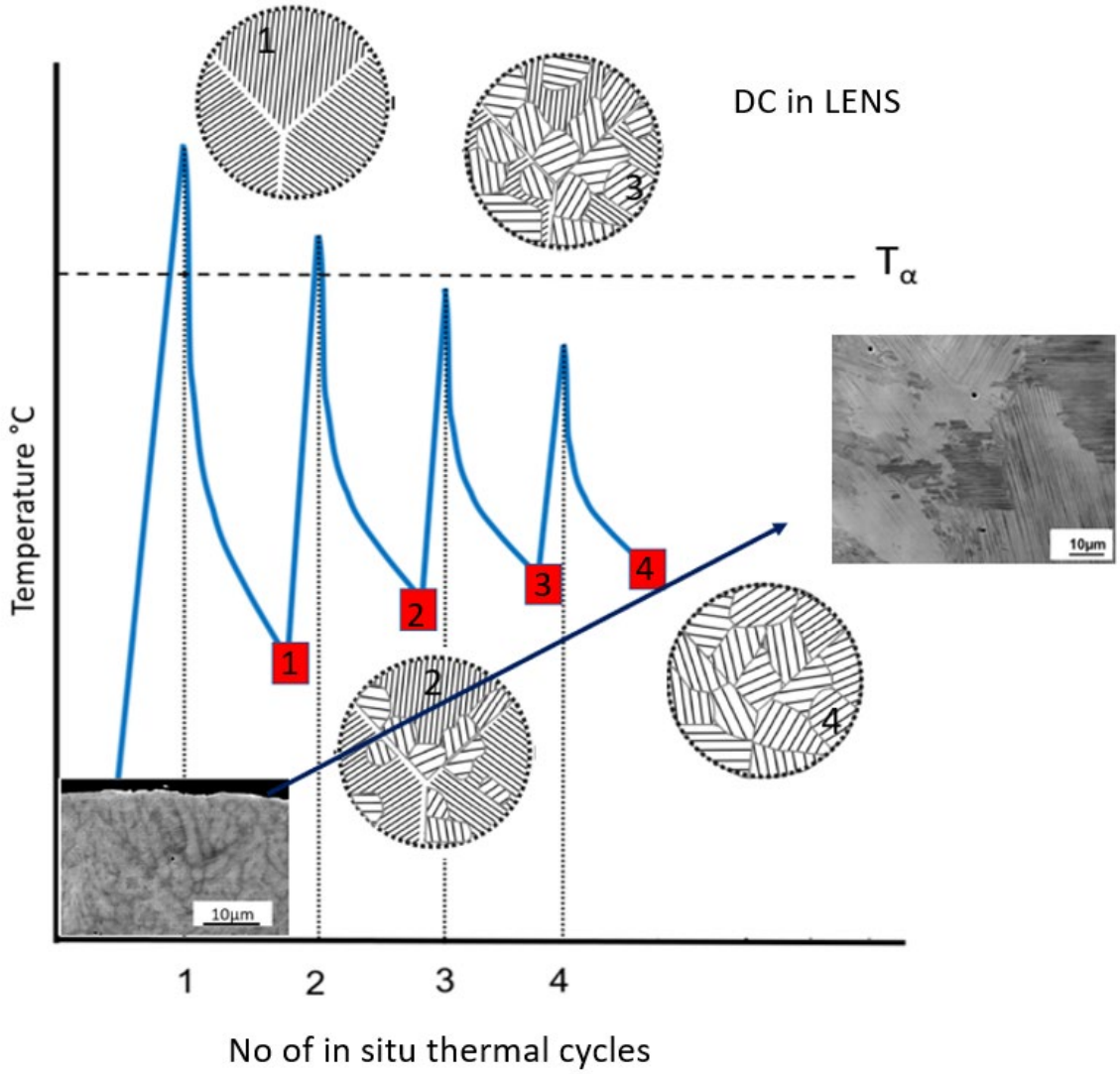

Figure 8.14: Schematic illustration of DC in LENS – The dendritic structure on solidification changes to primary lamellar structure and then undergoes discontinuous coarsening.

8.2.3 Alloy modification: Alloy design based on LENS/EBM Solid-state transformations studies

As discussed in chapter 6 and 7, Discontinuous coarsening takes place in both EBM and LENS manufacturing technologies. In EBM, coarsening appeared to be high whereas colony size was getting reduced. On the other hand, during LENS manufacturing, coarsening was comparatively lesser, but colony size was higher. Based on literature [3], better mechanical properties are attainable at the combination of decreased coarsening and reduced colony size, as represented in Figure 8.15. Arrow means from left to right DC takes place, correspondingly colony size decreases and lamellar spacing increases. Decreased colony size accounts for better

ductility and fine lamellar spacing provides high temperature strength and creep properties [3]. In contrary to the combination for betterment of properties, DC causes a decline in the colony size but individual lamellar spacing increases.

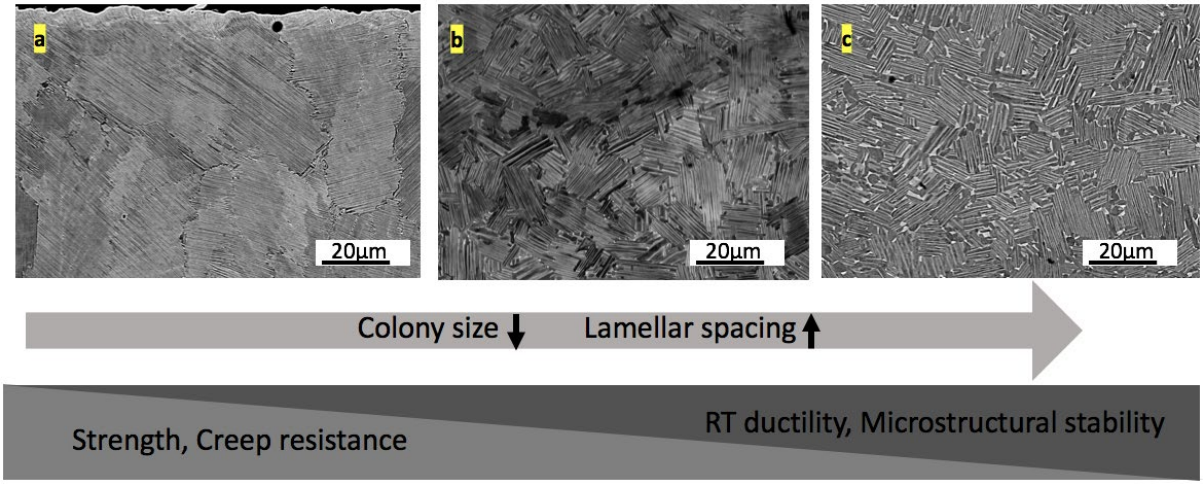

Figure 8.15: Illustration of the motivation for TiAl alloy development specific to AM. (a) primary lamellar colonies (b) partially coarsened lamellar colonies and (c) secondary lamellar colonies after DC.

The coarsening process of the EBM manufactured TiAl alloy can be altered based on the mechanical property requirement. It is noted that the finer lamellar observation in LENS was attributed by its higher cooling rate. The one possible way of getting higher cooling rate in EBM is by decreasing the build temperature, without affecting the process stability. When electron beam applied to a powder bed, the peak temperature of the melt pool was raised from the preheat temperature, which was the baseline. When reducing the build temperature, superheating of melt pool reduced and temperature gradient between melt pool and bottom layers is high leading to faster cooling rate and to a finer microstructure [69]. On printing TiAl at 1050 ºC and 950 ºC, decrease in individual lamellar coarsening could be observed in 950 ºC, proving this assumption. The difficulty in using this method to reduce the coarsening in EBM, is the process instability at lower temperatures. During EBM, a build temperature, minimum of 950 ºC is needed and if temperature is reduced further, arc trip arises due to the inadequate sintering of powder bed. There is a need of technology improvement in AM, mainly to print high temperature material. The maintenance of high temperature in build platform is a crucial aspect of the machine improvement. Also, the existing alloys must be fine-tuned specific to AM.

The other way to produce desired microstructural pattern and corresponding mechanical property improvement is alloy modification. In this experiment, 0.5 Si (at.%) was added with an intention of inducing silicide particle precipitation in lamellae. Tsuyama et al. [103] concluded that a range of 0.5 ~ 1 at.% Si added to TiAl is effective in creep property enhancement alongside the emergence of Ti_5Si_3 precipitate phases. Silicide prevents the coarsening of individual lamellae by precipitate pinning effect in lamellar interface, thereby causing a decrease in lamellar coarsening. A comparison of coarsening between Ti-48Al-2Cr-2Nb and modified alloy composition is shown in Figure 8.16. The lamellar coarsening was found to be restricted to an extent. At higher magnification, precipitation of silicide particles was observed.

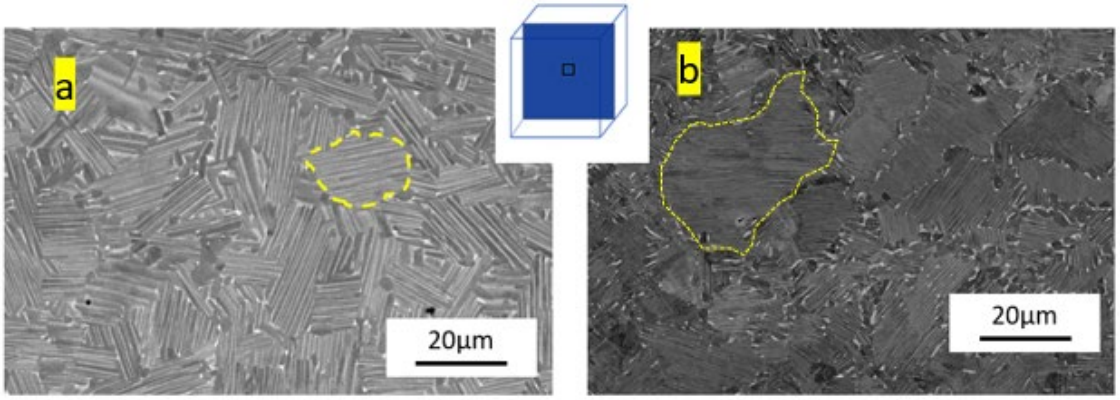

Figure 8.16: SEM microstructure of TiAl samples printed using different alloy compositions (a) using Ti-48Al-2Cr-2Nb and (b) using Ti-47.5Al-2Cr-2Nb-0.5Si.

Even though coarsening was decreased, process optimization of EBM using the modified powder was not an objective of this thesis. Higher phase fractions of β phase was observed in as-fabricated samples. Due to high arc tripping issue, preheating cycles for this modified alloy powder was taken up slowly by ramping up the current to average value. Due to the slow ramping up of current, it took almost double time for preheating of each layer. This extra heating was assumed to be responsible for more beta phase formation in as-fabricated samples. Modification of alloy composition as Ti-47.5Al-2Cr-2Nb-0.5Si was an objective but optimisation of AM process parameter for the modified alloy is not part of the current investigation. The intention was to check whether “Si” precipitate is forming at interlamellar region during EBM process.

8.3 Summary

Main objectives of this chapter were to analyze and compare the microstructural evolution in EBM and LENS fabricated TiAl samples. Alloy modification specific to AM was also explored. Nearly full density samples with minimal defects were fabricated by LENS. Process parameters influenced output quality and microstructural development, mainly power of laser beam and scanning speed.

Through downward conduction and forced convection by shield gas flow, heat got dissipated from melt pool in LENS. Recurrent heating and slow cooling rate experienced by the top part of the sample led to the formation of a lamellar microstructure there.

Temperature gradient (G), solidification rate (R) and cooling rate (T) are interrelated in such a way that T= GR, and these can be changed according to specific blends of power density and interaction time. Changes in G/R and GR regulates microstructural morphological characteristics.

The top layer appeared to be solidified dendritically and at inter-dendritic regions, Al segregation could be observed in EDS line elemental analysis, as shown in Figure 8.7. This could be concluded that the alloy primarily solidifies as α_2 phase and left over aluminium rich portion becomes γ phase, giving rise to the nanolamellar formation. Non equilibrium α_2 supersaturation condition, upon in situ cyclic heating, was taken back to equilibrium through this nanolamellar formation followed by discontinuous coarsening.

β phase formation was not observed in LENS and this is attributed by lack of preheating condition during LENS printing. In other words, it is possible to control β phase formation during EBM, by reducing preheating temperature or by reducing the ED. Al evaporation was negligible in case of LENS, attributed by Ar in printing environment instead of vacuum. This also contributed to the absence of beta phase in LENS fabricated samples.

Alloy modification was done with an intention to control the coarsening. Silicide precipitate pinning effect in lamellar interface was observed, causing decrease in lamellar coarsening.

Chapter 9: Conclusions and Suggestions for Future Work

9.1 Conclusions

In this study, titanium aluminide alloys mainly Ti-48Al-2Cr-2Nb, were additively manufactured using both EBM and LENS technologies. The effect of different process parameters, such as energy density (ED), build temperature and layer thickness, on the as-fabricated samples were analysed. Processing conditions during additive manufacturing (AM) significantly influences microstructural evolution of TiAl intermetallic alloy. Thermal cycling, which is inherent in EBM and LENS AM technologies, leads to solid state transformations (SST) reactions. Discontinuous Coarsening (DC) and beta phase formation completely replaces primary lamellar structure, by a secondary structure. The effect of in-situ heat cycles on microstructural evolution and different solid-state transformations (SST) were analysed along the build direction in detail. The following conclusions are drawn based on the current microstructural study.

1) A stable TiAl printing process is challenged by continuous arc tripping because of the charge build up in the powder. The build temperature in the range 900 ºC -1050 ºC and performing hardware adjustments to reduce heat losses from the powder bed during the melting was quite effective to prevent the arc trip in EBM of TiAl.

2) The EBM process window is relatively narrow in order to obtain desired microstructures and properties. There is a trade-off between creating a uniform microstructure that would need a higher energy input versus avoiding evaporation of lighter element like aluminium that favours a lower energy input. For a given energy input, smaller layer thickness of 70 μm was found to be effective in improving the uniformity along build direction with significant reduction in aluminium loss.

3) High energy input samples favour lamellar microstructural formation, due to its relatively lower cooling rate. Whereas low energy input results in duplex microstructure. The average lamellar colony size increases with increasing ED. The low energy input can result in layered microstructure in an as-fabricated sample. This is mainly due to the

inadequate in situ heat treatment that a solidified layer undergoes, during the building process.

4) Special focus was given to the effects of process temperature and time on phase formation and evolution. It was found that the amount of in situ aging and thermal cycling can result in different as-fabricated microstructures. The microstructure after solidification from melt pool, i.e. the primary structure is not at equilibrium state due to rapid solidification in additive manufacturing (AM). Primary lamellar structure (PLS) is far out of equilibrium with higher phase fraction of α_2. In addition to that, PLS has a high interface energy due to ultra-fine lamellae. These PLS instabilities cause gain boundary migration and undergoes discontinuous coarsening (DC). The primary lamellar structure is completely replaced by secondary structure after DC.

5) The second solid-state transformation observed in EBM process is precipitation of the β (ordered β) phase through dissolution of α_2 lamellae. Formation of beta phase is influenced by input ED and build temperature. Beta formation has significant influence on the lamellar colony size and discontinuous coarsening. Lamellar colony size was found to be lesser in beta rich regions.

6) Investigations on the occurrence of DC and its control during different AM methods were required for better understanding different SST in AM. DC studies carried out in LENS TiAl sample helped to obtain a better understanding of DC in general. DC in LENS was found to be lesser than EBM due to different process thermal conditions.

7) Based on the microstructural studies of EBM and LENS processed Ti-48Al-2Cr-2Nb samples, 0.5Si (at.%) was added with an intension to control DC. Results showed that silicide precipitated in lamellar colonies, resulting in a decrease in lamellar coarsening.

9.2 Future work

This research has made significant contribution to the theory in understanding the behaviour of TiAl alloy made by AM methods, such as EBM and LENS, however there are areas that require further investigation, especially the complexities in microstructural evolution and mechanical properties at high temperature. The details of proposed future work are described below.

1. Study the dynamic properties of reaction front (RF) of the grain boundary migration in the lamellar structure by in situ observation which could show the nucleation and growth of DC cells with repeated cycling. Complex thermal history associated with the EBM process and the lack of melt pool or thermal history is a challenging issue that require further investigation into the solid-state transformations and kinetics in the process. Advanced thermo mechanical systems and numerical simulations can be used to obtain thermal histories more efficiently.

2. TEM study of dislocation morphology and its distribution in lamellar interface and colony boundaries, for a better understanding of nucleation of discontinuous coarsening and beta formation in the AM, specifically in EBM and LENS.

3. For EBM manufacturing using newer alloys, process strategy development requires complicated sequential adjustment of parameters, experimentally. The EBM process need to be optimised for modified Ti-47.5Al-2Cr-2Nb-0.5Si alloy. After the optimisation, mechanical property study, mainly high temperature properties of as fabricated and heat-treated samples are needed to understand the effect of alloy modification on mechanical properties.

4. Develop a digital twin for TiAl microstructural evolution in EBM and LENS through close collaboration with experimental metallurgist and modelling expert to simulate the unique thermal histories in AM, in order to predict the following:

    - The microstructural features such as lamellar or duplex microstructure
    - Precipitation/morphology of the various phases within the material
    - The occurrence of defects

5. Ti-48Al-2Cr-2Nb alloy that was predominantly used in this study, was developed for a conventional process. Development of a TiAl based intermetallic alloy specifically for AM is another prospective area for further research.

Reference

1. Leyens C, Peters M. Titanium and titanium alloys: fundamentals and applications. John Wiley & Sons; 2003.
2. Lütjering G, Williams JC. Titanium. Springer Science & Business Media; 2007.
3. Appel F, Paul JD, Oehring M. Gamma titanium aluminide alloys: science and technology. John Wiley & Sons; 2011.
4. Bewlay BP, Nag S, Suzuki A, Weimer MJ. TiAl alloys in commercial aircraft engines. Materials at High Temperatures. 2016; 4:549-59.
5. Chen W, Li Z. Additive manufacturing of titanium aluminides. "Additive Manufacturing for the Aerospace Industry". Elsevier. 2019; 235-263.
6. Appel F, Oehring M, Wagner R. Novel design concepts for gamma-base titanium aluminide alloys. Intermetallics. 2000; 8:1283-312.
7. Zghal S, Naka S, Couret A. A quantitative TEM analysis of the lamellar microstructure in TiAl based alloys. Acta Materialia. 1997; 7:3005-15.
8. Beschliesser M, Chatterjee A, Lorich A, Knabl W, Kestler H, Dehm G, Clemens H. Designed fully lamellar microstructures in a γ-TiAl based alloy: adjustment and microstructural changes upon long-term isothermal exposure at 700 and 800° C. Materials Science and Engineering. 2002; 329:124-9.
9. Brotzu A, Felli F, Pilone D. Effect of alloying elements on the behaviour of TiAl-based alloys. Intermetallics. 2014; 54:176-80.
10. Gupta RK, Pant B, Sinha PP. Theory and practice of γ+ α_2 Ti aluminide: A review. Transactions of the Indian Institute of Metals. 2014; 2:143-65.
11. Clemens H, Mayer S. Design, processing, microstructure, properties and applications of advanced intermetallic TiAl alloys. Advanced Engineering Materials. 2013; 15: 191-215.
12. Wu X. Review of alloy and process development of TiAl alloys. Intermetallics. 2006;14: 1114-22.
13. Kothari K, Radhakrishnan R, Wereley NM. Advances in gamma titanium aluminides and their manufacturing techniques. Progress in Aerospace Sciences. 2012; 55:1-6.
14. Kim YW, Dimiduk DM. Progress in the understanding of gamma titanium aluminides. JOM. 1991; 43:40-7.
15. Djanarthany S, Viala JC, Bouix J. An overview of monolithic titanium aluminides based on Ti3Al and TiAl. Materials chemistry and physics. 2001; 723: 301-19.
16. Johnson DR, Inui H, Muto S, Omiya Y, Yamanaka T. Microstructural development during directional solidification of α-seeded TiAl alloys. Acta Materialia. 2006; 54: 1077-85.
17. Srivastava D, Hu D, Chang IT, Loretto MH. The influence of thermal processing route on the microstructure of some TiAl-based alloys. Intermetallics. 1999 ;71: 1107-12.
18. Hall EL, Huang SC. Microstructures of rapidly-solidified binary TiAl alloys. Acta Metallurgica et Materialia. 1990; 38: 539-49.
19. Kenel C, Leinenbach C. Influence of cooling rate on microstructure formation during rapid solidification of binary TiAl alloys. Journal of Alloys and Compounds. 2015; 637:242-7.
20. Denquin A, Naka S. Phase transformation mechanisms involved in two-phase TiAl-based alloys-I. Lamellar structure formation. Acta Materialia. 1996; 44: 343-52.

21. Zhu H, Seo DY, Maruyama K, Au P. Effect of lamellar spacing on microstructural instability and creep behavior of a lamellar TiAl alloy. Scripta materialia. 2006 54: 1979-84.
22. Zhu H, Maruyama K, Seo DY, Au P. Microstructural stability of fine-grained fully lamellar XD TiAl alloys by step aging. Metallurgical and Materials Transactions A. 2005;36: 1339.
23. Xia K, Wu X, Song D. Effects of Gd addition, lamellar spacing and loading direction on creep behaviour of a fully lamellar Ti–44Al–1Mn–2.5 Nb alloy. Acta materialia. 2004;52: 841-9.
24. Li W, Liu J, Zhou Y, Wen S, Tan J, Li S, Wei Q, Yan C, Shi Y. Texture evolution, phase transformation mechanism and nanohardness of selective laser melted Ti-45Al-2Cr-5Nb alloy during multi-step heat treatment process. Intermetallics. 2017; 85:130-8.
25. Schwaighofer E, Clemens H, Mayer S, Lindemann J, Klose J, Smarsly W, Güther V. Microstructural design and mechanical properties of a cast and heat-treated intermetallic multi-phase γ-TiAl based alloy. Intermetallics. 2014; 44:128-40.
26. Bolz S, Oehring M, Lindemann J, Pyczak F, Paul J, Stark A, Lippmann T, Schrüfer S, Roth-Fagaraseanu D, Schreyer A, Weiß S. Microstructure and mechanical properties of a forged β-solidifying γ TiAl alloy in different heat treatment conditions. Intermetallics. 2015; 58:71-83.
27. Wang JN, Yang J, Wang Y. Grain refinement of a Ti–47Al–8Nb–2Cr alloy through heat treatments. Scripta Materialia. 2005;52: 329-34.
28. Sun FS, Cao CX, Yan MG, Kim SE. Alloying mechanism of beta stabilizers in a TiAl alloy. Metallurgical and Materials Transactions A. 2001;32: 1573-89.
29. Appel F, Clemens H, Fischer FD. Modeling concepts for intermetallic titanium aluminides. Progress in Materials Science. 2016; 81:55-124.
30. Kastenhuber M, Klein T, Clemens H, Mayer S. Tailoring microstructure and chemical composition of advanced γ-TiAl based alloys for improved creep resistance. Intermetallics. 2018; 97:27-33.
31. Klein T, Rashkova B, Holec D, Clemens H, Mayer S. Silicon distribution and silicide precipitation during annealing in an advanced multi-phase γ-TiAl based alloy. Acta Materialia. 2016; 110:236-45.
32. Clemens H, Wallgram W, Kremmer S, Güther V, Otto A, Bartels A. Design of Novel β-Solidifying TiAl Alloys with Adjustable β/B2-Phase Fraction and Excellent Hot-Workability. Advanced engineering materials. 2008; 8: 707-13.
33. Voisin T, Monchoux JP, Hantcherli M, Mayer S, Clemens H, Couret A. Microstructures and mechanical properties of a multi-phase β-solidifying TiAl alloy densified by spark plasma sintering. Acta materialia. 2014; 73: 107-15.
34. Dahar MS, Tamirisakandala SA, Lewandowski JJ. Fatigue crack growth and fracture behavior of as-cast Ti-43.5 Al-4Nb-1Mo-0.1B (TNM) compared to Ti-48Al-2Nb-2Cr. Intermetallics. 2017; 91:158-68.
35. Martin JW, Martin JW, Doherty RD, Cantor B. Stability of microstructure in metallic systems. Cambridge University Press; 1997.
36. Hu D, Godfrey AB, Loretto MH. Thermal stability of a fully lamellar Ti-48Al-2Cr-2Nb-1B alloy. Intermetallics. 1998; 5: 413-417.

37. Karthikeyan S, Mills MJ. The role of microstructural stability on compression creep of fully lamellar γ-TiAl alloys. Intermetallics. 2005;13: 985-92.
38. Ramanujan RV. The coarsening of lamellae in Ti-48Al-2Mn-2Nb. Acta metallurgica et materialia. 1994;42: 2775-81.
39. Manna I, Pabi SK, Gust W. Discontinuous reactions in solids. International Materials Reviews. 2001;46: 53-91.
40. Li X, Bottler F, Spatschek R, Schmitt A, Heilmaier M, Stein F. Coarsening kinetics of lamellar microstructures: Experiments and simulations on a fully-lamellar Fe-Al in situ composite. Acta Materialia. 2017; 127:230-43.
41. Livingston JD, Cahn JW. Discontinuous coarsening of aligned eutectoids. Acta Metallurgica. 1974;22: 495-503.
42. Bartholomeusz MF, Wert JA. The effect of thermal exposure on microstructural stability and creep resistance of a two-Phase TiAl/Ti_3Al lamellar alloy. Metallurgical and Materials Transactions A. 1994;25 :2371-81.
43. Loria EA. Quo vadis gamma titanium aluminide. Intermetallics. 2001;9: 997-1001.
44. Baudana G, Biamino S, Klöden B, Kirchner A, Weißgärber T, Kieback B, Pavese M, Ugues D, Fino P, Badini C. Electron beam melting of Ti-48Al-2Nb-0.7 Cr-0.3 Si: feasibility investigation. Intermetallics. 2016; 73:43-9.
45. Milewski JO. Additive manufacturing of metals: from fundamental technology to rocket nozzles, medical implants, and custom jewellery. Springer; 2017.
46. Brandt M, editor. Laser Additive Manufacturing: Materials, Design, Technologies, and Applications. Woodhead Publishing; 2016.
47. Sames WJ, List FA, Pannala S, Dehoff RR, Babu SS. The metallurgy and processing science of metal additive manufacturing. International Materials Reviews. 2016;61: 315-60.
48. Herzog D, Seyda V, Wycisk E, Emmelmann C. Additive manufacturing of metals. Acta Materialia. 2016; 117:371-92.
49. Körner C. Additive manufacturing of metallic components by selective electron beam melting—a review. International Materials Reviews. 2016;61: 361-77.
50. DebRoy T, Wei HL, Zuback JS, Mukherjee T, Elmer JW, Milewski JO, Beese AM, Wilson-Heid A, De A, Zhang W. Additive manufacturing of metallic components–process, structure and properties. Progress in Materials Science. 2018; 92:112-224.
51. Lewandowski JJ, Seifi M. Metal additive manufacturing: a review of mechanical properties. Annual review of materials research. 2016; 46:151-86.
52. Gu DD, Meiners W, Wissenbach K, Poprawe R. Laser additive manufacturing of metallic components: materials, processes and mechanisms. International materials reviews. 2012;57: 133-64.
53. Murr LE, Gaytan SM, Ramirez DA, Martinez E, Hernandez J, Amato KN, Shindo PW, Medina FR, Wicker RB. Metal fabrication by additive manufacturing using laser and electron beam melting technologies. Journal of Materials Science & Technology. 2012; 28:1-4.
54. Cormier D, Harrysson O, Mahale T, West H. Freeform Fabrication of Titanium Aluminide via Electron Beam Melting Using Prealloyed and Blended Powders. Research Letters in Materials Science. 2007; 07:1-4.
55. Murr LE, Gaytan SM, Ceylan A, Martinez E, Martinez JL, Hernandez DH, Machado BI, Ramirez DA, Medina F, Collins S, Wicker RB. Characterization of titanium

aluminide alloy components fabricated by additive manufacturing using electron beam melting. Acta materialia. 2010; 58: 1887-94.
56. Schwerdtfeger J, Körner C. Selective electron beam melting of Ti–48Al–2Nb–2Cr: Microstructure and aluminium loss. Intermetallics. 2014; 49:29-35.
57. Biamino S, Penna A, Ackelid U, Sabbadini S, Tassa O, Fino P, Pavese M, Gennaro P, Badini C. Electron beam melting of Ti–48Al–2Cr–2Nb alloy: Microstructure and mechanical properties investigation. Intermetallics. 2011;19: 776-81.
58. Todai M, Nakano T, Liu T, Yasuda HY, Hagihara K, Cho K, Ueda M, Takeyama M. Effect of building direction on the microstructure and tensile properties of Ti-48Al-2Cr-2Nb alloy additively manufactured by electron beam melting. Additive Manufacturing. 2017; 13:61-70.
59. Mohammad A, Alahmari A, Mohammed M, Renganayagalu R, Moiduddin K. Effect of energy input on microstructure and mechanical properties of titanium aluminide alloy fabricated by the additive manufacturing process of electron beam melting. Materials. 2017;10: 211.
60. Slotwinski JA, Garboczi EJ. Metrology needs for metal additive manufacturing powders. Jom. 2015;67: 538-43.
61. Strondl A, Lyckfeldt O, Brodin H, Ackelid U. Characterization and control of powder properties for additive manufacturing. Jom. 2015; 3: 549-554.
62. Dawes J, Bowerman R, Trepleton R. Introduction to the additive manufacturing powder metallurgy supply chain. Johnson Matthey Technology Review. 2015; 3: 243-56.
63. Galati M, Iuliano L. A literature review of powder-based electron beam melting focusing on numerical simulations. Additive Manufacturing. 2018; 19:1-20.
64. Gong H, Rafi K, Gu H, Starr T, Stucker B. Analysis of defect generation in Ti–6Al–4V parts made using powder bed fusion additive manufacturing processes. Additive Manufacturing. 2014; 1: 87-98.
65. Brandl E, Palm F, Michailov V, Viehweger B, Leyens C. Mechanical properties of additive manufactured titanium (Ti–6Al–4V) blocks deposited by a solid-state laser and wire. Materials & Design. 2011;32: 4665-75.
66. Wang L, Felicelli S, Gooroochurn Y, Wang PT, Horstemeyer MF. Optimization of the LENS process for steady molten pool size. Materials Science and Engineering: A. 2008; 474:148-56.
67. Sharman AR, Hughes JI, Ridgway K. Characterisation of titanium aluminide components manufactured by laser metal deposition. Intermetallics. 2018; 93: 89-92.
68. Seidel A, Saha S, Maiwald T, Moritz J, Polenz S, Marquardt A, Kaspar J, Finaske T, Lopez E, Brueckner F, Leyens C. Intrinsic Heat Treatment Within Additive Manufacturing of Gamma Titanium Aluminide Space Hardware. JOM. 2019; 71: 1513-9.
69. Srivastava D, Chang IT, Loretto MH. The effect of process parameters and heat treatment on the microstructure of direct laser fabricated TiAl alloy samples. Intermetallics. 2001; 12:1003-13.
70. Mendenhall MH, Mullen K, Cline JP. An implementation of the Fundamental Parameters Approach for analysis of X-ray powder diffraction line profiles. Journal of research of the National Institute of Standards and Technology. 2015; 120: 223 -26.
71. Keist JS, Palmer TA. Development of strength-hardness relationships in additively manufactured titanium alloys. Materials Science and Engineering: A. 2017; 693:214-24.

72. Li Y, Yang Y, Wu Y, Wang L, Liu X. Quantitative comparison of three Ni-containing phases to the elevated-temperature properties of Al–Si piston alloys. Materials Science and Engineering: A. 2010; 26: 7132-7.
73. Strondl A, Lyckfeldt O, Brodin H, Ackelid U. Characterization and control of powder properties for additive manufacturing. Jom. 2015; 3: 549-54.
74. Cunningham R, Narra SP, Ozturk T, Beuth J, Rollett AD. Evaluating the effect of processing parameters on porosity in electron beam melted Ti-6Al-4V via synchrotron X-ray microtomography. Jom. 2016; 3: 765-71.
75. Juechter V, Franke MM, Merenda T, Stich A, Körner C, Singer RF. Additive manufacturing of Ti-45Al-4Nb-C by selective electron beam melting for automotive applications. Additive Manufacturing. 2018; 22: 118-26.
76. Cordero ZC, Meyer III HM, Nandwana P, Dehoff RR. Powder bed charging during electron-beam additive manufacturing. Acta Materialia. 2017; 124: 437-45.
77. Kan W, Chen B, Jin C, Peng H, Lin J. Microstructure and mechanical properties of a high Nb-TiAl alloy fabricated by electron beam melting. Materials & Design. 2018; 160: 611-23.
78. Wang H, Zhu D, Zou CM, Wei ZJ. Microstructure and nanohardness of Ti-48% Al alloy prepared by rapid solidification under different cooling rates. Transactions of Nonferrous Metals Society of China. 2011; 21: 328-32.
79. Liu Z, Kim H, Liu W, Cong W, Jiang Q, Zhang H. Influence of energy density on macro/micro structures and mechanical properties of as-deposited Inconel 718 parts fabricated by laser engineered net shaping. Journal of Manufacturing Processes. 2019; 42: 96-105.
80. Gäumann M, Bezencon C, Canalis P, Kurz W. Single-crystal laser deposition of superalloys: processing–microstructure maps. Acta materialia. 2001; 49:1051-62.
81. Zhang WJ, Reddy BV, Deevi SC. Physical properties of TiAl-base alloys. Scripta Materialia. 2001;45: 645-51.
82. Shen N, Chou K. Thermal modelling of electron beam additive manufacturing process: powder sintering effects. ASME International Manufacturing Science and Engineering Conference Processing 2012; l287-295.
83. Al-Bermani, SS, "An Investigation into Microstructure and Microstructural Control of Additive Layer Manufactured Ti-6Al-4V by Electron Beam Melting," The University of Sheffield, 2011.
84. Yue H, Chen Y, Wang X, Kong F. Effect of beam current on microstructure, phase, grain characteristic and mechanical properties of Ti-47Al-2Cr-2Nb alloy fabricated by selective electron beam melting. Journal of Alloys and Compounds. 2018; 750:617-25.
85. Sharma G, Ramanujan RV, Tiwari GP. Instability mechanisms in lamellar microstructures. Acta materialia. 2000;48: 875-89.
86. Ramanujan RV. Phase transformations in γ based titanium aluminides. International Materials Reviews. 2000;45: 217-40.
87. Denquin A, Naka S. Phase transformation mechanisms involved in two-phase TiAl-based alloys—II. Discontinuous coarsening and massive-type transformation. Acta materialia. 1996;44: 353-65.

88. Kaya M, Smith RW. The discontinuous coarsening reactions in the Pb-Cd and the Zn-Cd lamellar eutectic alloys-I. The driving force, initiation and the morphology. Acta Metallurgica. 1989; 37:1657-65.
89. Livingston JD, Cahn JW. Discontinuous coarsening of aligned eutectoids. Acta Metallurgica. 1974;22: 495-503.
90. Kaya M, Smith RW. The discontinuous coarsening reactions in the Pb-Cd and the Zn-Cd lamellar eutectic alloys—II. Growth kinetics. Acta Metallurgica. 1989; 37:1667-76.
91. Qin GW, Oikawa K, Sun ZM, Sumi S, Ikeshoji T, Wang JJ, Guo SW, Hao SM. Discontinuous coarsening of the lamellar structure of γ-TiAl-based intermetallic alloys and its control. Metallurgical and Materials Transactions A. 2001;32: 1927-38.
92. Fournelle RA. Discontinuous coarsening of lamellar cellular precipitate in an austenitic Fe-30 wt.% Ni-6 wt.% Ti alloy—II. Growth kinetics. Acta Metallurgica. 1979; 27:1147-55.
93. Shong DS, Kim YW. Discontinuous coarsening of high perfection lamellae in titanium aluminides. Scripta metallurgica. 1989;23: 257-61.
94. Yang J, Wang JN, Wang Y, Xia Q. Refining grain size of a TiAl alloy by cyclic heat treatment through discontinuous coarsening. Intermetallics. 2003; 11: 971-4.
95. Klassen A, Forster VE, Juechter V, Körner C. Numerical simulation of multi-component evaporation during selective electron beam melting of TiAl. Journal of Materials Processing Technology. 2017; 247: 280-8.
96. Saunders N. Phase equilibria in multi-component γ-TiAl based alloys. Gamma titanium aluminides: TMS Warrendale, PA. 1999:183-8.
97. Li J, Song B, Nurly H, Xue P, Wen S, Wei Q, Shi Y. Microstructure evolution and a new mechanism of B2 phase on room temperature mechanical properties of Ti-47Al-2Cr-2Nb alloy prepared by hot isostatic pressing. Materials Characterization. 2018; 140:64-71.
98. Fang L, Lin JP, Ding XF. Thermal cycling induced microstructural instability in fully lamellar Ti–45Al–8.5 Nb– (W, B, Y) alloys. Materials Chemistry and Physics. 2015; 167: 112-18.
99. Wu Y, Zhang S, Cheng X, Wang H. Investigation on solid-state phase transformation in a Ti-47Al-2Cr-2V alloy due to thermal cycling during laser additive manufacturing process. Journal of Alloys and Compounds. 2019; 799:325-33.
100. Kou S. Welding Metallurgy, A John Wiley & Sons. INC., Publication, New Jersey. 2003.
101. Guyon J, Hazotte A, Bouzy E. Evolution of metastable α phase during heating of Ti-48-Al-2Cr-2Nb intermetallic alloy. Journal of Alloys and Compounds. 2016; 656:667-75.
102. Sames WJ, Unocic KA, Dehoff RR, Lolla T, Babu SS. Thermal effects on microstructural heterogeneity of Inconel 718 materials fabricated by electron beam melting. Journal of Materials Research. 2014; 17: 1920-30
103. Tsuyama S, Mitao S, Minakawa KN. Alloy modification of γ-base titanium aluminide for improved oxidation resistance, creep strength and fracture toughness. High Temperature Aluminides and Intermetallics, Elsevier. 1992; 451-456.